BRL

CONTRACT REPORT NO. 352

CORRELATION STUDY OF THE UH-IB HELICOPTER BLAST TEST RESULTS FROM THE DICE-THROW EVENT

Prepared by

A Division of Kaman Sciences Corporation
83 Second Avenue
Burlington, Massachusetts 01803

October 1977

USA ARMAMENT RESEARCH AND DEVELOPMENT COMMAND
USA BALLISTIC RESEARCH LABORATORY
ABERDEEN PROVING GROUND, MARYLAND

Destroy this report when it is no longer needed.
Do not return it to the originator.

Secondary distribution of this report by originating or sponsoring activity is prohibited.

Additional copies of this report may be obtained from the National Technical Information Service, U.S. Department of Commerce, Springfield, Virginia 22161.

The findings in this report are not to be construed as an official Department of the Army position, unless so designated by other authorized documents.

The use of trade names or manufacturers' names in this report does not constitute indorsement of any commercial product.

REPORT DOCUMENTATION PAGE

READ INSTRUCTIONS BEFORE COMPLETING FORM

1. REPORT NUMBER: BRL CONTRACT REPORT NO. 352
2. GOVT ACCESSION NO.
3. RECIPIENT'S CATALOG NUMBER

4. TITLE (and Subtitle): Correlation Study of the UH-1B Helicopter Blast Test Results From The Dice-Throw Event

5. TYPE OF REPORT & PERIOD COVERED: Final Report 1 October 1976 - 31 May 1977

6. PERFORMING ORG. REPORT NUMBER: KA TR-138

7. AUTHOR(s): Garabed Zartarian, Eldine L. Cole, William N. Lee

8. CONTRACT OR GRANT NUMBER(s): DAAD05-76-C-0772

9. PERFORMING ORGANIZATION NAME AND ADDRESS: A Division of Kaman Sciences Corporation, 83 Second Avenue, Burlington, Massachusetts 01803

10. PROGRAM ELEMENT, PROJECT, TASK AREA & WORK UNIT NUMBERS

11. CONTROLLING OFFICE NAME AND ADDRESS: Directorate, U.S. Army Ballistic Research Laboratory, Aberdeen Proving Ground, Maryland 21005

12. REPORT DATE: OCTOBER 1977

13. NUMBER OF PAGES: 207

14. MONITORING AGENCY NAME & ADDRESS (if different from Controlling Office): US Army Materiel Development & Readiness Command, 5001 Eisenhower Avenue, Alexandria, VA 22333

15. SECURITY CLASS. (of this report): Unclassified

15a. DECLASSIFICATION DOWNGRADING SCHEDULE

16. DISTRIBUTION STATEMENT (of this Report)

Approved for public release; distribution unlimited.

17. DISTRIBUTION STATEMENT (of the abstract entered in Block 20, if different from Report)

18. SUPPLEMENTARY NOTES

19. KEY WORDS (Continue on reverse side if necessary and identify by block number)

Vulnerability	DICE-THROW Test
Blast Effects	Helicopter
Gust Effects	Helicopter Rotor

20. ABSTRACT (Continue on reverse side if necessary and identify by block number)

This report summarizes the results of a correlation study conducted in conjunction with the UH-1B helicopter blast test during the DICE THROW event. The processed structural and motion response data from the hovering and droned helicopter are presented. They are correlated with corresponding analytical predictions based primarily on the helicopter code HELP and the aircraft structural code NOVA-2. The monitored blast-induced responses include:

(1) The flapwise bending moments and the flapping angles of both the tail and main rotor blade systems.

(2) The lateral bending moments at two fin and two tail boom stations.

(3) The overall rigid-body motions of the vehicle consisting of the altitude variations, the attitude and angular rate variations in the yaw, pitch, and roll degrees-of-freedom.

(4) The strains at selected points on a tail boom panel, a stiffener, and a longeron.

Considering the qualities of the available input data for the analyses and of the measurements, the experimental results are generally in reasonable agreement with the predictions from the HELP code. The NOVA-2 predictions for panel, stiffener, and longeron strains fare poorly when compared with experiment. In some instances, significant differences are found between experiment and analysis. Whenever possible, the reasons for the disagreements are identified and discussed.

FOREWORD

This report was prepared by Kaman AviDyne, a Division of Kaman Sciences Corporation, Burlington, Massachusetts, for the U.S. Army Ballistic Research Laboratory (BRL), under Contract No. DAAD05-76-C-0772. The work was performed within the Structural Mechanics Group, headed by Mr. Emanuel S. Criscione. Mr. Robert D. Mayerhofer of BRL was the technical monitor and the DICE-THROW Helicopter Test Project Engineer. The senior author served as the project leader for Kaman AviDyne. Mr. Al Williamson of the U.S. Army Mobility Research and Development Laboratory (Fort Eustis) instrumented the vehicle, conducted the tests, and acquired the experimental data. Mr. Eldine L. Cole of Kaman Sciences at Colorado Springs performed all the data processing.

The authors wish to express their appreciation to Messrs. Mayerhofer and Williamson for their cooperation and assistance. Thanks are also due to Mr. Michael Tomayko of the Kaman AviDyne staff for providing programming and computational support.

TABLE OF CONTENTS

TABLE OF CONTENTS (CONT'D)

LIST OF ILLUSTRATIONS

LIST OF ILLUSTRATIONS (CONT'D)

LIST OF ILLUSTRATIONS (CONT'D)

LIST OF ILLUSTRATIONS (CONT'D)

LIST OF ILLUSTRATIONS (CONT'D)

LIST OF ILLUSTRATIONS (CONT'D)

LIST OF TABLES

SECTION 1
INTRODUCTION

During the DICE THROW event, a hovering UH-1B helicopter was subjected to the blast field from a 628 ton ANFO (HE) burst. This effort represents a continuation of a series of tests (DIAL PACK, MIXED COMPANY, and PRE-MINE THROW IV) to acquire a data base for assessing the blast vulnerability of helicopters to nuclear bursts.

In the DIAL PACK event, the test objectives were very limited in that only "qualitative damage data" were sought from a parked helicopter. Furthermore, the rotors were stationary and the emphasis was placed on observing the structural damage to fuselage components. The aircraft was situated so as to receive a 2.3 psi overpressure shock from broadside. In MIXED COMPANY, conducted at Grand Junction, Colorado, on 13 November 1972, an attempt was made to obtain quantitative data of blast-induced vehicle rigid-body motion responses as well as certain rotor blade and fuselage structural responses from a hovering and droned UH-1B. The distance from ground zero and the orientation were such that the vehicle was to receive a 1.3 psi overpressure shock (also directly from its portside) from a 500 ton TNT burst. Unfortunately, the helicopter was not airborne during the test due to a malfunction in the autopilot/remote controller system. Consequently, the test failed to fulfill some of its objectives inasmuch as the obtained quantitative data applied only to a parked helicopter with rotors shut off. The PRE-MINE THROW IV test, conducted successfully at Yucca Lake, Nevada Test Site, on 17 August 1974, was a repeat effort of the earlier attempt, but with a lower yield burst (100 ton nitromethane). The vehicle was therefore positioned closer to ground zero. It did receive the desired level shock ($\sim$1.36 psi) but, as expected because of the lower yield, the overpressure positive phase duration was rather short (about 235 msecs) to induce sizeable rigid-body motions. The experimental results and the analytical-experimental correlations for the PRE-MINE THROW IV test are documented in Reference 1.

The prime objective of the DICE THROW test was to acquire the same sort of data but for significantly higher overpressure and positive phase duration levels. In fact, it was hoped that the input would be high enough to cause a severe (but not catastrophic) damage. Relying on some pre-test calculations (Reference 2), it was decided to position the vehicle at around 2700 ft from ground zero so that it would be subjected to a 1.8 psi overpressure shock. Based on some data on structural allowables, the calculations predicted a possible severe damage to the tail boom. In addition to the higher input levels, there were some changes made in the instrumentation, e.g., acceleration measurements were replaced by additional measurements on the rotor blades, etc.

This report documents the experimental data from DICE-THROW along with the experimental-analytical correlation results. They pertain primarily to the following responses:

(1) The tail and main rotor flapwise bending moments and flapping angles.

(2) The vehicle rigid-body motions, including the altitude deviation and the attitudes and rates in the yaw, pitch, and roll degrees-of-freedom.

(3) The fin and tail boom lateral bending moments.

(4) Blast-induced strains in tail boom structural elements such as panels, a stiffener, and a longeron.

The purpose of obtaining the responses under items (1)-(3) was to provide experimental data and assessment of predictions based on the HELP code. The development and application details are covered in Reference 3. The responses under item (4) were obtained to check the overpressure analysis incorporated in the NOVA code. The details of the NOVA code may be found in Reference 4.

Section 2 presents summary tables of the various measurements of interest and describes the data reduction procedures. Section 3-8 inclusive present the processed experimental data, brief descriptions of and comments about the analytical models and techniques used, and the analytical-experimental correlations according to the following schedule:

Section 3 - Establishment of the blast model (for use in the calculations based on HELP) and of the panel loadings (for use in the calculations based on NOVA).

Section 4 - Flapwise bending moment and motion responses of the tail and main rotor blades.

Section 5 - Overall vehicle rigid-body motion responses.

Section 6 - Fin and tail boom lateral bending moment responses.

Section 7 - Tail boom panel, stringer, and longeron strain responses.

Section 8 - A summary and the conclusions drawn from this correlation study.

SECTION 2

DATA ACQUISITION AND REDUCTION

2.1 Measurements

Active measurements made on the helicopter during the experiment included 9 different types with a total of 44 data channels. Four 14-track magnetic tape recorders were required. Each data channel used an instrumentation amplifier to adjust the signal level for optimum utilization of the FM channel bandedge. Overall system bandwidth was limited by these amplifiers to be 15 kHz, a value considered more than adequate for high fidelity recording of the sought measurements.

The No. 8 channels of all four tape recorders were used to include a 100 kHz reference signal. Also, the No. 13 channels were reserved for the IRIGB plus FIDU signals for referencing the times to burst time. The No. 14 channels were not utilized.

Tape recorder track assignment and channel identification are given in Table 2.1.

The data return can be considered quite good as only one channel (D-09) was completely lost. This was apparently due to pre-test failure of the pressure transducer on the anthromorphic dummy in the pilot seat. The calibration for another channel, namely that for the main rotor collective pitch (B-12), was not established. A few words need be added at this point, however, concerning the calibration constants. During the correlation phase, a number of questions were raised, casting doubts about the accuracies of some of the cal constants. A review of the calibration procedures and recorded data revealed errors for some channels; and for others, there are indications that the calibration constants may not be as accurate as hoped for. In fact, in some instances, the last and most important calibration sequences were found to be invalid, and the necessary calibration data had to be deduced in "round-about ways" from earlier calibration data. Some of these problems and uncertainties are discussed further in Section 2.3. The calibration problems are deferred to the correlation sections where each channel is covered individually.

As a general statement, the signal-to-noise ratio (SNR) was quite satisfactory and the measurement systems performed as expected.

2.2 Data Reduction Procedure

The original data tape recordings were used for playback and data reduction because previous experience has shown that the quality of a dubbed copy is measurably degraded. Dub copies of the tapes were therefore made and kept as protection in the event of damage to the masters.

Reduction from analog tape records to computer plots of digitized data is handled as a two-stage process at KSC. The first step involves playback of analog tapes and subsequent analog-to-digital conversion (ADC) of selected portions of the data. Next these digitized data records are converted to physical units by application of calibration data and plotted as amplitude-time histories using the digital computer for numerical computations and plotting.

The data reduction system and procedure are essentially those of Reference 1 and their details are not repeated here. In what follows, only changes due to special problems arising from the more recent data are discussed.

2.2.1 Playback and ADC

A block diagram of the playback system configured for ADC is shown in Figure 2.1. Three information channels on the tape are played back simultaneously: 1) The 100 kHz reference frequency for tape speed compensation (TSC), 2) The IRIG-B time code with blast zero (T-ZERO) superimposed, and 3) The data channel under consideration.

The 100 kHz reference frequency was recorded on channel 8 of each tape recorder to be used during playback as an input to the servo speed control circuit in the tape reproducer. This circuit adjusts the tape speed so that the reference frequency is 100 kHz during playback of the data, thus eliminating errors in both amplitude and time base that would otherwise be introduced if the reproduced speed was different from the recorded speed. The servo system is an electro-mechanical system with relatively low frequency response (>300 Hz) that is designed to eliminate wow and correct for differences in record and playback speeds.

The higher frequency tape speed errors known as flutter are compensated for using strictly electronic circuitry. This system uses the same reference frequency and an FM discriminator to detect frequency deviations. An error signal is fed to the data discriminator that compensates for amplitude errors due to speed changes. The flutter TSC system will compensate speed-induced amplitude errors of $\pm$ 7 1/2 percent with a bandwidth from dc to 4 kHz. It is important to note that it does not deal with any time base errors.

A shock-induced transient was observed in the 100 kHz reference signal on all recorders during the critical measurement period after blast arrival at the helicopter. The nature of this signal upset the servo system to an extent that it could not be used during playback. A complete description of this problem along with its implications on the accuracy of the data are presented in Section 2.3. Evidence that the flutter compensation for this disturbance was completely successful is also presented in Section 2.3.

A tunable FM discriminator is used to detect the baseband data signal to be digitized. The low-pass output filter (LPOF) which is an integral part of the discriminator set was selected to be compatible with channel bandwidth and the desired sampling rate for ADC. Output of the tunable discriminator is fed in parallel to the ADC and a storage oscilloscope used to monitor the record just digitized.

A third tape channel with the IRIG-B time code is used to provide a trigger signal that initiates the ADC and is also simultaneously an external trigger for the oscilloscope. In normal usage, the variable trigger pulse generator is set for the IRIG time that is desired to start the digitizing process. The blast zero reference marker that was superimposed on the IRIG time code channel caused the decoder to lose sync with the time code and recovery time for the circuit is longer than the delay to blast arrival at the helicopter. It was therefore necessary to use a delay trigger generator to produce a trigger pulse delayed from 0800 hours, before the time code interference from T-ZERO. Further discussion of this problem is also deferred to Section 2.3.

As an aid to bookkeeping and double check on the delay trigger generator setup, a time-interval meter (TIM) was gated on at T-ZERO by the marker on IRIG time and off by the delayed pulse that initiated the ADC.

Finally, a pulse rate generator is required to establish the sampling interval of the ADC. The sample rate is selected with consideration for the desired data bandwidth and record length. The digitized data are transferred to digital magnetic tape under control of the CYBER 73 computer for subsequent data processing.

2.2.2 Digital Data Processing

The digitized data records are paired with corresponding calibrations (which have also been digitized) and converted to appropriate physical units of amplitude vs. time with the aid of a basic data reduction program DATDUC. Input information includes data from the ADC log sheet such as sample interval, time of the first point digitized, and the file number of the data record to be processed. The value of the calibration signal is also input as DATDUC calculates the conversion factor from digitized counts to physical units (i.e. the sensitivity of the ADC in terms of physical units per digital increment). This scale factor is applied to each data point as a corresponding time array is generated. DATDUC has the capacity for numerical integration, differentiation, digital filtering, curve fitting, trend removal and other similar operations common to data processing.

A plotting subroutine is used to generate report quality plots of the final answer. Input parameters to the plot package facilitate choice of scale factors and ranges to accommodate most desires and requirements of the user.

Calibration information for each data channel is presented in Table 2.2.

2.3 Special Problems

Several unexpected difficulties were encountered during the course of the data reduction effort. This section describes the major problems along with an assessment of their impact on the accuracy of the measurements involved. One class of problems affects all of the data while another deals with channels on a one to one basis. The first two subjects of discussion of the former type are presented in subsection 2.3.1 and 2.3.2 followed by specific problems with specific questionable data that have been compromised in some way.

2.3.1 Tape Speed Compensation

Difference between record and playback speed can introduce error in the data that is manifest in distortion of both amplitude and time base. These effects are often very significant and can introduce large errors if not accounted for and corrected. The normal operation of the systems for tape speed control described in Section 2.1 was defeated by severe shock-induced transients that occurred on all tape records at 08:00:01.900. Since this is approximately 90 milliseconds after air blast arrival at the aircraft, the data would be distorted in regions of peak response and particular interest.

With trusting faith that the tape speed servo control (TSSC) and the tape speed compensation (TSC) systems would do their proper function, the data were all digitized and plotted. It was later noticed that certain of the bending moment channels showed discrepancies by comparison with quick-look oscillograph records. Investigation revealed that each time the tape was played over, the data waveforms were different. In an effort to uncover the reason for this response, the 100 kHz reference signal was input to the FM data discriminator.

The block diagram in Figure 2.2 will help in describing the results of the investigation. Observe that the normal system operation calls for both S1 and S2 to be closed. The scope trace seen in Figure 2.3a shows that the reference frequency transient deviation results in an amplitude error about 3% of bandedge with the TSSC disabled by S1. When S1 is closed and the TSSC is active, it is clearly seen in Figure 2.3b that the error is increased to 6%. The servo system has a very high open loop gain and short time constant. This gives an excellent response time and close control but it also tends to be unstable when shocked with energy above its bandwidth. Thus, in the particular case of DICE THROW the TSSC is seen to degrade the data due to the transient on the reference signal.

The TSC has a much higher frequency response and is able to compensate electronically to remove essentially all of the amplitude distortion from the output signal. The photo in Figure 2.3c shows this and represents the final configuration used in playback of all of the data presented later in this report.

A side effect of this "fix" to the problem is that the time base is distorted, especially in the region from around 85 to 140 milliseconds after blast arrival. Since the average signal appears to be near zero due to the oscillatory nature of the transient, the long-term time base error is probably close to zero.

The reference frequency was monitored with a frequency counter to determine correction factors between quasi-steady state record vs. playback speed. In all cases, this discrepancy was less than 0.5% and no correction was deemed necessary. The sampling interval is readily adjusted to correct for this sort of error if necessary.

In summary, the error in amplitude was effectively compensated for by the TSC; however, short term fluctuations of $\pm$3% in time base are likely in the range from 85-140 milliseconds from zero time shown on the plots. Outside this range, the error is negligible. The data shown in Figure 2.3 is for tape recorder A; however, it is representative of the situations with the other three recorders.

2.3.2 Zero Time Correlation

Each tape recorder had the IRIG-B time code on track 13 for time correlation both between machines and as absolute reference for the data. In an effort to conserve data channels, the T-ZERO fiducial marker was superimposed on the IRIG. The reasoning was that the time code reader would reject the step level shift and the channel could serve a dual purpose. In fact, this was not the case.

The transient at T-ZERO was enough to cause the reader to lose sync and it takes more than 1.7 milliseconds to recover and lock back on the code. Consequently the time code was used to generate a trigger mark at 08:00:00.000 and an external delay generator then regenerated a delayed pulse at the set time. The measured reference frequency was used to correct the time delay because of the long times involved. Note that even a 0.5% error amounts to a 9 millisecond correction in 1800.

The procedure was to use a time-interval meter to measure the delay from 0800 hrs to ADC start and then calculate the correction factor based on the ratio of record to playback tape reference frequency.

2.3.3 Problems With Some Specific Channels

Most of the test data were of good quality and had clean calibration signals to go with them. The troublesome channels are listed here with a few words describing the problem and value of the data.

(a) Slip Ring Noise

Blade bending moment measurements on both main and tail rotors were transmitted through slip rings. One of these channels (A-03) was very noisy before blast arrival. After shock arrival, the channel appears to have functioned well, except for times 8 to 15 msecs after shock arrival. Final data dropout due to slip ring interference is observed on channels A-03 (as noted above) and A-02. The final plots have been hand-faired through these sections of dropout.

(b) Defective Sensors

Channels which were lost or compromised due to apparent malfunction of the sensors are: A-05, A-04, B-12, C-01, and D-09.

A-05 is observed on the oscillograph composite to have excessive noise pre-blast and the zero level wanders around after blast passage. This pattern of action is indicative of a poorly bonded strain gage and the confidence in this data channel is certainly reduced due to this unexplained and unlikely performance outside of the measurement period.

In A-04, the signal does not return to the pre-blast levels long after shock encounter, as it should. (See the B-03 signal which is the A-04 counterpart for the red blade.) It appears that shortly after shock arrival, one of the strain gages (in the bending moment bridge circuit) may have been loosened causing a noisy signal with a drift in the zero level.

B-12 may be seen to behave intermittently before blast arrival and appears to respond properly at T-ZERO. The measurement circuit was malfunctioning during calibration however and one can only guess at the calibration. Peak signal deviation was 40 percent of bandedge. The calibration limits on the other control channels were between 75 and 100 percent of bandedge. Therefore, one can speculate that the peak deflection observed might be in the vicinity of 5 degrees to the right. This makes a lot of unfounded assumptions and the only safe conclusion one should draw is that the temporal waveform is correct but the calibration is unknown.

C-01 is a main rotor bending moment channel that experienced a burst of noise during the negative peak excursion between 120 and 220 milliseconds after blast arrival. This noise may have been due to slip ring interference or gage intermittent failure. The negative peak can still be seen in the presence of noise and the general wave shape has been faired by hand on the data plot.

D-09 was the dummy pressure channel and no indication of proper operation of this gage is seen. This data channel is assumed to be a total loss giving no useful information.

2.3.4 Recommendations

Two important recommendations are strongly urged for future tests of this type. First, the IRIG timing channels should be dedicated and not mixed with blast zero or other fiducial markers. Secondly, the instrumentation racks should be shock-mounted. It is a simple matter to shock isolate the instrumentation racks with crushable foam or honeycomb to provide an energy absorbing cushion. This will avoid the transients on the data and reference channels that were experienced during the DICE THROW test. Similar transients were noted on data from the PRE-MINE THROW IV event but they were not as severe.

2.4 Composite Oscillograph Records

Composite oscillograph records have been made up that show the general character of each data channel over a much longer period of time than is seen in the digitized records. They are presented in Figures 2.4 through 2.10. They have been grouped to show similar or related types of data together:

Figure 2.4. Composite of Main Rotor Data

Figure 2.5. Composite of Tail Rotor Data

Figure 2.6 Composite of Tail Boom and Fin Lateral Bending Moment Data

Figure 2.7 Composite of Panel, Stiffener, and Longeron Strain Data

Figure 2.8 Composite of Altitude and Controls Data

Figure 2.9 Composite of Aircraft Attitude and Attitude Rate Data

Figure 2.10 Composite of Pressure Data

2.5 Real Time Oscillograph Traces

Figure 2.11 presents a sequence of consecutive frames from the real time oscillograph traces that were recorded during the test. The time covers a span from T-59 to T+70 seconds.* The traces include

*T indicates burst time.

autopilot and remote control inputs as well as altitude. Time divisions 1 second apart appear as vertical lines with annotations every 10 seconds showing approximate times referenced to blast arrival at the aircraft.

TABLE 2.1 TAPE RECORDER TRACK ASSIGNMENT AND CHANNEL IDENTIFICATION

RECORDER-CHANNEL	CHANNEL IDENTIFICATION	COMPONENT	LOCATION	TYPE OF MEASUREMENT
A - 01	MR/B 35.0R	Main Rotor (MR)	Sta 35, Red Blade	Flapwise Bending Moment
A - 02	MR/B 82.0W	Main Rotor	Sta 82, White Blade	Flapwise Bending Moment
A - 03	TR/B 10.5R	Tail Rotor (TR)	Sta 10.5, Red Blade	Flapwise Bending Moment
A - 04	TR/B 15.5W	Tail Rotor	Sta 15.5, White Blade	Flapwise Bending Moment
A - 05	TP/S 49T I	Panel (P)	Sta 49, Inner Surf.	Vertical Strain Near Long. (Fig. 7.3)
A - 06	TP/S 58A I	Panel	Sta 58, Inner Surf.	Horiz. Strain Near Frame (Fig. 7.3)
A - 07	TS/S 49	Stiffener (S)	Sta 49	Strain (Fig. 7.3)
A - 08	100K	-	-	100 kHz Reference Signal
A - 09	F/B 52	Fin (F)	Fin Sta 52	Lateral Bending Moment
A - 10	P/A	Gyro	-	Pitch Attitude
A - 11	R/R	Gyro	-	Roll Rate
A - 12	LO	Longitudinal Stick	-	Longitudinal (F/A) Cyclic Pitch Cont.
A - 13	IRIGB+FIDU	-	-	Signal for Referencing Time
B - 01	MR/B 82.0R	Main Rotor (MR)	Sta Red Blade	Flapwise Bending Moment
B - 02	MR/B 105.6W	Main Rotor	Sta 105.6, White Bl.	Flapwise Bending Moment
B - 03	TR/B 15.5R	Tail Rotor (TR)	Sta 15.5, Red Blade	Flapwise Bending Moment
B - 04	TR/B 20.4W	Tail Rotor	Sta 20.4, White Blade	Flapwise Bending Moment
B - 05	TP/S 49 TO	Panel (P)	Sta 49, Outer Surface	Vertical Strain Near Long. (Fig. 7.4)
B - 06	TP/S 58 AO	Panel	Sta 58, Outer Surface	Horiz. Strain Near Frame (Fig. 7.3)
B - 07	TB/B 47	Tail Boom (TB)	Tail Boom Sta. 47	Lateral Bending Moment

TABLE 2.1 (Ct'd). TAPE RECORDER TRACK ASSIGNMENT AND CHANNEL IDENTIFICATION

RECORDER CHANNEL	CHANNEL IDENTIFICATION	COMPONENT	LOCATION	TYPE OF MEASUREMENT
B - 08	100K	-	-	100 kHz Reference Signal
B - 09	TB/P 28	Tail Boom (TB)	Sta 28	Pressure Difference
B - 10	R/A	Gyro	-	Roll Attitude
B - 11	Y/R	Gyro	-	Yaw Rate
B - 12	COL	Collective Stick	-	Collective Pitch Control
B - 13	IRIGB+FIDU	-	-	Signal for Referencing Time
C - 01	MR/B 105.6R	Main Rotor (MR)	Sta 105.6, Red Blade	Flapwise Bending Moment
C - 02	MR/FA	Main Rotor	-	Flapping Angle
C - 03	TR/B 20.4R	Tail Rotor (TR)	Sta 20.4, Red Blade	Flapwise BEnding Moment
C - 04	TR/FA	Tail Rotor	-	Flapping Angle
C - 05	TP/S 49 CI	Panel (P)	Sta 49, Inner Surf.	Vertical Strain at Center (Fig. 7.3)
C - 06	TP/S 49 CH	Panel	Sta 49, Inner Surf.	Horizontal Strain at Center (Fig. 7.3)
C - 07	TB/B 112	Tail Boom (TB)	Tail Boom Sta 112	Lateral Bending
C - 08	100K	-	-	100 kHz Reference Signal
C - 09	F/P 37	Fin (F)	Fin Sta. 37	Pressure
C - 10	Y/A	Gyro	-	Yaw Attitude
C - 11	ALT	Radar	-	Altitude
C - 12	PD	Pedal	-	Tail Rotor Collective Pitch Control
C - 13	IRIGB+FIDU	-	-	Signal for Referencing Time

TABLE 2.1 (Ct'd). TAPE RECORDER TRACK ASSIGNMENT AND CHANNEL IDENTIFICATION

RECORDER CHANNEL	CHANNEL IDENTIFICATION	COMPONENT	LOCATION	TYPE OF MEASUREMENT
D - 01	MR/B 132.0R	Main Rotor (MR)	Sta 132, Red Blade	Flapwise Bending Moment
D - 02	MR/A R	Main Rotor	Red Blade	Azimuth
D - 03	TR/B 25.5R	Tail Rotor (TR)	Sta 25.5, Red Blade	Flapwise Bending Moment
D - 04	TR/A R	Tail Rotor	Red Blade	Azimuth
D - 05	TP/S 49 CO	Panel (P)	Sta 49, Outer Surf.	Vertical Strain at Center (Fig. 7.3)
D - 06	TL/S 49	Longeron (L)	Sta 49	Longeron Strain (Fig. 7.3)
D - 07	F/B 32	Fin (F)	Fin Sta 32	Lateral Bending
D - 08	100K	-	-	100 kHz Reference Signal
D - 09	D/P	Dummy	-	Pressure on Anthromorphic Dummy
D - 10	P/R	Gyro	-	Pitch Rate
D - 11	LA	Lateral Stick	-	Lateral Cyclic Pitch Control
D - 12	C/P	Camera	Cabin	Pressure at Camera Stand
D - 13	IRIGB+FIDU	-	-	Signal for Referencing Time

TABLE 2.2 CALIBRATION DATA

CHANNEL IDENTIFICATION			CAL RESISTOR (OHMS)	CAL EQUIV.	CAL UNITS	POS DEVIATION
A-01	MR/B	35.0R	40K	6978	ft-lb	Up
A-02	MR/B	82.0W	50K	2432	ft-lb	Up
A-03	TR/B	10.5R	25K	672	ft-lb	Out
A-04	TR/B	15.5W	25K	431	ft-lb	Out
A-05	TP/S	49TI	50K	3309	με	Comp
A-06	TP/S	58AI	50K	3309	με	Comp
A-07	TS/S	49	50K	3309	με	Comp
A-09	F/B	52	50K	74,600	in-lb	Right
A-10	P/A		*	6.43	deg	Down
A-11	R/R		*	17.58	deg/sec	Left
A-12	LO		**	9.43A 13.5F	deg	Aft
B-01	MR/B	82.0R	50K	2244	ft-lb	Up
B-02	MR/B	105.6W	50K	2118	ft-lb	Up
B-03	TR/B	15.5R	25K	431	ft-lb	Out
B-04	TR/B	20.4W	25K	312	ft-lb	Out
B-05	TP/S	49TO	50K	3309	με	Comp
B-06	TP/S	58AO	50K	3309	με	Comp
B-07	TB/B	47	50K	375,380	in-lb	Right
B-09	TB/P	28	100K	8.48	psid	Pos
B-10	R/A		*	6.86	deg	Left
B-11	Y/R		*	18.84	deg/sec	Right
B-12	COL		**	7.20D 7.80U	deg	Down

*Center to Band Edge (0 to +40% Deviation).

**Manual control operation limit to limit.

TABEL 2.2. (Ct'd). CALIBRATION DATA

CHANNEL IDENTIFICATION			CAL RESISTOR (OHMS)	CAL EQUIV.	CAL UNITS	POS DEVIATION
C-01	MR/B	105.6R	50K	2041	ft-lb	Up
C-02	MR/Fa		**	24	deg	Red Down
C-03	TR/B	20.4R	25K	312	ft-lb	Out
C-04	TR/Fa		**	16	deg	Red Out
C-05	TP/S	49CI	50K	3309	με	Comp
C-06	TP/S	49CH	50K	3309	με	Comp
C-07	TB/B	112	50K	270,700	in-lb	Right
C-09	F/P	37	100K	6.52	psi	pos
C-10	Y/A		*	11.39	deg	Left
C-11	Alt		*	120	ft	Up
C-12	PD		**	6.67R 19.17L	deg	Right
D-01	MR/B	132.0R	50K	1785	ft-lb	Up
D-02	MR/AZ	R	--	--	---	---
D-03	TR/B	25.5R	25K	362	ft-lb	Out
D-04	TR/AZ	R	--	--	---	---
D-05	TP/S	49CO	50K	3309	με	Comp
D-06	TL/S	49	50K	3309	με	Comp
D-07	F/B	32	50K	44,600	in-lb	Right
D-09	D/P	Dummy	100K	6.60	psi	Pos
D-10	P/R		*	15.72	deg/sec	Up
D-11	LA		**	7.55R 10.68L	deg	Right
D-12	C/P	Cabin	100K	7.14	psi	Pos

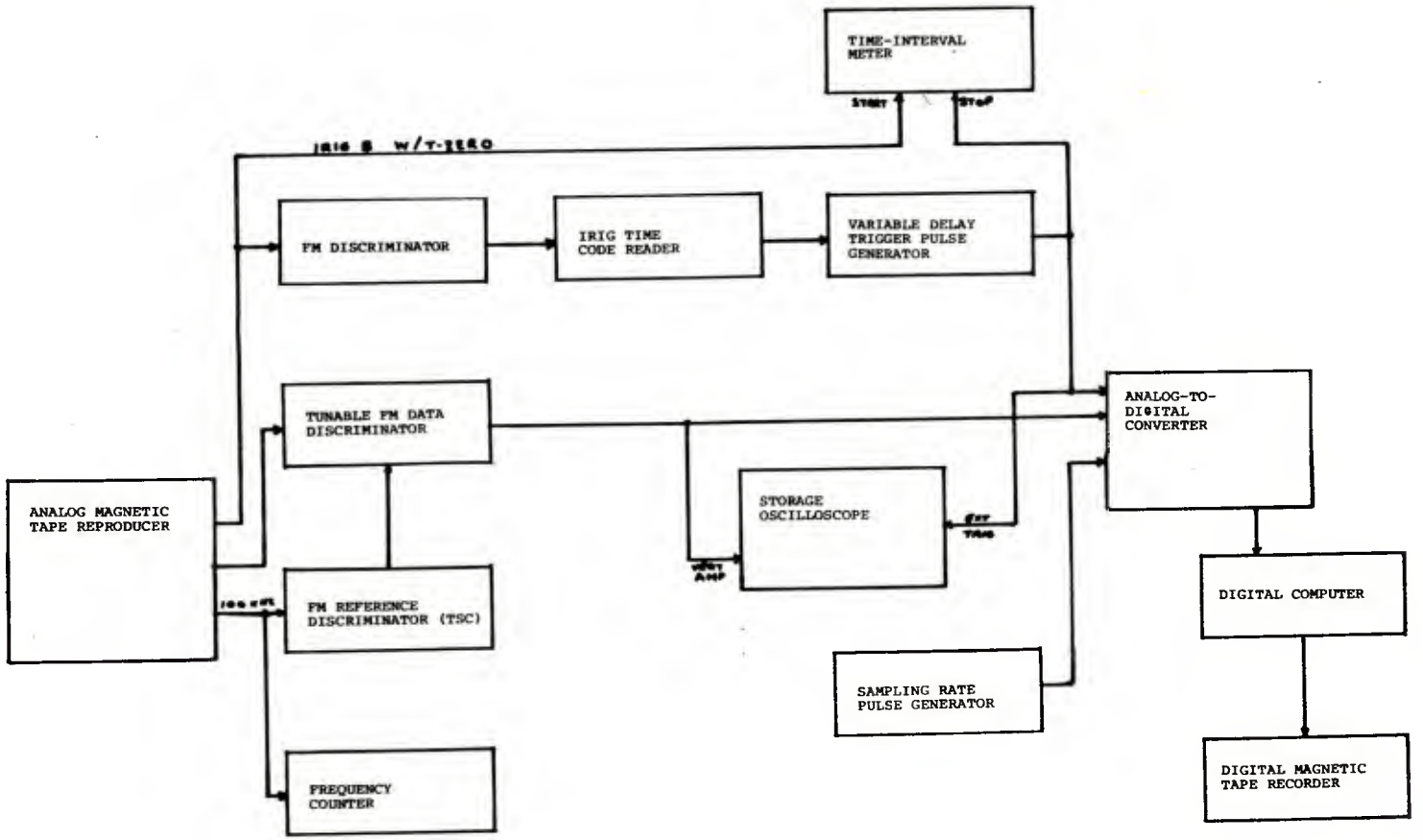

Figure 2.1. Block Diagram - Data Playback System

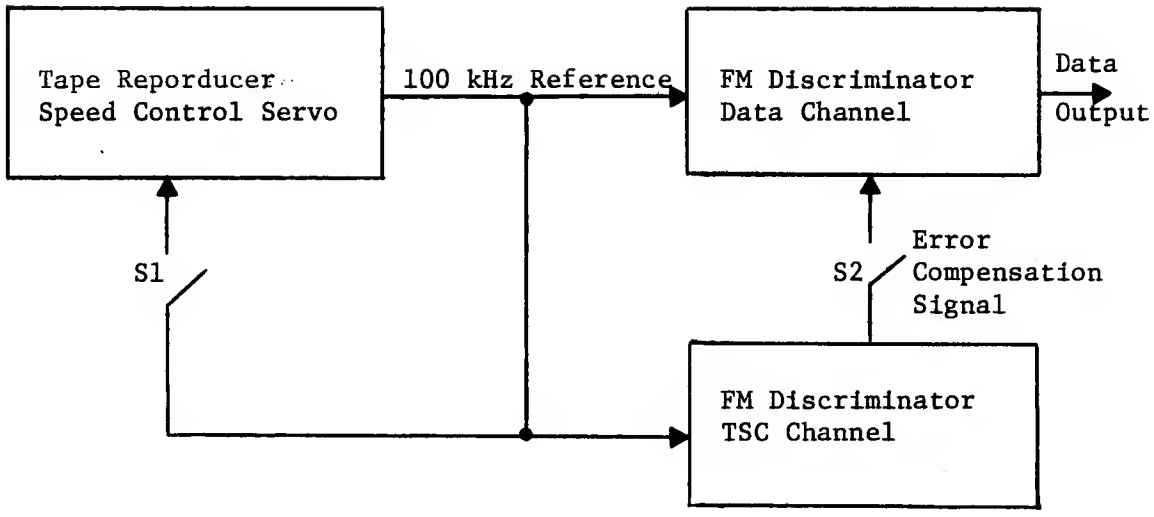

Figure 2.2. Tape Speed Control and Compensation System

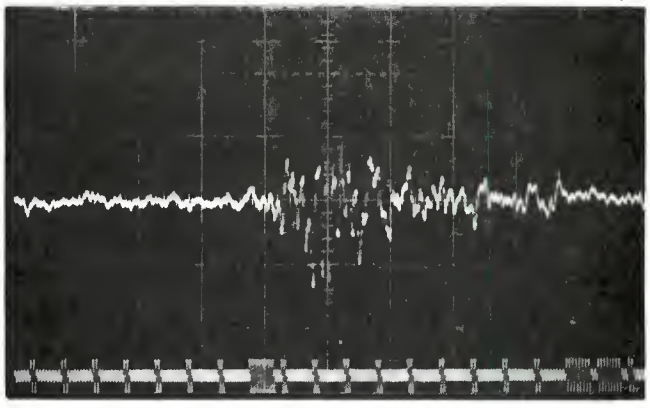

a

RECORD ID. 100 KHZ REF
VERT SENS 0.2 VOLTS/DIV
SWEEP RATE 20m SEC/DIV
TAPE AND TRACK ID A-8
COMMENTS TSSC-OFF
TSC-OFF
DISCR: 108 KHz ± 40%
BEV: ± 8 Volts

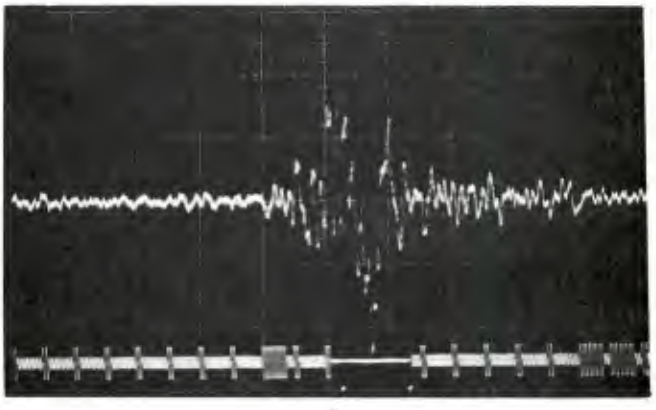

b

RECORD ID. 100 KHZ REF
VERT SENS 0.2 VOLTS/DIV
SWEEP RATE 20m SEC/DIV
TAPE AND TRACK ID A-8
COMMENTS TSSC-ON
TSC-OFF
DISCR: 108 ± 40%
BEV: ± 8 Volts

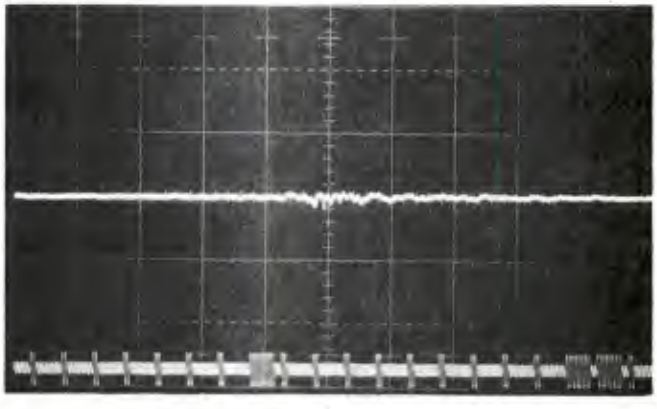

c

RECORD ID. 100 KHZ REF
VERT SENS 0.2 VOLTS/DIV
SWEEP RATE 20m SEC/DIV
TAPE AND TRACK ID A-8
COMMENTS TSSC-OFF
TSC-ON, CONFIGURATION
USED FOR DATA REDUCTION

Figure 2.3. Tape Speed Compensation Test Results

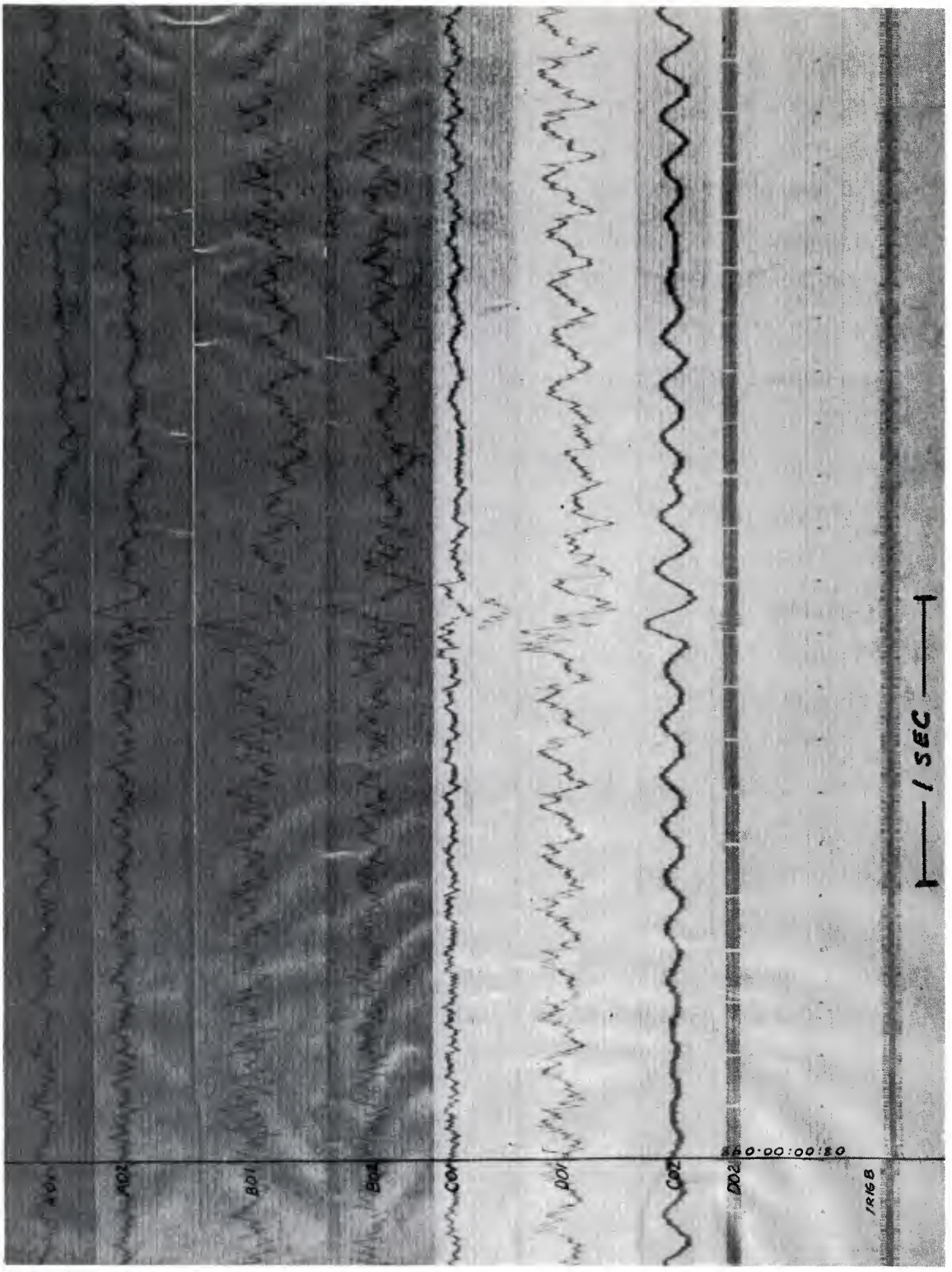

Figure 2.4. Composite of Main Rotor Data

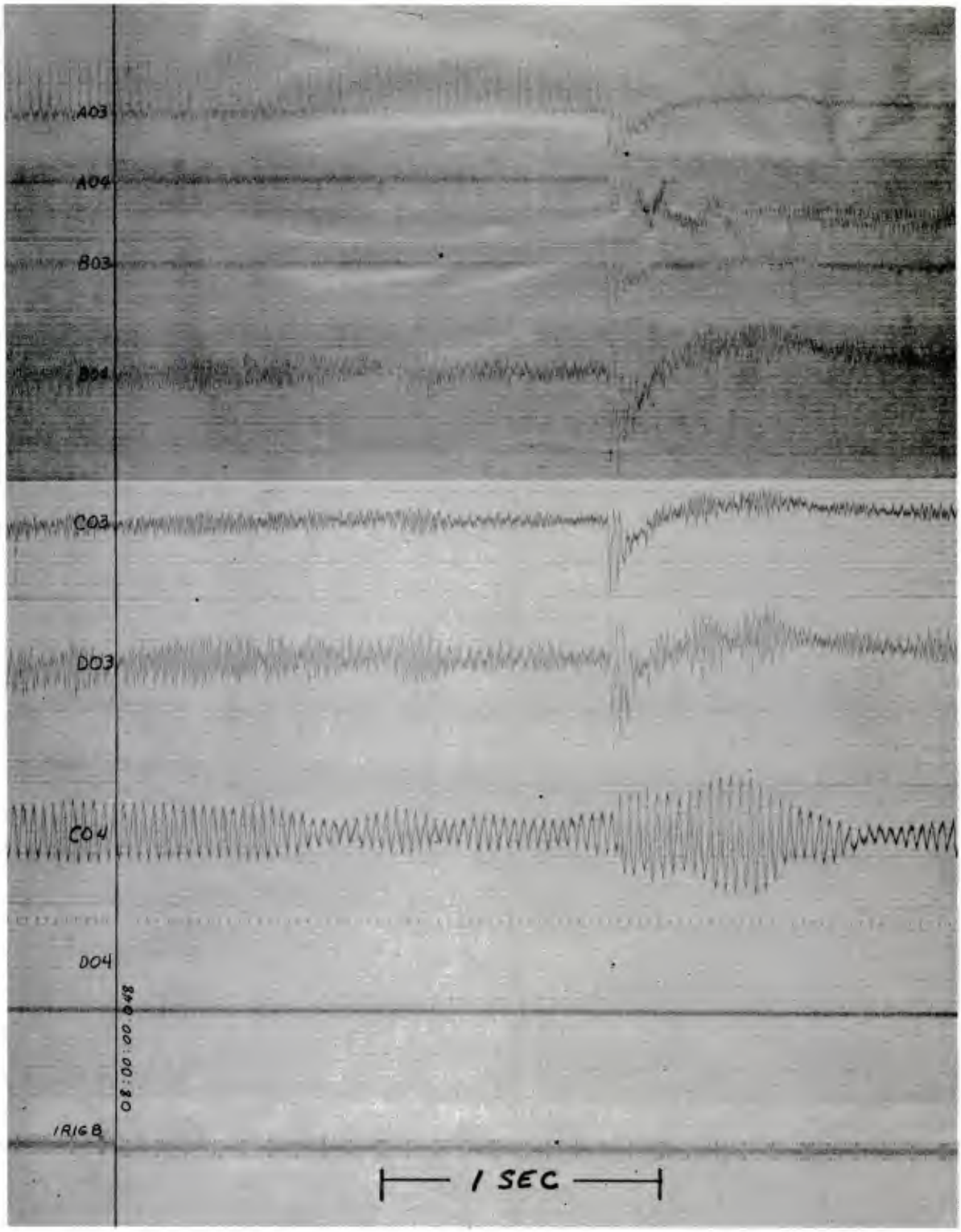

Figure 2.5. Composite of Tail Rotor Data

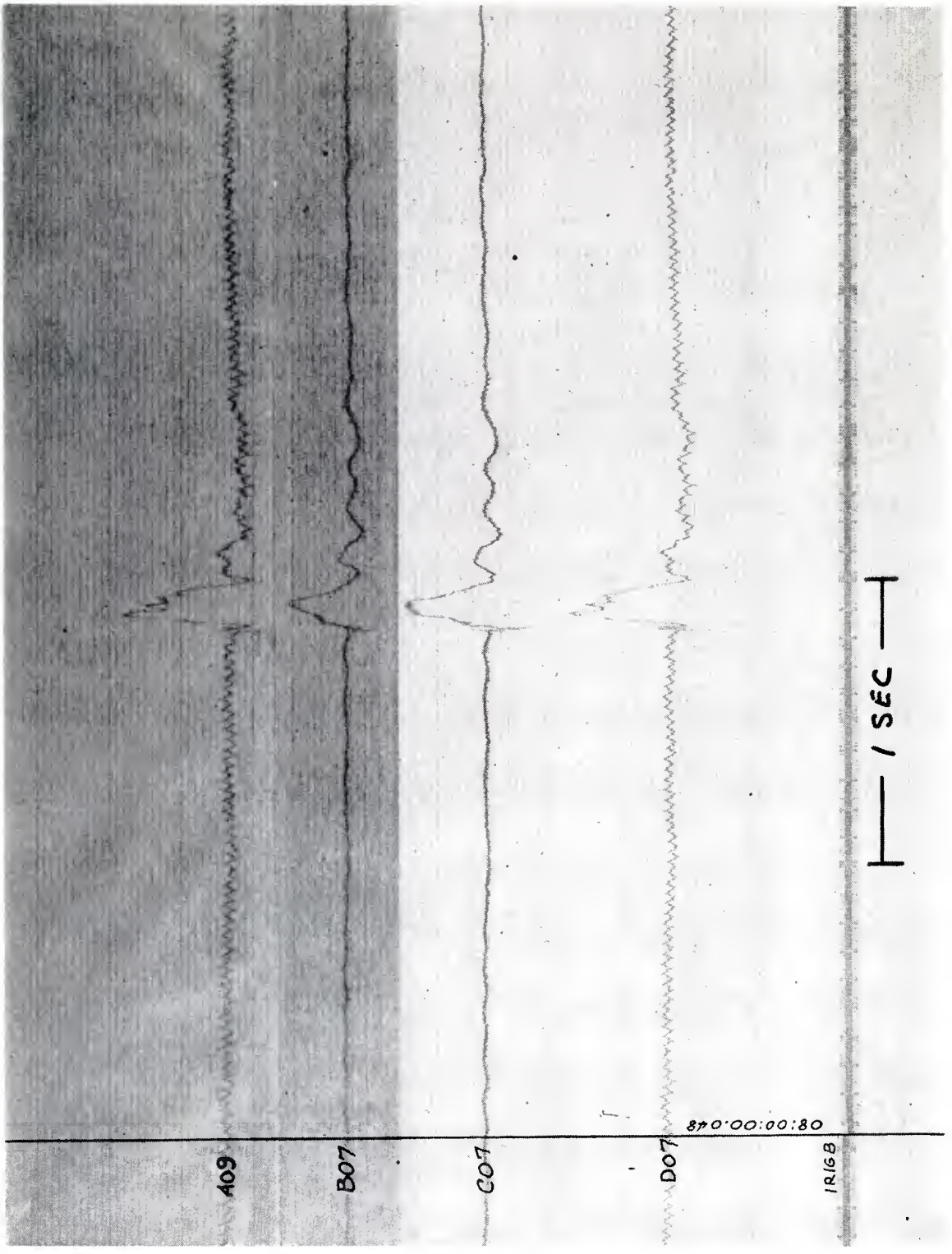

Figure 2.6. Composite of Tail Boom and Fin Lateral Bending Moment Data

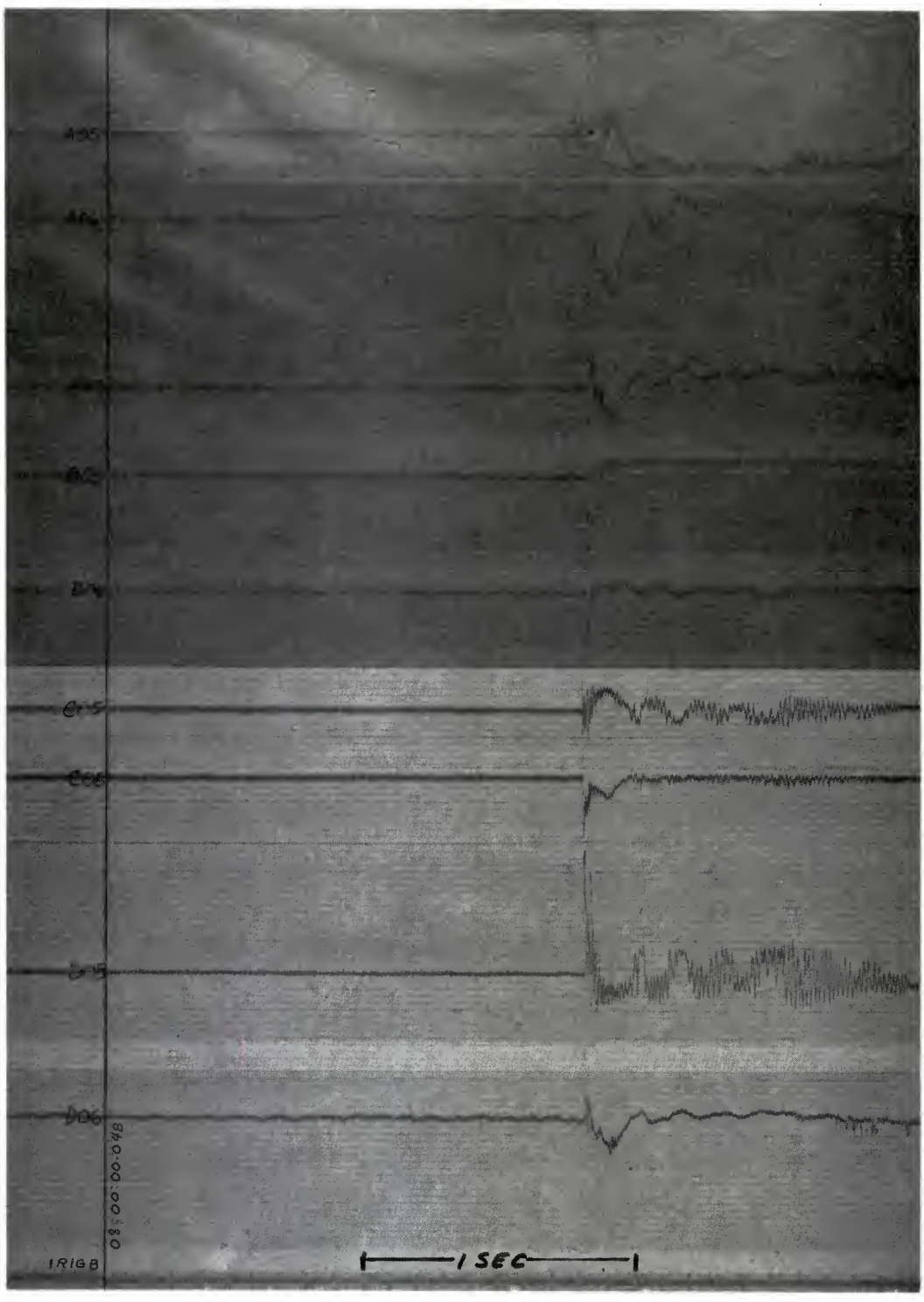

Figure 2.7. Composite of Panel, Stiffener, and Longeron Strain Data

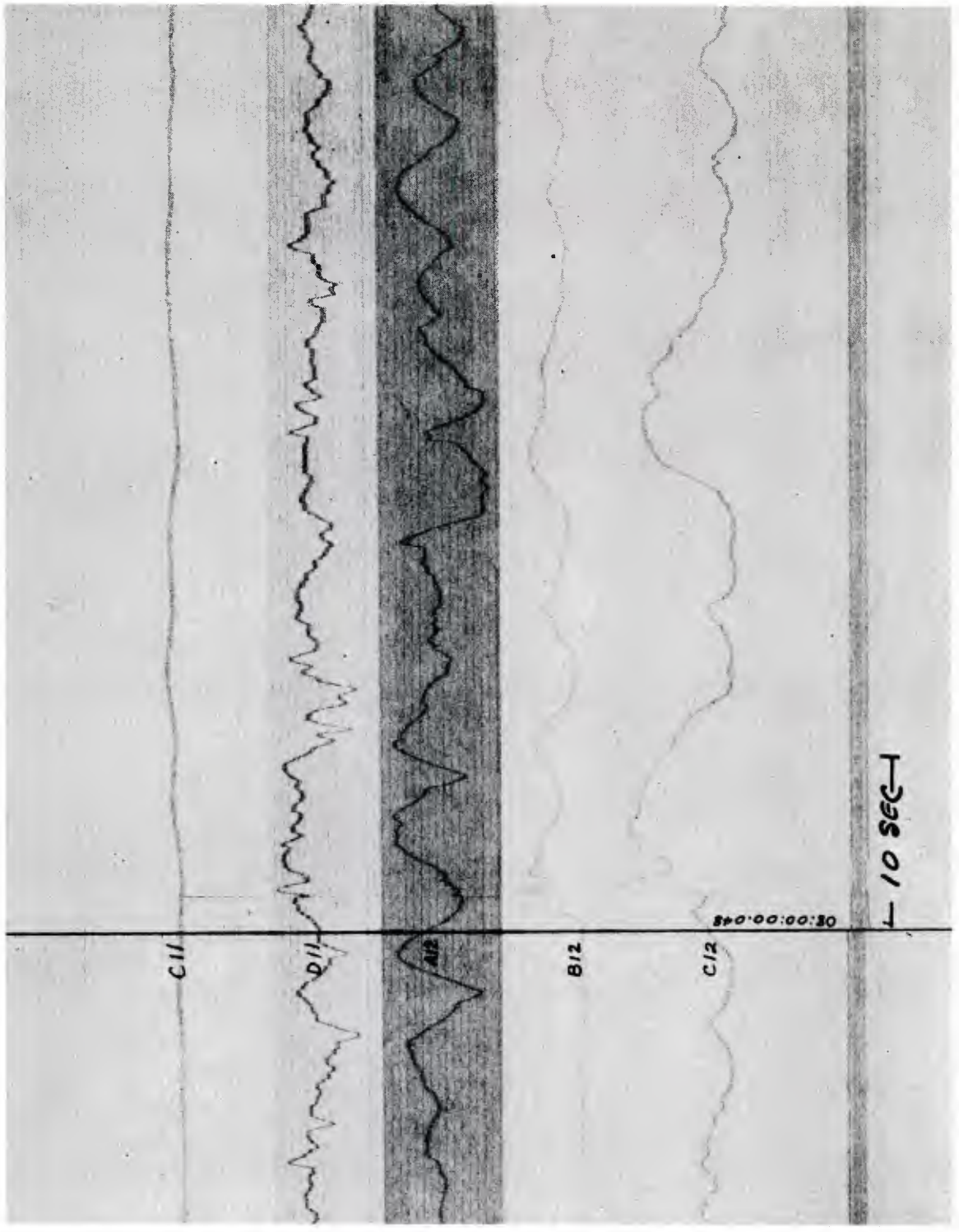

Figure 2.8. Composite of Altitude and Controls Data

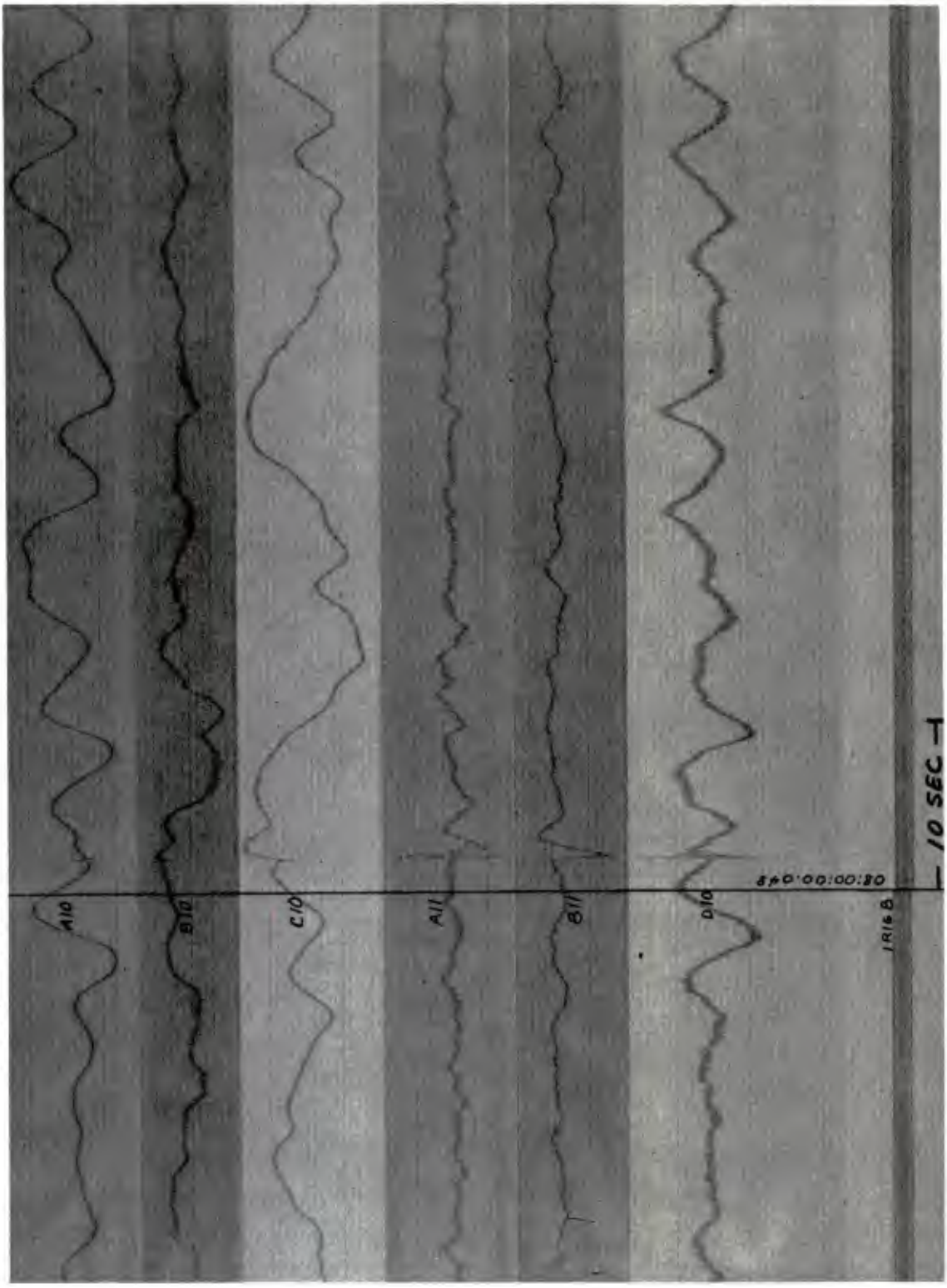

Figure 2.9. Composite of Aircraft Attitude and Attitude Rate Data

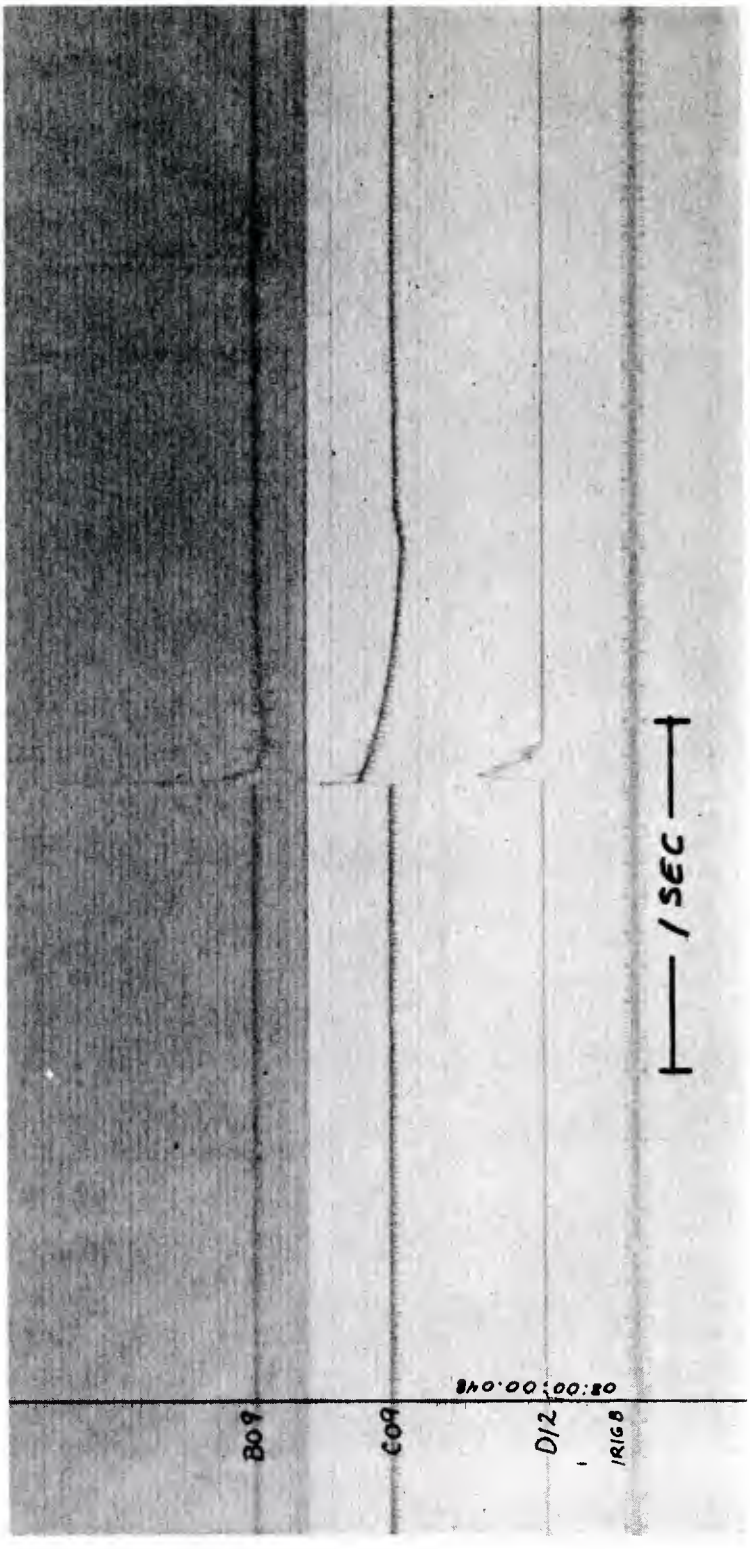

Figure 2.10. Composite of Pressure Data

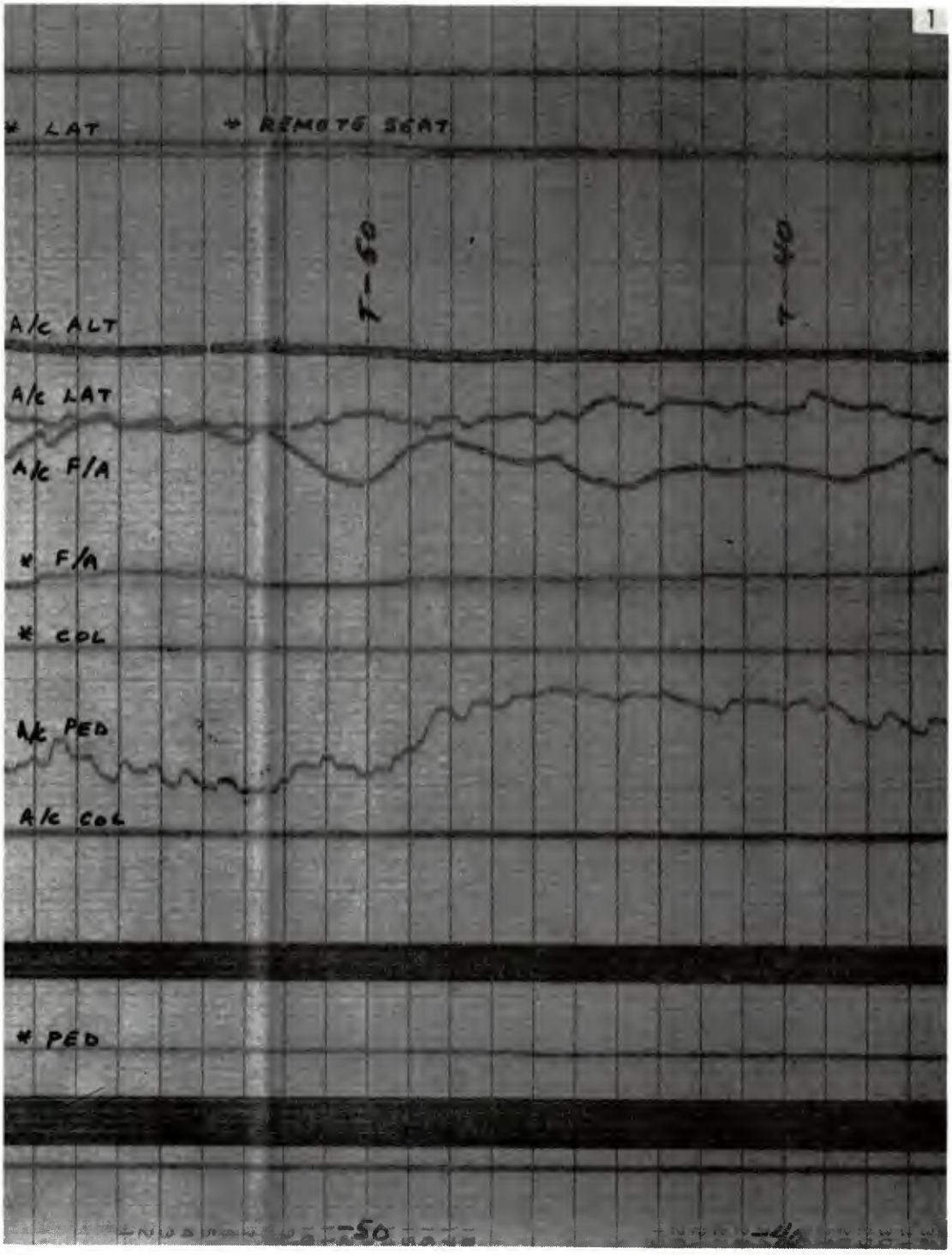

Figure 2.11. Real-Time Oscillograph Traces for Autopilot and Remote Controls and Altitude. Frame 1 - T-59 to T-36 sec.

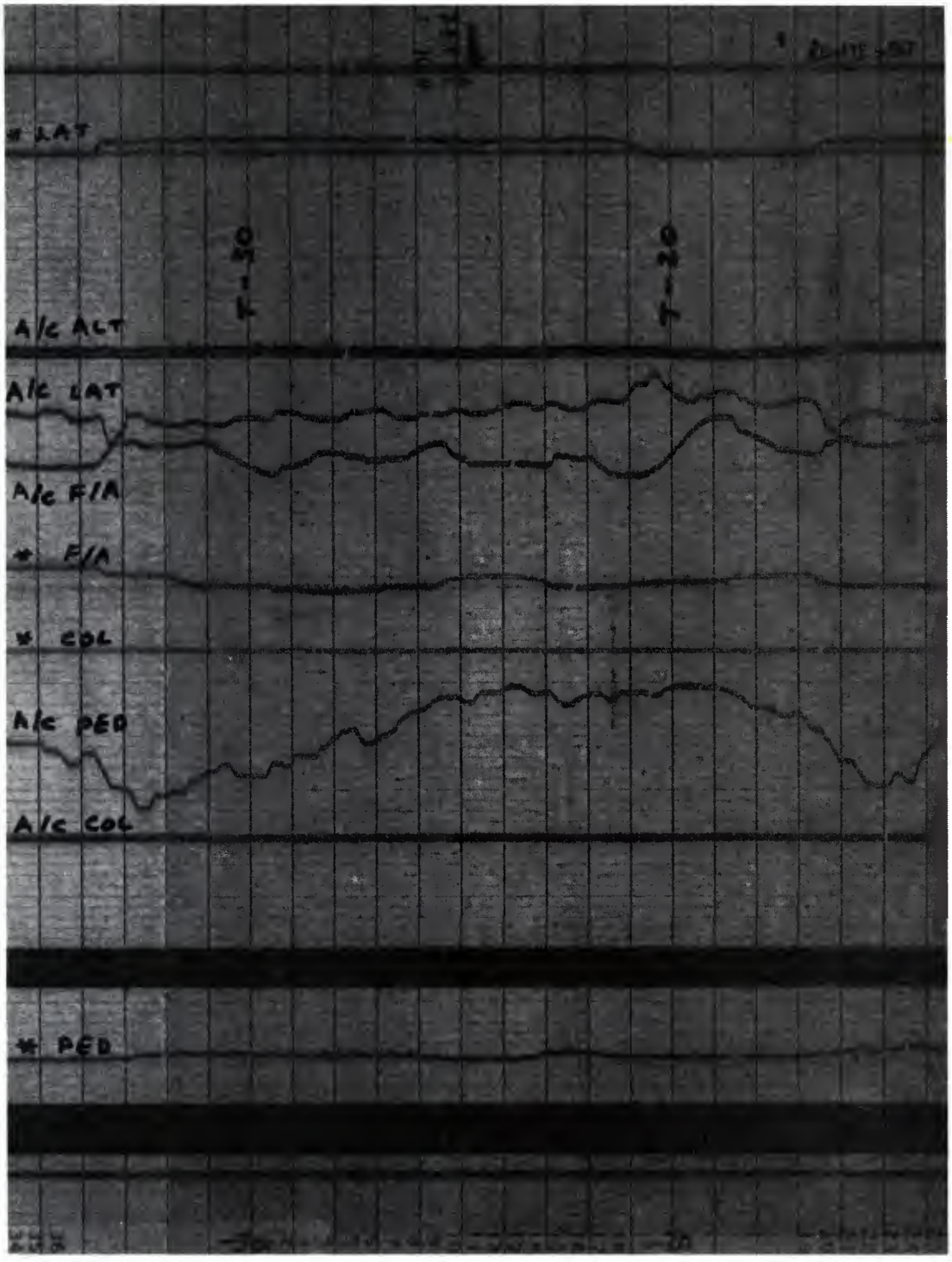

Figure 2.11. Real-Time Oscillograph Traces for Autopilot and Remote Controls and Altitude. Frame 2 - T-36 to T-13 sec.

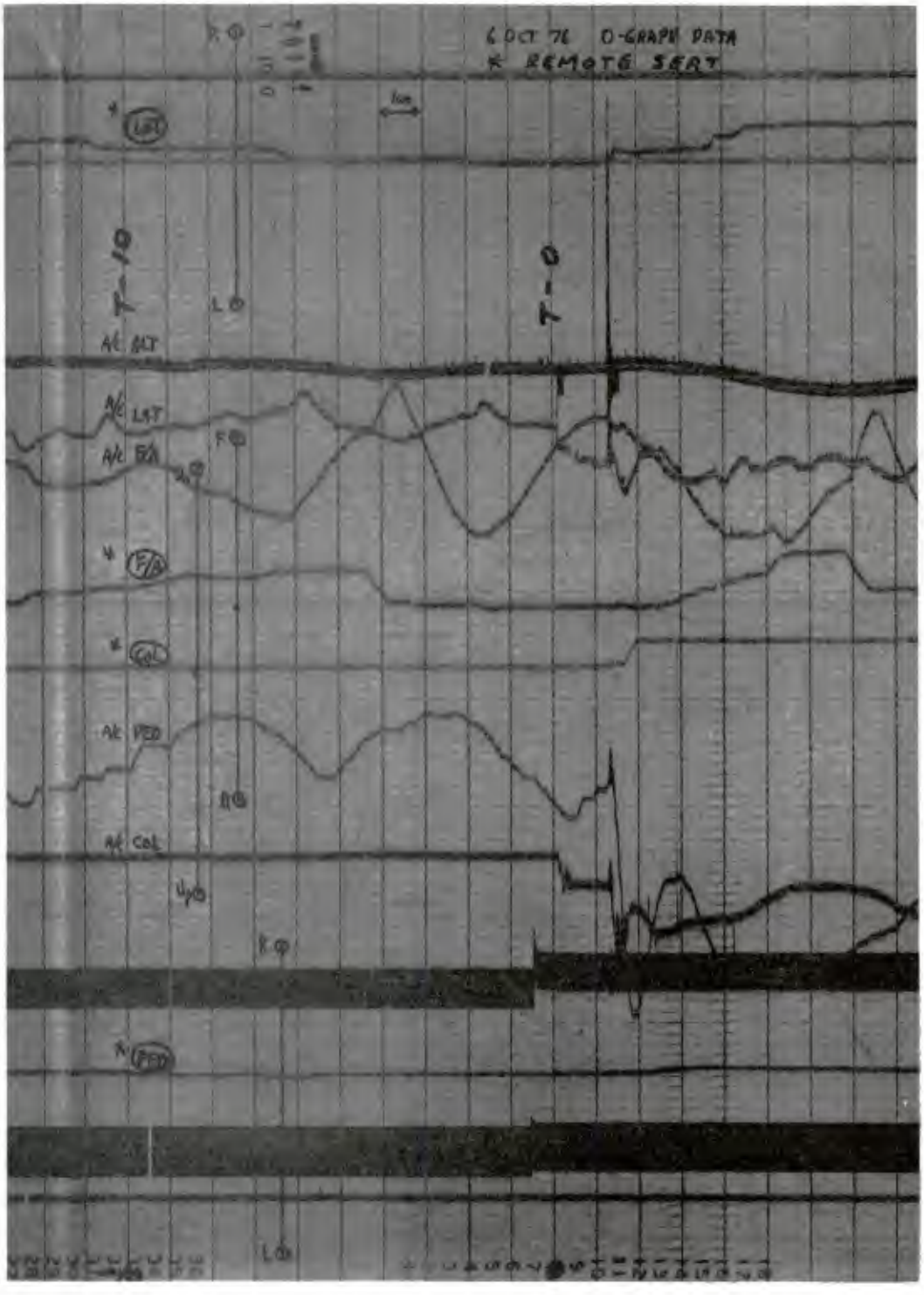

Figure 2.11. Real-Time Oscillograph Traces for Autopilot and Remote Controls and Altitude. Frame 3 - T-13 to T+9 sec.

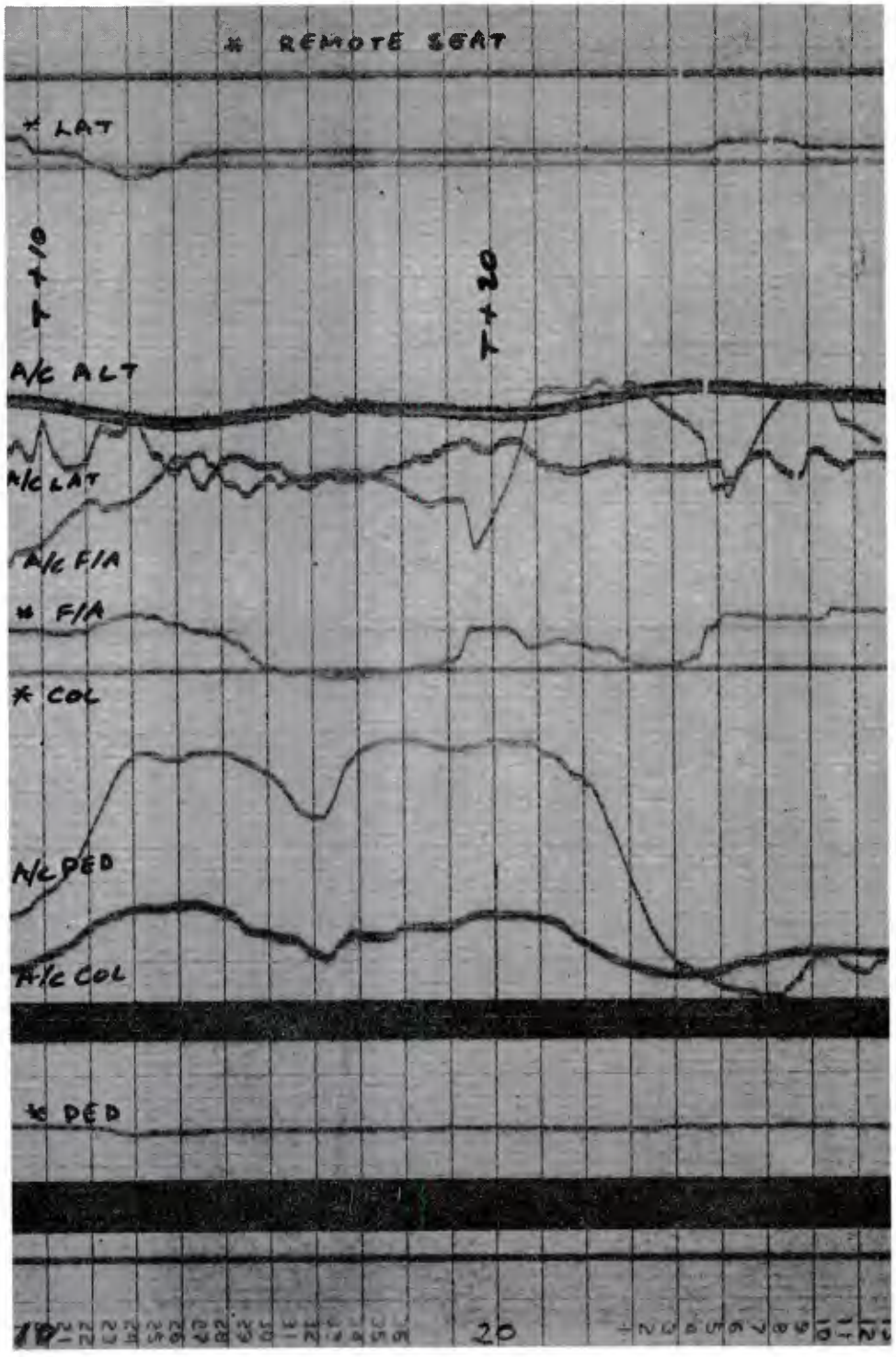

Figure 2.11. Real-Time Oscillograph Traces for Autopilot and Remote Controls and Altitude. Frame 4 - T+9 to T+29 sec.

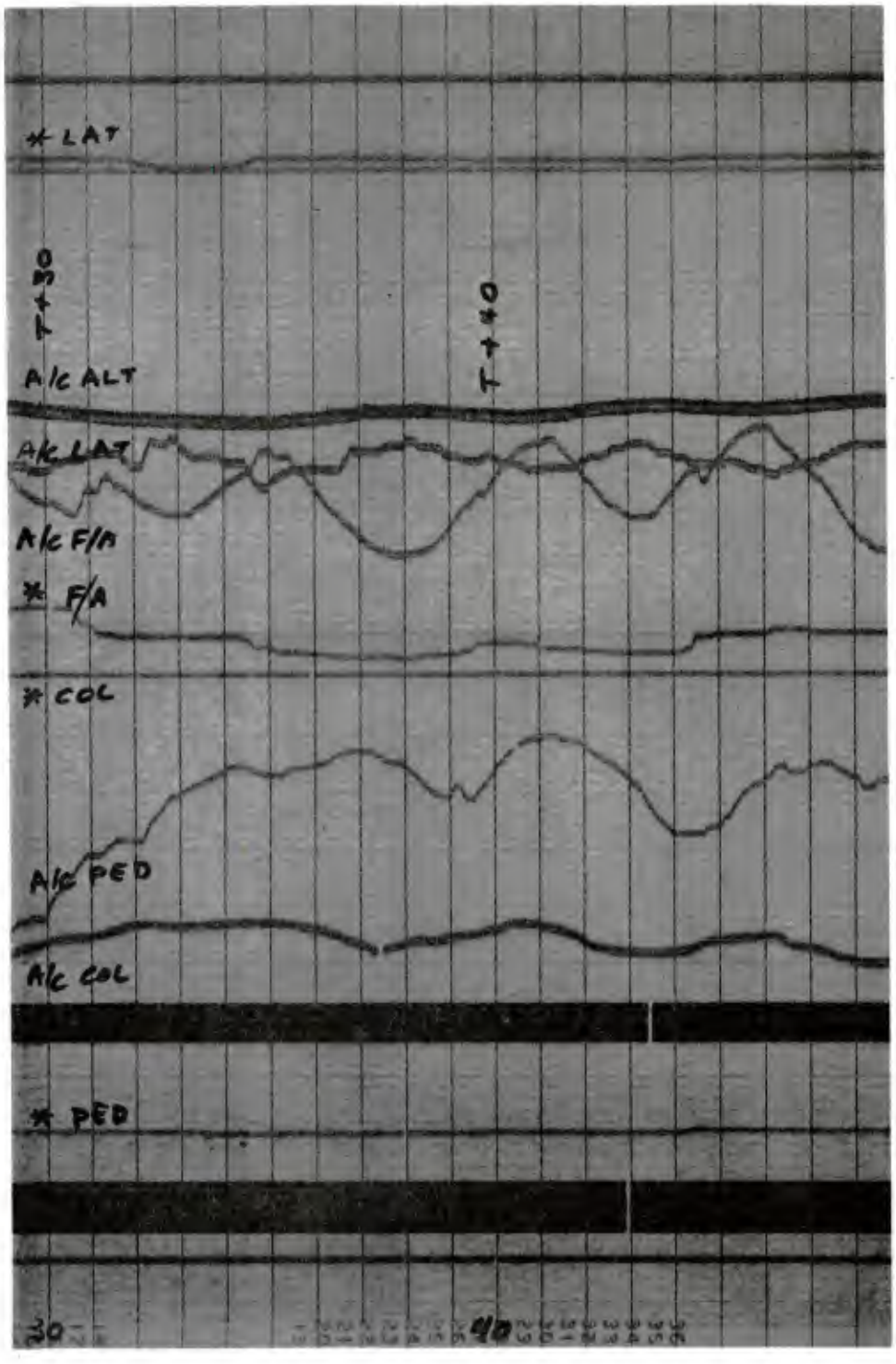

Figure 2.11. Real-Time Oscillograph Traces for Autopilot and Remote Controls and Altitude. Frame 5 - T+29 to T+49 sec.

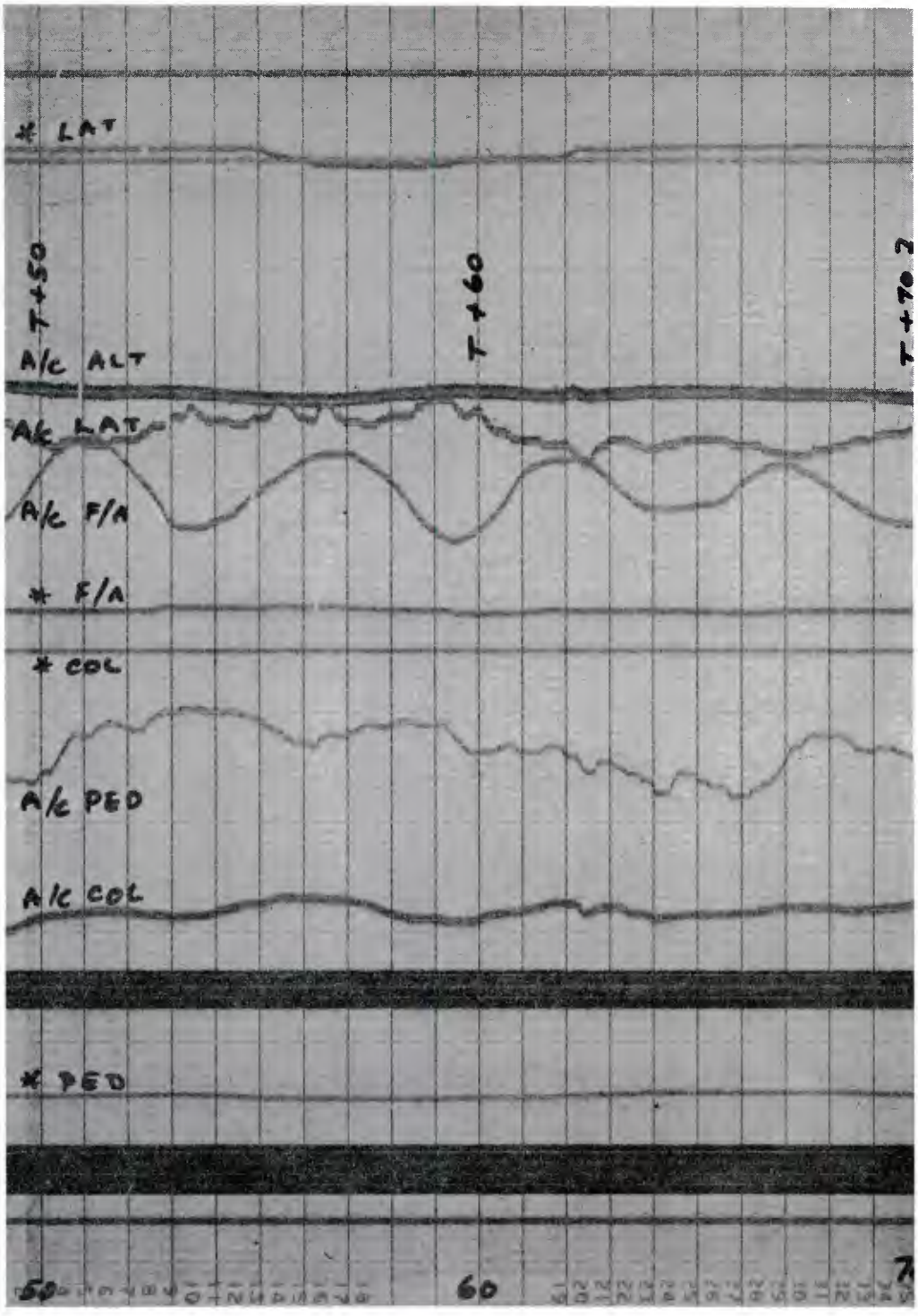

Figure 2.11. Real-Time Oscillograph Traces for Autopilot and Remote Controls and Altitude. Frame 6 - T+49 to T+70 sec.

SECTION 3

ESTABLISHMENT OF THE BLAST MODEL AND OF THE PANEL PRESSURE LOADINGS

3.1 Ambient Conditions

The atmospheric conditions which prevailed just before test time (0800, 6 October 1976) are as follows:

Ambient Temperature = T_∞ = 9.7° C = 49.5° F = 509.2° R

Ambient Pressure = p_∞ = 850 millibars = 12.33 psi

Wind Velocity = V_w = 4.1 Kts, 200° referenced to True North

Relative Humidity = 71%

The above measurements were taken at Stallion Range Command Post which is about 12 miles from the test site. This information was received by private communication from Messrs. George Teele and Robert Mayerhofer of BRL. From the temperature and pressure data, the ambient density and speed of sound are estimated to have been

Ambient Density = ρ_∞ = 0.002032 slugs/ft^3 for dry air

Ambient Speed of Sound = a_∞ = 1106.2 ft/sec.

The effect of relative humidity on density is negligible, being less than 0.4%. With the prevailing wind being light, the wind effects were also neglected. It should be mentioned, however, that there appeared to be some local disturbances evidenced by the fact that the pilot had some difficulty in stabilizing the vehicle and that the helicopter was undergoing sizeable motions just prior to shock arrival.

3.2 Establishment of a Suitable Blast Model

The blast routine in the HELP code, BLAST, which is called upon to calculate the blast field parameters (i.e., density, material velocity, etc...) at each aerodynamic point and at each time step of the transient solution, utilizes the latest Air Force Weapons Laboratory 1KT, sea level nuclear blast field model (HYDRA, 1KT). It is provided with a table of the standard atmosphere conditions (ATMOS) to generate its input requirements. Normally, the weapon yield, the burst altitude, and the range are specified. For the given burst altitude, the values of the ambient conditions are first calculated by interpolation of the ATMOS table. The ambient conditions, the weapon yield, and the range are then used by the scaling laws which are built in the BLAST routine to yield the desired blast field parameters.

In the present application, two factors arise which need be dealt with. The first is that the ambients conditions do not totally match the standard conditions at some altitude; secondly, the burst is on the ground, and not in the free atmosphere. In inputting the atmospheric conditions, two alternatives may be followed:

(i) By choosing a burst altitude in the standard atmosphere where the ambient conditions are matched as closely as possible with those existing at test time. In so doing, the BLAST routine can be exercised in its normal procedure, i.e., utilizing the standard ATMOS table.

(ii) By replacing the standard ATMOS with a "dummy ATMOS", wherein the atmosphere is assumed to be uniform, i.e., the same at all altitudes, and the ambient conditions are set equal to those for the actual atmosphere at test time.

The second alternative is more accurate and was followed for the present calculations. It was effected through a slight modification of the input statements in the BLAST routine.

The BLAST routine in the HELP code assumes a nuclear burst in the free atmosphere. Nevertheless, the same routine can be used for the present case where the burst is from a high explosive (HE) and on the ground, provided some adjustments are made in certain input parameters. In order to simulate the actual blast field in the calculations using a free-atmosphere nuclear burst, it is necessary to find an "equivalent pair" of yield and slant range which gives the same peak free-field overpressure (p_{so}) level and the same positive overpressure phase duration (t_p^+). In the correlation study for the PRE-MINE THROW IV Event, it was found that a 300-Ton nuclear yield in the free atmosphere gave at a slant range of 1998 ft essentially the same p_{so} and t_p^+ as the actual 100-Ton HE (nitromethane in PRE-MINE THROW IV) yield on the ground at a slant range of 1920 ft (which happened to be the distance between the helicopter and ground zero). Thus, in PRE-MINE THROW IV, the input adjustments called for a tripling of the yield and a slight increase in the slant range from 1920 ft to 1998 ft.

The situation in DICE THROW was found to be somewhat different because:

(i) The explosive was ANFO, estimated to be around 628 Tons, rather than nitromethane, and

(ii) The measurements indicated that there were considerable variations in the blast field parameters with azimuth.

The actual slant range was 2725 ft. The measured p_{so} and t_p^+ at the helicopter were 1.80 psi and 343 msecs, respectively. The source of this data is discussed in Section 3.3. To duplicate the same p_{so}

and t_p^+ values in the computations to follow, the BLAST routine in HELP was exercised, using the dummy ATMOS referred to earlier, to obtain p_{so} and t_p^+ for several combinations of yield and slant range. By interpolating these results, it was determined that the equivalent pair of yield and slant range to use in the BLAST routine is

Yield = 1.236 KT

Slant Range = 2562 ft

in order to obtain the measured values of p_{so} and t_p^+, 1.80 psi and 343 msecs, respectively.

3.3 Presure Measurements

Two pressure measurements supply the information needed for input to the BLAST routine and for the pressure loadings on one of the tail boom panels.* The fin pressure sensor, C-09, located at fin station 37, was sealed on its inner side so that it measured the actual overpressure variation p(t) at an exterior point on the left side of the fin. The tail boom pressure sensor, B-09, located at the center of a left side panel (at tail boom station 28), was not sealed on its inner side. Thus, it was configured to read the pressure difference $\Delta p(t)$ between the outer and inner points of the cited location. The measurement from this transducer channel gave in effect the average pressure loading on the panel whose center was at tail boom station 28. It is assumed that the same loading also applies for the neighboring panel (with center at tail boom station 49) which is analyzed in Section 7. Short duration traces for these two measurements, with and without digital filtering, are presented in Figures 3.1 - 3.4. The raw data presented in Figures 3.1 - 3.2 are unfiltered digitally; the indicated 15KHz filtering reflects the frequency response limitation of the pressure channels. Figures 3.3 - 3.4 duplicate the previous two, with the exception that the data have been processed through a 5KHz digital filter. Figure 3.5 is a long duration trace for the fin overpressure processed through a 1 KHz digital filter to obtain the actual overpressure positive phase duration. The cross-over point in the last trace indicates that t_p^+ was approximately 343 msecs.

In Figures 3.1 and 3.2, the peak overpressures (at time $t=0^+$) appear considerably above 4psi. This is due to "ringing" of the transducers following the sudden pressure jump at shock arrival time. The ringing signals are believed to have been eliminated by the 5KHz filtering in Figures 3.3 - 3.4. In the latter, the peak reflected pressures are

---

*Two other pressure measurements were made, one on the anthropomorphic dummy and the other on the camera stand near the cabin. These are of no interest for the correlations presented in this report.

slightly below 4.0 psi, and "fall more in line" with the extensions of the traces for times 1-5 msecs after shock arrival. A reasonable estimate from Figure 3.4 for the peak reflected pressure (i.e., p_r = p(t=0)) is about 3.82 psi. Since the shock was head-on to the surfaces where the two sensors were located, the p_r-value thus measured can be related to the peak free-field overpressure, p_{so}, through the well-known relation

$$p_r = 2\, p_{so}\, \frac{7p_\infty + 4p_{so}}{7p_\infty + p_{so}}$$

If p_r is taken to be 3.82 psi, and since p_∞ = 12.33 psi, p_{so} turns out to be 1.8 psi. This value of p_{so} is further verified through a baseline measurement in close proximity to the helicopter.*

The modifications to the input of the BLAST routine, covered earlier in Section 3.2, were based on these experimental data.

3.4 Panel Pressure Loading Model

As discussed earlier, the trace in Figure 3.4 represents the time-variation of the pressure difference between the sides of a left side panel whose center is located at tail boom station 28. This particular panel was not instrumented to measure the blast-induced strains. The strain correlations discussed in a later section refer to the responses of an adjoining panel which has its center located at tail boom station 49. There, it is assumed that the blast-induced pressure loading is uniform over the panel and that it is approximately that shown in Figure 3.4.

In the strain analyses, the pressure loading can be inputted in either of the following two ways:

(i) Use directly the digital tape from which Figure 3.4 was generated, or

(ii) Devise a reasonable fit to the curve in Figure 3.4 over the time range of interest.

The second alternative is simpler to effect and is preferred here. A curve fit, consisting of a series of straight lines connecting the points tabulated below, is deemed adequate for present purposes.

---

*After examining the baseline data, Mr. Mayerhofer and the senior author agreed that the free-field overpressure was in the neighborhood of 1.8 psi rather than 2.2 psi indicated in the preliminary data sheets from BRL.

Time (in msecs)	Δp (in psi)
<0	0
0+	3.82
1.47	2.05
1.75	3.22
2.91	2.00
7.29	1.00
8.00	1.43
8.84	0.93
17.15	0.53
25.00	0.46

A linear interpolation subroutine, available in the computer program, is then used to obtain the Δp's for all time steps called for in the transient solution.

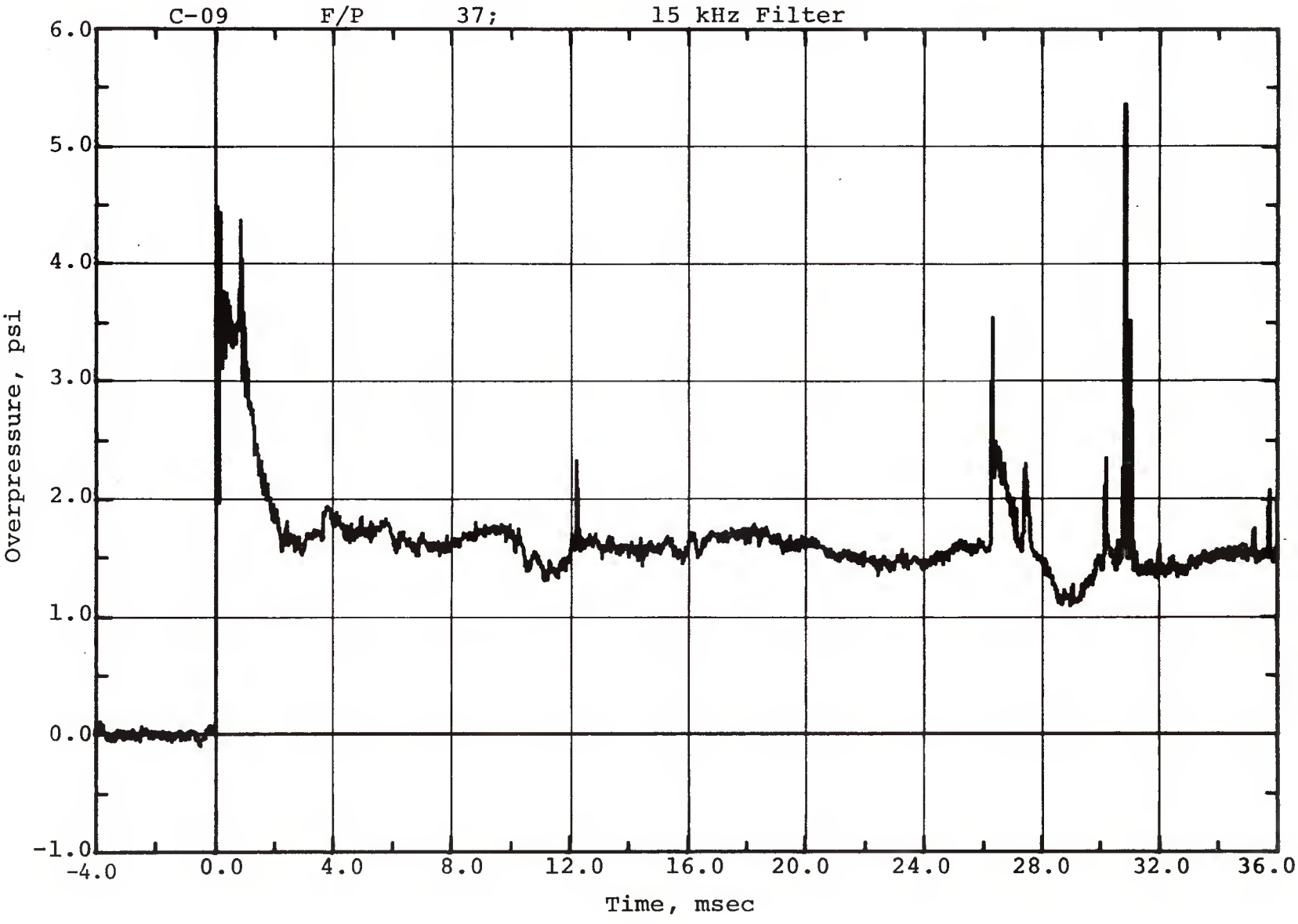

Figure 3.1. Time-Variation of Overpressure at Fin Station 37. Unfiltered

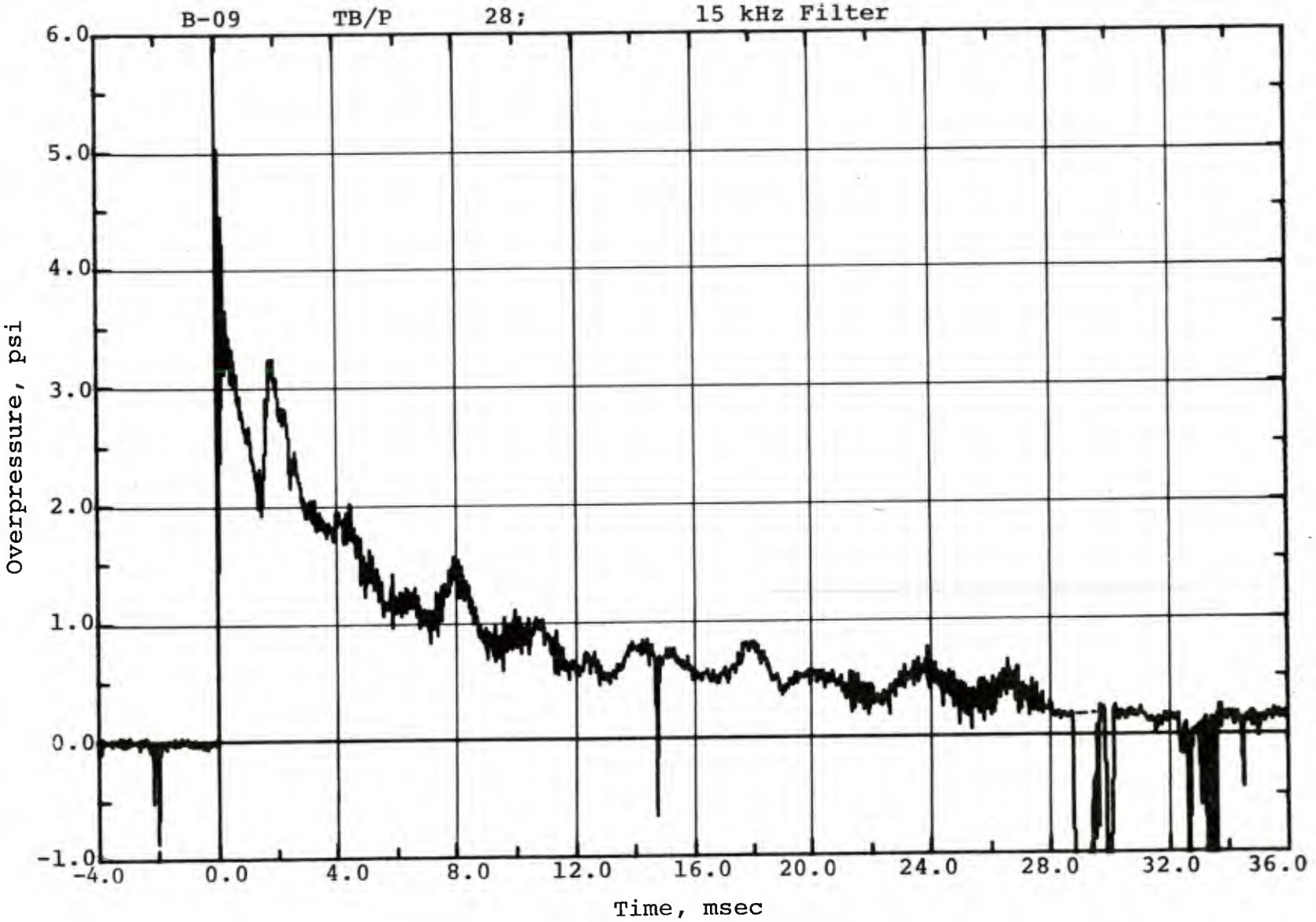

Figure 3.2. Time-Variation of Overpressure Differential at Center of Panel. Tail Boom Station 28. Unfiltered

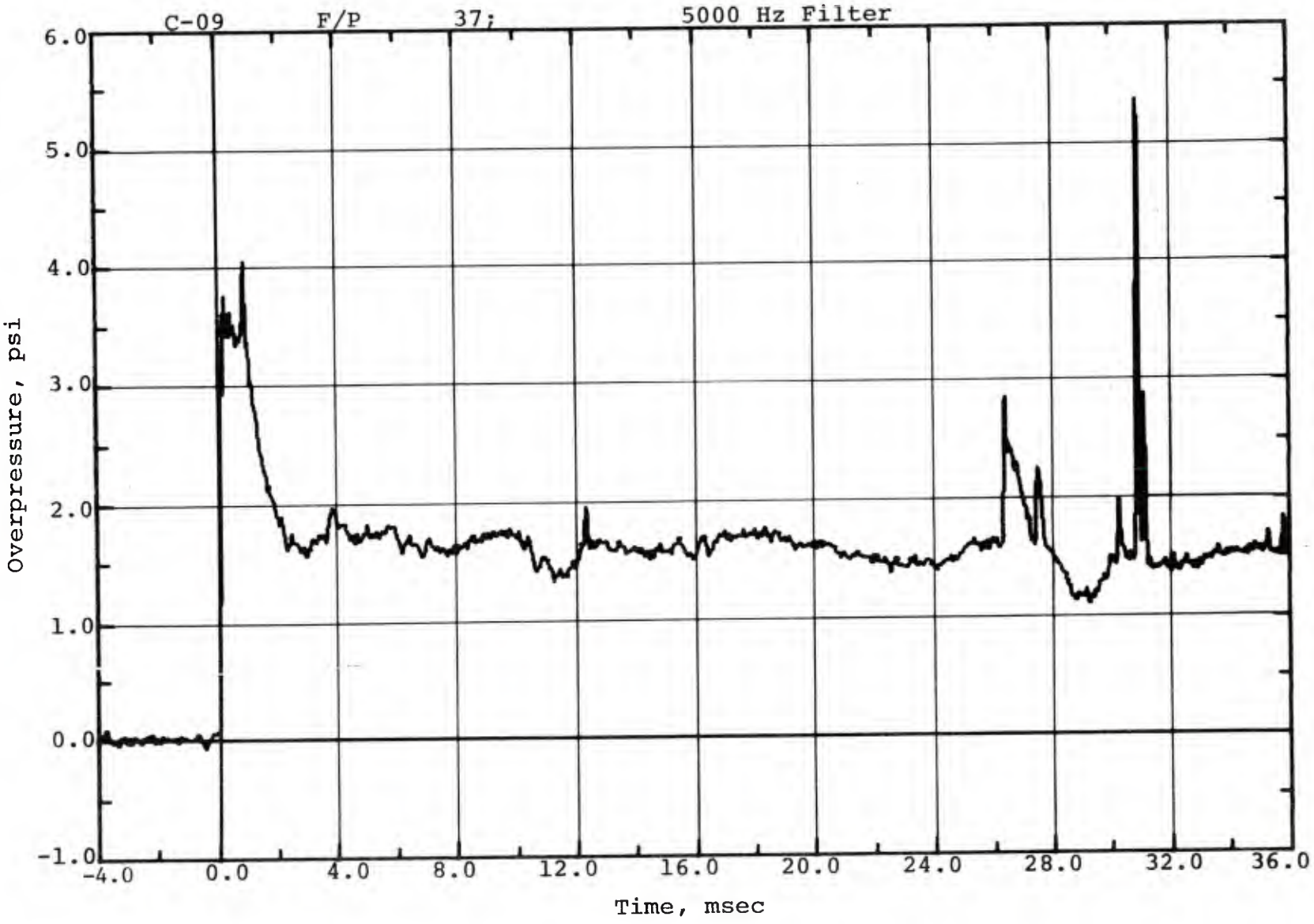

Figure 3.3. Time-Variation of Overpressure at Fin Station 37. Processed Through a 5 KHz Digital Filter

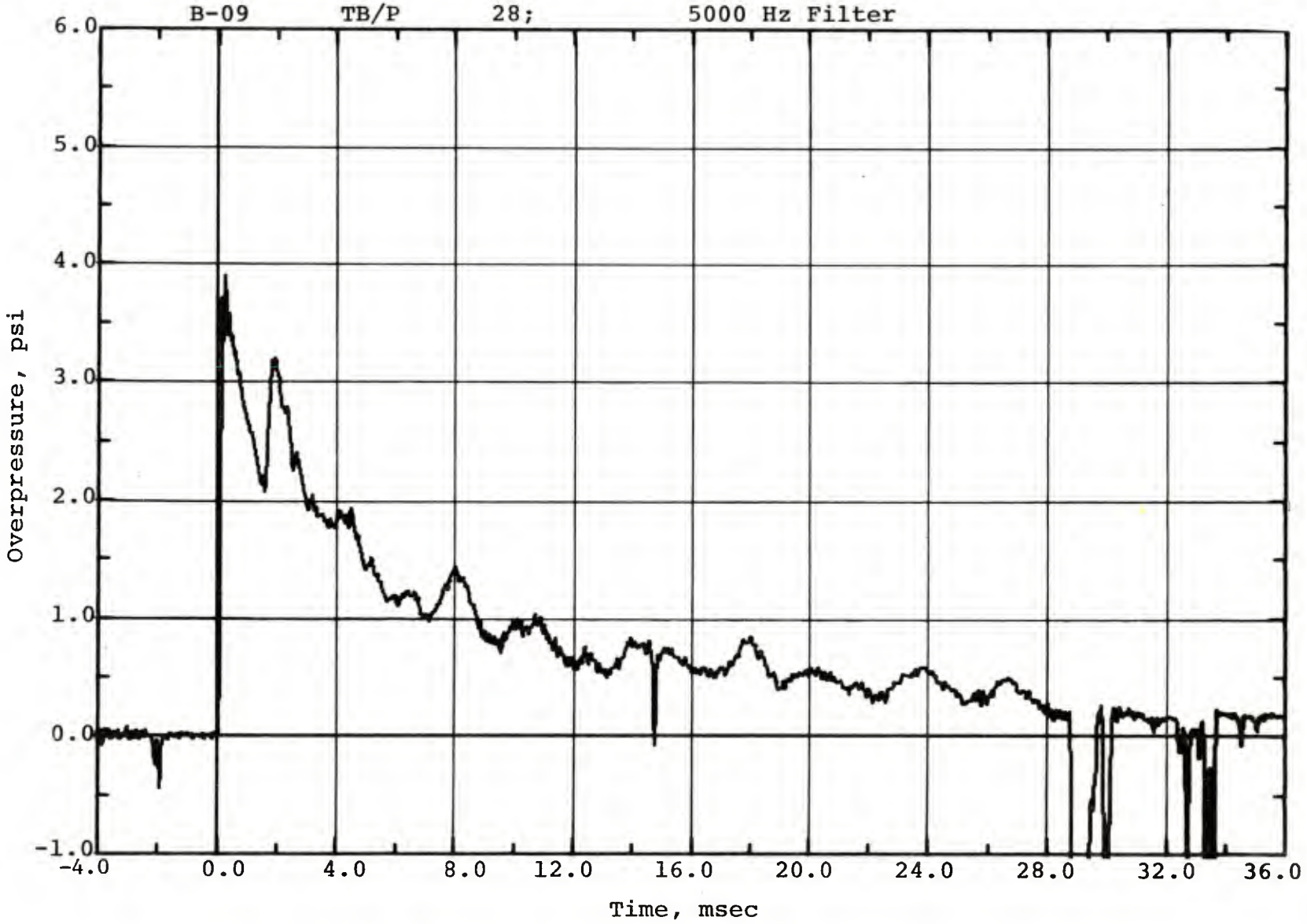

Figure 3.4. Time-Variation of Overpressure Differential at Center of Panel. Tail Boom Station 28. Processed Through a 5 KHz Digital Filter

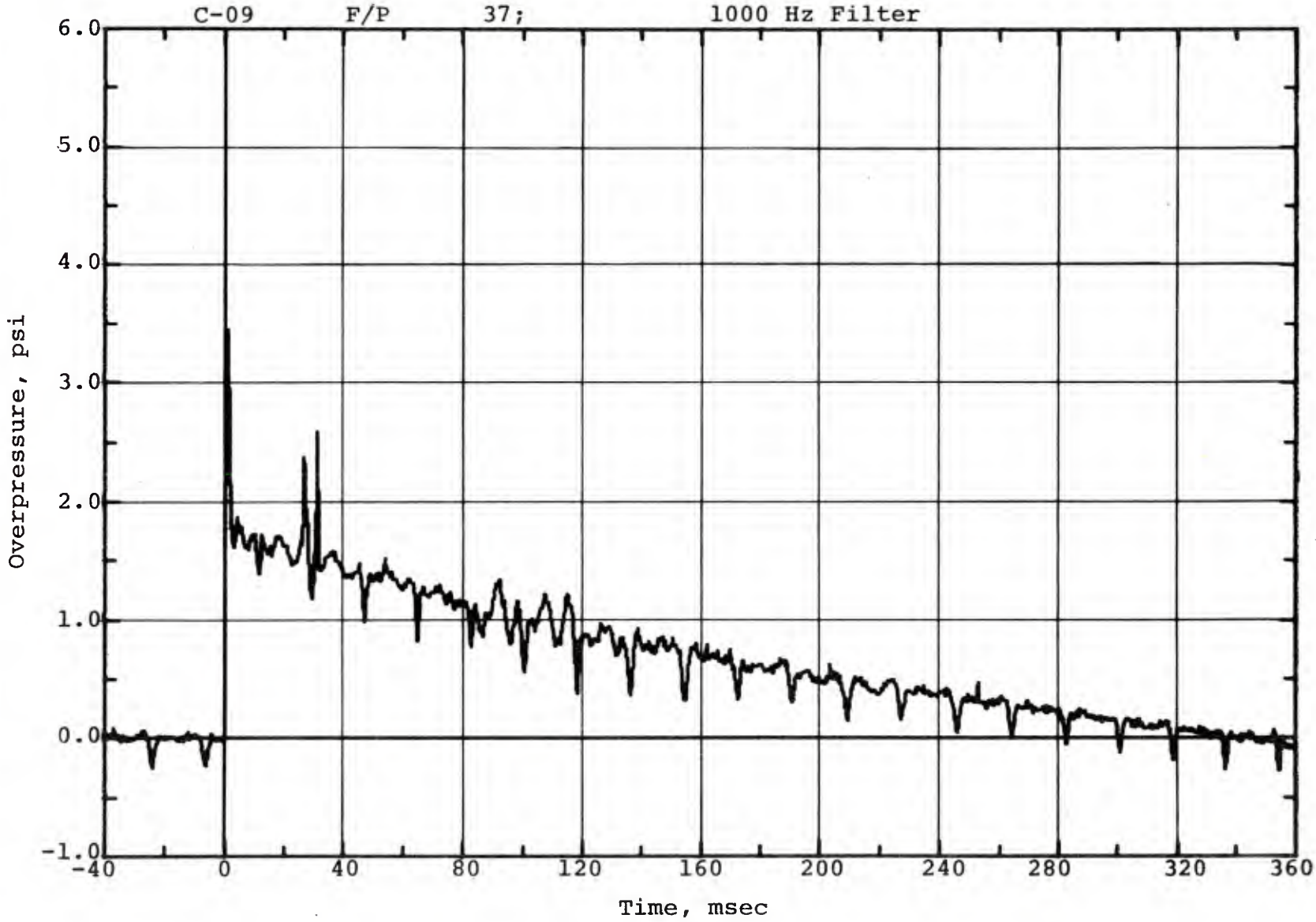

Figure 3.5. Time-Variation of Overpressure at Fin Station 37. Processed Through a 1 KHz Digital Filter. Long Duration Trace

SECTION 4

FLAPWISE BENDING MOMENT AND MOTION RESPONSES OF THE TAIL AND MAIN ROTOR BLADES

This section presents the analytical procedures and the analytical-experimental correlations for the flapwise bending moment and motion (flapping) responses of the tail and main rotor blades.

4.1 Description of the Rotor Systems

The geometrical, operational, inertial (i.e., mass distribution), and structural characteristics for the teetering two-bladed tail and main rotor systems, which are needed in the present analysis, are summarized in Table 4.1 and Figures 4.1 - 4.4. These data are the same as those used in the correlations following the PRE-MINE THROW IV Test (Reference 1), but with the following exceptions:*

(i) Slight changes in both the tail and main rotor rotational speeds, due to different weight and operating conditions, and

(ii) Inclusion of a small rigid tab on the main rotor blade. Its effect was neglected in the PRE-MINE THROW IV correlation. The tab increases the blade chord by 3.25 in. between blade stations 220.1 and 232.7.

To complete the input requirements for this phase of the analysis, the helicopter was trimmed to its pre-blast operating conditions using the MODEOP=1 option of the HELP code (Reference 3) to obtain the pre-blast values of the collective and cyclic pitch control angles which make up the total blade angle θ according to

$$\theta(r) = \theta_t(r) + \theta_c + \theta_r \cos\psi + \theta_p \sin\psi$$

Here $\theta_t(r)$ is the twist angle at station r, θ_c is the collective pitch angle, and θ_r and θ_p are the lateral and longitudinal cyclic pitch angles, respectively. Also, ψ is the blade azimuth measured from its aftmost position and positive in the direction of rotation. Expressed in degrees, these turn out to be (see Section 5).

---

*It is assumed that the helicopter tested during DICE THROW had the same rotor blades as the helicopter tested during PRE-MINE THROW IV. The parts designations in both cases were: 204-011-001-15 for the main rotor blades and 204-011-702-15 for the tail rotor blades. However, there were some modification notes along with the serial numbers of the DICE-THROW rotor blades. What these modifications amount to is unknown.

$\theta(r) = \theta - 6.85$ for the tail rotor blades, and

$\theta(r) = -10\frac{r}{R} + 14.35 + 1.31\cos\psi - 2.19\sin\psi$ for the main rotor blades.

The sign convention is such that a positive θ results in an upward force from the main rotor and a force from the tail rotor causing a nose right moment. Note that the tail rotor angle is independent of r and ψ since the blade has no twist or cyclic pitch controls.

The pre-blast thrusts from the two rotors are also found from the trimming procedure, and they turn out to be

T = 317.2 lbs to the right from the tail rotor (i.e., causing a nose left moment)

T = 5769 lbs from the main rotor.

It should be pointed out that the trim values given above are calculated with the assumption that the helicopter was steady, i.e., it was not in a disturbed state. The oscillograph traces for the vehicle motion responses presented in Section 2 indicate that the helicopter was undergoing large angular oscillations prior to shock arrival, requiring large control inputs from the autopilot. The situation was far more severe than during the PRE-MINE THROW IV Test. The influence of these oscillations should be considered in the blade flapwise bending moment correlations which will be taken up later in this section.

4.2 Analysis Techniques

In a vulnerability/survivability analysis, the predicted extreme values of the responses are most important. In the present case, the negative peak values of the tail rotor blade flapwise bending moments during the first 40 msecs are the largest (in magnitude), or very nearly so, for the entire response period.* During this short interval $0 \leq t \leq 40$ msecs, the vehicle motions and the associated changes in the blade angle (i.e., the control angle commanded by the autopilot) are sufficiently small so that they have little influence on the extreme values of the blade bending moment responses. For example, it is estimated that, in response to the blast, the autopilot put in a tail rotor collective pitch movement (pedal) of less than 0.1 deg and the yaw rate was less than

*The sign convention here is such that a positive force towards the right of the helicopter causes a negative blade bending moment.

2.5 deg/sec. Based on these observations, it is justified to conduct the tail rotor blade response analysis according to the MODEOP=4 option of the HELP code (Reference 3). This mode of operation neglects the effects of vehicle rigid-body motions and the autopilot induced control angle and treats each rotor independently.

The situation is somewhat different with the main rotor blades. There, the extreme or near extreme values are realized during the first 360 msecs or so. During this longer period ($0 \leq t \leq$ 360 msecs), the vehicle motions and the autopilot induced collective and cyclic pitch increments are considerably more significant in their effects on the main rotor blade responses. There is available a more comprehensive option in the HELP code (MODEOP=3) which could have been used to include these effects. The latter mode of operation analyzes the complete problem, i.e., the vehicle motions and both rotors simultaneously. However, it is extremely demanding in computer time.

The MODEOP=4 option was nevertheless used for both rotors in this application. The previous experience with the PRE-MINE THROW IV correlation revealed little difference between the MODEOP=3 and MODEOP=4 results for the first 50 to 60 msecs of response. As pointed out earlier, MODEOP=4 calculations should prove adequate for the tail rotor blade responses which are far more critical than the main rotor blade responses for an encounter with the blast directly from the side of the helicopter, as is the case here.

For the main rotor blade responses, both MODEOP options should predict essentially the same values for the first peak which, according to analysis, usually occurs during the first 120 msecs or so. Both options utilize simplifying approximations to calculate the induced velocity ν. As will be discussed in more detail later, the manner in which ν is estimated has relatively large effects on the total blast-induced bending moments on the main rotor, which receives the shock from the side (i.e., not head-on like the tail rotor). The simplifying approximations for calculating the induced velocity variations of the main rotor blades lead to errors which overshadow the effects of vehicle motions and autopilot inputs. This is another justification for using the less demanding MODEOP=4 option for the main rotor in preference over MODEOP=3.

The elastic deformation of each blade is represented by a linear combination of three pre-selected assumed modes which satisfy known boundary conditions. In addition, a constraint is imposed to insure continuity of the blade bending moments in going from one blade to the other. (Although more modes would have been preferrable for accuracy in computing the bending moment responses, the analysis in the HELP code was restricted to the use of a few assumed modes by practical considerations.) In the chosen option, the program first performs the elastic rotor trim to define the pre-blast operating conditions, i.e., the initial conditions of the generalized coordinates and their velocities

associated with each of the assumed modes and with the rigid-body flapping mode. It then proceeds to the transient solution to calculate the total responses. The transient solution is achieved by integrating numerically the equations of motion representing the assumed elastic modes as well as the rigid-body flapping mode. The time step, Δt, chosen for the numerical integration must be sufficiently small to avoid numerical instabilities. As a rule of thumb, Δt should be less than one fortieth of the period for the highest natural frequency appearing in the analysis. In the case of a rotor blade, this would be the highest blade frequency resulting from the assumed mode approach. For the main rotor, the choice of Δt was 0.5 msecs. For the tail rotor, with its higher rotational and elastic mode frequencies, it was found necessary to reduce Δt to the lower value of 0.05 msecs.

To insure that (a) the rotors were trimmed properly, and (b) there were no numerical instabilities in the solution, the program was first run for each rotor with its chosen Δt and with a zero-strength blast input. For both rotors, no numerical instability was encountered and the transient solutions averaged over one rotor revolution agreed with the trimming subroutine outputs.

The program was then exercised on each rotor and for a free atmosphere nuclear burst with Yield = 1.236 KT and slant range = 2562 ft, the "equivalent blast model" discussed in Section 3.2. The azimuthal positions of the tail and main rotor red blades were estimated for the shock arrival time from the rotor blade azimuth traces (Channels D-02 and D-04) and the measured rotor speeds. These were inputted in the program as required.

The program can be directed to print out the structural and motion responses as well as the instantaneous blast field flow parameters (e.g., density, components of the material velocity at the hub, etc..) after each n time steps of the solution, where n is specified by the analyst. (Usually n is taken to be 10 to avoid excessive amount of printout.) Of interest here are the flapwise bending moment distributions for both blades and the flapping angle. For each blade, the total bending moments, i.e., including those due to pre-cone, are computed at ten stations along the span. The stations are at the inboard edges of the ten equal segments representing each blade. For the two rotors, these stations are located at the following distances (in inches) from the axes of rotation:*

---

*To allow direct comparisons between the analytical and experimental time-variations of the blade bending moments, it is desirable to have the sensor locations at these stations. Due to some construction features of the blades, it was not possible to do this with all gages. The strain gage locations were: r = 10.5, 10.5, 20.4, 25.6 for the tail rotor blades and r = 35, 82, 105.6 and 132 for the main rotor blades.

r = 0, 5.1, 10.2. 15.3, 20.4, 25.5,..., 45.9 for the tail rotor

r = 0, 26.4, 52.8, 79.2, 105.6, 132..., 237.6 for the main rotor.

The program may be instructed to calculate and use the induced velocity ν in either of two ways by setting the control parameter NUOPT equal to 1 or 2. With NUOPT=1, ν is calculated on a quasi-steady basis during the transient solution, i.e., it is related to the instantaneous thrust and to the gust velocity components. With ν=2, it is set to its pre-blast (trim) value and kept constant during the transient solution. These two procedures bracket the true average value of ν over the rotor disk. The assumption that ν does not vary along the span, and for that matter is the same on both blades, is implicit in both of these procedures. A more accurate formulation for computing the temporal and spatial variations of ν, particularly for the period of shock traversal over the rotor disk (as is the situation in the present case), would be very difficult and impractical to include in this already complex code. For high forward speeds, temporal variations in ν are small; and the response results using NUOPT=1 and 2 show little differences between them. For hover, however, the results may be quite different. Consider the tail rotor blades first. With the shock head-on to the tail rotor, the material velocity (gust) component normal to the rotor disk is much larger than blast-induced changes in ν. Inaccuracies in estimating ν should produce little percentage errors in the bending moment responses. With the same orientation, the normal gust component, Δw_{gn}, to the main rotor disk is small compared with ν-changes (due to the gust component parallel to the disk and rotor thrust variations); and the effects of ν-changes on the bending responses exceed those due to Δw_{gn}. The consequences of using either of the two simplified options for calculating ν will be further discussed in connection with the main rotor bending moment correlations.

The collective and cyclic pitch angles just before shock arrival are assumed to be equal to their trim values; furthermore, they retain these values during blast encounter. The above assumptions in the MODEOP=4 analysis introduce errors for two reasons:

(1) Even though the autopilot system was on, the helicopter was undergoing fairly large oscillations, and the blade collective and cyclic pitch angles are known to have been off their trim values. In fact, if one examines the motion and stick position oscillograph traces for the few seconds preceding shock arrival, one notes magnitudes of oscillaton which in some cases are almost as large as those following shock encounter. (See quick-look traces presented in Section 2.)

(2) In the case of MODEOP=4, the control angle inputs from the autopilot as a result of blast encounter are neglected.

Since the blade bending moments (especially for teetering rotors with precones) are very strongly influenced by blade angle changes, it is reasonable to expect noticeable differences between the experimental and analytical bending moment distributions and peaks, particularly if the vehicle is very much off its trim condition at shock arrival time and for times when the autopilot inputs became fairly large. In connection with reason (2), the point was discussed earlier. Repeating, the neglect of the autopilot commands in the MODEOP=4 analysis is expected to introduce errors in the analytical blade bending moments much beyond t=40 msecs.

Off-trim conditions could have been accounted for because they are known from the test results; but the effort would have been substantial, in as much as it would have necessitated modifications to several parts of the HELP program.*

A few words need be said about the aerodynamic subroutines which generate the airloads on the blades. First of all, these subroutines utilize two-dimensional steady-state data on a quasi-steady basis. The data includes the variations of lift (c_ℓ) and drag (c_d) coefficients with angle of attack and Mach number for a "nominal" Reynolds number. Since both blade sections are symmetric, one can confine α-variations between 0 and 180°. For this purpose, the aerodynamic information supplied by Schramm in Reference 5 has been used for both the tail and main rotor blades. The c_ℓ - and c_d - variations with α and M as given by Schramm are "representative" for blades of type and size dealt with here. They have a number of simplifying features, one of which is the approximation of c_ℓ near the stall region. This may affect the peak calculated responses, since the blade angles at some spanwise stations can reach and exceed their stall angles due to the material velocity behind the shock.

*The HELP code was developed to provide an analytical tool in general vulnerability studies. Since pre-blast off-trim conditions are unknown in such studies, it would serve no purpose to modify the program so that it accepts off-trim conditions.

4.3 Tail Rotor Flapwise Bending Moment Correlations

Long duration oscillograph traces of the flapwise bending moments at four stations along the red blade (A-03, B-03, C-03, D-03 at stations 10.5, 15.5, 20.4, 25.5, respectively) and at two stations along the white blade (A-04, B-04 at stations 15.5 and 20.4, respectively) were examined to define the period of significant responses and to obtain some qualitative descriptions of the pre-blast and post-blast behaviors of the channels. Short segments of these traces were presented in Figure 2.5. Figures 4.5-4.10 show the digitally processed traces for the same channels. They are confined to the shorter period - 10 msecs $\leq t \leq$ 90 msecs in order to show clearly the details in the responses.* To ease the experimental-analytical comparisons, the plotting scales for these traces were taken to be the same as those in the corresponding analytical curves presented in Figures 4.11 - 4.14.

The following observations from the experimental traces should be mentioned:

1. In the A-03, data, a large positive spike exists between approximately t = 7 msecs and 15 msecs. This is an extraneous signal and that segment of the response was masked out in Figure 4.5. Thus the first negative peak from the A-03 channel is lost. Based on signals from the other red blade channels and previous results in PRE-MINE THROW IV, the lost negative peak was very likely the largest.

2. The white blade, station 15.5 trace (A-04) shows malfunction of the channel a few tens of milliseconds following shock arrival, as evidenced by the fact that it does not return to near its pre-blast level like the other channels after several seconds of response. (See oscillograph trace for A-04 in Figure 2.5).

3. In all cases the extreme bending moments are associated with negative peaks. With the sole exception of the A-04 channel which appears to have malfunctioned at later times, these negative peaks occur before t = 40 msecs. The first and second negative peaks, both occurring before t = 40 msecs, are of comparable magnitude, with the first peaks being larger in the red blade channels and smaller in the white blade channels.

4. The A-03 trace exhibits positive spikes prior to shock arrival. (See oscillograph trace.) The period between these spikes corresponds with the period of one tail rotor revolution. They are attributed to slip ring noise. Fortunately, they disappear after shock arrival.

*In all discussions to follow, t should be interpreted as time from shock arrival at the component in question, unless stated otherwise.

5. There are "beats" in the signals from all channels, pre-blast and post-blast; they may not be too apparent in the short segments of the oscillograph traces presented here. They are more severe than in the corresponding traces from PRE-MINE THROW IV. The situation is worst with the D-03 channel in that the "beat amplitudes" are larger fractions of the total blast induced response amplitudes.

6. The peak-to-peak values of bending moment just prior to shock arrival are measured from the oscillograph traces to have been approximately 800, 500, 400, 500, 800, 800 in-lbs for A-03,..., D-03, A-04, B-04 channels, respectively. They are not displayed sufficiently in Figures 4.5 - 4.10 due to the cutoffs below -10 msecs. These peak-to-peak variations are not regular to permit establishing accurate values of average pre-blast bending moments. From oscilloscope traces (not presented in this report), rough estimates for the average pre-blast levels are 600, 350, 550, 250, 350, 250 in-lbs for the A-03,...D-03, A-04, B-04 channels, respectively.

According to the analysis, there should be no time-variations of bending moment at any blade station and no differences between the bending moments at the same spanwise stations on the two blades during pre-blast since the flight velocity is zero (hover) and there are no cylic pitch variations. But the experimental traces show appreciable pre-blast peak-to-peak variations and differences in pre-blast average levels, as indicated in item (6) above. The wind velocity was not of sufficient magnitude to have caused peak-to-peak variations of these magnitudes and differences between corresponding points on the two blades. Likely contributing factors are:

(i) Possible differences in the two blades, i.e., not perfectly matched,

(ii) Effects of the induced velocity at the tail rotor due to the main rotor, and especially,

(iii) Fin interference effects.

All three factors are unaccounted for in the analysis.

The correlations are done in two parts: (a) time-variations at the sensor stations, and (b) the maximum positive and negative peaks along the blade. The experimental-analytical comparisons are also partially summarized in Table 4.2. Referring to Figures 4.11 - 4.14, the experimental time-variations of bending moment response at blade stations 10.5, 15.5, 20.4, and 25.5 are compared with the corresponding analytical results for stations 10.2, 15.3, 20.4, and 25.5. The analytical and experimental stations either coincide or are close enough to each other to make direct and fair comparisons. Based on experience from the

PRE-MINE THROW IV study, the NUOPT=1 option of the HELP code is preferred and used to generate the analytical responses. For stations 15.3 and 20.4, the average values of the analytical responses for the red and white blades are shown, since the analysis indicates small differences at corresponding points on the two blades (with a hover condition and with the blast being nearly head-on to the tail rotor disk).

Generally, the predicted response curves resemble their experimental counterparts. Closer examinations reveal that although the analysis does not duplicate the local details in the experimental traces, it does display similar trends and features. The following specific observations are also worthy of note:

(1) As stated earlier, the pre-blast peak-to-peak variations are not predicted by analysis. But the average values can be compared with the analytical pre-blast levels. From Table 4.2, one notes that the analysis overpredicts the pre-blast levels for the two inboard stations of the red blade, and underestimates those for the two outboard stations of the same blade. One cause for these differences may be that the analytical trim does not correspond nearly with the "actual trim", since the weight and c.g. conditions are not known accurately. From the same table, one can also note differences between the average pre-blast values at corresponding points on the two blades. These give some indication of the measurement accuracies, in as much as the average responses at corresponding points of the two blades should be the same. The various discrepancies between different channels and between experiment and analysis may be due in part to calibration errors including zero - shifts in the various channels. Slight drifts have been detected in the data of some channels taken during the last calibration sequence nearly two hours before test time.

(2) The analytical negative peak values for A-03 (Sta. 10.2) are considerably higher than the measured ones. This is in contrast with the outcome following the PRE-MINE THROW IV correlation. There, the predictions for a nearby station (Sta.11) underestimated slightly the first negative peak. (See Figure 4.9 of Ref. 1).

(3) In view of the operating conditions and the blast orientation, the station 15.5 channels, B-03 (Red) and A-04 (White), should agree within a few percent in all aspects (including total exercusions between various positive and negative peaks). The blast response levels are somewhat higher for the red blade; and analysis is in closer agreement with this channel, being within less than 20% in the peak-to-peak excursions included in Table 4.2. The results from A-04, the channel which shows gage malfunction at later times, are suspect.

(4) For the same reasons as in (3), the station 20.4 channels, C-03 (Red) and B-04 (White), should also agree within a few percent in all aspects. In this case, they do; and the analytical results are in fairly good agreement, being less than 12% in the peak-to-peak excursions.

(5) As to the D-03 (Sta 25.5) channel, the experimental positive peaks are higher and negative peaks lower than predicted; but the analytical peak-to-peak excursions are in fairly good agreement with experiment.

Since peak values (especially the negative peaks in this case) are most important, the spanwise distributions of the extreme values, i.e., largest negative and positive peaks, are also presented in Figure 4.15 for the period $0 \leq t \leq 60$ msecs. Included in this figure is the "yield allowable boundary" furnished by Bell Helicopter. The maximum negative peaks reach this boundary, especially near stations 18-24.

Considering the quality of the response data and of the analysis input data, and in view of the similarities in the shapes of the response curves, the experimental-analytical correlations are deemed satisfactory. Based on these results and the corresponding ones from the PRE-MINE THROW IV correlation study, one can state confidently that the HELP code does provide a reliable means for estimating rotor blade flapwise bending moments for the most critical head-on or near head-on (to the rotor disk) encounters. The same cannot be said about the far less severe condition with a side-on shock. One such situation is the case of the main rotor in the present test which is discussed next.

4.4 Main Rotor Flapwise Bending Moment Correlations

Oscillograph traces for the main rotor flapwise bending moments at four stations along the red blade (A-01, B-01, C-01, D-01 at stations 35, 82, 105.6, 132, respectively) and at two stations along the white blade (A-02, B-02 at stations 82 and 105.6, respectively) provide some very useful information in explaining the disagreements between the analytical and experimental results for these channels. Short segments of these traces were presented in Figure 2.4. The corresponding traces from the digital processing are given in Figures 4.16a-4.21a, for the period $-40 \leq t \leq 360$ msecs. They are repeated over the longer time span - 500 msecs to + 500 msecs in Figures 4.16b-4.21b to show the pre-blast variations.

The following observations should be apparent from the oscillograph or digitized traces:

(1) There are large pre-blast peak-to-peak variations, in the sense that they are large fractions of the post-blast peak-to-peak excursions, unlike the situation with the tail rotor bending responses where the blast-induced responses are predominant. In the case of D-01, for instance, the ratio of pre-blast to post-blast peak-to-peak variations is roughly 0.5. The pre-blast variations persist after shock arrival and consequently "cloud" the blast-induced portions of the

total responses. From Figures 4.16-4.21, their peak-to-peak values amount to about 17000, 5000, 4000, 5000 in-lbs for stations 35, 82, 105.6 and 132, respectively. These values are roughly 50% higher than in the PRE-MINE THROW IV correlation. (See Ref. 1, item (1) on page 4-9.)

(2) The noise between times t=110 msecs and t=225 msecs indicates a temporary malfunction of the C-01 (Sta. 106.5, Red) channel, with the result that the first large negative peak is lost.

(3) A large and extraneous spike appears at around 150 msecs in the A-02 channel (Sta. 82, White) data. Fortunately, the temporary malfunction did not cause a loss of a peak value. In Figures 4.20a-b, this spike has been omitted and replaced by a dashed line.

(4) The A-01, B-01, B-02 traces bear little semblance to their counterparts from PRE-MINE THROW IV. (See Figure 4.13 - 4.15, Reference 1.) This is understandable in view of the following differences between the two tests: (a) the weight and c.g. conditions which affect the trim (thus pre-blast) conditions, (b) the disturbances which affect the control inputs, and (c) perhaps most important, the azimuth location of the blades at intercept time. From the red blade azimuth trace (D-02), it is estimated that the ψ-angle for the red blade (measured from its aftmost position and in the direction of rotation) was about 242°. In PRE-MINE THROW IV, the same angle was about 317°.

The predicted responses are shown in Figures 4.22 - 4.28 for red blade stations 26.4, 52.8, 79.2, 105.6, 132 and for white blade stations 79.2 and 105.6. Two sets of curves are given, one based on the NUOPT=1 option of the HELP code and the other on the NUOPT=2 option. Except for the A-01 (Sta 35, Red) trace, the experimental responses presented in Figures 4.16a - 4.21a may be compared directly with the corresponding predictions in Figures 4.22 - 4.28. It is apparent that the correlations are generally poor both in wave shapes and in peak values. Factors which contribute to these poor correlations need be discussed in some detail.

According to the analysis which does not account for off-trim conditions, interference effects from the fuselage, fin, and tail rotor, and which neglects wind effects, the pre-blast peak-to-peak bending moment variations are less than about 600 in-lbs everywhere along both blade spans, because the vehicle velocity is zero and the trim cyclic pitch controls are invariant and fairly small. These peak-to-peak variations are an order of magnitude less than the experimental values indicated in observation (1) above.

The analytical responses shown in Figures 4.22 - 4.28 for times $t \geq 0$ reflect predominantly the blast-induced parts since the pre-blast variations are relatively small. In contrast, as pointed out earlier, the experimental responses for $t > 0$ include the continuations of the large pre-blast variations which "cloud" the blast-induced parts.

Secondly, the manner in which the induced velocity ν is estimated in the analysis changes drastically the characters and extents of the responses, as seen by the differences in the NUOPT=1 and NUOPT=2 curves in Figures 4.22-4.28. These differences may be explained if one examines the situation of a side-on blast encounter. With the shock directly from the left side of the vehicle, the tail rotor is engulfed instantaneously, and the material velocity behind the shock is perpendicular to the rotor disk. Changes in the inflow velocity are minor when compared with the material velocity which increases (or decreases) the blade angles of attack. Errors in estimating ν would be insignificant from the view point of total blast-induced responses. With the same shock orientation, however, the shock travels over the main rotor disk, the traversal time being of the order of 10 msecs, inducing an asymmetric loading on both blades. With the component of material velocity normal to the disk being small, the changes in ν and in the relative wind speeds for the blade airfoil sections are primarily responsible for the additional blade loadings. Thus ν-changes become much more important; and inaccuracies in estimating ν are reflected strongly in the final post-blast responses. In the analysis, the approximations which allow "practical" estimations of ν are very drastic when rapid changes occur in the rotor operating conditions. First, the computed ν is an averaged value over the disk, a situation which is not obviously true, especially during shock traversal over the disk. Secondly, the induced velocity is strongly influenced by changes in wind velocity parallel to the disk, as the latter changes from 0 (pre-blast hover) to almost the magnitude of the material velocity (since the material velocity is nearly parallel to the main rotor disk). And thirdly, it takes time for ν to adjust, i.e., the quasi-steady approach using the momentum theory is not totally justified for early times. To clarify some of the points made above, consider the two NUOPT-options which have been used. With NUOPT=2, the induced velocity retains its pre-blast average value of about 31 ft/sec; and the blast-induced loadings result solely from the small gust velocity Δw_{gn} in a direction perpendicular to the rotor disk and changes in the relative wind speeds for the airfoil sections. Δw_{gn} turns out to be around 3 or 4 ft/sec when the material velocity behind the shock is at its peak. With NUOPT=1 on the other hand, the major gust velocity component (parallel to the rotor disk) lowers ν rapidly from its initial value of 31 ft/sec by as much as 15-17 ft/sec. Thus the effects due to ν-reduction overshadow those due to Δw_{gn}. The actual ν-reductions at early times are not expected to be as large as those predicted on a quasi-steady basis by the NUOPT=1 option, nor ν is expected to stay at the same level as in the pre-blast phase.

It should be clear from the above discussions that any attempt to improve the analysis must consider an accounting of the heretofore neglected interference effects and a complete reassessment of the manner in which the ν's are computed in the program. From a practical consideration, the needed modifications appear too demanding. Fortunately, the problems referred to above are not important issues in actual applications. They are most troublesome for a rotor in a hovering condition and receiving the gust directly from its side, as was the case of the main rotor in the tests. From a vulnerability viewpoint, however, the side-on blast orientation is not critical for the rotor. In fact, the extreme bending moments on rotors for side-on orientations should be far below their yield allowables.

Due to the noted poor correlations of analysis with experiment for the time-variations of the main rotor blade bending moments, no effort was made to superimpose the experimental data atop the analytical curves presented in Figures 4.22-4.28, as was done in the case of the tail rotor. However, the analytical and experimental results for the spanwise distributions of the extreme response values for the main rotor are presented in Figures 4.29-4.30. The first of these is for the red blade and the other for the white blade, with both confined to the extremes occurring between t=0 and t=360 msecs.* The analysis is according to the NUOPT=1 option. From data supplied by Bell, the yield allowable boundaries are well beyond these curves. For instance, the yield allowables are $\pm$ 11.1 x 10^4, $\pm$ 6.45 x 10^4, and $\pm$ 4.84 x 10^4 in-lbs for stations 62, 100, and 120, respectively.

The analysis overpredicts both the maximum and minimum extremes, especially for the innermost stations. It underpredicts the minimum peak for the outboard station. In any event, the extremes are well within the region bounded by the yield allowable curves, indicating that the main rotor is not a critical component when the burst is from its side.

4.5 Blade Flapping Angles

Figures 4.31-4.32 present digitally processed, short duration traces for the tail and main rotor flapping angles (C-04, C-02). The corresponding longer duration oscillograph traces were given earlier. (See Figures 2.5 and 2.4).

Consider the tail rotor case first. For the pre-blast period, the oscillations show some "irregular beats" in their amplitudes, with the

---

*All extremes or near extremes (i.e., positive or maximum and negative or minimum) occur during this period. The sole exception is the A-01 trace which shows a higher negative peak at $t \cong 700$ msecs than the negative peaks during the indicated period. Also, due to the fact that the MODEOP=4 mode is used in the analysis, the analytical extremes derived from peaks occurring much beyond t=120 msecs are questionable, as discussed in Section 4.2.

maximum amplitude being about 2.0 degrees.* For the period $0 \leq t \leq 0.5$ sec. approximately, the amplitudes reach values over twice as high as the maximum pre-blast amplitudes. Thereafter, the pre-blast pattern resumes. This behavior is quite similar to the one observed during PRE-MINE THROW IV; in the latter, however, the amplitude level was lower and the beats were less pronounced.

With a hover condition and no cyclic pitch controls, the analysis predicts essentially zero flapping angle prior to shock arrival. Since the shock is nearly head-on to the rotor desk, it also predicts very small oscillations for the flapping angles. During the first 100 msecs, the analytical results indicate that the amplitude should increase first, stabilize for a short time at around 0.05 degrees and then start decreasing slowly. Although the same sort of behavior is noted in the experimental trace C-04, the amplitudes are far larger. It is believed that the primary causes for the lack of correlation are the fin and main rotor interference effects and the rigid body motions of the vehicle, all of which have been neglected in the analysis.

As to the main rotor case, the pre-blast portion of the C-02 trace shows severe beats in the oscillations; furthermore, the peaks of some oscillations are clipped. Some of the clipped peaks are at high amplitudes and others at low amplitudes. This is similar to the behavior noted in the corresponding trace from PRE-MINE THROW IV. The amplitude beats are far more pronounced in C-02. For example, the amplitudes around $t = -3$ secs are over five times the amplitudes around $t = -1.5$ secs. The amplitudes increase for the first two cycles or so following shock arrival, and then start decaying. The pre-blast pattern resumes thereafter.

The prediction curve shown in Figure 4.33 may be compared with its experimental counterpart (Figure 4.32). Several factors contribute to the poor correlation. The major ones are: the neglect in the analysis of the fuselage interference and rigid body motion effects, and the off-trim, unsteady conditions which prevailed before shock arrival.

---

*The oscillograph traces given in Figure 2.5 are too short to show clearly these beats.

TABLE 4.1 MAIN AND TAIL ROTOR DATA

CHARACTERISTICS	FOR MAIN ROTOR	FOR TAIL ROTOR
Pre-Blast Flight Condition	Hover	Hover
Rotor Speed, Ω, (rad/sec)	34.390	175.40
Radius, R, (ft)	22.0	4.25
Chord, c, (ft)	1.75*	0.70
Rotor Axis Relative to Vertical Axis of Vehicle, γ_f and γ_s (deg)	$\gamma_f = 3^o$ Forward Tilt $\gamma_s = 0^o$ Side Tilt	$\gamma_f = 0^o$ Forward Tilt $\gamma_s = 90^o$ Side Tilt
Precone Angle, β_p,	4.0	1.5
Linear Twist Root to Tip (deg)	-10.0	0
Allowable Flapping Angles with Respect to Mast (deg)	$\pm$12	$\pm$8
Hinge Cant Angle, δ_3, (Pitch-Flap Coupling), (deg)	0	-35
Blade Sectional Shape	NACA 0012	NACA 0015
Spanwise Mass Distribution	See Fig. 4.1	See Fig. 4.2
Spanwise Flapwise Bending Stiffness Distribution	See Fig. 4.3	See Fig. 4.4

*Exclusive of flap. See text, Section 4.1, for details of flap.

TABLE 4.2. SUMMARY OF EXPERIMENTAL AND ANALYTICAL RESULTS FOR THE FLAPWISE BENDING MOMENTS OF THE TAIL ROTOR BLADES

	CHANNEL: A-03, RED BLADE STATION 10.5				
	EXPERIMENT		ANALYSIS (NUOPT=1)		
	BM	t_p	BM	t_p	
Average Pre-Blast	~600	-	1465	-	BM = Bending Mom., in-lbs.
1st. Neg. Peak	NA	-	-7000	15.0	t_p = Time of Peak, msecs.
1st. Pos. Peak	400	26.0	1480	25.5	NA = Not Available
2nd. Neg. Peak	-5600	40.7	-7080	40.0	~ Approx. Value
2nd Pos. Peak	0	52.8	1280	51.0	
1st. Neg. to 1st Pos.	NA	-	8480	-	
1st Neg. to 2nd Pos.	NA	-	8280	-	
1st. Pos. to 2nd Neg.	-6000	-	-8560	-	
2nd. Neg. to 2nd Pos.	-5600	-	8360	-	

	CHANNEL: B-03, RED BLADE STATION 15.5				CHANNEL: A-04, WHITE BLADE STATION 15.5			
	EXPERIMENT		ANALYSIS (NUOPT=1)		EXPERIMENT		ANALYSIS (NUOPT=1)	
	BM	t_p	BM	t_p	BM	t_p	BM	t_p
Average Pre-Blast	~350		874	-	~350		875	-
1st. Neg. Peak	-4250	14.0	-4730	~12.5	-3500	11.4	-4730	~12.5
1st. Pos. Peak	500	26.2	850	25.5	80	26.0	850	25.5
2nd. Neg. Peak	-3750	38,3	-4660	~38.0	-3720	40.8	-4660	~38.0
2nd. Pos. Peak	230	52.3	750	50.8	-190	50.0	750	50.8
1st. Neg. to 1st. Pos.	4750		5580	-	3580		5580	-
1st. Neg. to 2nd. Pos.	4480		5480	-	3310		5480	-
1st. Pos. to 2nd. Neg.	-4250		-5510	-	-3800		-5510	-

TABLE 4.2. SUMMARY OF EXPERIMENTAL AND ANALYTICAL RESULTS FOR THE FLAPWISE BENDING MOMENTS OF THE TAIL ROTOR BLADES (CONTINUED)

	CHANNEL: C-03, RED BLADE STATION 20.4				CHANNEL: B-04, WHITE BLADE STATION 20.4			
	EXPERIMENT		ANALYSIS (NUOPT=1)		EXPERIMENT		ANALYSIS (NUOPT=1)	
	BM	t_p	BM	t_p	BM	t_p	BM	t_p
Average Pre-Blast	~550	-	438	-	~250	-	400	-
1st. Neg. Peak	-2550	15.0	-3150	12.5	-2300	14.0	-3150	12.5
1st. Pos. Peak	1100	27.2	450	25.5	820	26.4	450	25.5
2nd. Neg. Peak	-2050	39.0	-3100	38.5	-2550	39.8	-3100	38.5
2nd. Pos. Peak	850	51.7	480	~50.5	200	49.5	480	~50.5
1st. Neg. to 1st. Pos.	3650	-	3600	-	3120	-	3600	-
1st. Neg. to 2nd. Pos.	3400	-	3600	-	2500	-	3600	-
1st. Pos. to 2nd. Neg.	-3150	-	-3550	-	-3370	-	-3550	-

	CHANNEL: D-03, RED BLADE STATION 25.5			
	EXPERIMENT		ANALYSIS (NUOPT=1)	
	BM	t_p	BM	t_p
Average Pre-Blast	~250	-	190	-
1st. Pos. Peak	1200	3.6	680	3.0
1st. Neg. Peak	-1525	13.8	-1970	12.5
2nd Pos. Peak	1050	26.8	850	25.0
2nd Neg. Peak	-1250	38.1	-1950	37.8
3rd Pos. Peak	1000	50.5	740	~50.0
1st. Pos. to 1st Neg.	-2705	-	-2650	-
1st. Pos. to 2nd Neg.	-2450	-	-2630	-
1st. Neg. to 3rd Pos.	2525	-	2700	-

BM = Bending Mom., in-lbs.
t_p = Time of Peak, msecs.
NA = Not Available
~ Approx. Value

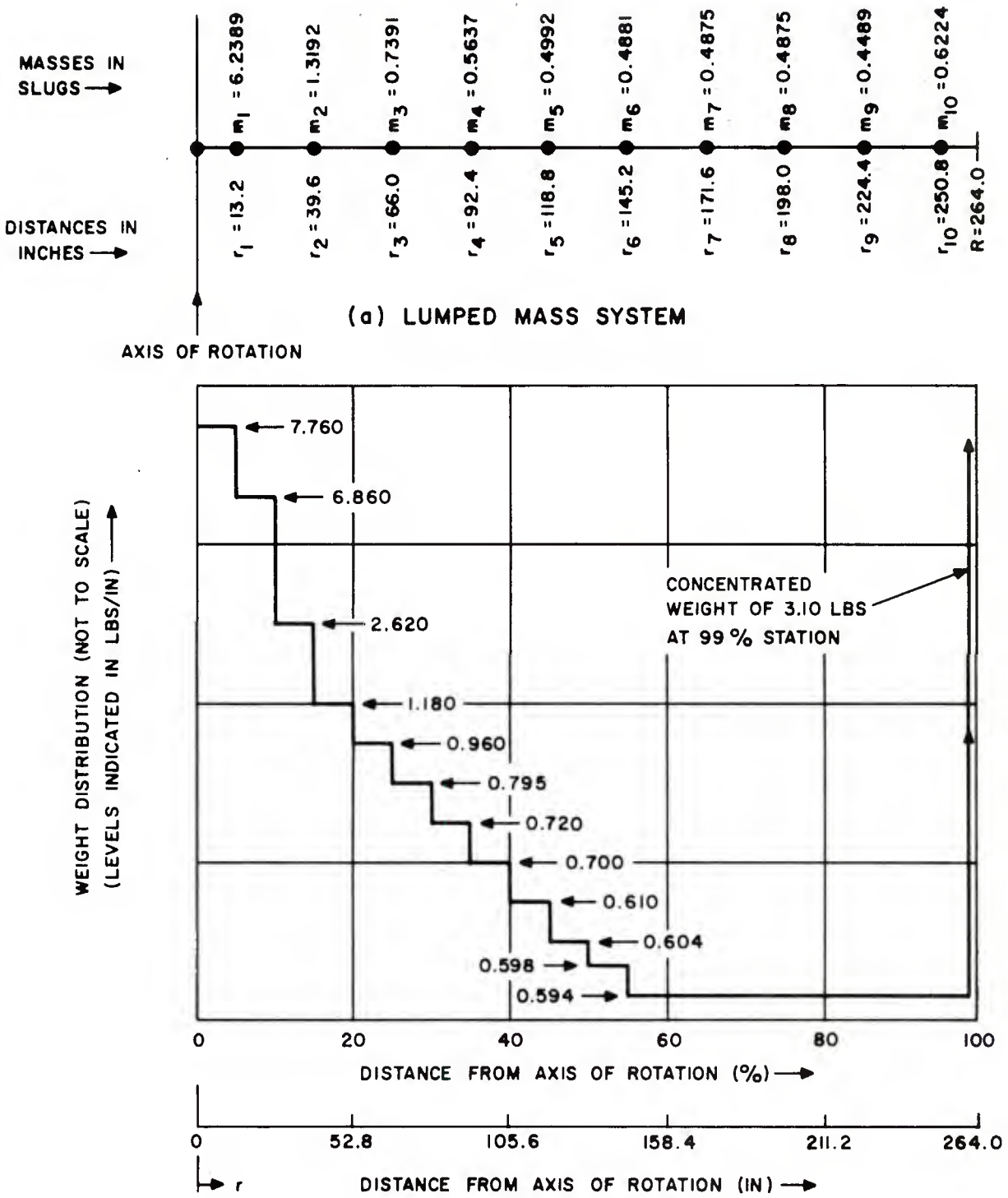

Figure 4.1. Nominal Spanwise Mass (Weight) Distribution of Main Rotor Blade and Equivalent Lumped Mass System Used in Analysis

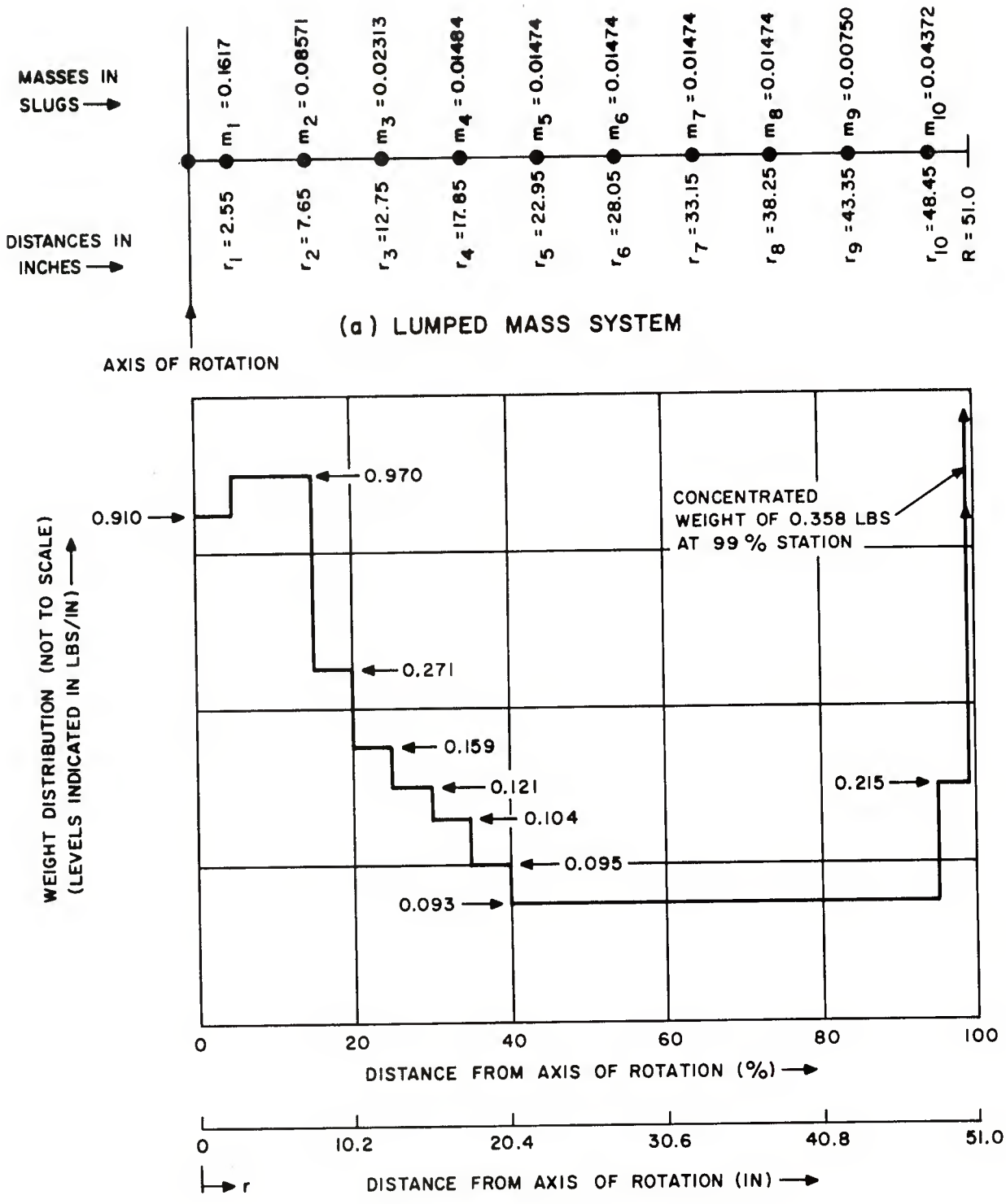

Figure 4.2. Nominal Spanwise Mass (Weight) Distribution of Tail Rotor Blade and Equivalent Lumped Mass System Used in Analysis

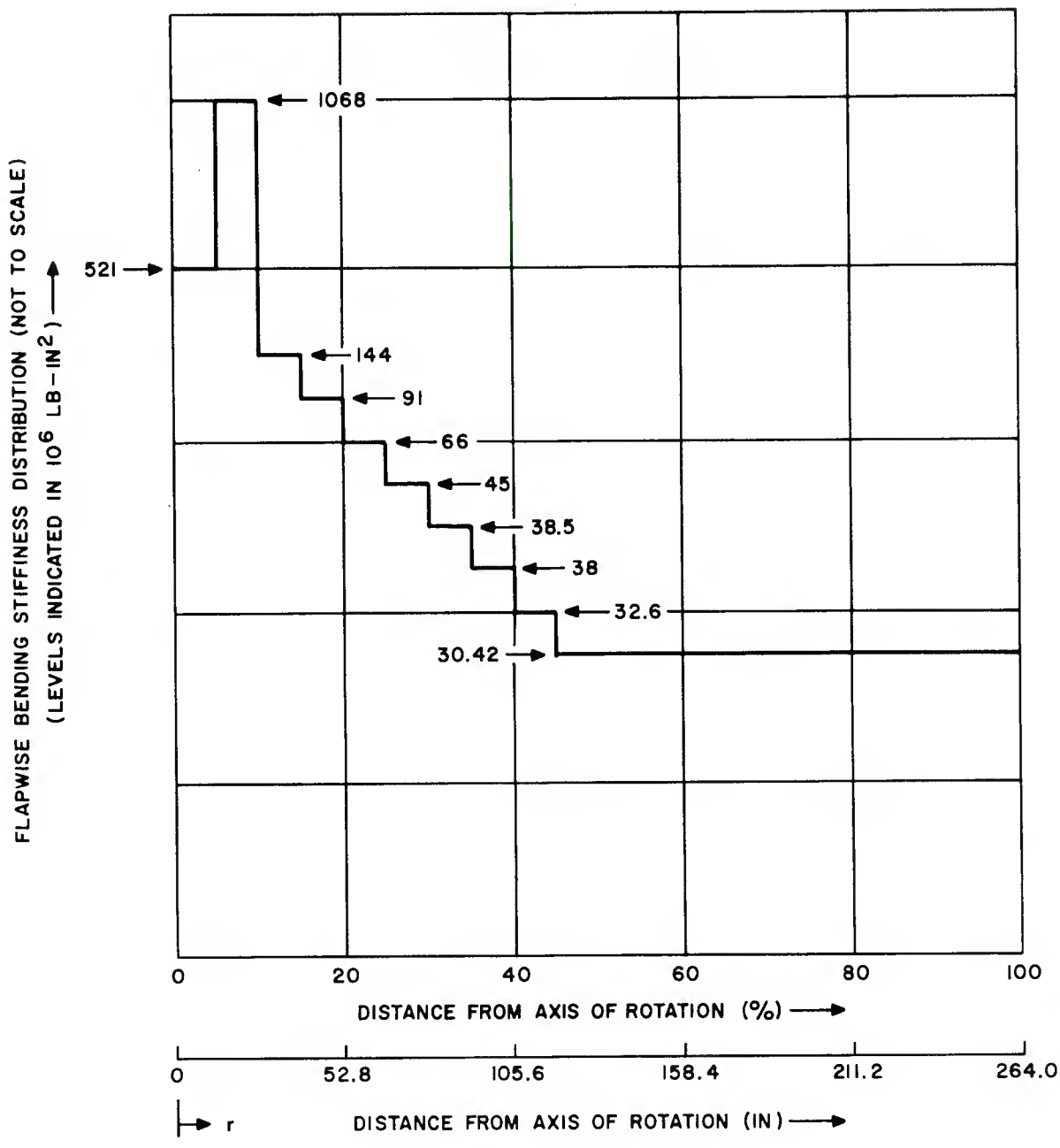

Figure 4.3. Flapwise Bending Stiffness (EI) Distribution for Main Rotor Blade. (Nominal)

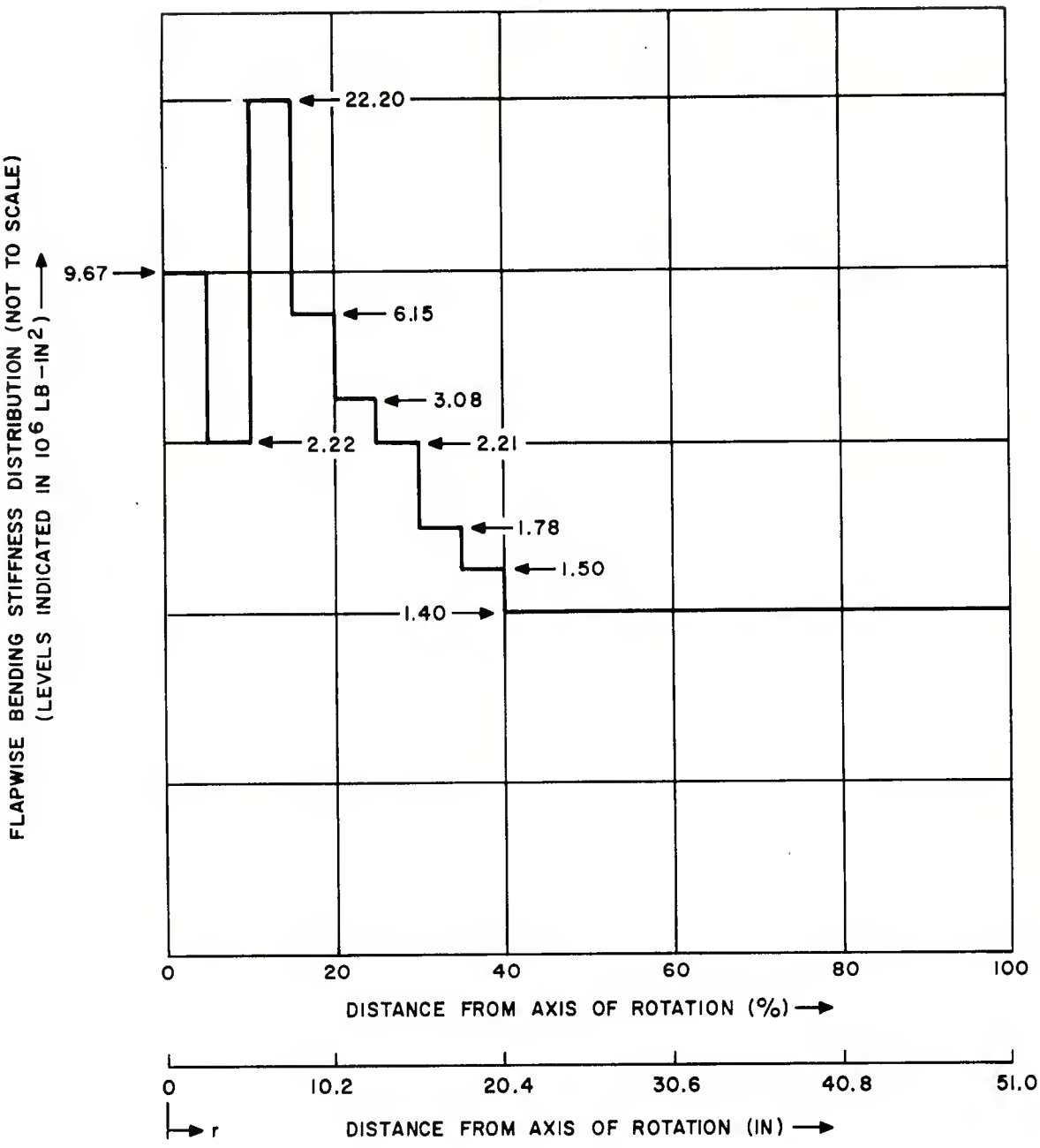

Figure 4.4. Flapwise Bending Stiffness (EI) Distribution for Tail Rotor Blade. (Nominal)

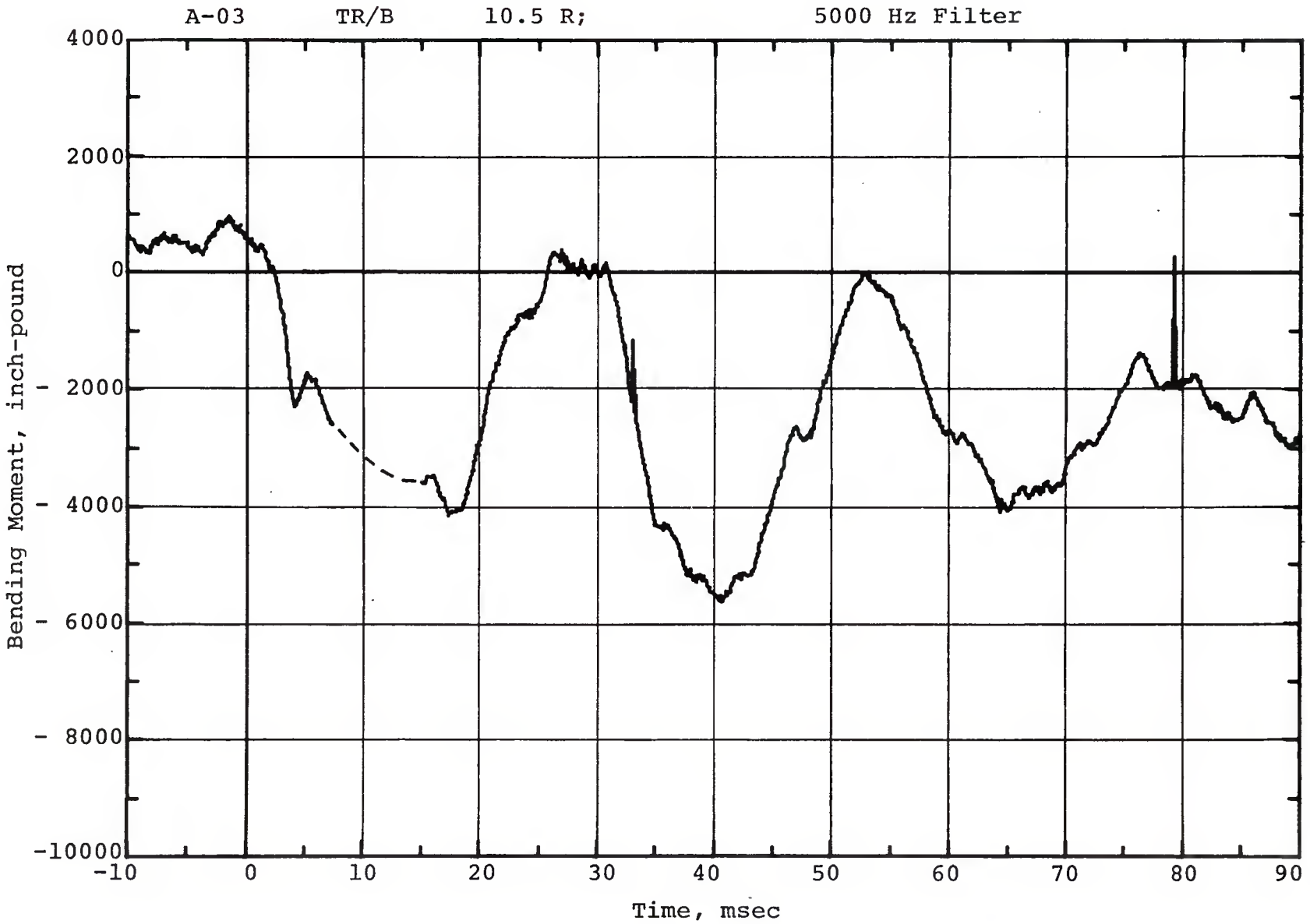

Figure 4.5. Time-Variation of Total Flapwise Bending Moment At Tail Rotor Red Blade Station 10.5. Channel A-03

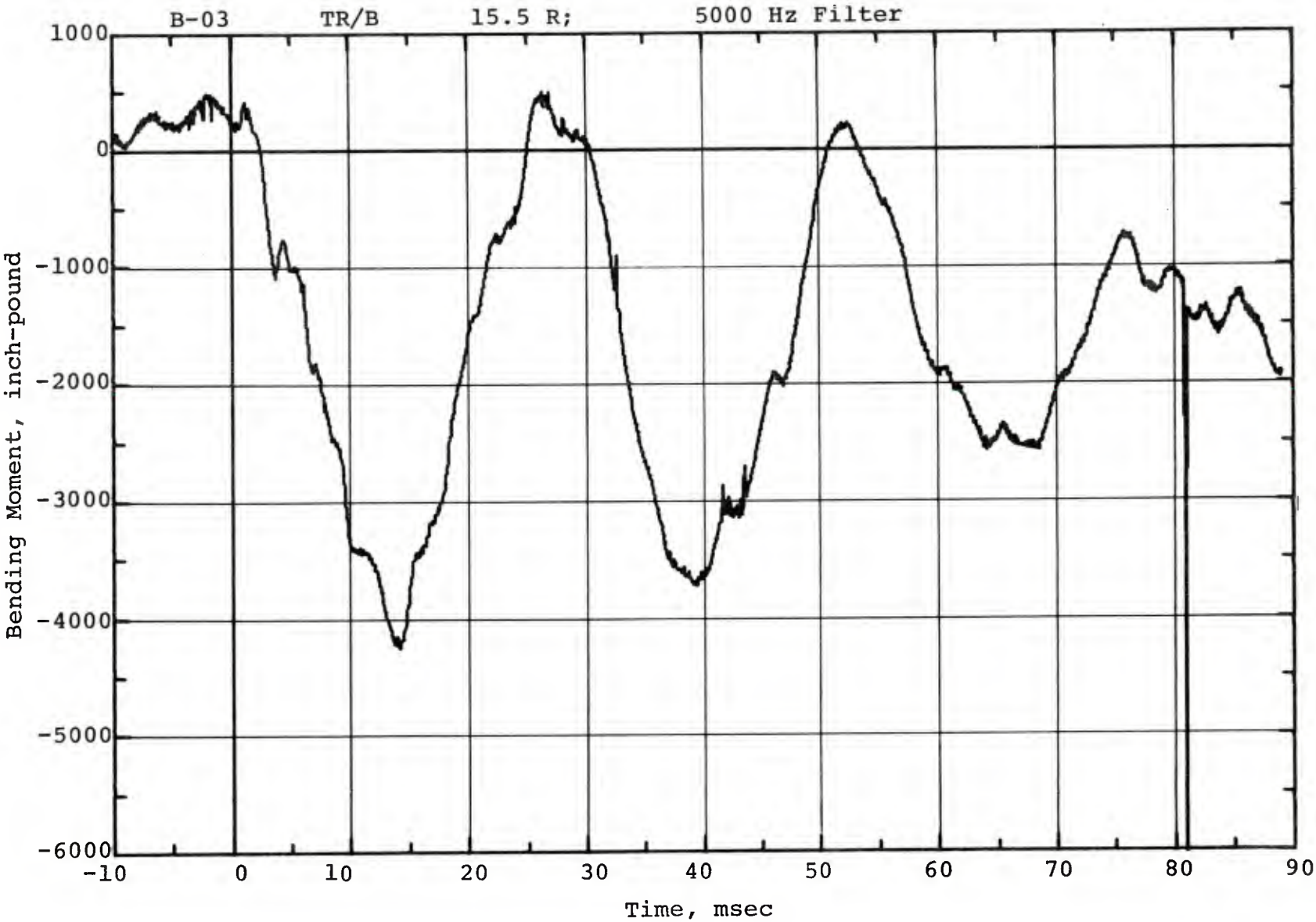

Figure 4.6. Time-Variation of Total Flapwise Bending Moment At Tail Rotor Red Blade Station 15.5. Channel B-03

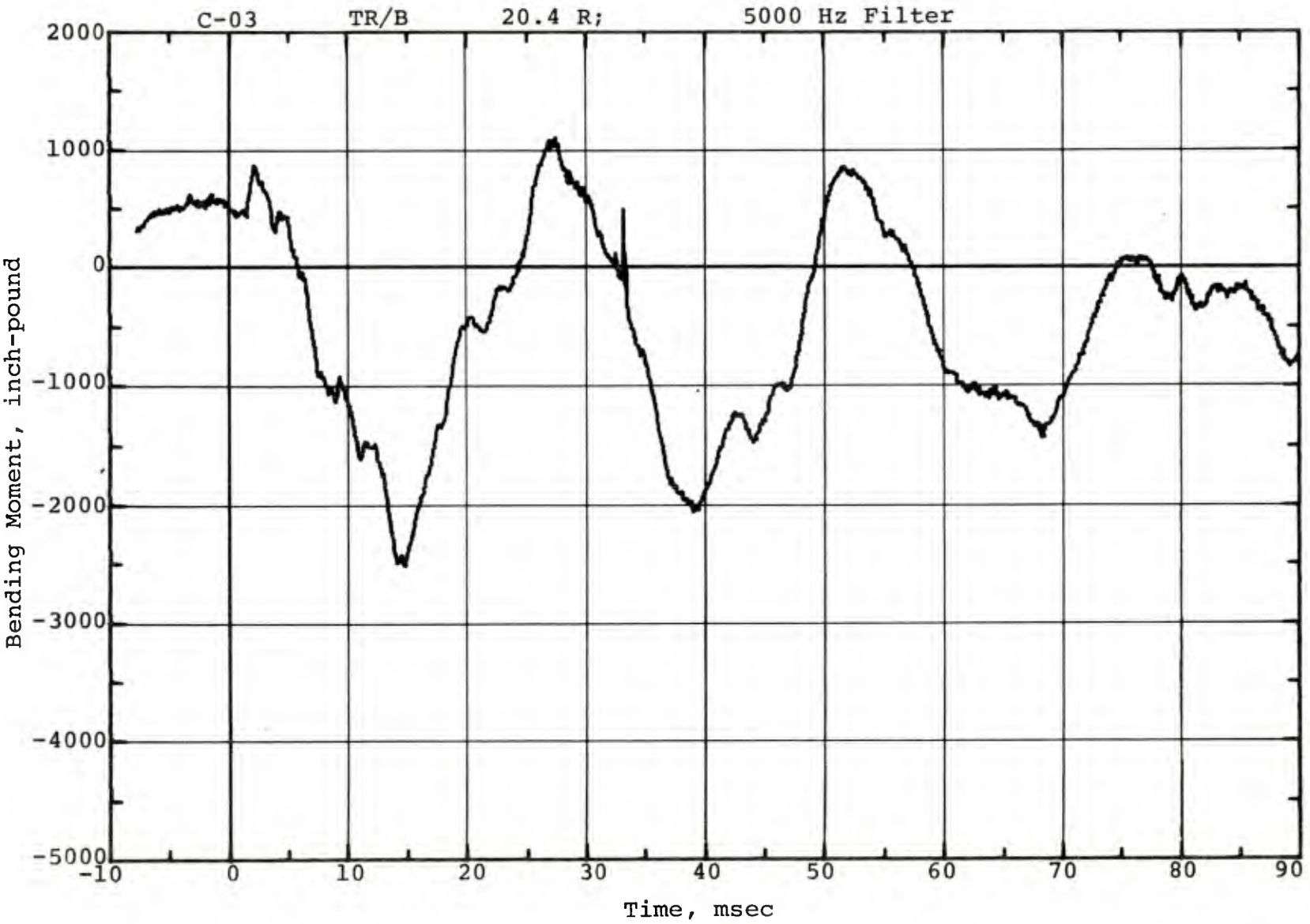

Figure 4.7. Time-Variation of Total Flapwise Bending Moment At Tail Rotor Red Blade Station 20.4. Channel C-03

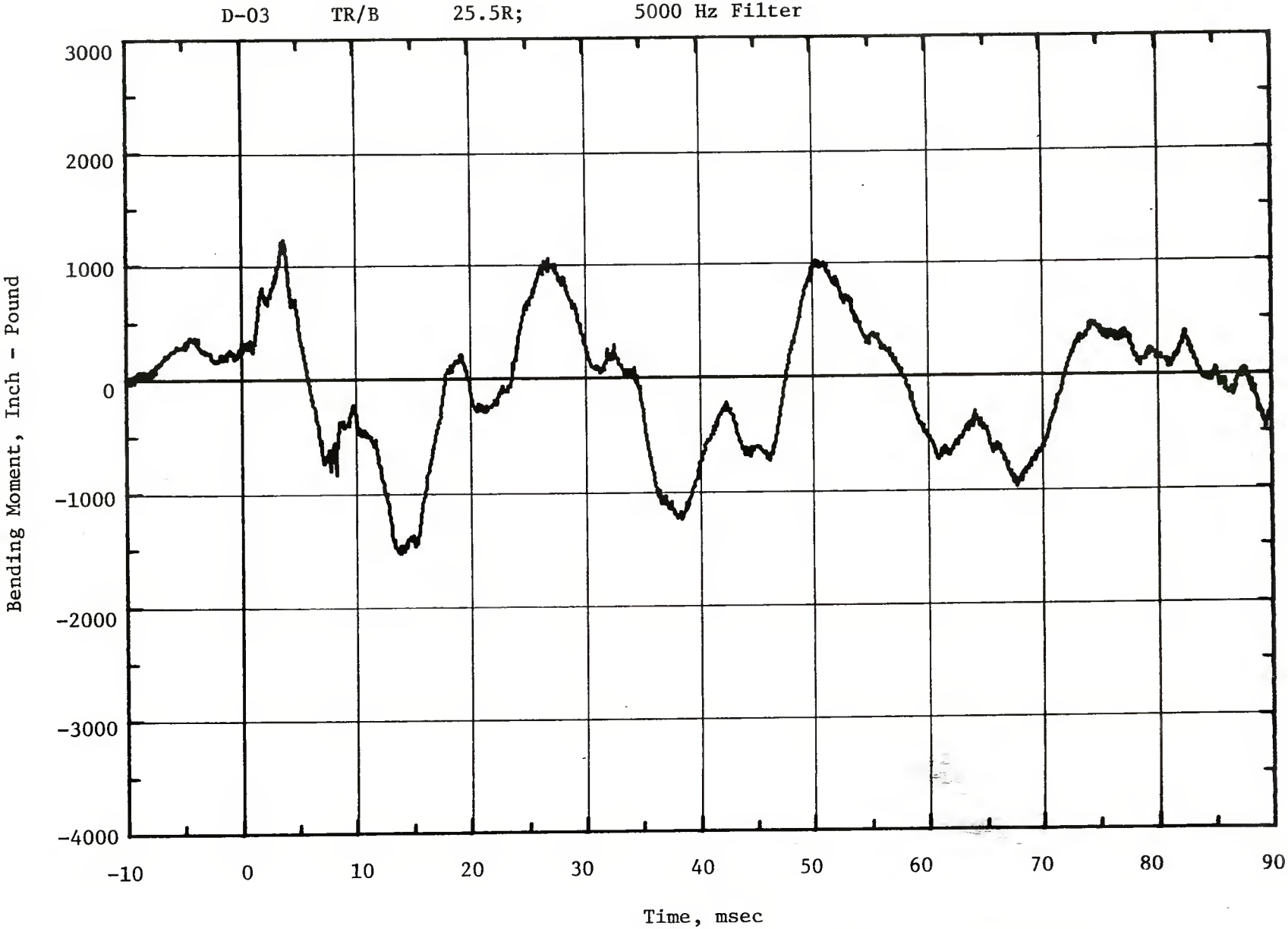

Figure 4.8. Time-Variation of Total Flapwise Bending Moment At Tail Rotor Red Blade Station 25.5. Channel D-03

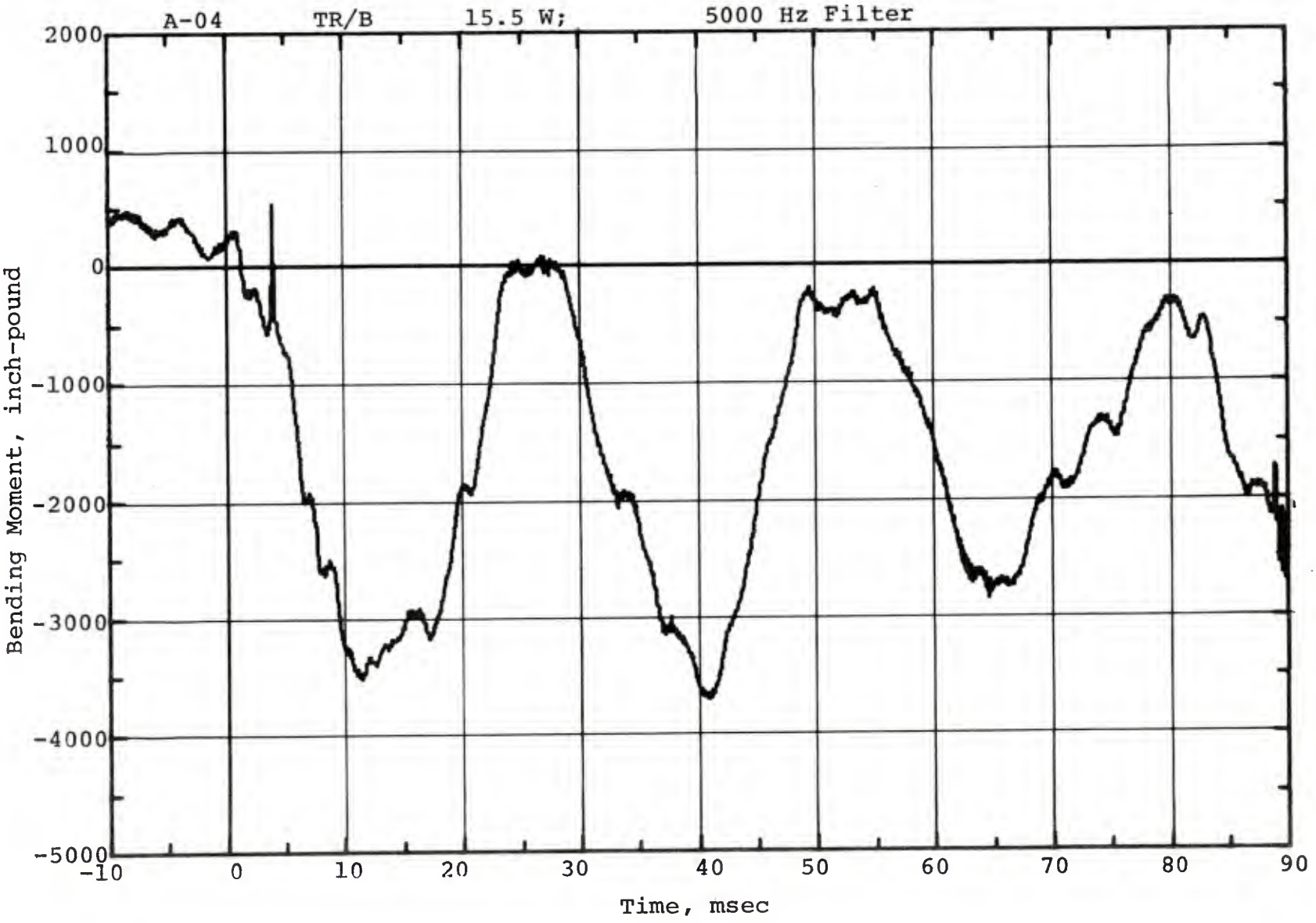

Figure 4.9. Time-Variation of Total Flapwise Bending Moment At Tail Rotor White Blade Station 15.5. Channel A-04

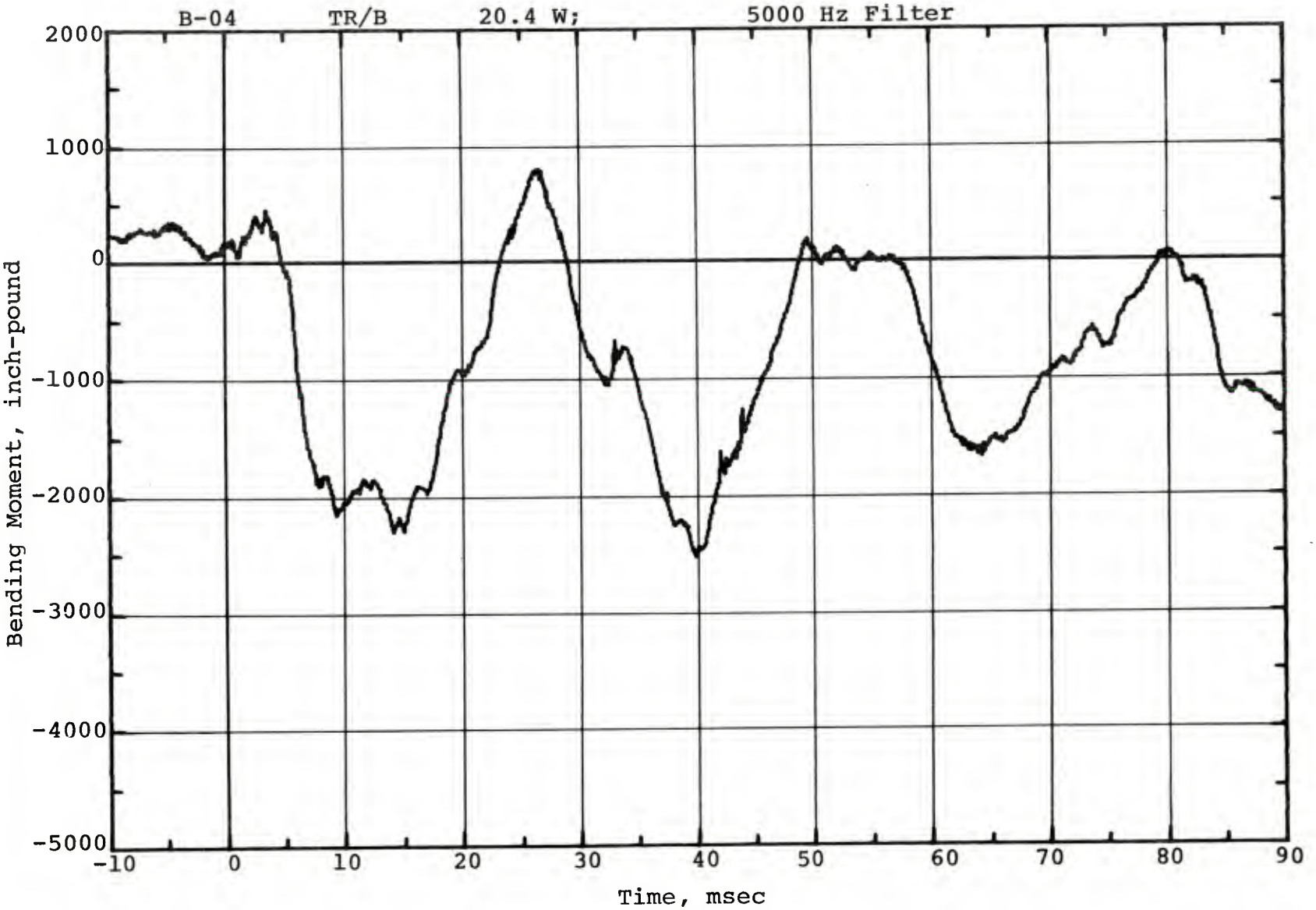

Figure 4.10. Time-Variation of Total Flapwise Bending Moment At Tail Rotor White Blade Station 20.4. Channel B-04

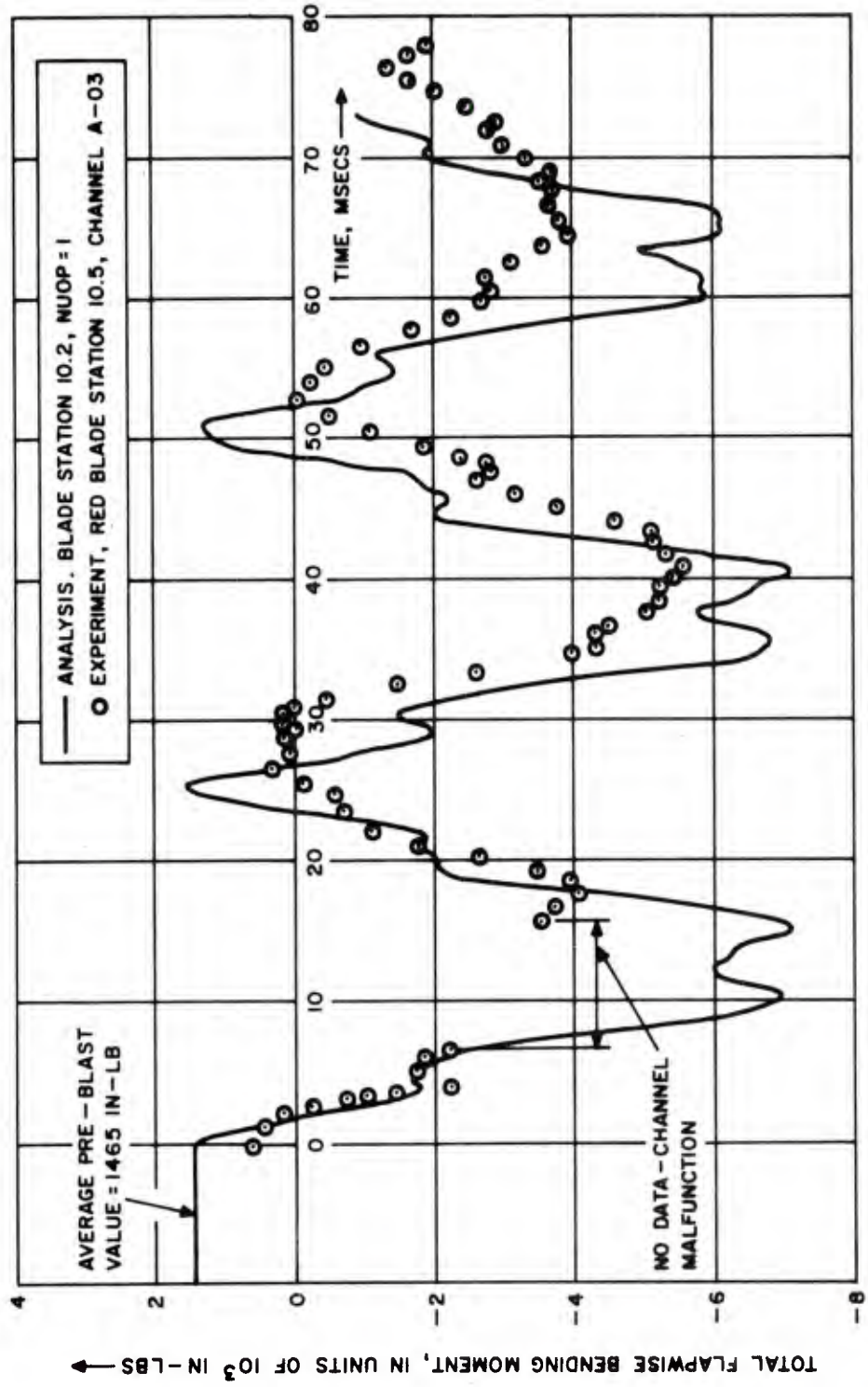

Figure 4.11. Time-Variation of Total Flapwise Bending Moment. Tail Rotor Blade Station 10.5. Analytical and Experimental. Red Blade. Channel A-03

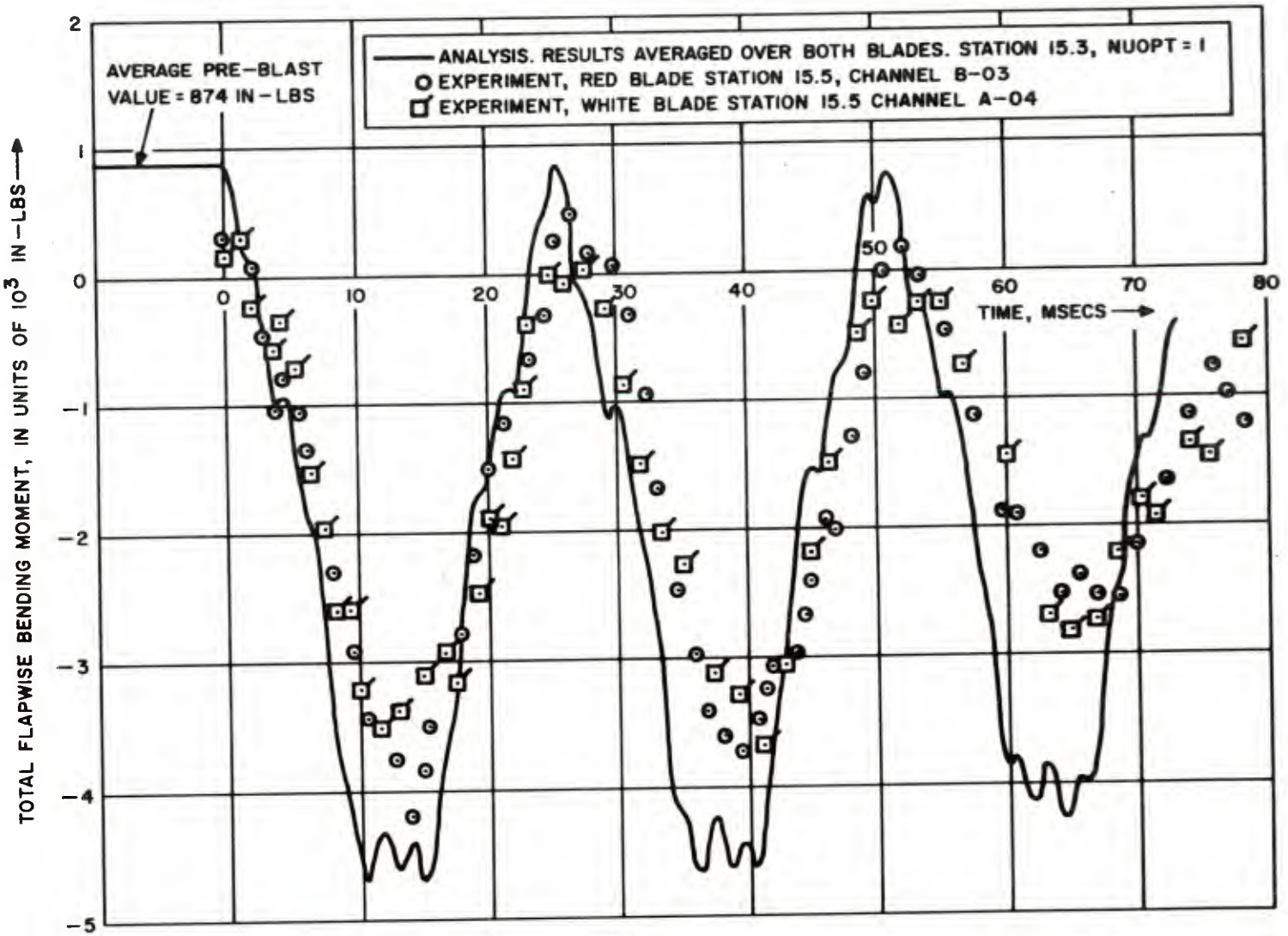

Figure 4.12. Time-Variation of Total Flapwise Bending Moment. Tail Rotor Blade Station 15.5. Analytical and Experimental. Both Blades. Channels B-03 and A-04

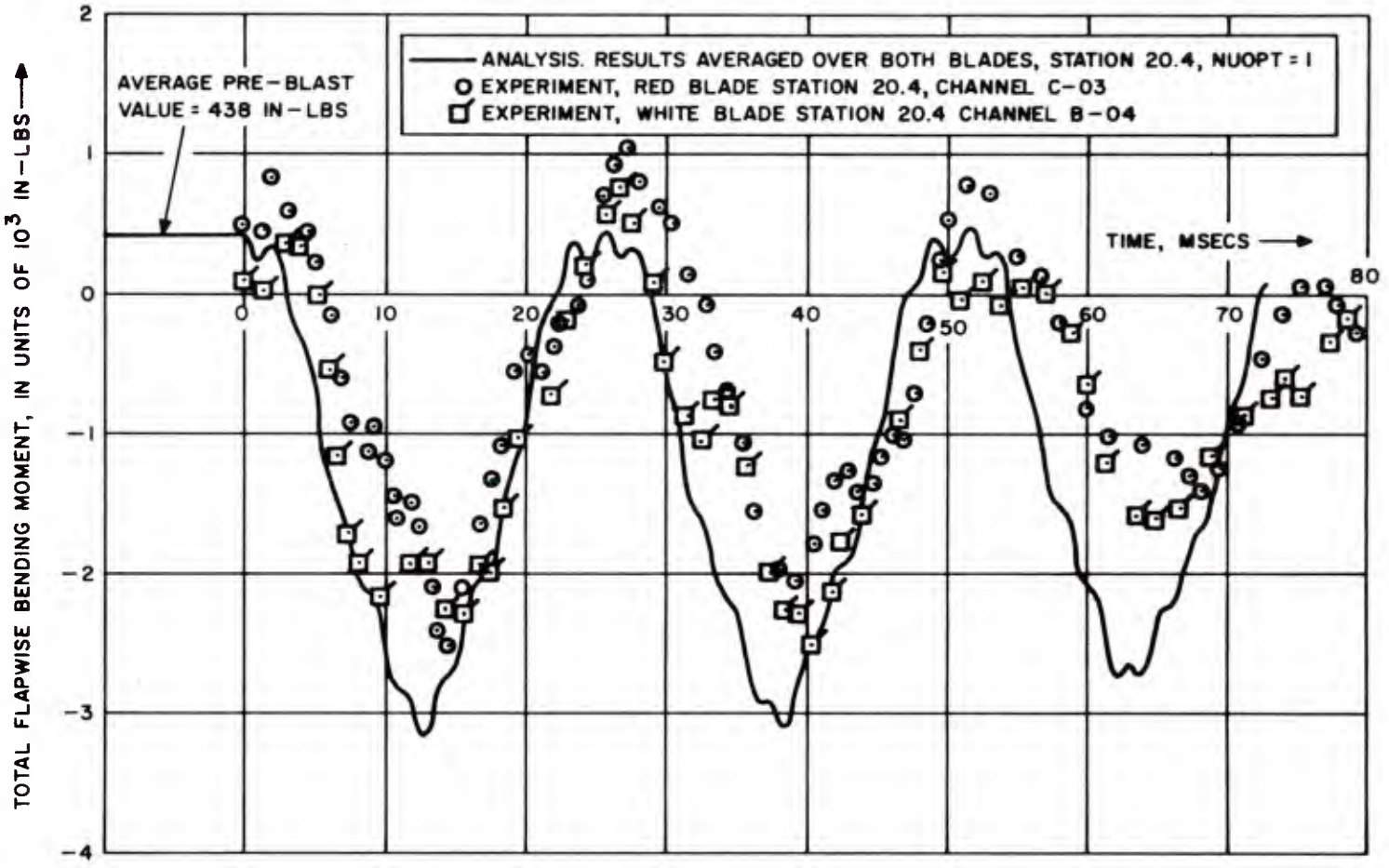

Figure 4.13. Time-Variation of Total Flapwise Bending Moment. Tail Rotor Blade Station 20.4. Analytical and Experimental. Both Blades. Channels C-03 and B-04

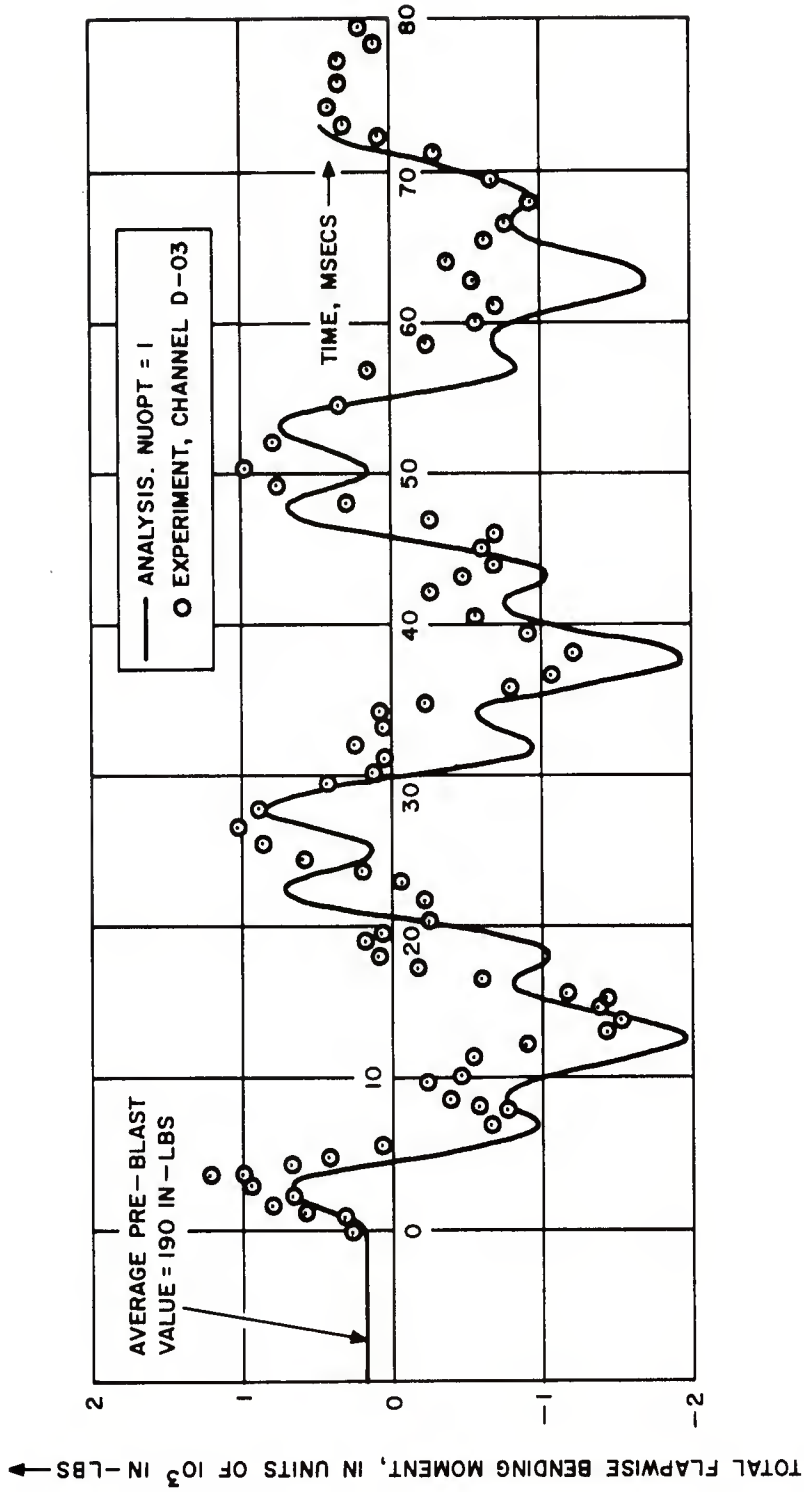

Figure 4.14. Time-Variation of Total Flapwise Bending Moment. Tail Rotor Blade Station 25.5. Analytical and Experimental. Red Blade. Channel D-03

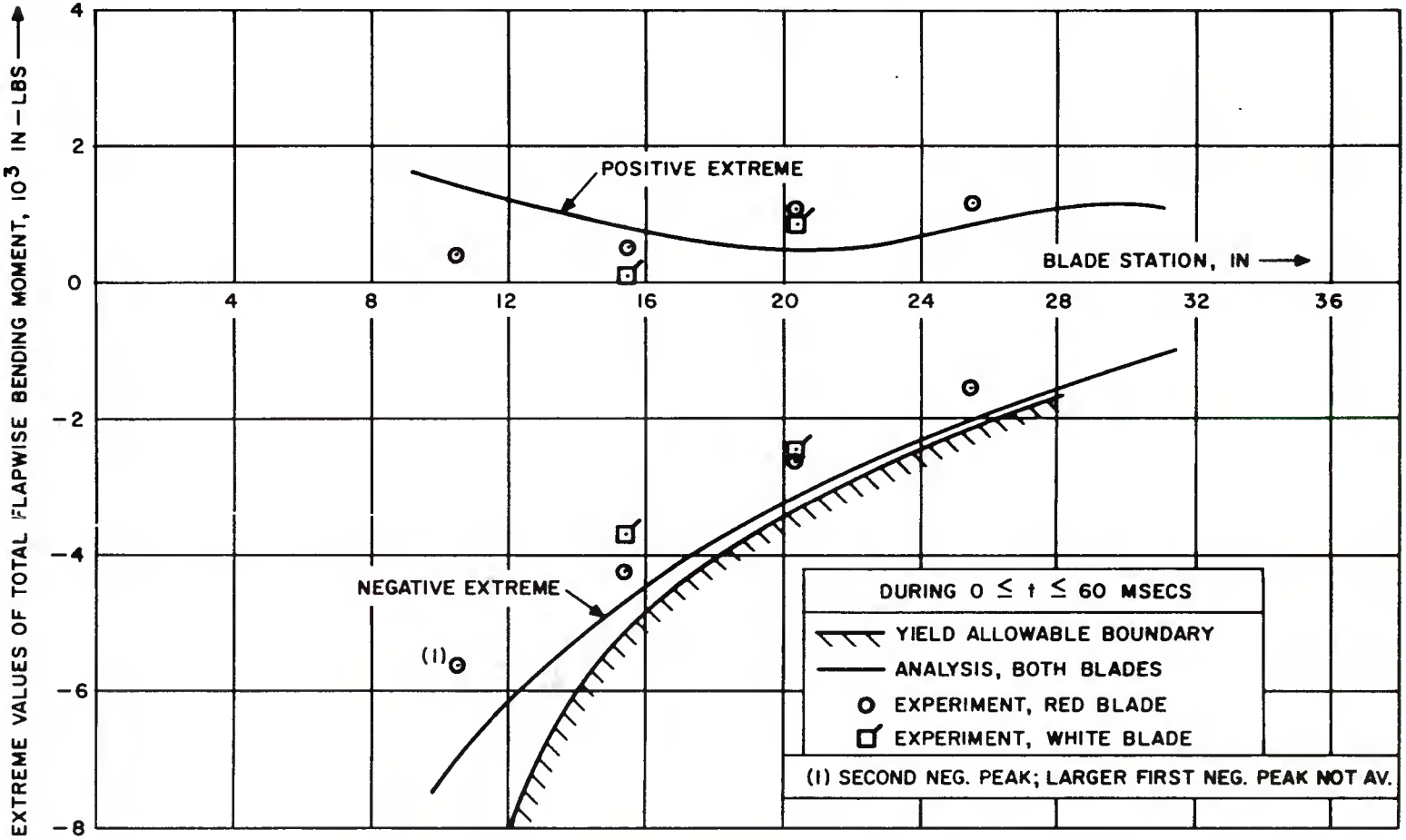

Figure 4.15. Spanwise Distributions of Extreme Values of Total Flapwise Bending Moments. Tail Rotor Blades. Analytical and Experimental

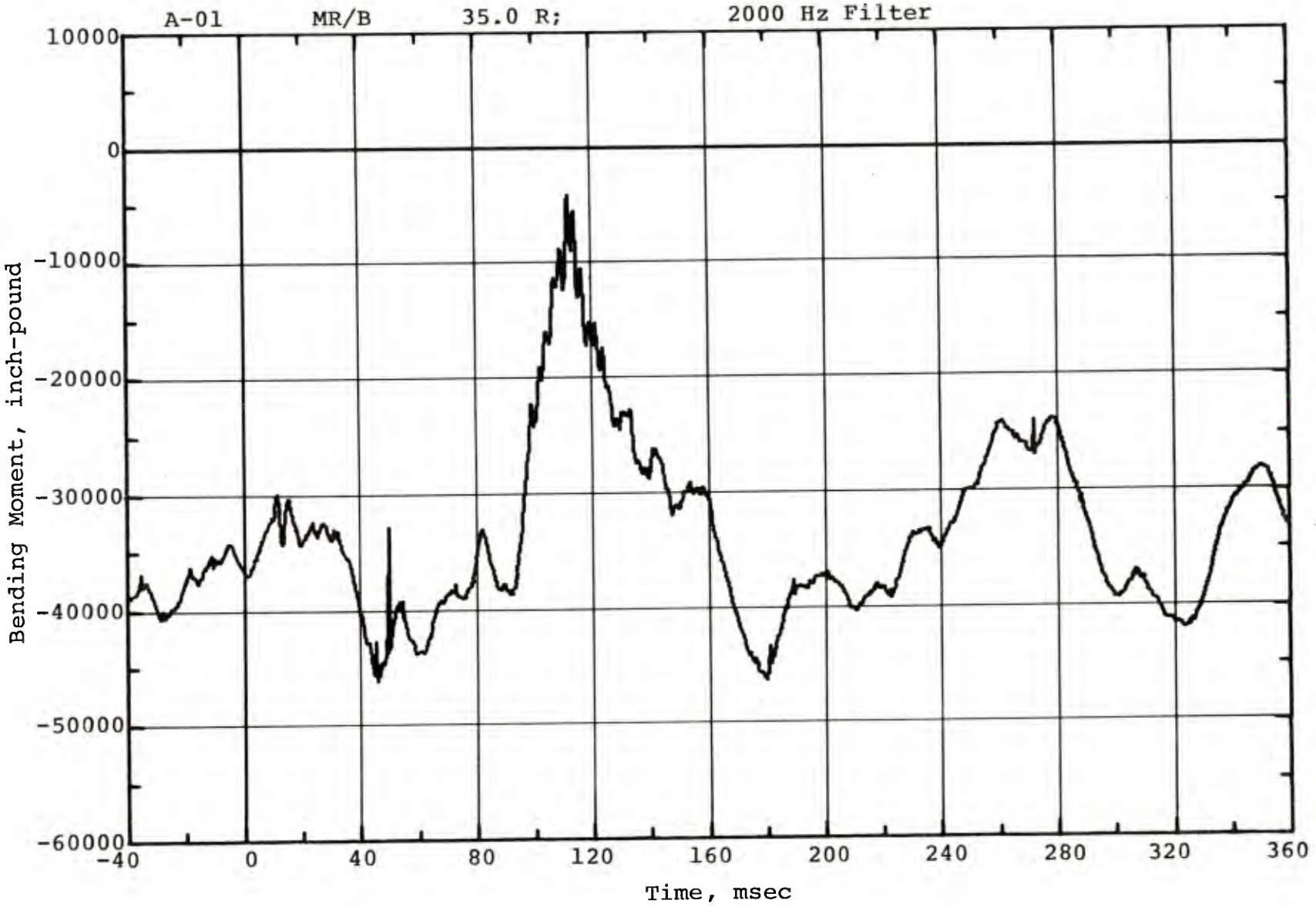

Figure 4.16a. Time-Variation of Total Flapwise Bending Moment. Main Rotor Red Blade Station 35. Channel A-01

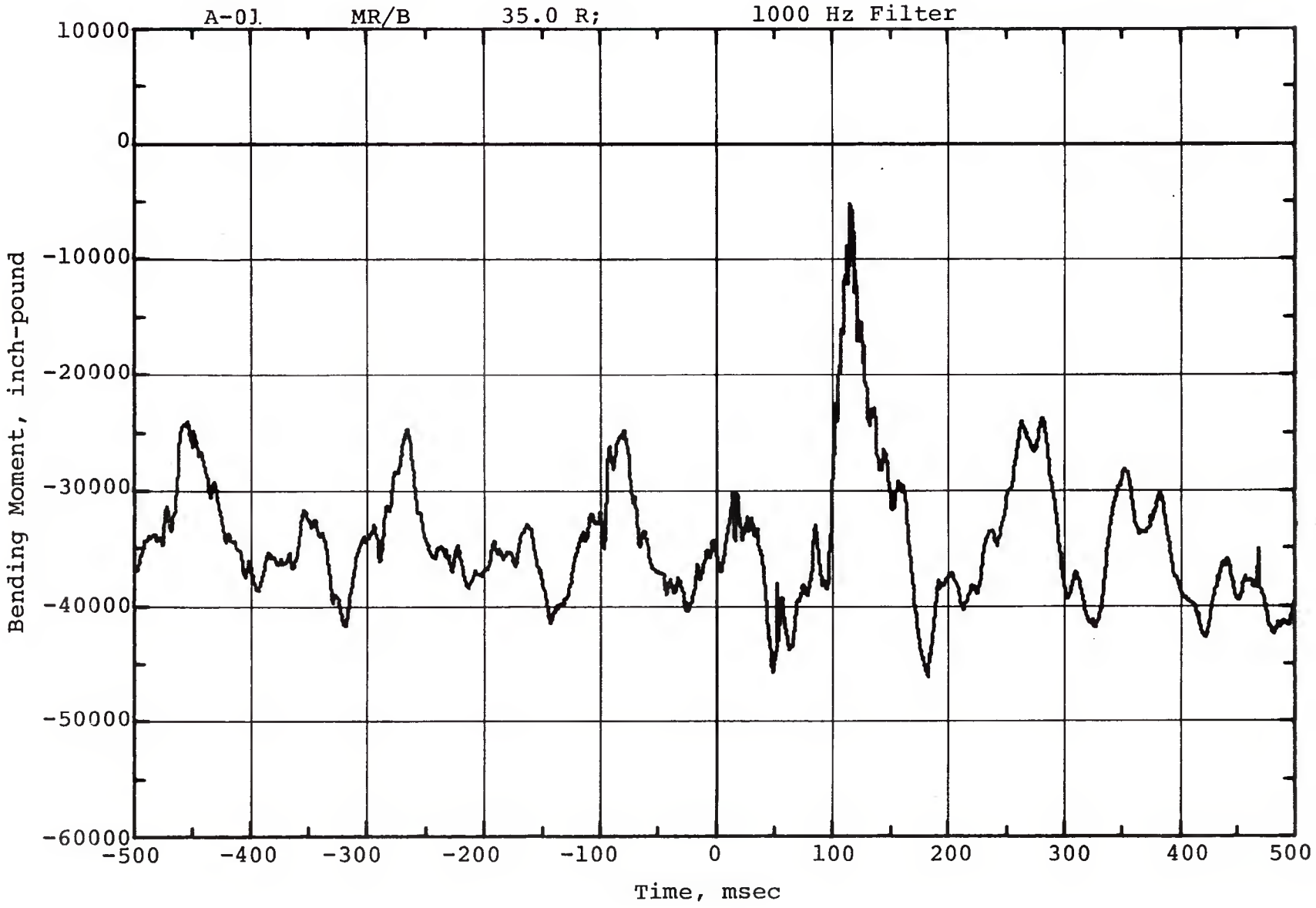

Figure 4.16b. Time-Variation of Total Falpwise Bending Moment. Main Rotor Red Blade Station 35. Channel A-01

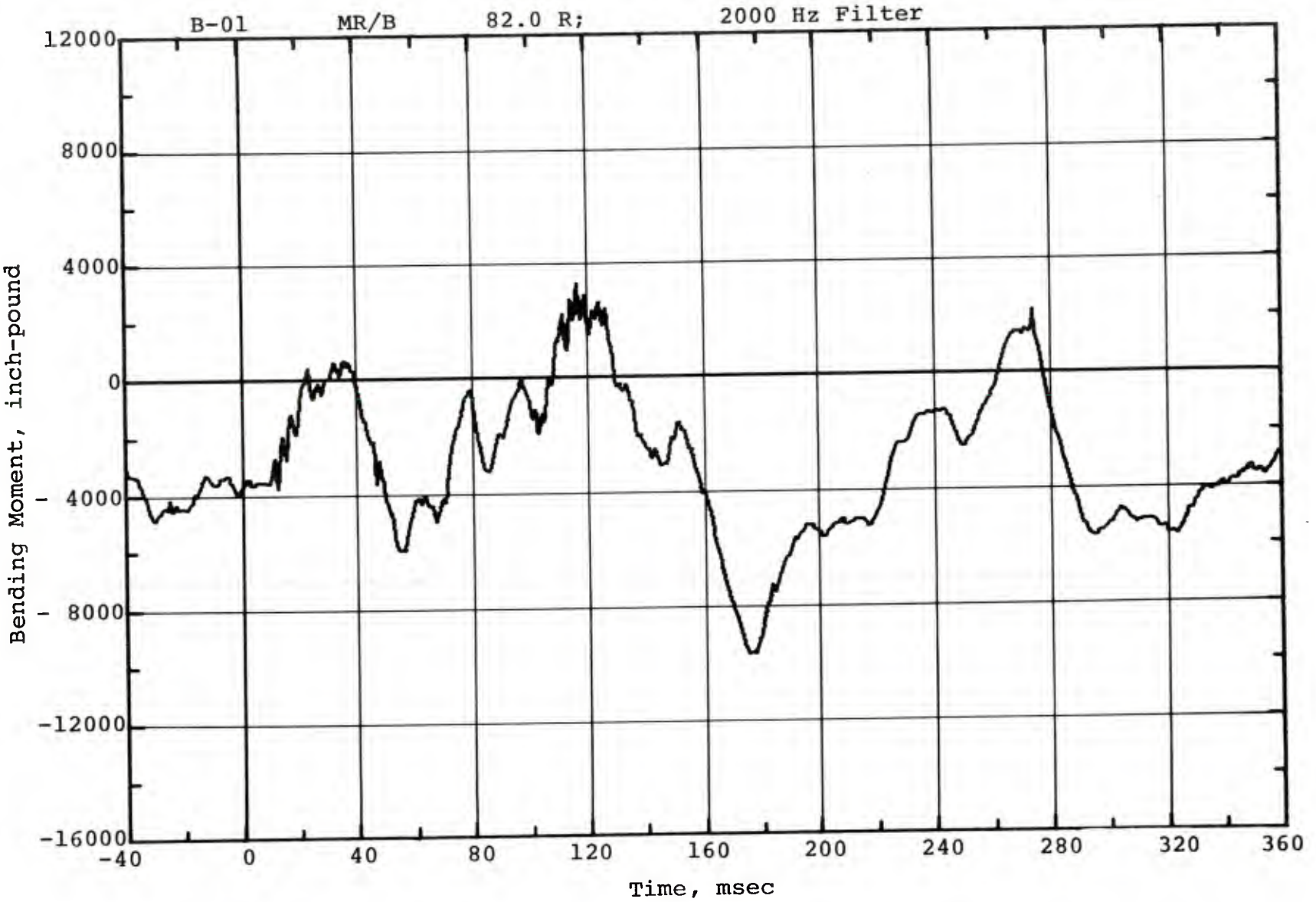

Figure 4.17a. Time-Variation of Total Flapwise Bending Moment. Main Rotor Red Blade Station 82. Channel B-01

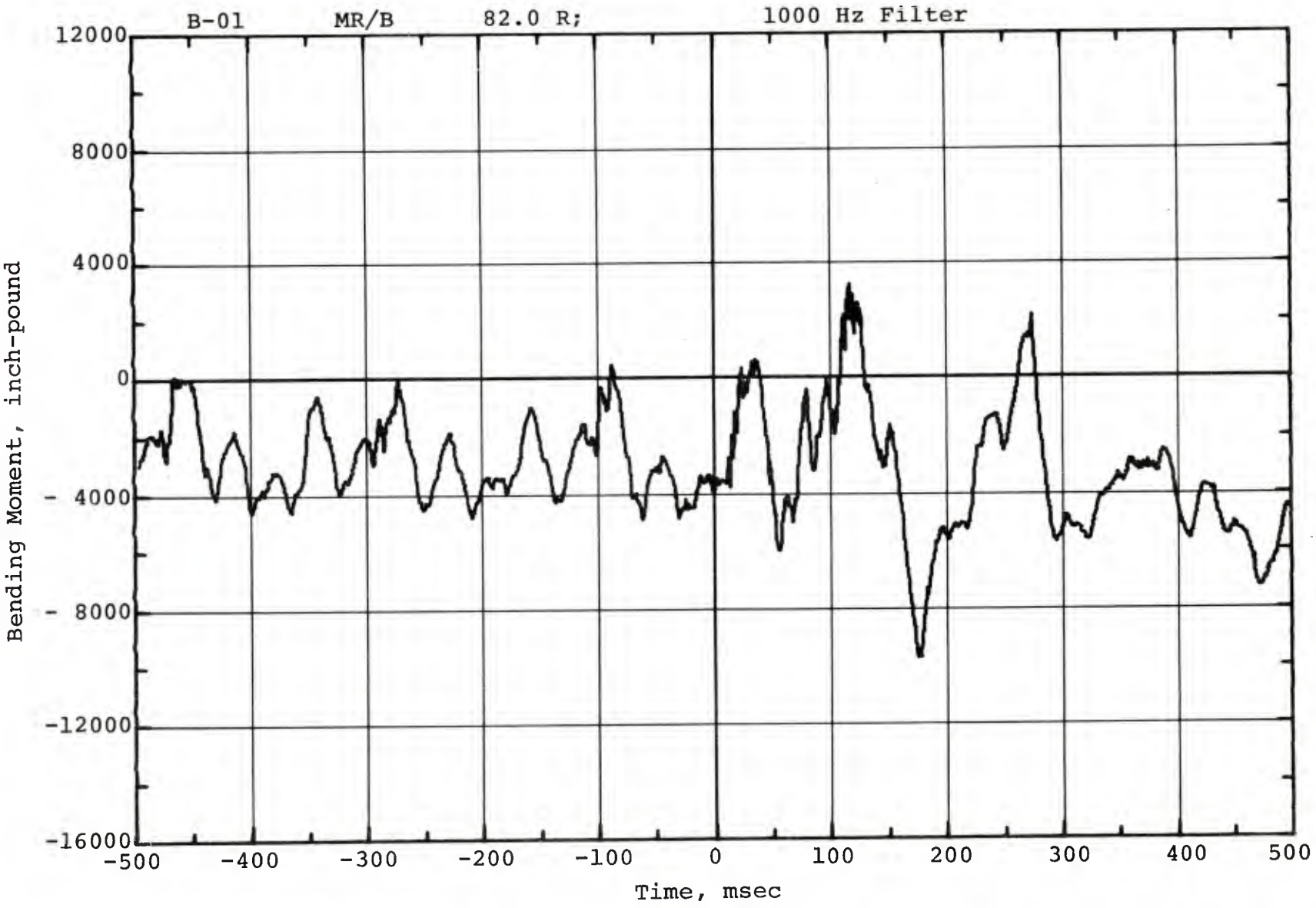

Figure 4.17b. Time-Variation of Total Flapwise Bending Moment. Main Rotor Red Blade Station 82. Channel B-01

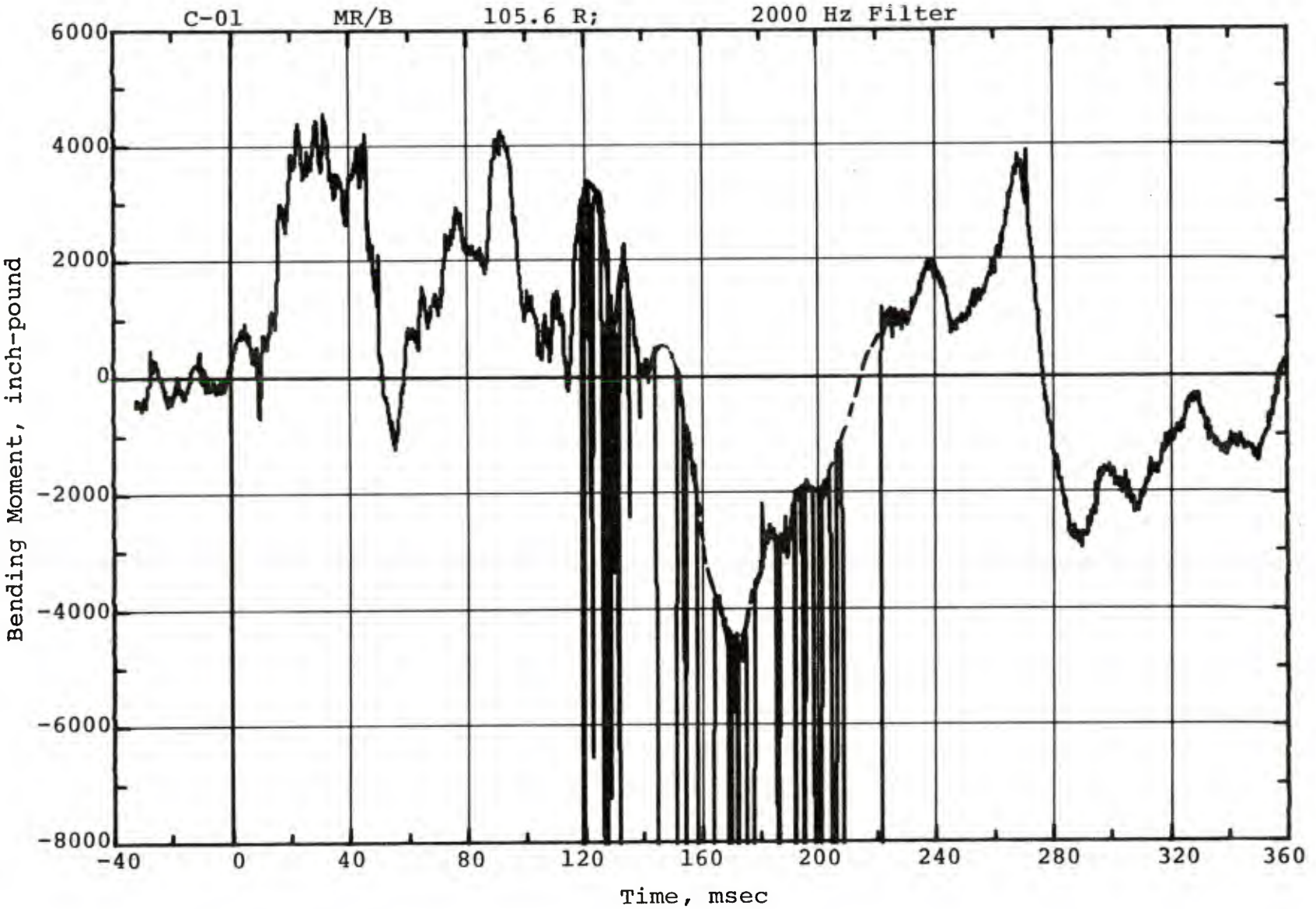

Figure 4.18a. Time-Variation of Total Flapwise Bending Moment. Main Rotor Red Blade Station 105.6 Channel C-01

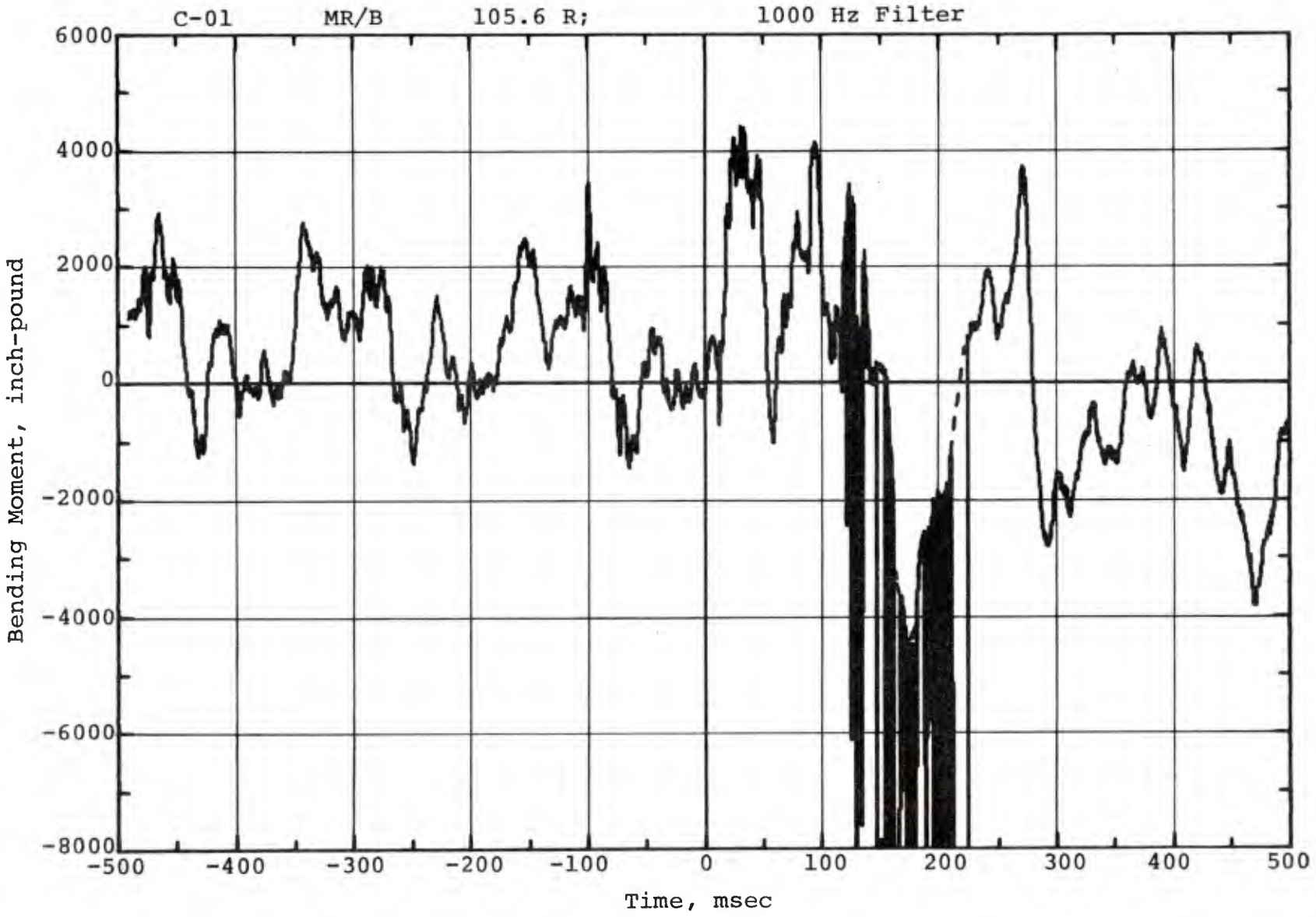

Figure 4.18b. Time-Variation of Total Flapwise Bending Moment. Main Rotor Red Blade Station 105.6. Channel C-01

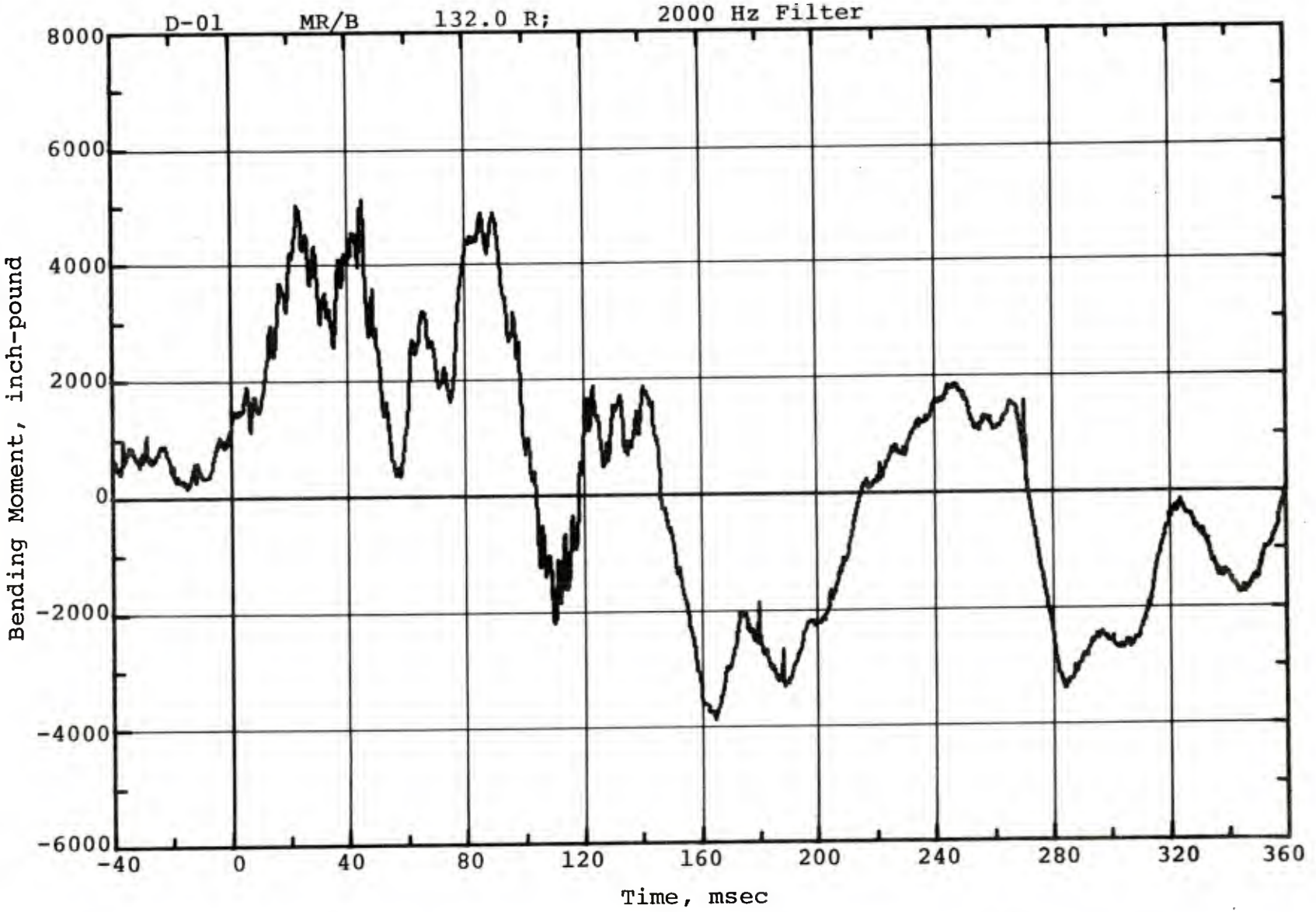

Figure 4.19a. Time-Variation of Total Flapwise Bending Moment. Main Rotor Red Blade Station 132. Channel D-01

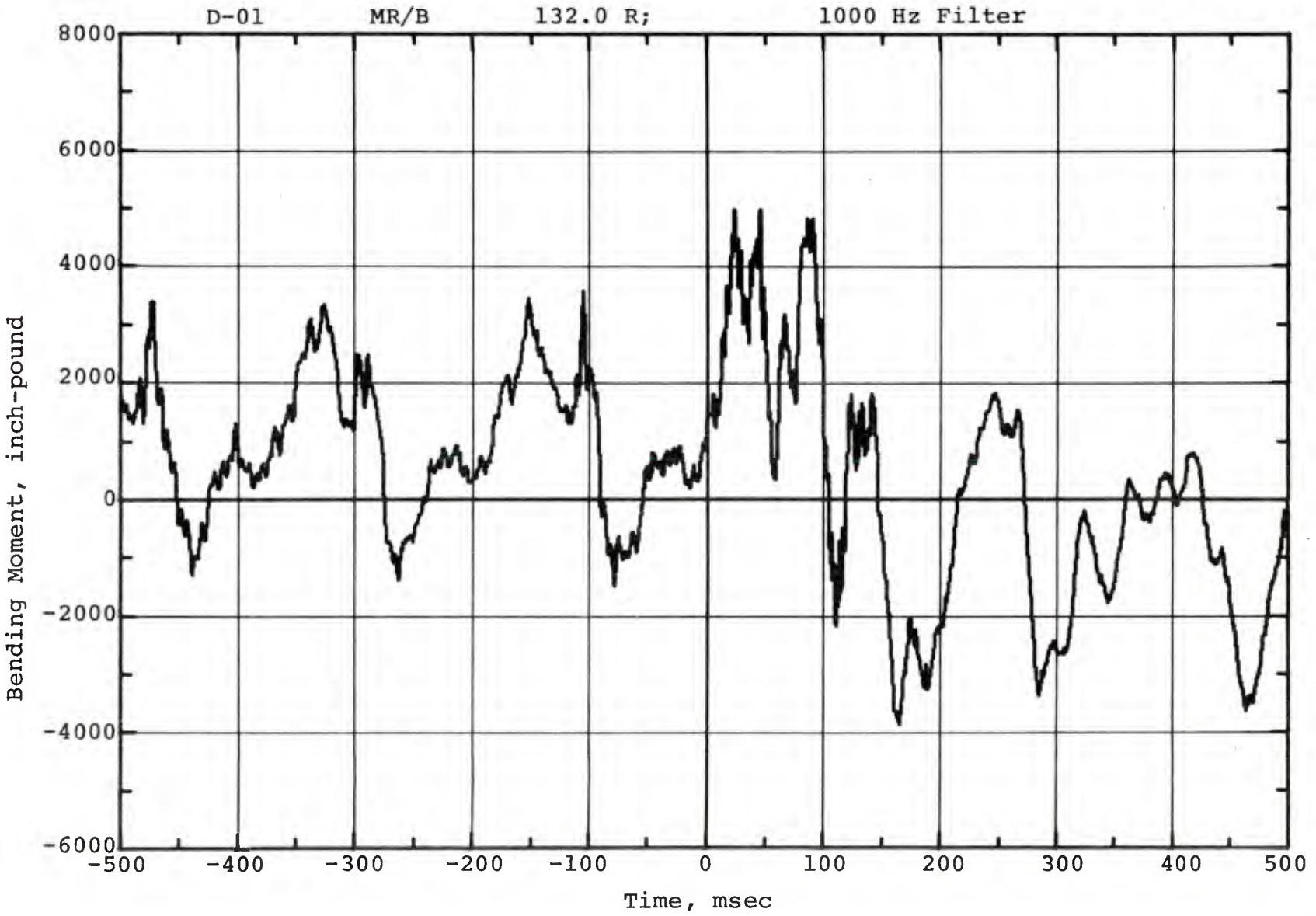

Figure 4.19b. Time-Variation of Total Flapwise Bending Moment. Main Rotor Red Blade Station 132. Channel D-01

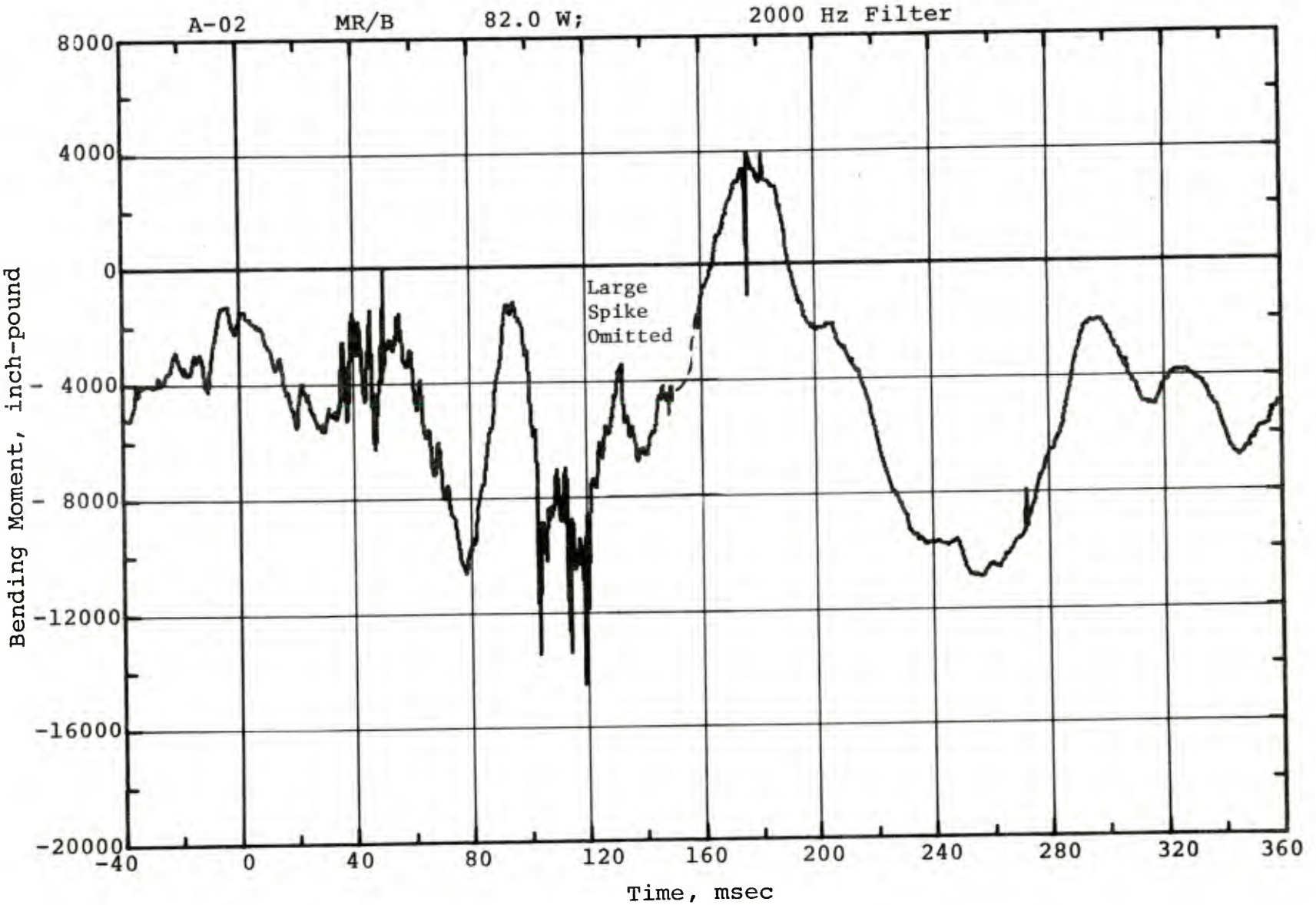

Figure 4.20a. Time-Variation of Total Flapwise Bending Moment. Main Rotor White Blade Station 82. Channel A-02

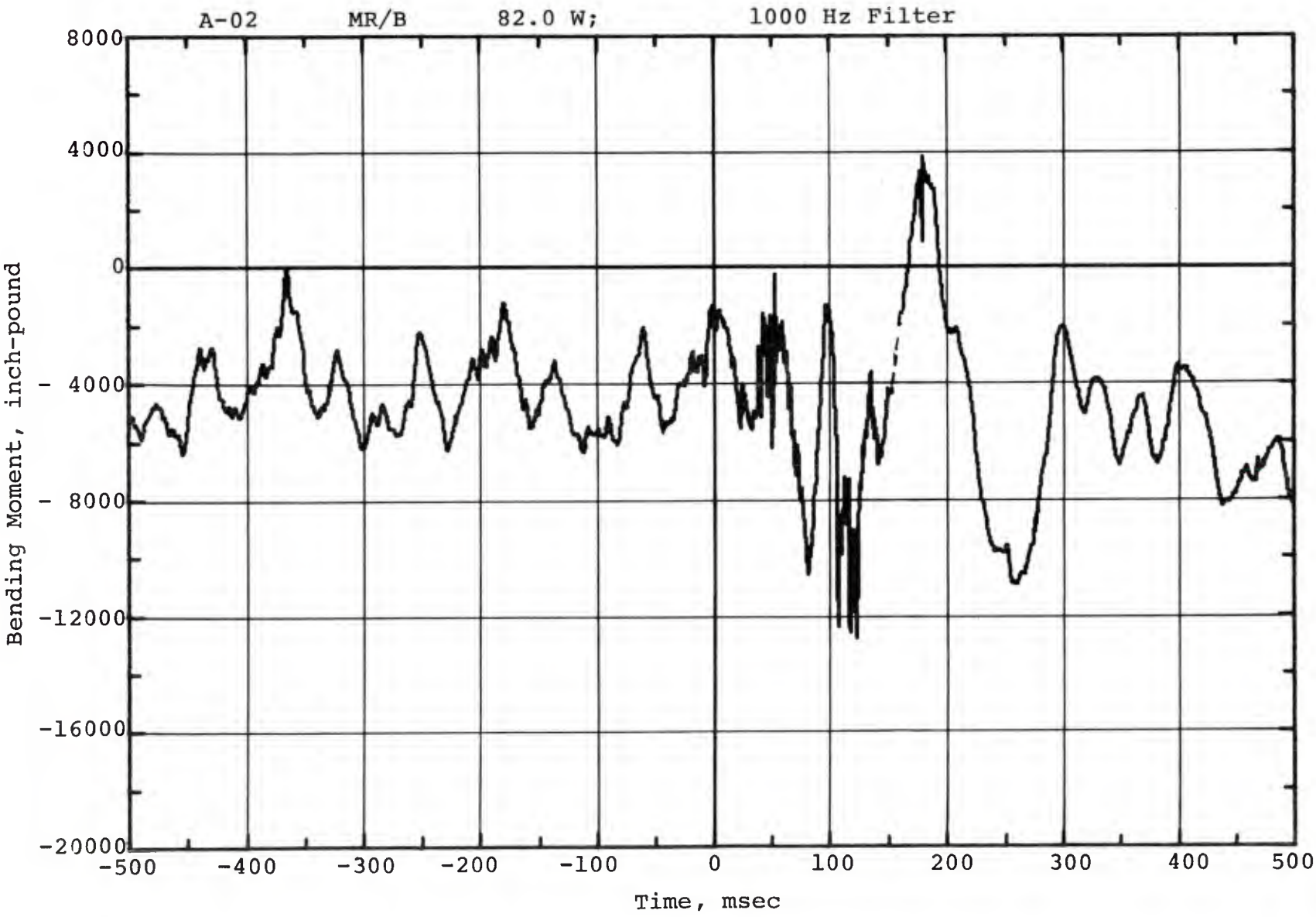

Figure 4.20b. Time-Variation of Total Flapwise Bending Moment. Main Rotor White Blade Station 82. Channel A-02

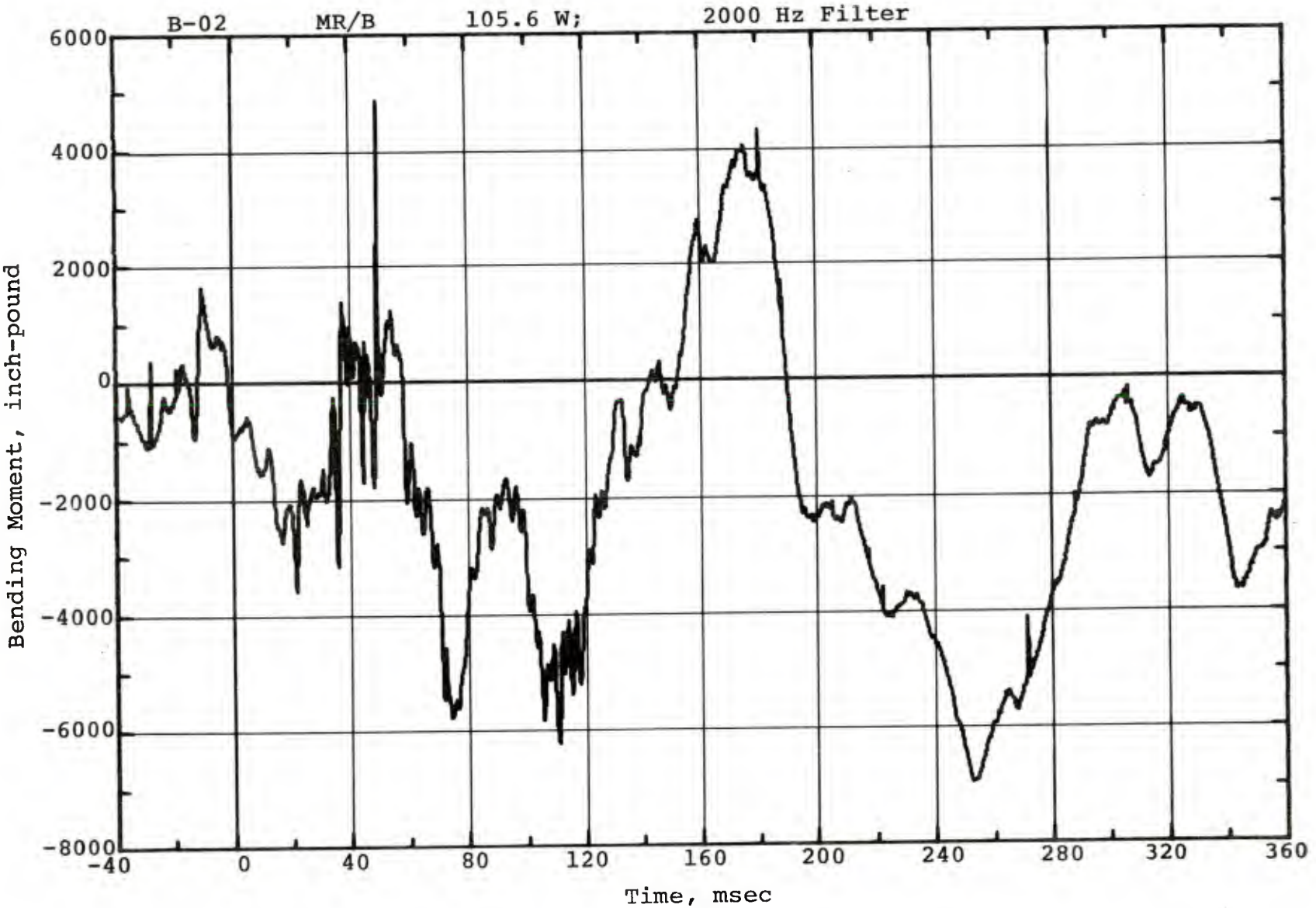

Figure 4.21a. Time-Variation of Total Flapwise Bending Moment. Main Rotor White Blade Station 105.6. Channel B-02

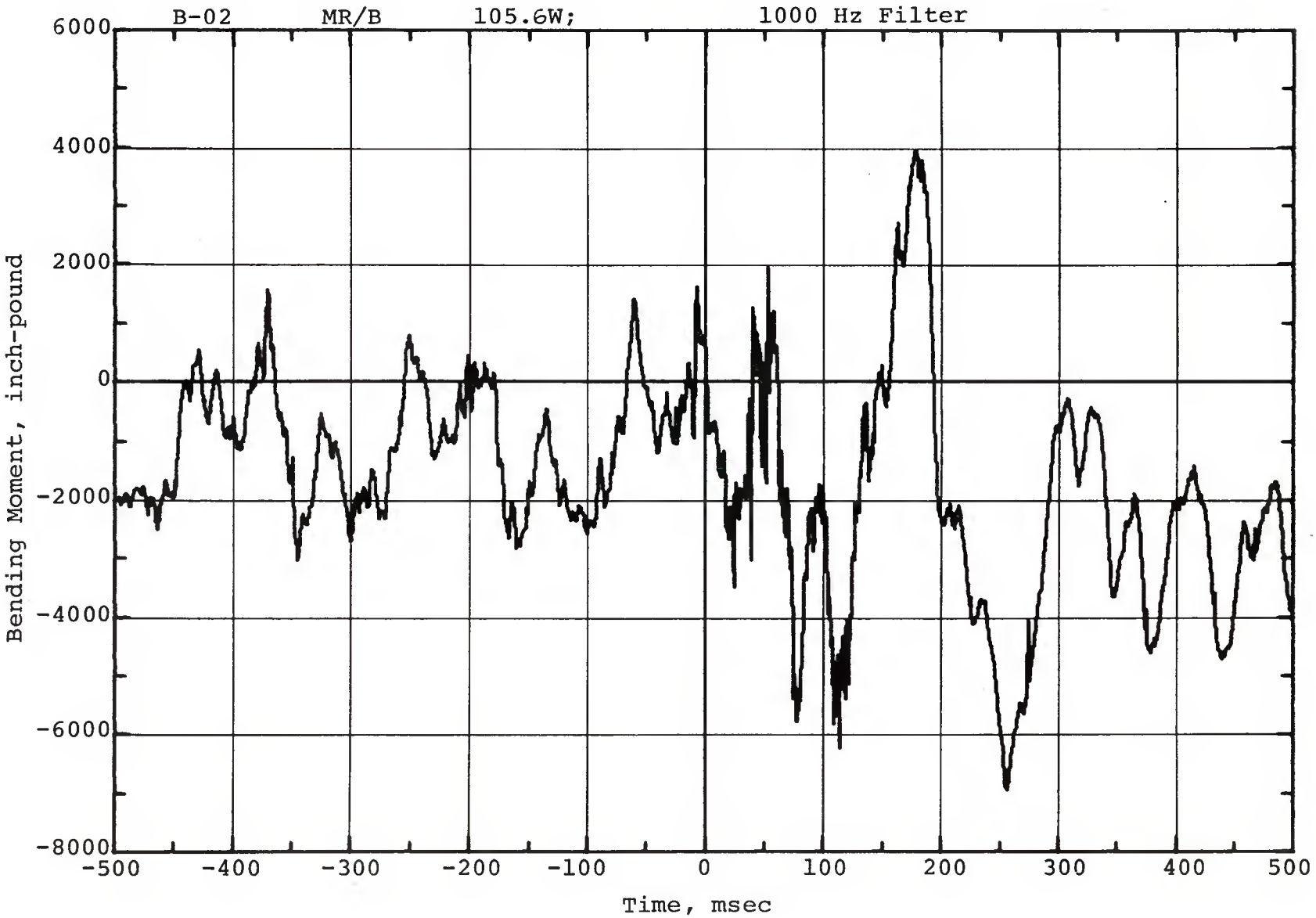

Figure 4.21b. Time-Variation of Total Flapwise Bending Moment. Main Rotor White Blade Station 105.6. Channel B-02

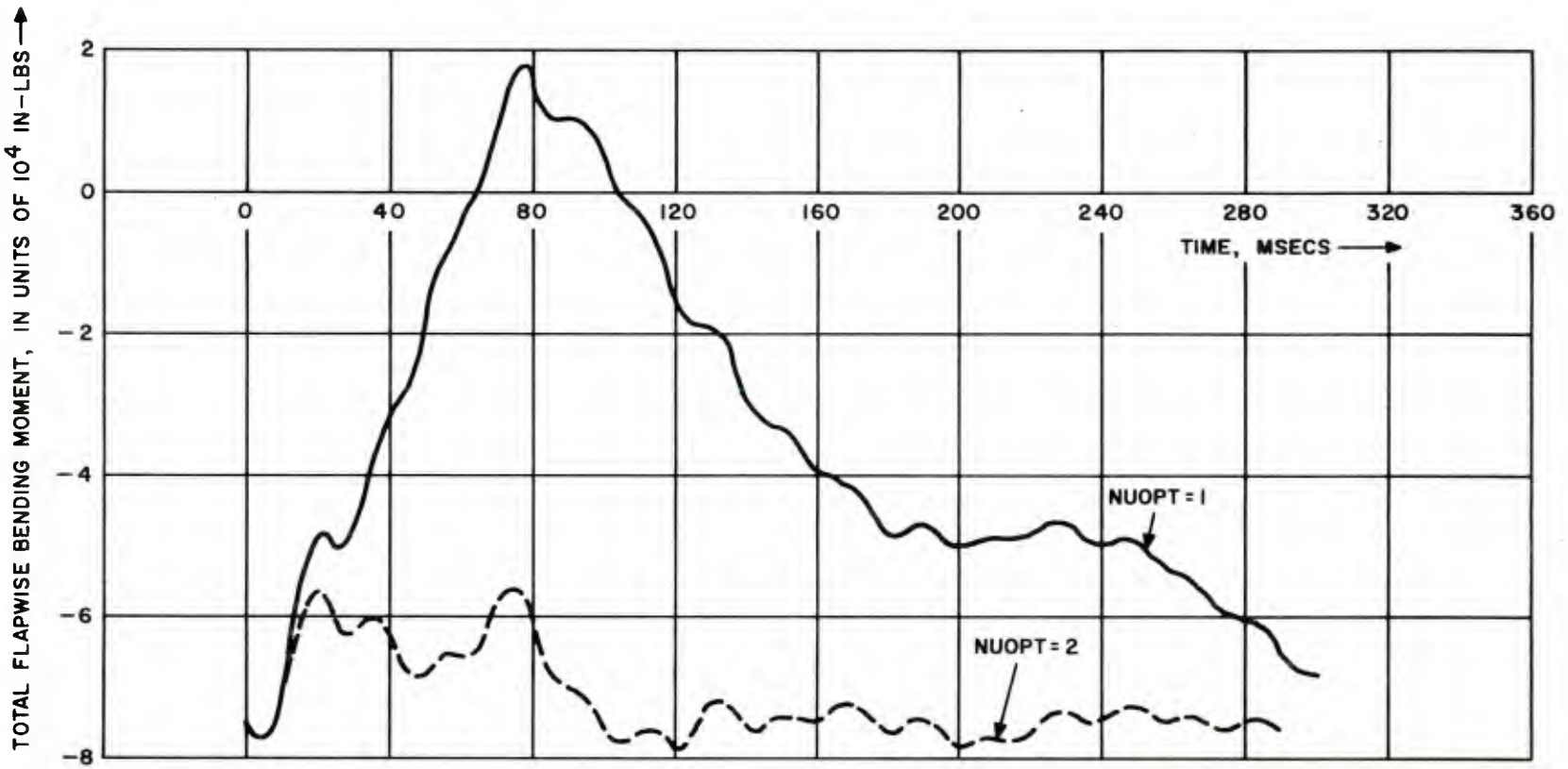

Figure 4.22. Time-Variation of Total Flapwise Bending Moment. Main Rotor Blade Station 26.4. Analysis for Red Blade. NUOPT=1, 2

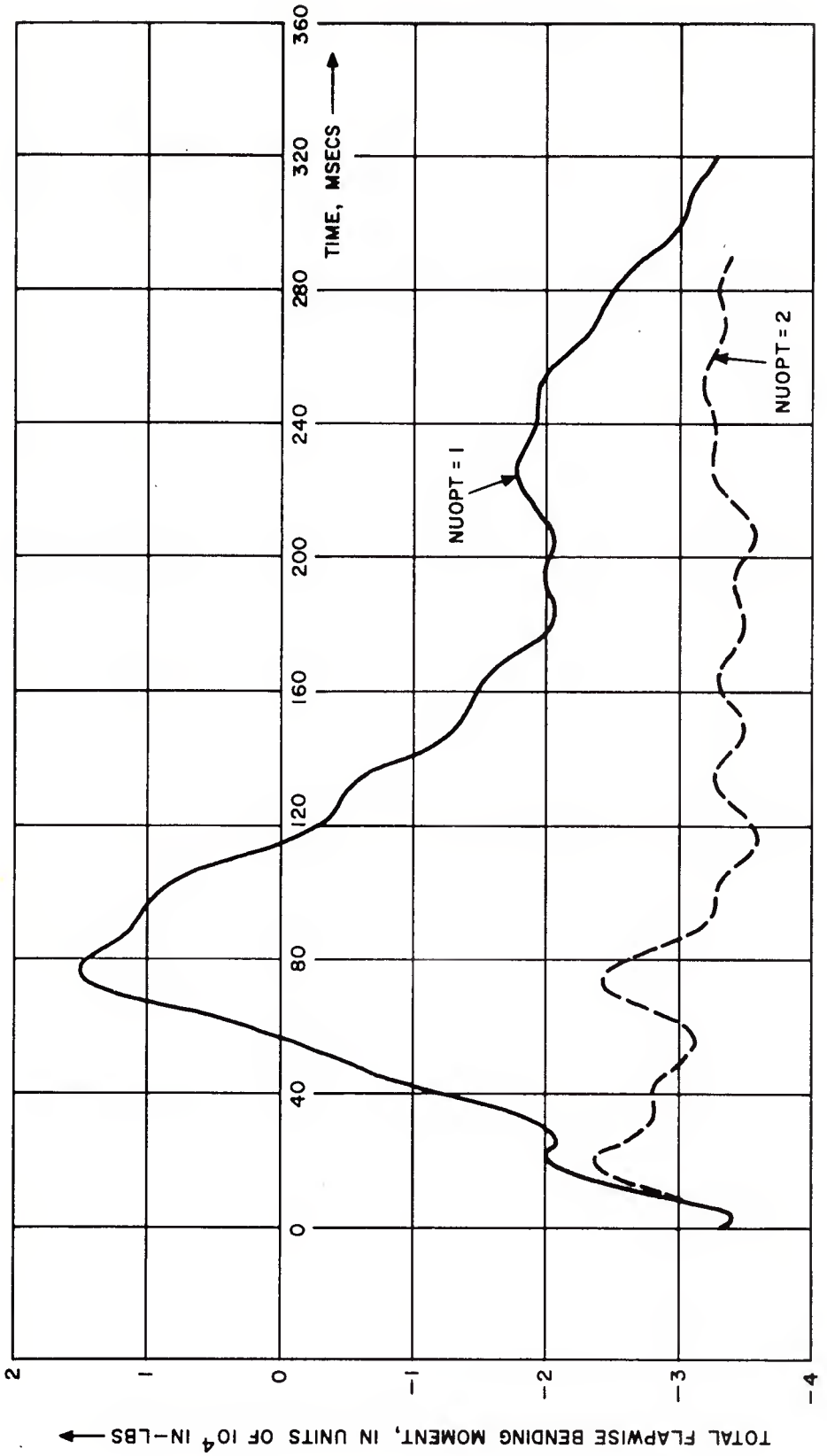

Figure 4.23. Time-Variation of Total Flapwise Bending Moment. Main Rotor Blade Station 52.8. Analysis for Red Blade. NUOPT=1, 2

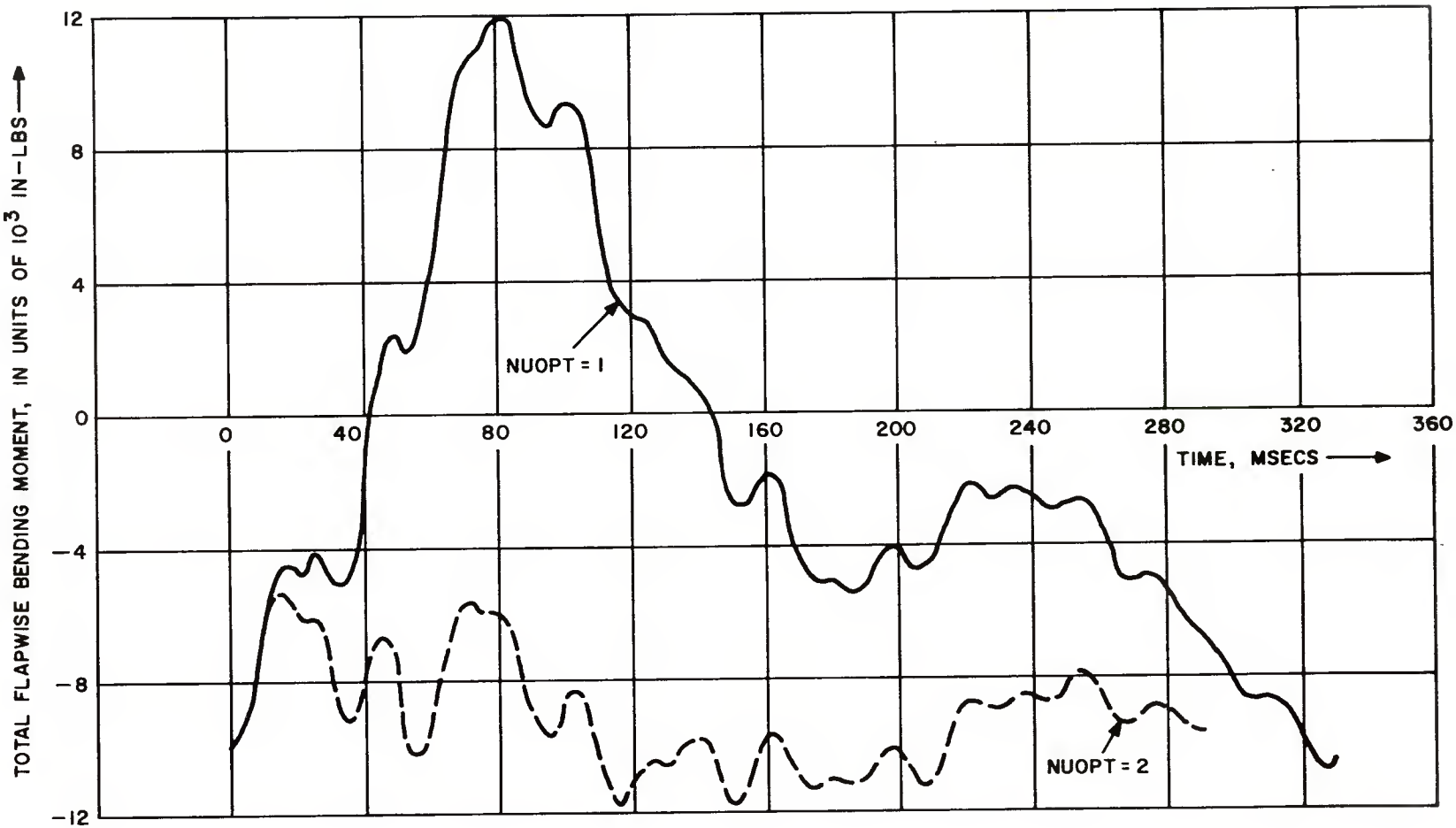

Figure 4.24. Time-Variation of Total Flapwise Bending Moment. Main Rotor Blade Station 79.2. Analysis for Red Blade. NUOPT=1, 2

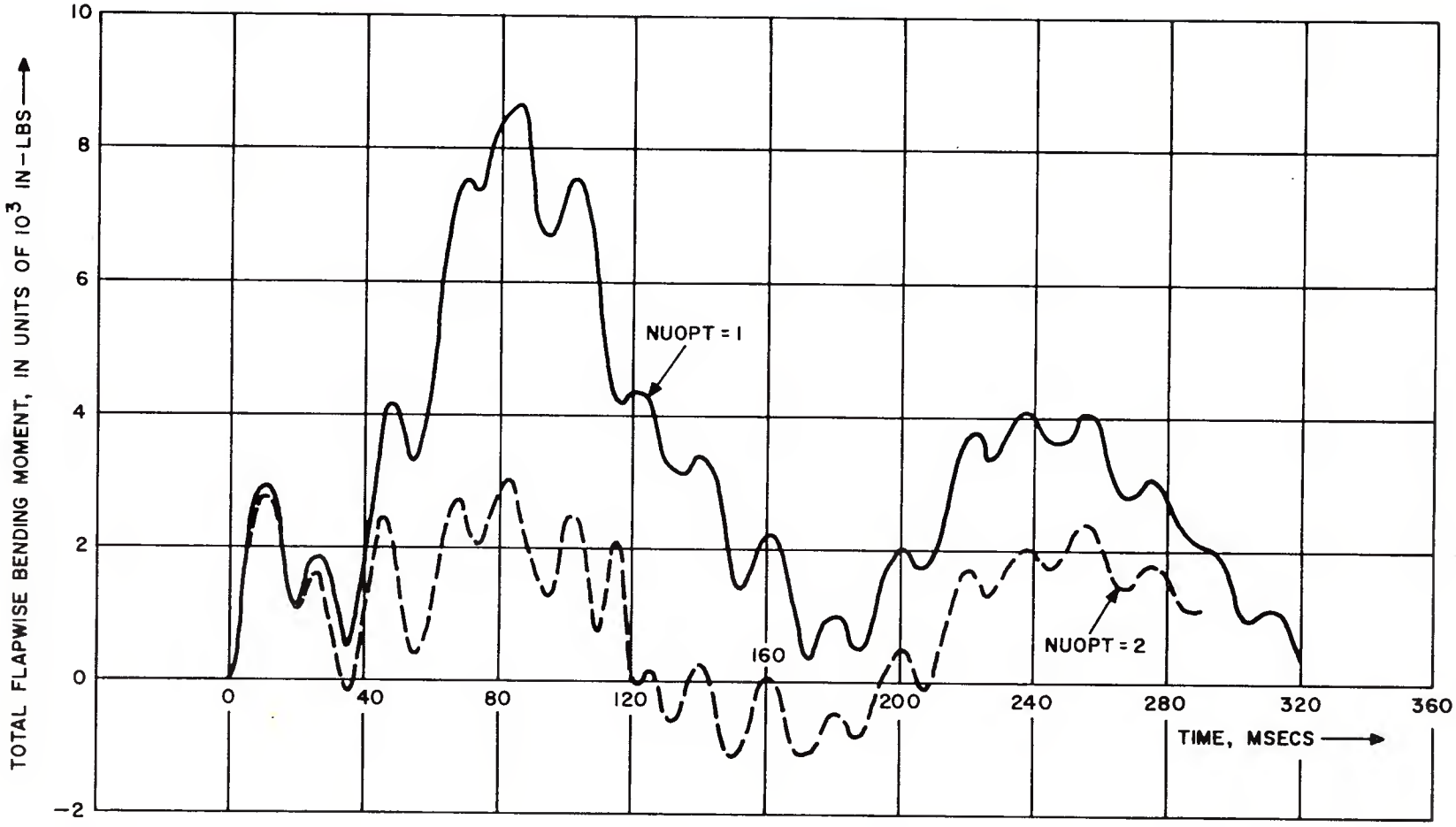

Figure 4.25. Time-Variation of Total Flapwise Bending Moment. Main Rotor Blade Station 105.6. Analysis for Red Blade. NUOPT=1, 2

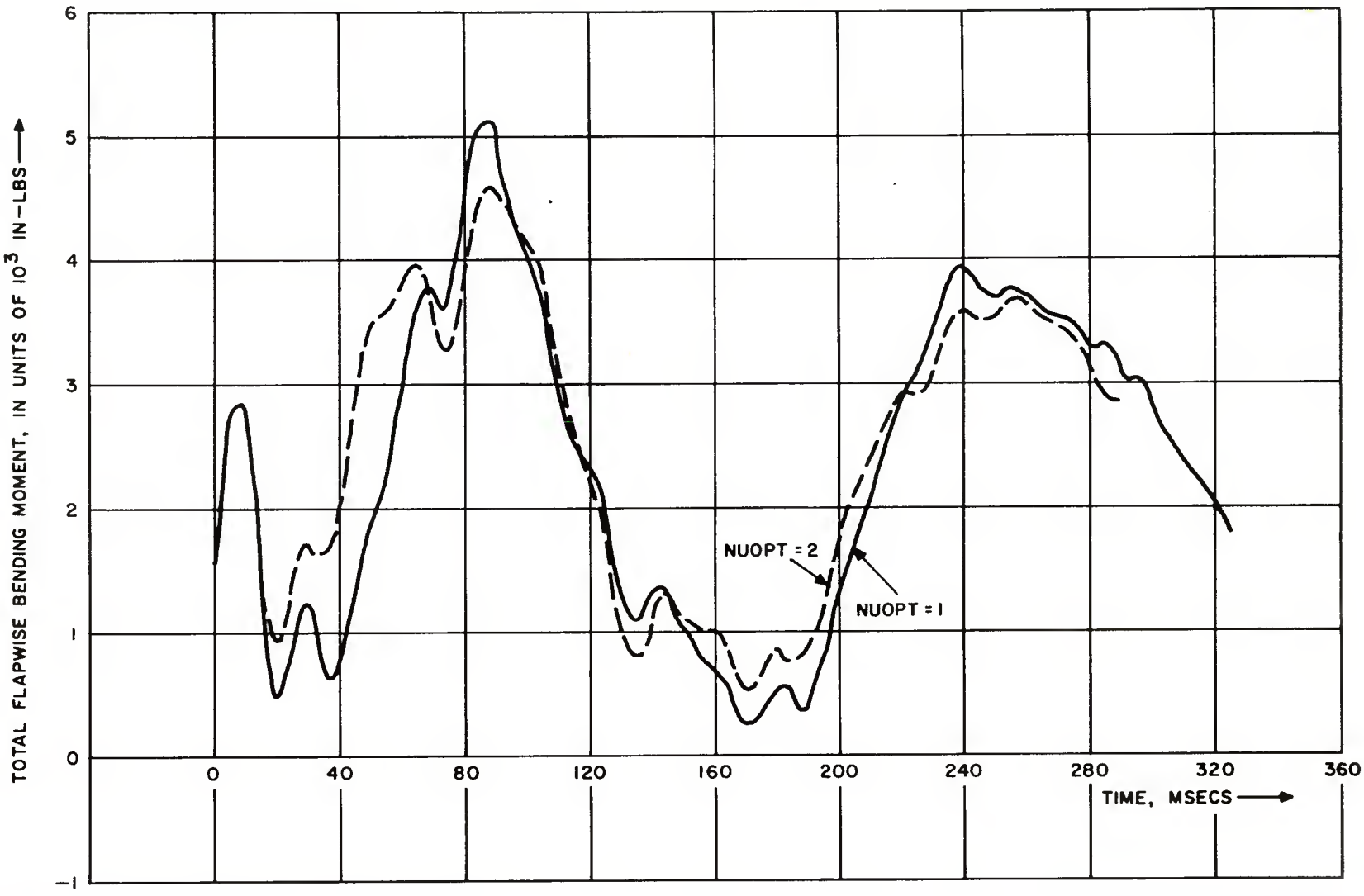

Figure 4.26. Time-Variation of Total Flapwise Bending Moment. Main Rotor Blade Station 132. Analysis for Red Blade. NUOPT=1, 2

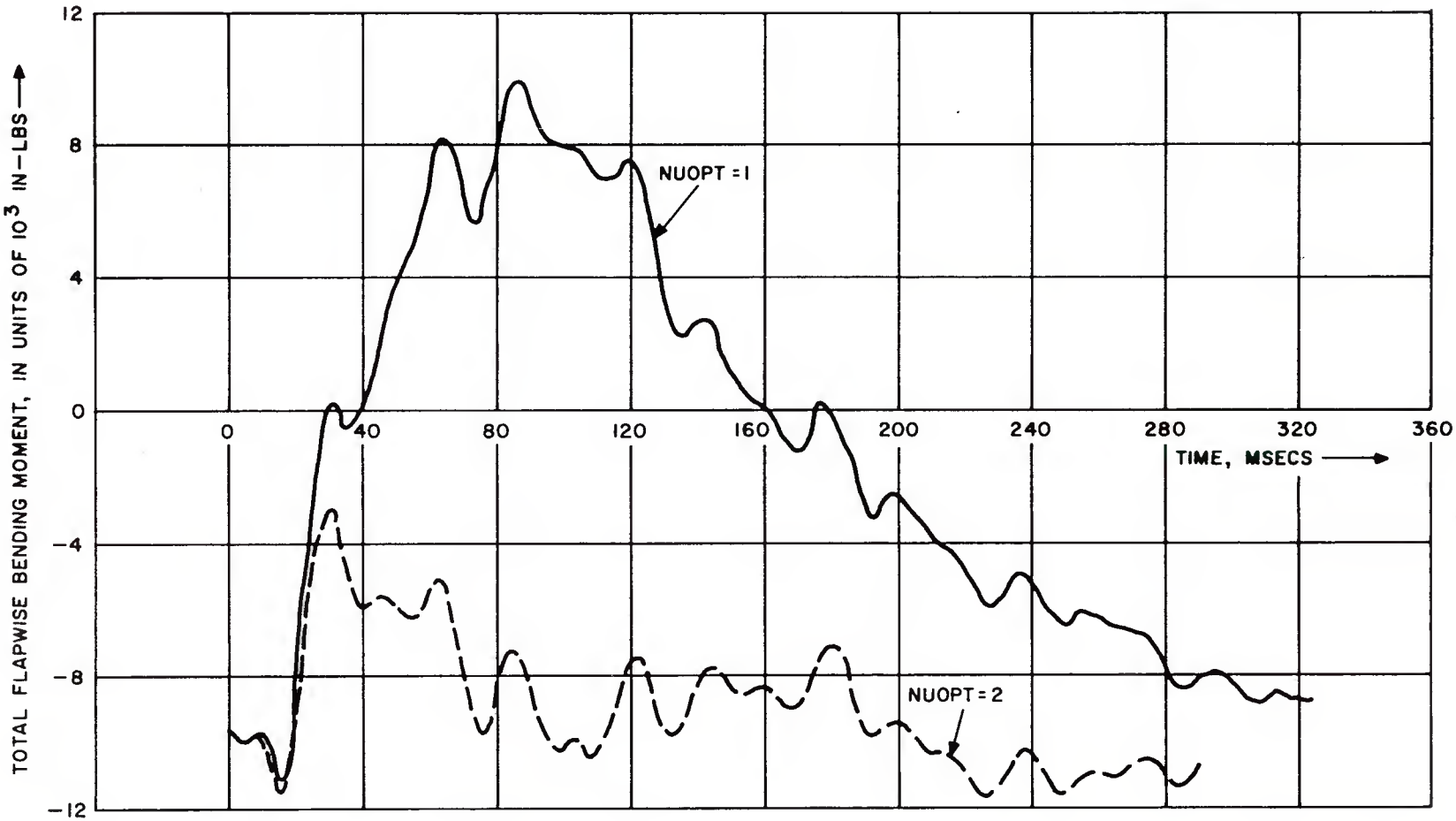

Figure 4.27. Time-Variation of Total Flapwise Bending Moment Main Rotor Blade Station 79.2. Analysis for White Blade. NUOPT=1, 2

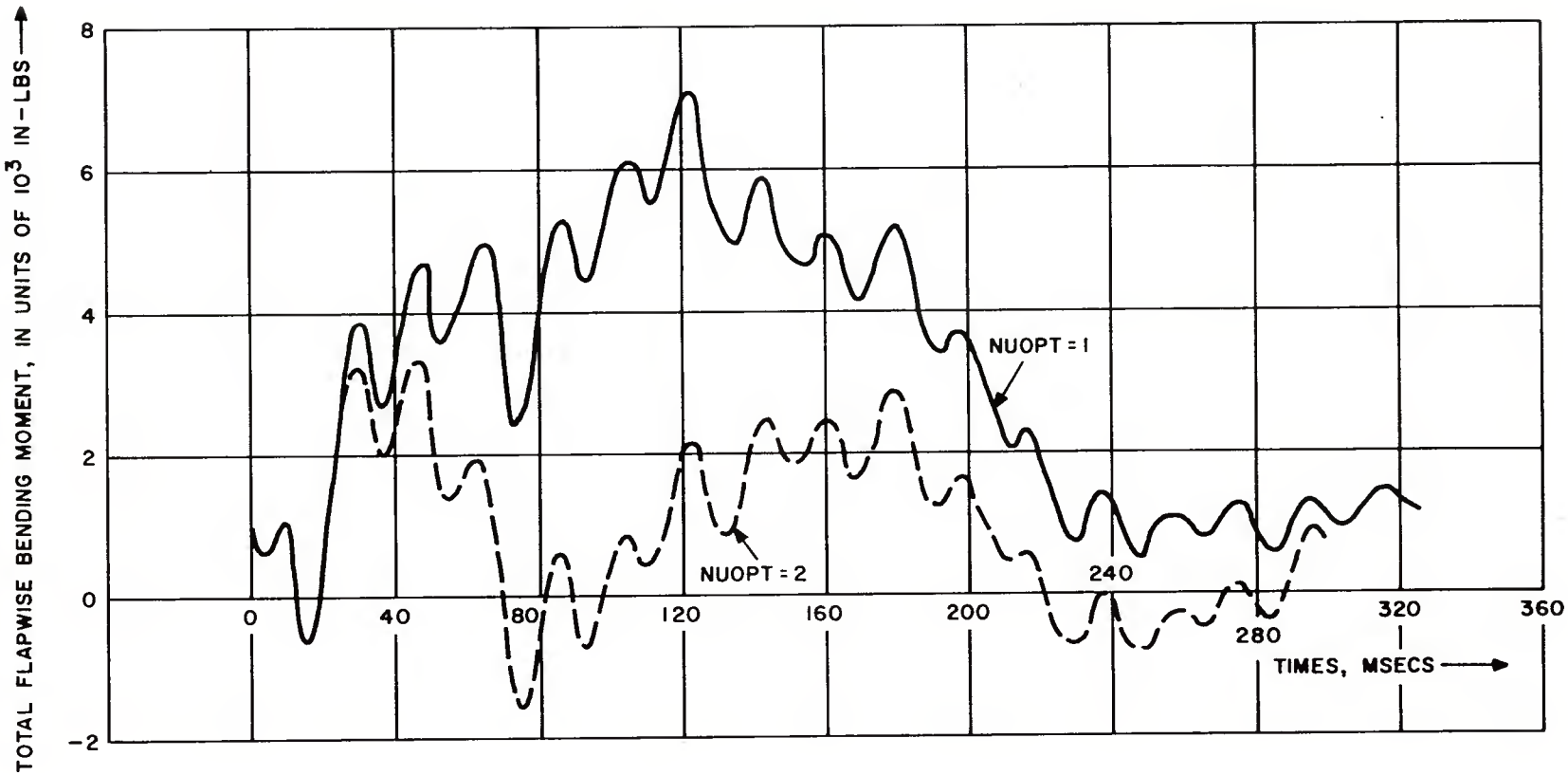

Figure 4.28. Time-Variation of Total Flapwise Bending Moment. Main Rotor Blade Station 105.6. Analysis for White Blade. NUOPT=1, 2

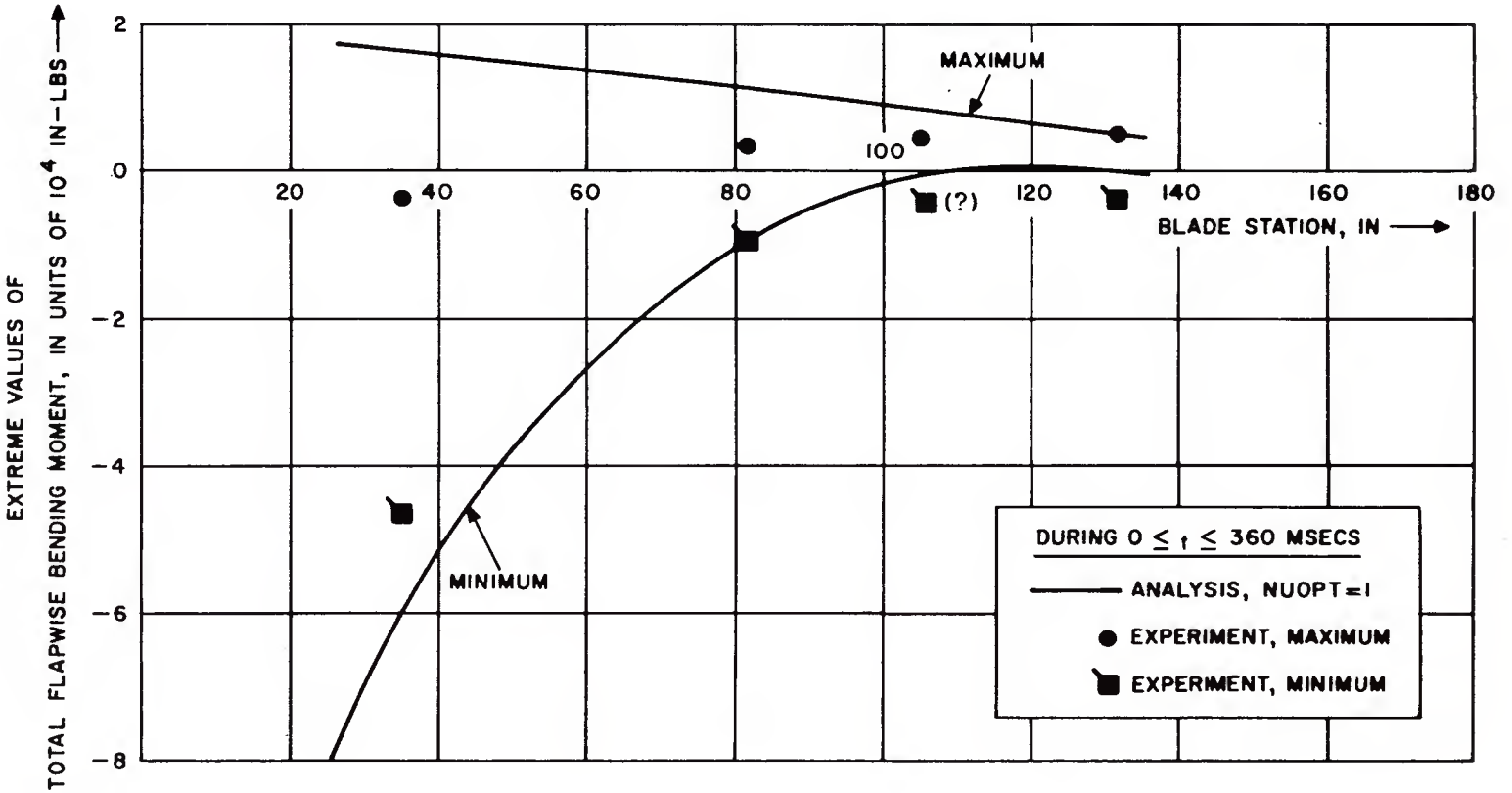

Figure 4.29. Spanwise Distributions of Extreme Values of Total Flapwise Bending Moments. Main Rotor Red Blade. Analytical and Experimental.

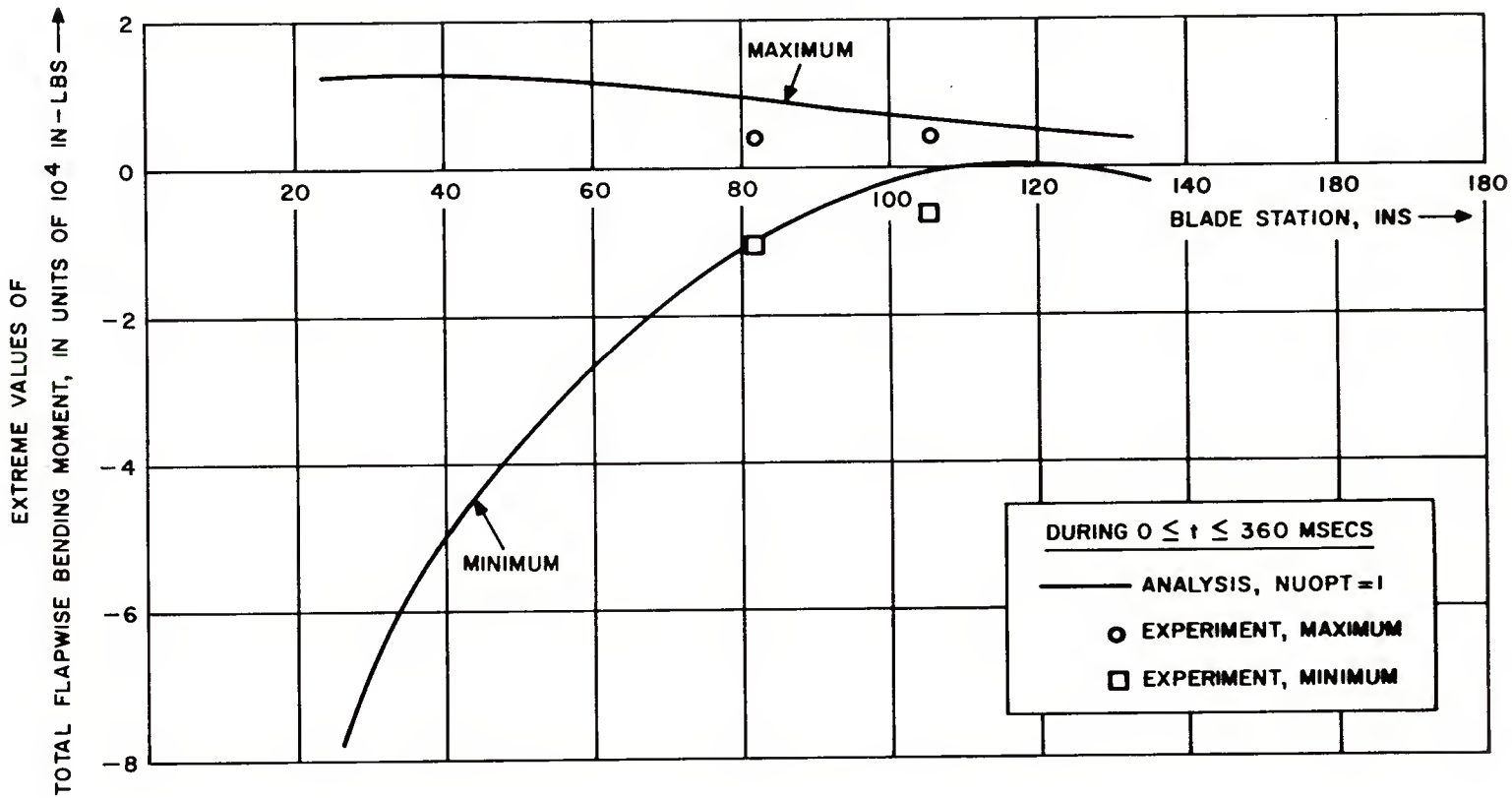

Figure 4.30. Spanwise Distributions of Extreme Values of Total Flapwise Bending Moments. Main Rotor White Blade. Analytical and Experimental

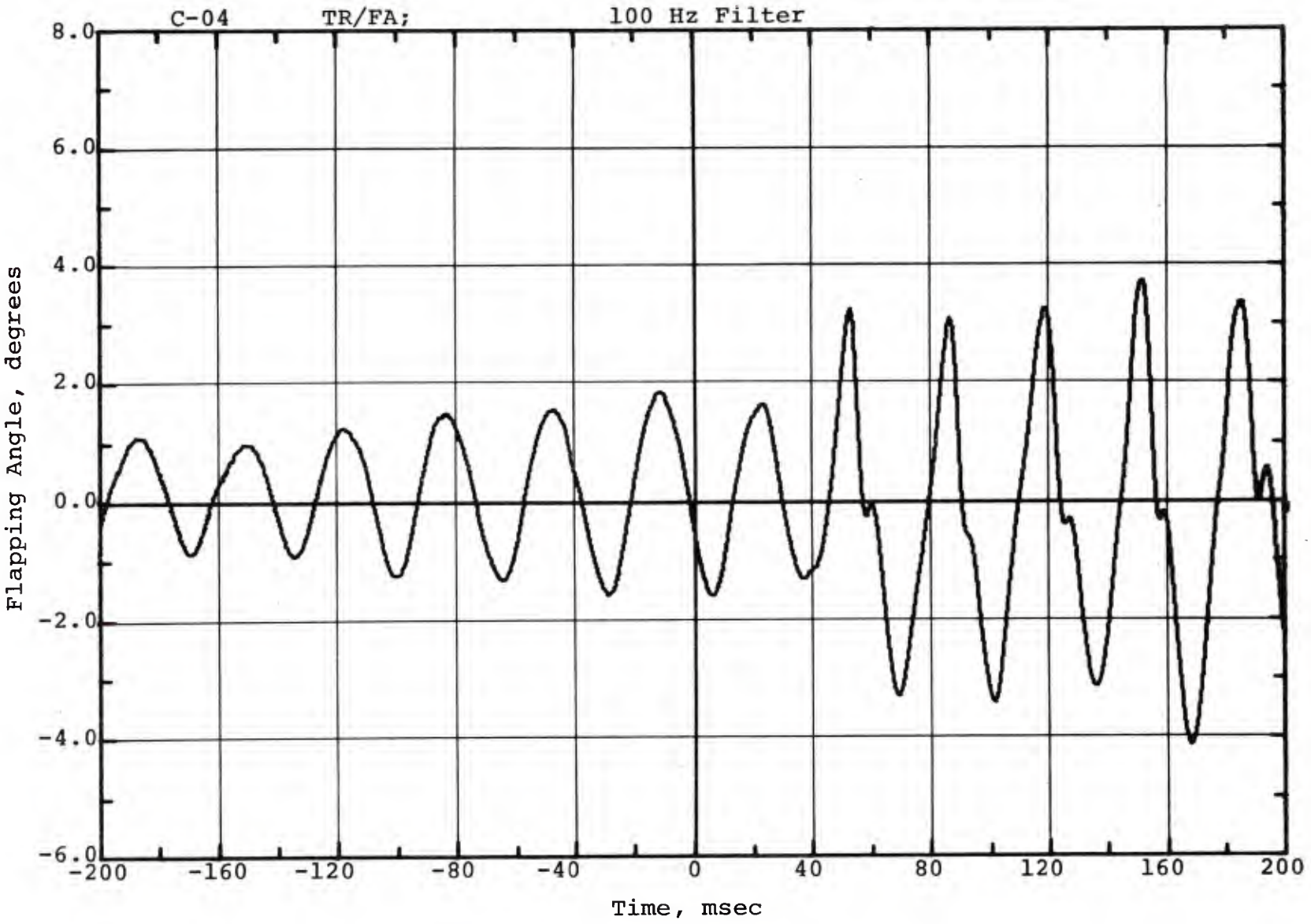

Figure 4.31. Time-Variation of Tail Rotor Red Blade Flapping Angle. Channel C-04

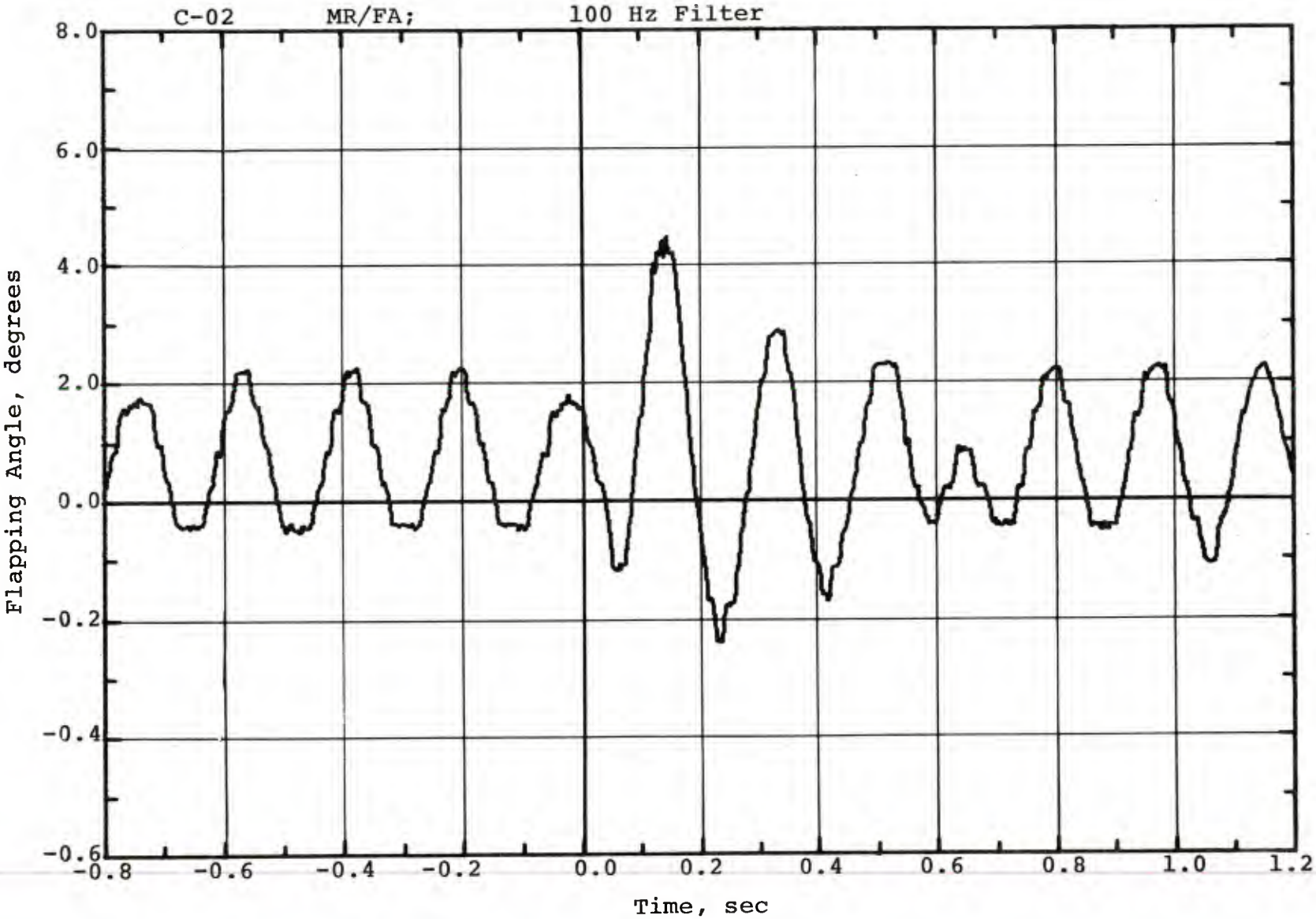

Figure 4.32. Time-Variation of Main Rotor Red Blade Flapping Angle. Channel C-02

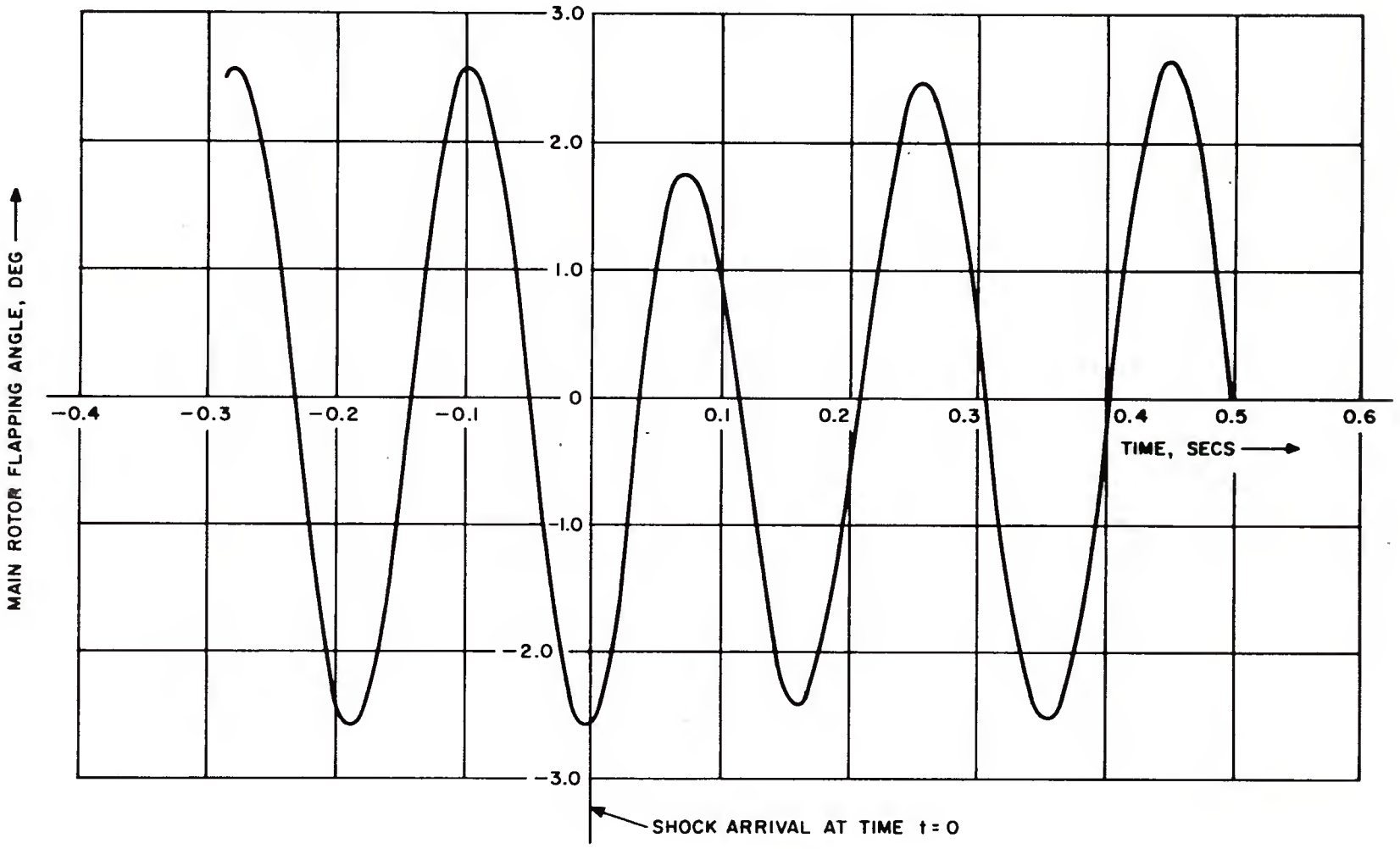

Figure 4.33. Time-Variation of Main Rotor Red Blade Flapping Angle. Analytical.

SECTION 5
RIGID BODY MOTION RESPONSES

This section presents the analyses and the analytical-experimental comparisons for several responses describing the overall rigid-body motions of the helicopter. Of primary interest are the correlations associated with the time-variations of:

(i) The altitude,

(ii) The yaw, pitch, and roll attitudes, and

(iii) The yaw, pitch, and roll rates.

An attempt has been made to correlate concurrently the blade control angles resulting from the autopilot commands.

5.1 Vehicle and Autopilot Data

The best estimates for the total vehicle weight and its center of gravity location just prior to shock arrival are 5680 lbs (176.5 slugs) and fuselage station 133.2 in., respectively. They are somewhat different from the 5950 lbs and 129.5 in. values estimated for the PRE-MINE THROW IV Test. (See Table 7, Reference 1.) Since no estimates were provided for the mass moments of inertia (I_{xx}, I_{yy}, I_{zz}) and for the products of inertia (I_{xy}, I_{xz}, I_{yz}), the values used in the PRE-MINE THROW IV correlation are retained here. They are:

Roll Inertia $I_{xx} = 2478$ slug-ft^2

Pitch Inertia $I_{yy} = 8615$ slug-ft^2

Yaw Inertia $I_{zz} = 7211$ slug-ft^2

$I_{xz} = 1010$ slug-ft^2

$I_{xy} = I_{yz} = 0.$ (Vehicle assumed symmetric about x-z plane)

The rotational inertia parameters are referenced to the conventional right-handed body-fixed axis system used in the analysis and exclude the contributions from the main and tail rotor blades as required by the HELP code. The rest of the vehicle data was obtained from Bell Helicopter and is based on nominal design values.

As to the autopilot (ASE) functions, the feedbacks may be approximated by first order systems. The equations given below are updated versions of the corresponding expressions given in Reference 1. They include additional terms representing feedbacks neglected previously and reflect changes in some of the gains and time constants.

(1) Altitude Channel

This channel is represented here by

$$\Delta\dot{\theta}_{mc} + 20\ \Delta\theta_{mc} = -\ 2\ (h(t)h_H) -\ 0.2 \int_o^t (h(t)-h_H)dt$$

where

$\Delta\theta_{mc}$ is the incremental main rotor collective pitch angle, deg.,

h(t) is the instantaneous vehicle altitude, ft.,

h_H is the hold altitude (assumed to be the trim altitude in the analysis), ft., and

a dot indicates differentiation with respect to time in secs.

(2) Yaw Channel

There are two contributions to the incremental tail rotor collective pitch angle, i.e.,

$$\Delta\theta_{tc} = \Delta\theta_{tc}^{(1)} + \Delta\theta_{tc}^{(2)}$$

The first, $\Delta\theta_{tc}^{(1)}$, is due to the yaw deviation and the yaw rate. The second, $\Delta\theta_{tc}^{(2)}$, results from a built-in design feature which adjusts the tail collective pitch angle whenever the main rotor collective pitch angle is changed. The latter is given by the simple relation

$$\Delta\dot{\theta}_{tc}^{(2)} + 20\ \Delta\theta_{tc}^{(2)}(t) = -\ 20\Delta\theta_{mc}$$

where $\Delta\theta_{tc}^{(2)}$ is in degrees and with its positive sense causing a nose <u>right</u> moment. As the the first part, $\Delta\theta_{tc}^{(1)}$, it can be represented approximately as follows:

$$\Delta\dot{\theta}_{tc}^{(1)} + 20\ \Delta\theta_{tc}^{(1)} = -\ 4.6\ r(t) - 6.716\ (\Psi(t)-\Psi_H)$$

$$-\ 1.208 \int_o^t (\Psi(t)-\Psi_H)dt$$

where

$\Delta\theta_{tc}^{(1)}$ is in degrees, with its positive sense causing a nose right moment,

$r(t)$ is the yaw rate, deg/sec., positive nose right,

$\Psi(t)$ is the instantaneous azimuth angle, deg., positive when nose is to the right of the azimuth reference, and

Ψ_H is the hold azimuth angle, deg.

(3) Pitch Channel

The total contribution to the longitudinal cyclic pitch control is given in two parts, $\Delta\theta_{mp} = \Delta\theta_{mp}^{(1)} + \Delta\theta_{mp}^{(2)}$, with

$$\dot{\Delta\theta}_{mp}^{(1)} + 12.5\ \Delta\theta_{mp}^{(1)} = -1.07q(t) - 5.725\ (\Theta(t) - \Theta_H)$$

$$\dot{\Delta\theta}_{mp}^{(2)} + 0.3\ \Delta\theta_{mp}^{(2)} = 0.16q(t)$$

where

$\Delta\theta_{mp}^{(1)}$ and $\Delta\theta_{mp}^{(2)}$ are in degs.,

$q(t)$ is the pitch rate, deg/sec., positive nose up,

$\Theta(t)$ is the pitch attitude, degs., and

Θ_H is the hold pitch attitude, degs., (assumed to be the same as the trim pitch attitude in the analysis).

(4) Roll Channel

The total contribution to the lateral cyclic pitch control is also given in two parts, $\Delta\theta_{mr} = \Delta\theta_{mr}^{(1)} + \Delta\theta_{mr}^{(2)}$, with

$$\Delta\theta_{mr}^{(1)} + 12.5\ \Delta\theta_{mr}^{(1)} = 1.31\ p(t) + 4.677\ (\Phi(t)-\Phi_H)$$

$$\dot{\Delta\theta}_{mr}^{(2)} + 0.3\ \Delta\theta_{mr}^{(2)} = 0.16\ p(t)$$

where

$\Delta\theta_{mr}^{(1)}$ and $\Delta\theta_{mr}^{(2)}$ are in degs.,

$p(t)$ is the roll rate deg./sec., positive "right wing down",

$\Phi(t)$ is the roll angle, deg., positive "right wing down", and

Φ_H is the hold roll attitude, degs., positive in the same sense as $\Phi(t)$, (assumed to be the trim roll angle in the analysis).

The main rotor incremental blade pitch angle, commanded by the autopilot is then,

$$\Delta\theta_m = \Delta\theta_{mc} + \Delta\theta_{mp}\ \sin\psi_b + \Delta\theta_{mr}\ \cos\psi_b$$

where all angles are in degrees, and ψ_b is the blade azimuth angle from its aftmost position and in its direction of rotation. Thus a positive $\Delta\theta_{mp}$ causes a nose up pitching moment (i.e., F/A stick back), while a positive value of $\Delta\theta_{mr}$ causes a negative rolling moment (i.e., lateral stick left). As to the tail rotor which has only collective pitch control, the incremental blade pitch angle is simply

$$\Delta\theta_t = \Delta\theta_{tc}$$

which is independent of blade azimuth position.

It should be noted that there are no displacement or rate limiters in any of the channels. The time constants for the "main loops" are: 50 msecs $(\frac{1}{20/\text{sec}})$ for the altitude and yaw channels and 80 msecs $(\frac{1}{12.5/\text{sec}})$ for the others. The "minor loops" in the pitch and roll channels (associated with $\Delta\theta_{mp}^{(2)}$ and $\Delta\theta_{mr}^{(2)}$) have relatively long time constants, i.e., $\frac{1}{0.3/\text{sec}} = 3.33$ secs.

When the HOLD modes of the yaw, pitch, and roll channels are operative, the ASE system tries to hold the attitudes of the vehicle to their positions at the time the HOLD commands are turned on. For the altitude on the other hand, the ASE system is designed to bring and hold the vehicle altitude to either 60 ft (with the HOLD-HIGH mode) or 5 ft (with HOLD-LOW mode). In other words, the stabilization altitudes of 60 ft and 5 ft are preselected. The remote pilot (seated in the bunker a few hundred feet from the vehicle) can override the autopilot; and by trimming procedures or otherwise, he can change the hold values.

5.2 Analytical Techniques

The MODEOP=1 option of the HELP code is utilized to obtain all the rigid-body motion and associated responses. This mode of operation considers the vehicle to be completely rigid, and assumes the blast-induced loads are those from the "gust phase". It neglects the very short duration "overpressure effects" and estimates the airloads utilizing, in a quasi-steady fashion, the instantaneous densities and material velocities at the "aerodynamic control points" within the blast field. The details of the HELP code analysis may be found in the first two volumes of Reference 3. The blast-induced rotor forces are estimated according to the NUOPT=1 option for the rotor induced velocity.

Initially, the program trims the vehicle to its pre-blast state. The trimming procedure provides the initial conditions for the transient solution. These conditions turn out to be

$$h_T = 60 \text{ ft}, \ \Psi_T = 0, \ \Theta_T = 5.28 \text{ deg}, \ \Phi_T = -1.61 \text{ deg}$$

while $\dot{\Psi}_T = \dot{\Theta}_T = \dot{\Phi}_T = 0$. The subscript T is included to stress the point that these are trim values. The analysis takes the (constant) trim values h_T, Ψ_T, Θ_T, and Φ_T as the hold values; it retains them during the transient phase, i.e., it assumes that there are no inputs from the remote pilot which would change the hold values and add to the commanded controls. The reason why HELP was programmed this way should be apparent. It is a vulnerability code; and in vulnerability studies, the analyst has no knowledge as to the transient state of the vehicle just before shock arrival and as to the inputs from the remote pilot.

Associated with the above are the initial conditions on the main rotor and tail rotor collective pitch angles and the main rotor cyclic pitch angles. They were found to be:

$(\theta_{mc})_T$ = 14.35 deg., $(\theta_{tc})_T$ = 6.85 deg, $(\theta_{mp})_T$ = 2.19 deg, and

$(\theta_{mr})_T$ = 1.31 deg.* while $(\dot{\theta}_{mc})_T = (\dot{\theta}_{tc})_T = (\dot{\theta}_{mp})_T = (\dot{\theta}_{mr})_T = 0$.

The program is run first in the transient mode with no blast to check the trim procedure and to insure that there are no numerical instabilities in the results. This phase also gives the slight oscillatory variations about the average (trim) values of certain responses.

The program is then run in the transient mode with the blast input which approximates the test condition in the manner described in Section 3. In both transient solutions, i.e., with no blast and with blast, the time step in the numerical integrations was chosen to be 1 msec, but the solutions were printed out every 10 msecs for the period $0 \leq t \leq 10$ secs.

5.3 Some Observations and Comments

Before the presentations of the experimental-analytical comparisons a few words need be said concerning the quality of the experimental data, the difficulties encountered during the correlations, and the shortcomings of the analysis in view of some experimental evidence. The observations and brief comments outlined below should be considered in drawing conclusions as to the prediction capabilities of the analysis. *

---

*The negative sign for the tail rotor blade collective, θ_{tc}, results from the sign conventions used in the analysis. A negative θ_{tc} gives a tail rotor force which gives a nose left moment. Also, the collective pitch angle of the main rotor is defined so that the twist angle at the blade tip is -10 degs.

**Some of these observations and comments pertain also to the responses covered in other sections, e.g., the flapwise bending moments of the main and tail rotor blades.

(1) Large transient angular motions prior to shock arrival. The pilot experienced a great deal of difficulty in stabilizing the vehicle after takeoff for the test. Long-duration oscillograph traces, short segments of which are shown in the figures at the end of Section 2, indicate that the vehicle was undergoing transient motions prior to shock arrival. Looking at the C-11 trace, the altitude appears to have been relatively stable. On the other hand, the extents of the yaw, pitch, and roll attitude variations were large. From the traces, the extreme values during the few seconds before shock arrival are found to have been approximately

For yaw: Ψ=+1 deg. at t=-3.5 sec and Ψ=-5 deg. at t=-0.7 deg.

for pitch: Θ=+4.4 deg at t=-5.5 sec, Θ= 2.6 deg at t=-2.7 sec,

and Θ = + 2.2 deg at t = -0.1 sec.

For roll: Φ=-4.3 deg at t=-3 sec, Φ=-5.5 deg at t=-0.1 sec.

Thus, the pre-blast pitch attitude excursion amounted to 7 degs. which is greater than the maximum excursion during the 9 second period after shock arrival. The pre-blast roll and yaw attitude excursions were less in magnitude than for the same post-shock period of 9 seconds; but they were still substantial. Signals resulting from these large magnitude pre-blast yaw, pitch, and roll oscillations mask the blast-induced signals, making it difficult to correlate and derive definitive conclusions as to how well the analysis predicts the motion responses. It is unfortunate that the pilot was unable to fully stabilize the vehicle before shock arrival.

(2) Inputs from the remote pilot.

The pilot was instructed to stabilize the vehicle as best he could and, except in a case of emergency, to refrain from applying remote controls from a few seconds before to a few seconds after shock arrival. Inadvertently, he did apply significant amounts of remote controls, as evidenced by the oscillograph traces. (Sketches of the remote stick and pedal movements are presented later in this section.) The remote inputs pertain to control deflections and possible changes in hold conditions. Those monitored include: the collective stick (COL), the pedal (PED), the fore-and-aft (F/A) and lateral (LAT) stick. As indicated in a Bell Helicopter documentation, the COL and PED stick movements introduce "collective rate" and "yaw rate" commands, while the F/A and LAT stick movements introduce proportional commands (presumably blade cyclic pitch angles proportional to the stick deflections). The COL and PED positions as fractions of their total travels are known, but the necessary information to translate them into changes in hold conditions or changes in main and tail rotor blade angles were not provided.

Some of the cited remote inputs influence the trim (HOLD) conditions. There are other "secondary" controls which were not monitored; and if employed, they could also have affected the trim.

(3) Inconsistencies in the data.

Some inconsistencies have been detected between the results from related channels. They are pointed out later in the detailed correlation discussions for the various channels. It suffices at this point to cite one such occurrence. For example, the rates of change (slopes) of the yaw attitude (azimuth) trace, (Ψ from C-10), should equal nearly the yaw rates (r values from B-11) at the same times; but they do not. Inconsistencies of this sort between channels may result from improper definitions of the zero levels and/or errors in the calibration constants for one or both channels.

(4) Uncertainties in the calibration data.

In view of the data inconsistencies (item 3 above), questions were raised as to the accuracies of the calibration data. In some instances errors were found and corrected; in others, the questions could not be resolved because of inadequate calibration procedures. The attitude and rate gyros used in this test were the same ones used earlier during the MIXED COMPANY and PRE-MINE THROW IV tests. For DICE THROW, these channels were not recalibrated thoroughly, i.e., much reliance was placed on the calibration data from the earlier tests.

A few words need be said about the angular rates and the pitch and roll attitude measurements. One can specify the vehicle angular velocity (relative to inertial space) in terms of its components along the inertial axes ($\bar{x}$, $\bar{y}$, $\bar{z}$) or along the body-fixed axes (x, y, z) which move in space. With very small attitude angles and rates, the results are the same; i.e., the rates are $\dot{\Phi}$, $\dot{\Theta}$, and $\dot{\Psi}$. The results are different if one (or more) of the rates is large, even though the attitude angles are small. In the present application, large yaw rates are encountered. It is the understanding here that the measured roll rate (p), pitch rate (q), and yaw rate (r) are the components along the body-fixed axes and they are used as such in the correlations. Furthermore, the body-fixed axis system used for the rate measurements is the same one used for the attitude measurements.

As to the attitude angle measurements, the body-axes to which they are referenced need be defined carefully. Consider the pitch attitude, Θ, which is the angle that the body x-axis makes with the horizontal plane. If the measurement is

referenced to a body-fixed x-axis which is different from the body-fixed x-axis used in the analysis, the measured and predicted Θ's will be off by a fixed amount, say $\Delta\Theta_d$, reflecting the angle between the experimental and analytical x-axes. In comparing Θ's, this poses no problem, since it involves only a shift in the zero level of the measured Θ. However, even though $\Delta\Theta_d$ is a constant, it can lead to differences between the measured and predicted roll rates which are dependent on time. This is because of the term $r\Theta$ in the relation $\dot{\Phi} = p + r\Theta$, where r may be large during certain periods of the response. The same sort of difficulty in the roll rate correlation is expected if the experimental and analytical pitch trims are different, due either to a difference in the definitions of the body-fixed x-axes or other factors (e.g., vehicle weight and c.g. conditions). Similar arguments lead to the realization that if the experimental and analytical roll attitude angles are off, their difference can lead to time-dependent errors in the pitch rate, since $\dot{\Theta} = q - r\Phi$.

(5) Channel malfunctions

Channel malfunctions, in the form of slight drifts and jumps in the zero levels are observed in some traces. For example, the main rotor collective trace (B-12) shows a sudden sizeable jump at t - 1 sec; but there are no indications of a remote collective input at that time or a subsequent change in altitude which one would expect from a control command of this magnitude.

(6) Vehicle inertia and autopilot data.

The vehicle weight and its c.g. location were estimated roughly. Slight changes in the c.g. location can alter the trim. The three mass moments of inertia I_{xx}, I_{yy}, I_{zz} and the product of inertia, I_{xz}, were assumed to have the nominal values for the 6000 lb G.W. condition as supplied by Bell Helicopter. How accurate these values are for the actual lower weight condition is not known. The equations describing the autopilot functions have been updated, based on the latest specifications (9/22/76) from Bell Helicopter. But one should realize that these equations are still simplified representations of the actual autopilot system. And, as mentioned earlier, no information is available to translate the remote control inputs into increments of rotor blade angles and/or changes in the hold conditions.

(7) Shortcomings of the analysis.

As acknowledged earlier, the HELP code does not account for the unsteadiness of the vehicle prior to shock arrival (item (1) and for the remote pilot inputs (item 2), both of which

affect strongly the post-blast rigid-body responses. For a fair evaluation of the prediction capabilities of the analysis, these effects should be included in the analysis. This is feasible, a posteriori, if one has (a) confidence in and uses the measurements describing the vehicle initial conditions (i.e., at t=0), (b) the experimental values for the "HOLD" conditions, and (c) accurate measurements of the remote pilot input and can interpret them properly. No such attempt was made here. Even if one had total and reliable inputs for these factors, the necessary program modifications would have been extensive and too expensive to be justifiable for this single application.

5.4 Altitude Deviation and Main Rotor Collective Pitch

The experimental time-variation of altitude deviation, Δh, is presented in Figure 5.1 for the period $-1 \leq t \leq 9$ secs. The deviation was taken about the average pre-blast altitude of 66 ft. Although not apparent in this figure, the observed altitude deviations from this average value are relatively small for a few seconds just before shock arrival. Figure 5.2 shows the calculated time-variation of Δh. Experimental points taken from Figure 5.1 are included for comparison purposes.

The spikes during the first 50-100 msecs in Figure 5.1 are obviously spurious and should be discarded. As expected, the vehicle started to rise following shock encounter. The rise was about 1ft ($\Delta h \cong 1$ ft) over the first second. It then descended about 12 ft ($\Delta h \cong -11$ ft) over the next 4.5 seconds. In contrast, the analysis predicts a 4.4 ft rise over the first two seconds followed by a 7.1 ft decline over the next four seconds. The analytical-experimental difference is attributed mainly to the remote collective stick input. The sketch below describes the signal obtained from the oscillograph trace for the remote collective stick movement. The deflection figures are approximate and are given in percent of total stick travel.

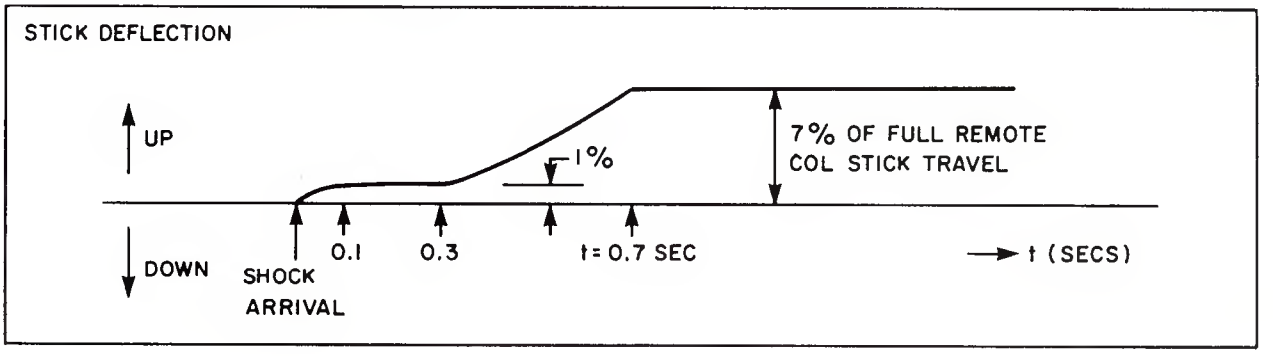

Since no appropriate data are available, the 7% down stick movement cannot be related quantitatively, in an approximate fashion, to hold altitude and main rotor blade angle variations. According to a Bell Helicopter documentation, a down stick movement puts in a "rate command" to lower the altitude. Following a private discussion with Mr. H. Conoley of BHC, it turns out that this control effectively changes the hold altitude. If so, the autopilot, sensing the command to a lower altitude, puts in initially a larger negative collective pitch increment and tries to eventually stabilize the vehicle at some lower altitude. (Note that this effective hold altitude change is not a step change, i.e., the full remote control change is applied over the first 0.7 sec.) From Figure 5.1, it appears that this new hold altitude was around 57 ft, some 9 ft below the original level; and the vehicle first reached there at around t = 4.5 secs.

The B-12 channel gives the aircraft (A/C) collective stick position which is the autopilot collective command in response to the vehicle motion and remote control input. In Figure 5.3, this is interpreted in terms of the main rotor blade collective pitch change, since the blade angle is related directly to the A/C stick movement. The corresponding analytical result shown in Figure 5.4 assumes no changes in hold altitude, i.e., does not account for the remote control input. Unfortunately, the B-12 channel was malfunctioning and its calibration data was found to be incorrect.* One interesting observation should be pointed out however. As seen in Figure 5.3, the blade collective pitch increment is negative for the first 4 secs or so, which happens to be the period when the vehicle is above the 57 ft level; and from long duration oscillograph traces, $\Delta\theta_{mc}$ seems to oscillate about the zero level thereafter.**

All the indications point to an expectation that the analytical-experimental altitude correlation would have been vastly improved, over that indicated by Figure 5.1, had the contributions of the remote collective control been properly included in the analysis.

5.5 Azimuth, Yaw Rate, and Pedal Control

The experimental time-variations of the yaw attitude (azimuth) is presented in Figure 5.5a for the period $-1 \leq t \leq 9$ secs. Figure 5.5b is a stretched version of the same plot covering the shorter time span $-1 \leq t \leq 4$ secs. Figure 5.6 shows the corresponding experimental result for the yaw rate.

Before proceeding with the experimental-analytical comparisons, the related yaw attitude and yaw rate traces were checked for consistency. This check need be discussed, in view of the fact that it revealed a likely calibration error.

---

*No valid calibration data is available.

**Note that in Figure 5.3 the up direction si to be interpreted as a negative increment in $\Delta\theta_{mc}$.

From the rigid-body kinematics of aircraft, the time rate of change of the azimuth angle Ψ, $\dot{\Psi}$, is related to the yaw rate, r, according to

$$\dot{\Psi} = (q \sin\Phi + r \cos\Phi)\sec\Theta$$

where q is the pitch rate, Θ is the pitch angle, and Φ is the roll angle. In this equation, the rates (Ψ, q, r) are in radians/sec and the Euler angles (Ψ, Φ, Θ) are in radians. Since Θ, Φ are small at all times,

$$\dot{\Psi} \cong q\,\Phi + r$$

Furthermore, $q << r$ and $q\Phi <<< r$ generally; therefore,

$$\dot{\Psi} \cong r \qquad \text{or} \qquad (\dot{\Phi}/r) \cong 1$$

Stated alternatively, the ratio $\bar{C} \equiv (\dot{\Phi}/r)$ should be nearly unity (i.e., within a few percent), except possibly at times when r is very small. The check referred to earlier amounts to taking the slopes of the Ψ-trace (C-10) at several t's and comparing them with the r-values for the same times from the r-trace (B-11).

One notes from Figure 5.5b that the times for zero slopes correspond nearly with the times of the t-axis crossings (i.e., r=0) of the yaw rate in Figure 5.6. This indicates that the zero level of the r-curve (Figure 5.6) is correct. But this doesn't confirm whether the vertical scales of the r- and Ψ-traces are consistent.

Consider the results for Φ and r as they are given in Figures 5.5b and 5.6.* By taking the slopes graphically from Figure 5.5b at a few times and comparing them with the r-values at the same times from Figure 5.6, one finds that the ratio $\bar{C}$ varies from about 1.9 to 2.3 depending on time, with an average value of 2.1. This indicates that the vertical scale of r and/or of Ψ is in error. Since the zero-level of the r-trace appears correct, one can also conduct another check which requires that

$$\Psi(\bar{t}) - \Psi(0) = \int_0^{\bar{t}} r\, dt$$

*Actually, longer duration traces were used in this checking procedure to cover more time points.

This was done also. Consider the case with $\bar{t}$ = 0.68 seconds which is the time when the vehicle is at its maximum yaw left position. If the $\Psi(0)$ value is taken at top of the spike near t=0, i.e., $\Psi(0)$= -2.7 deg., and with $\Psi(t=0.68)$ = -8.5 deg., the deviation is $\Psi(t=0.68)-\Psi(t=0)$=-5.8 degs. The value of the r-integral between t=0 and 0.68 is approximately -2.73 deg. The ratio

$$((\Psi(\bar{t})-\Psi(0))/\int_0^{\bar{t}} r\,dt)$$ is once more around 2.1.

The second check confirms the 2.1 factor and further suggests that there occurred a jump in the zero-level of the Ψ-curve of about 1.5 deg. (Note the sudden rise of 1.5 deg at t=0 on the Ψ-curve.)

Assuming that the Figure 5.5 result for Ψ is correct, (except for the sudden zero shift at time t=0 just noted) the vertical scale of the r-plot must be multiplied by a factor of 2.1.* As will be seen later, applying the 2.1 factor to Figure 5.6 brings the experimental results much more in line with the predicted yaw rates.

The prediction curve for the yaw attitude deviation, $\Delta\Psi$, is presented in Figure 5.7 for the period $-1 \leq t \leq 4$ secs. Included in the figure are some experimental points for $\Delta\Psi = \Psi(t) - \Psi(0)$, taking $\Psi(t)$'s from Figure 5.5 and assuming $\Psi(0)$=-2.7 as discussed above. The analysis duplicates the first and major negative peak fairly well. Both the experimental and analytical peaks occur at t=0.68 sec. Also its magnitude is about -6.4 deg analytically as compared with -5.8 deg experimentally. Shortly after the peak, the agreement between experiment and analysis starts to deteriorate.

Consider next the prediction curve for the yaw rate which is shown in Figure 5.8 for the period $-1 \leq t \leq 4$ secs. Included also in this figure are some experimental points for $\bar{r}$. The ordinates of the points taken from Figure 5.6 were multiplied by 2.1 before inclusion in Figure 5.8 for reasons discussed earlier. As in the attitude deviation case, the analysis predicts the first and major negative peak fairly well. The analytical peak is nearly flat for the period $0.18 \leq t \leq 0.26$ secs. and the experiment shows this peak to be around t=0.18 secs. Also, the peak magnitude is about - 16.1 deg/sec. analytically as compared with (-7.1)(2.1)=-14.9 deg/sec, the adjusted experimental value. The analysis overestimates the positive peak substantially. It is interesting to point out that the ratio of the magnitudes between the positive

---

*If instead one assumes that the r-plot is correct and the inconsistency is due solely to an error in the Ψ-calibration, the Ψ-vertical will have to be divided by 2.1. With this reduction in Ψ values, the Ψ-excursions due to the blast will be much lower than one would expect based on the results from PRE-MINE THROW IV.

(nose right) and negative (nose left) peaks of r was higher in PRE-MINE THROW IV than in DICE-THROW (compare Figure 5.6 with Figure 6.8 of Reference).

Consider next the remote pedal input. The sketch below describes the signal obtained from its oscillograph trace. The deflection figure is very approximate and is given in percent of total pedal travel.

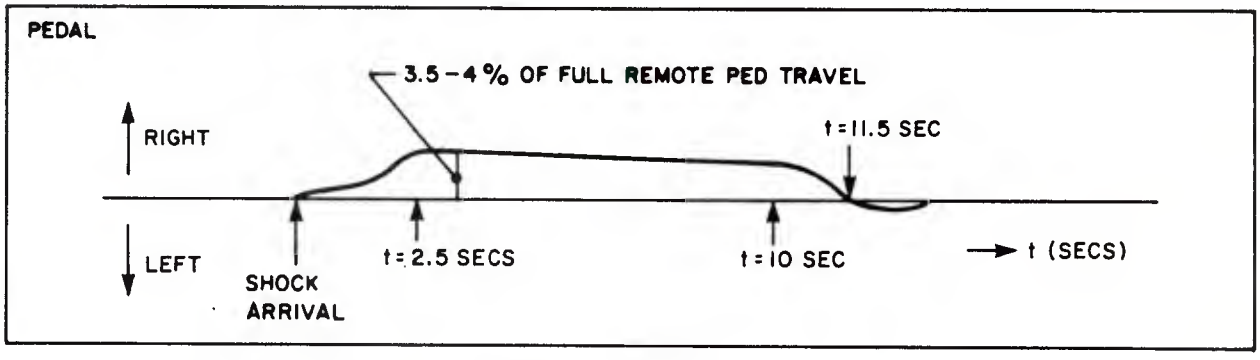

For the first half second or so, there is little remote control input; and this is the period over which the experimental-analytical correlations are reasonable, for the yaw attitude deviation and yaw rate. Figure 5.9 shows the measured total A/C pedal control deflection (C-12). The ordinate represents the autopilot input, in response to the vehicle motion and remote pedal input. It is interpreted in terms of the tail rotor collective pitch angle increment, $\Delta\theta_{tc}$, since the blade angle is proportional to the A/C pedal movement. (Here, as before, the sign of $\Delta\theta_{tc}$ is taken such that a positive increment results in a tail rotor force causing a nose right moment.) Although not covered by Figure 5.9, long duration traces show large $\Delta\theta_{tc}$-variations prior to shock arrival, amounting to as much as 7.5 deg. The related analytical result shown in Figure 5.10 is for $\Delta\theta_{tc}$ due to autopilot, assuming zero $\Delta\theta_{tc}$ at t=0 and with no remote pedal input.

As in the case of the altitude and COL channels, no appropriate data are available to relate quantitatively the 3 1/2to 4% pedal right movement to the actions of the yaw loops of the autopilot. The remote pedal provides a "rate command" proportional to its deflection. Assuming that its action is effectively a change in the hold azimuth condition, as in the case of the remote collective changing the hold altitude, a right pedal should initiate a stabilization at a more positive yaw attitude. This means higher positive $\Delta\theta_{tc}$'s and higher positive yaw rates once the blast disturbance has subsided. Instead, the yaw rate to the right is less than predicted during $0.7 \leq t \leq 4$ secs., approximately. Also, the attitude trace shows the vehicle around $\Psi = -6.5$ deg during $1.5 \leq t \leq 5$ secs, some 1.5 deg further left than at time t=0. Concurrently, with the vehicle to the left of the hold azimuth, the $\Delta\theta_{tc}$ stayed positive, indicating a nose right command by the autopilot. Since the blast-induced excitation had terminated by the time t=1.5 sec. one cannot

follow through with these thoughts and explain why the vehicle did not return more rapidly to its hold azimuth position. One then questions whether the remote pedal movement can be interpreted simply as a change in hold azimuth. The interaction of the remote control with the autopilot action may be much more complex than assumed above. Another factor which complicates matters is the built-in coupling between the pedal and altitude channels: when the main rotor collective pitch changes, the tail rotor collective pitch is also changed. (See equation for $\Delta\theta_{tc}^{(2)}$ in Section 5.1.).

The poor correlations between experiment and analysis beyond "early times", i.e., say $t \geq 0.7$ secs, for the yaw responses (attitude deviation and yaw rate) are believed to be due to the presence of remote inputs and possibly also due to the large vehicle motions just before shock arrival, both of which are unaccounted for in the analysis.

5.6 Pitch Attitude, Pitch Rate, and Longitudinal Cyclic Pitch

The experimental time-variations of pitch attitude and pitch rate, Θ and q, are presented in Figures 5.11a and 5.12 for the period $-1 \leq t \leq 4$ secs. As noted earlier in Section 5.3, the pre-blast pitch attitude peak-to-peak excursion amounted to as much as 7 degrees between t=-5.5 secs and t=-2.7 secs. This is larger than the variation observed from the post-blast response during the first 10 secs or so.

Before proceeding with the experimental-analytical comparisons, the related pitch attitude and pitch rate channels were checked for consistency. There appears to be also an inconsistency between the pitch channels for the reasons discussed below.

From the rigid-body kinematics of aircraft, the time rate of change of pitch attitude angle Θ, $\dot{\Theta}$, is related to the pitch rate, q, according to*

$$\dot{\Theta} = q \cos\Phi - r\sin\Phi$$

where the rates are in rad/sec and the angles in rads. Since the roll Euler angle Φ is always small,

$$\dot{\Theta} \cong q - r\Phi$$

*This assumes that the q- and r-measurements are the components along the body-fixed axes and that the attitude and rates measurements are referenced to the same body axis system. See comments under item (4), Section 5.3.

With $\dot{\Theta}$, q, r expressed in deg/sec and Φ in degrees, the above equation is replaced by

$$\dot{\Theta} \cong q - r\frac{\Phi}{57.3} \quad \text{or} \quad q \cong \dot{\Theta} + r\frac{\Phi}{57.3}$$

In this case, even though Φ is small, the term $(r\Phi/57.3)$ is generally not negligible compared with q or $\dot{\Theta}$, and thus it must be retained. The above relations were used a number of ways in an attempt to check the consistency between the q- and the (Θ, r, Φ) - traces. It was hoped that this effort would lead to the possible sources for inconsistencies should they be revealed.

The pre-blast period was considered first. By taking a few points, say at t=-1, -0.75, and 0 secs, there appeared some indication that the zero-level as well as the vertical scale of the q-trace are in error. If one multiplies the vertical scale of Figure 5.12 by about 2.1 first and then shifts its zero level up by about 0.8 deg/sec, the pre-blast results from q-trace agree with those from the other three. When the same adjustment was tried for points during the post-blast period, the check did not reveal the sought consistency within reading errors. Recognizing possible shifts in the zero levels of one or more traces following shock encounter, different adjustments were next tried for the post-blast period alone. They were also unsuccessful. A drawback in these procedures is that they only check the q-trace assuming the Θ-trace (Figure 5.11), the r-trace (Figure 5.6 adjusted by the factor 2.1 as discussed in Section 5.5), and the Φ-trace to be presented later are correct.

With the failure of all attempts to reconcile the results from the four traces, the only conclusions that can be drawn from this effort are: (a) one (or more) of the channels has calibration errors, and (b) there was a definite shift in the zero level of the q-trace shortly after shock arrival.

The analytical results for the pitch attitude deviation and pitch rate are presented in Figures 5.13-5.14. The prediction calls for a $\Delta\Theta$ = - 1.5 deg during the first 1.2 seconds; this is in reasonable agreement with experiment which shows a drop of about 1.2 deg. (from Θ=2.2 deg to 1.0 deg.). Soon thereafter, the agreement between analysis and experiment starts deteriorating. Between t=1.2 secs and t=3.0 secs approximately analysis predicts a return to near the pre-blast pitch attitude. In contrast, experiment shows a further nose down pitch condition (down to as low as Θ = -0.8 deg) due to a significant movement of the remote F/A (fore-and-aft) stick. The time history of this remote control is depicted in the sketch below.

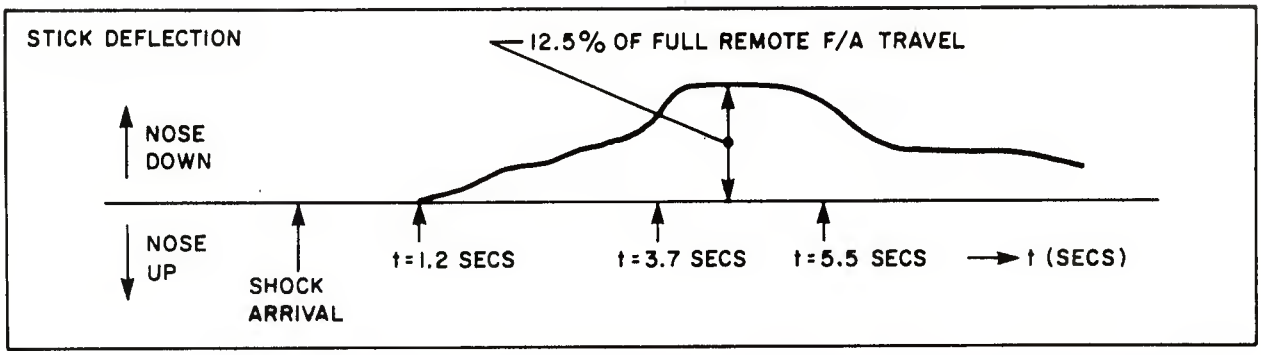

The maximum F/A stick deflection was about 12.5% of its total available travel. Again, no data is available to relate this deflection to changes in longitudinal cycle pitch control.

Although the pitch attitude correlation is reasonable for the period $0 \leq t \leq 1.2$ secs, the same cannot be said about the q-correlation (compare Figures 5.12 and 5.14). Beside the uncertainties in the experimental q-trace as discussed earlier, there is another factor which should be pointed out. During early times, say $0.1 \leq t \leq 0.4$ secs, the yaw rate is large; and if the trim roll angle is incorrect, the computed pitch rate may be way off. For example, consider the situation at time t=0.2. From the analysis, r = -17.5 deg/sec, $\dot{\Theta}$ = -1.8 deg/sec., both of which agree more or less with experiment. With the trim roll angle Φ_T = -1.61 deg (Section 5.2) and the predicted $\Delta\Phi$ being + 0.15 deg., Φ(t=0.2) =-1.46 deg. The expected pitch rate is then

$$q = \dot{\Theta} + r\left(\frac{\Phi}{57.3}\right) = -1.8 + \frac{(-17.5)(-1.46)}{57.3} = -1.35 \text{ deg/sec.}$$

Suppose the experimental value for $\Phi(t=0)$=-5.5 deg is taken as Φ_T; with $\Delta\Phi$ = 0.15 deg., one has $\Phi(t=0.2)$ = -5.35 deg and

$$q = -1.8 + \frac{(-17.5)(-5.35)}{57.3} = -0.17 \text{ deg/sec,}$$

indicating a large change from the previous -1.35 deg/sec value. Thus, for the period $0.1 \leq t \leq 0.4$ secs, during which the yaw rates are large, a difference of the order of a few degrees in the trim roll attitudes reflects strongly in the q-responses. Here the predicted and observed Φ_T values vary by nearly 4 degs. This difference is believed to be a major contributor to the lack of correlation between the analytical and experimental pitch rates. (It is interesting to point out that in PRE-MINE THROW IV, the pitch attitude was about + 1^o at shock arrival time; and the q levels and trends shown in Figure 6.15b of Reference are much different than those shown in Figure 5.12 here.)

The experimental time-variation of the aircraft (A/C) fore-and-aft stick deflection is presented in Figure 5.15. The stick deflection is interpreted in terms of main rotor blade longitudinal cyclic pitch angle. This signal includes the deflections of the remote F/A control. The corresponding analytical result is shown in Figure 5.16. The ordinate there is the incremental longitudinal cyclic pitch angle dictated by the autopilot in response to the blast encounter. For the 1.2 secs or so, the analysis calls for a 1.0 deg increment in θ_{mp}; the experiment shows it to be over twice this amount. Beyond t=1.2 secs, the observed variation in θ_{mp} is attributed to the large F/A remote input which is unaccounted for in the analysis.

5.7 Roll Attitude, Roll Rate, and Lateral Cyclic Pitch

The experimental time-variations of roll attitude and roll rate, Φ and p, are presented in Figures 5.17a and 5.18 for the period $-1 \leq t \leq 4$ secs. A consistency check, similar to those used in the preceding two sections for the yaw and pitch channels, is available also for the roll channels. The condition which must be met for consistency is:*

$$\dot{\Phi} \cong p + r\,\frac{\Theta}{57.3} \qquad \text{or} \qquad p \cong \dot{\Phi} - r\,\frac{\Theta}{57.3}$$

Due to the noise in both attitude and rate channels, it is difficult to obtain reasonably accurate values of the slopes $\dot{\Theta}$ and the rates p; and the reading errors are too large to conduct this check as deeply as before. Consider the times t = 0.68 secs, and t = 3.1 secs. At t = 0.68 secs, r = 0, and $\dot{\Phi}$ should equal to p. $\dot{\Phi} \approx 1.76$ deg/sec, while the p-reading can be anywhere between 2.0 and 2.6 deg/sec. For t = 3.1 secs, Θ = - 0.86 deg, r = -0.74 deg/sec., and $\dot{\Phi}$ = 3.6 deg/sec, requiring $p = 3.6 - (-0.735)\frac{(-0.86)}{57.3} = 3.59$ deg/sec. But p-plot gives a value a little less than 2 deg/sec. These results give some indication of an inconsistency. The source of this inconsistency could not be traced.

The Φ - and p-traces show that the vehicle acquired an incremental negative (left) roll angle for a short time after shock arrival (during about $0 \leq t \leq 0.5$ secs), a fact confirmed by movies taken during the test. This is not as one would expect if one considers only the blast-induced incremental tail rotor force which causes a roll right moment. However, the blast-induced fuselage forces, which are extremely large during the overpressure phase, should not be overlooked. With the center of action of the fuselage forces below the vehicle c.g., these forces could have induced a left rolling moment. In fact, this appears to have been the case. The fuselage force during the short overpressure phase must have

*Recall once more the comments made under item (4), Section 5.3.

been "nearly impulsive" and of sufficient magnitude to impart almost a sudden negative roll velocity.

Consider next the analytical results for $\Delta\Phi$ and p shown in Figures 5.19 - 5.20. The correlations between these and their experimental counterparts are poor. One notes that the initial predicted roll motion is to the right. This is not surprising because the analysis treats the fuselage aerodynamic forces according to the "drag phase" formula, i.e., omits entirely the "overpressure phase loading," and concentrates whatever fuselage forces it computes along the body x-axis. Thus, it effectively sets the rolling moment contribution from the fuselage equal to zero. This is believed to be one major cause for the disagreements between experiment and analysis for the roll channels.

For the sake of completeness, the time-variation of the aircraft lateral stick movement, interpreted as time-variation of main rotor lateral cyclic pitch angle, is presented in Figure 5.21. The positive ordinate direction is such that the control deflection commands a roll right moment. It includes a contribution from the remote lateral stick. The sketch below depicts the remote lateral stick movement as recorded by an oscillograph.

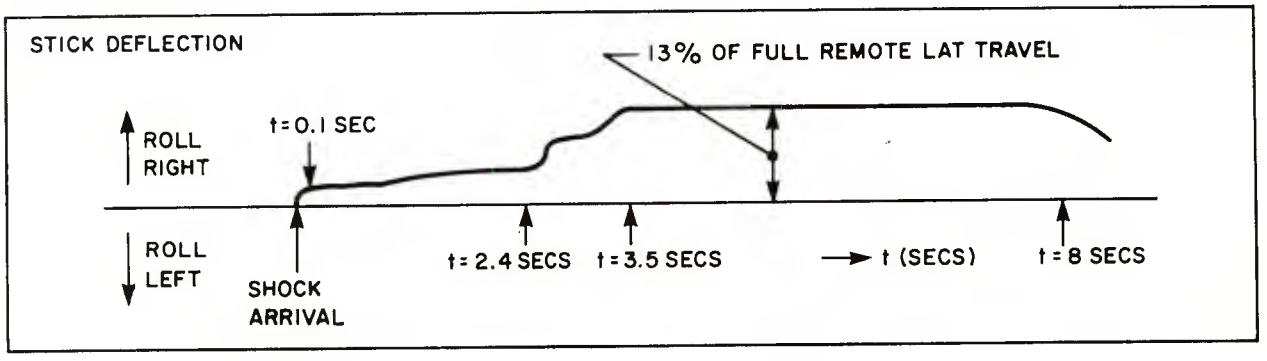

The computed time-variation of the incremental lateral cyclic pitch angle, $-\Delta\theta_{mr}$, due to the autopilot responding to the blast, is shown in Figure 5.22. The analysis excludes the effects of the remote control input.

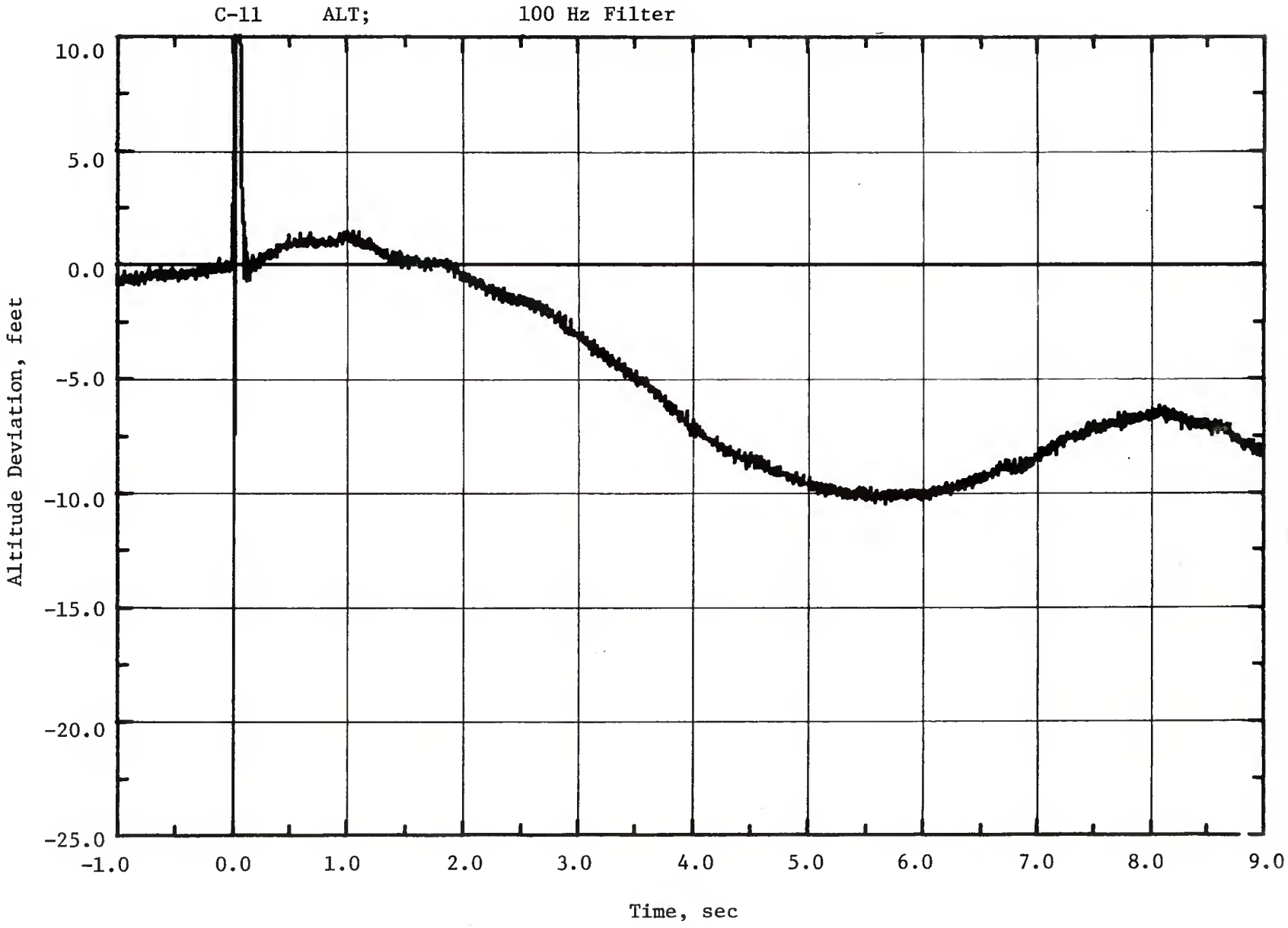

Figure 5.1. Time-Variation of Altitude Deviation. Channel C-11

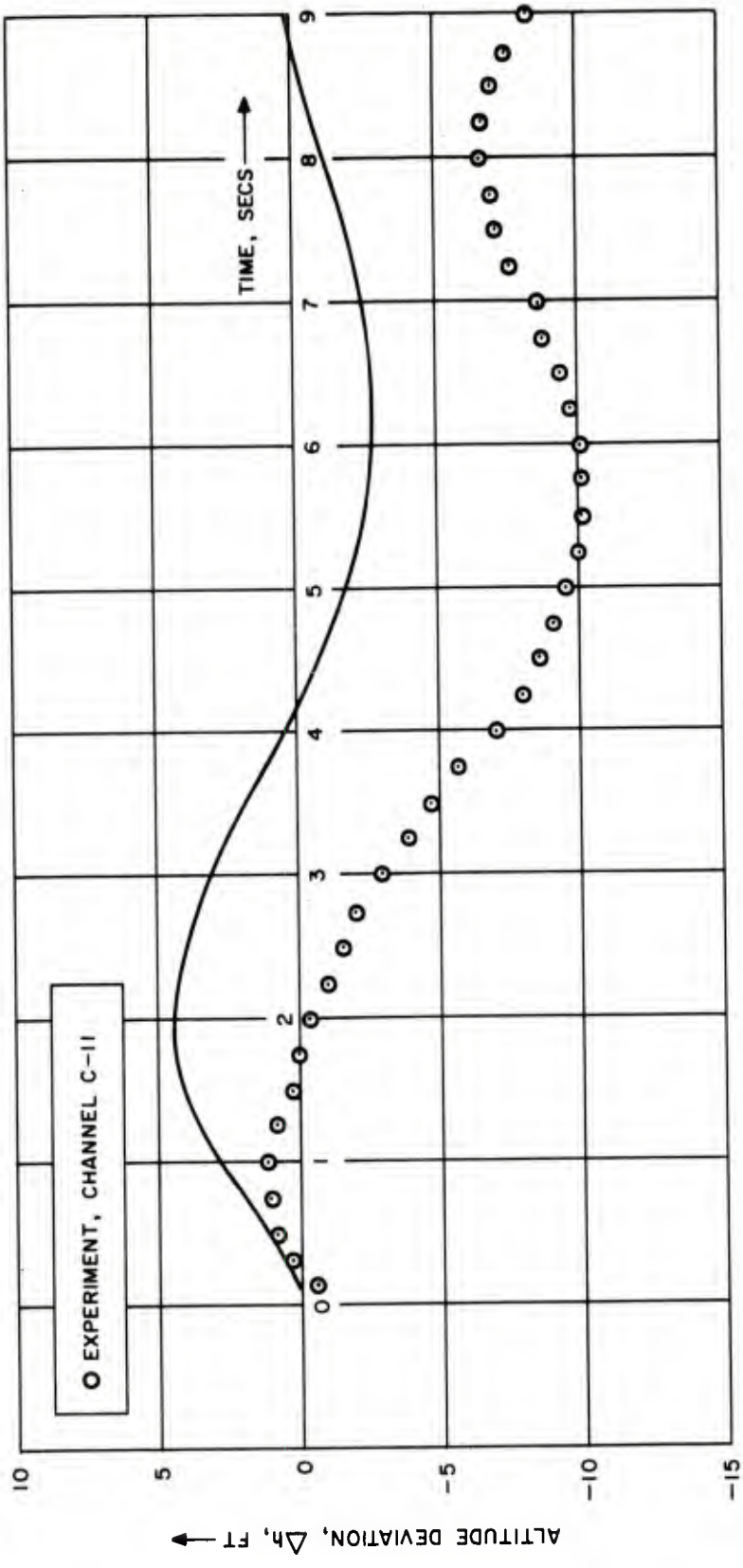

Figure 5.2. Time-Variation of Altitude Deviation. Analytical and Experimental

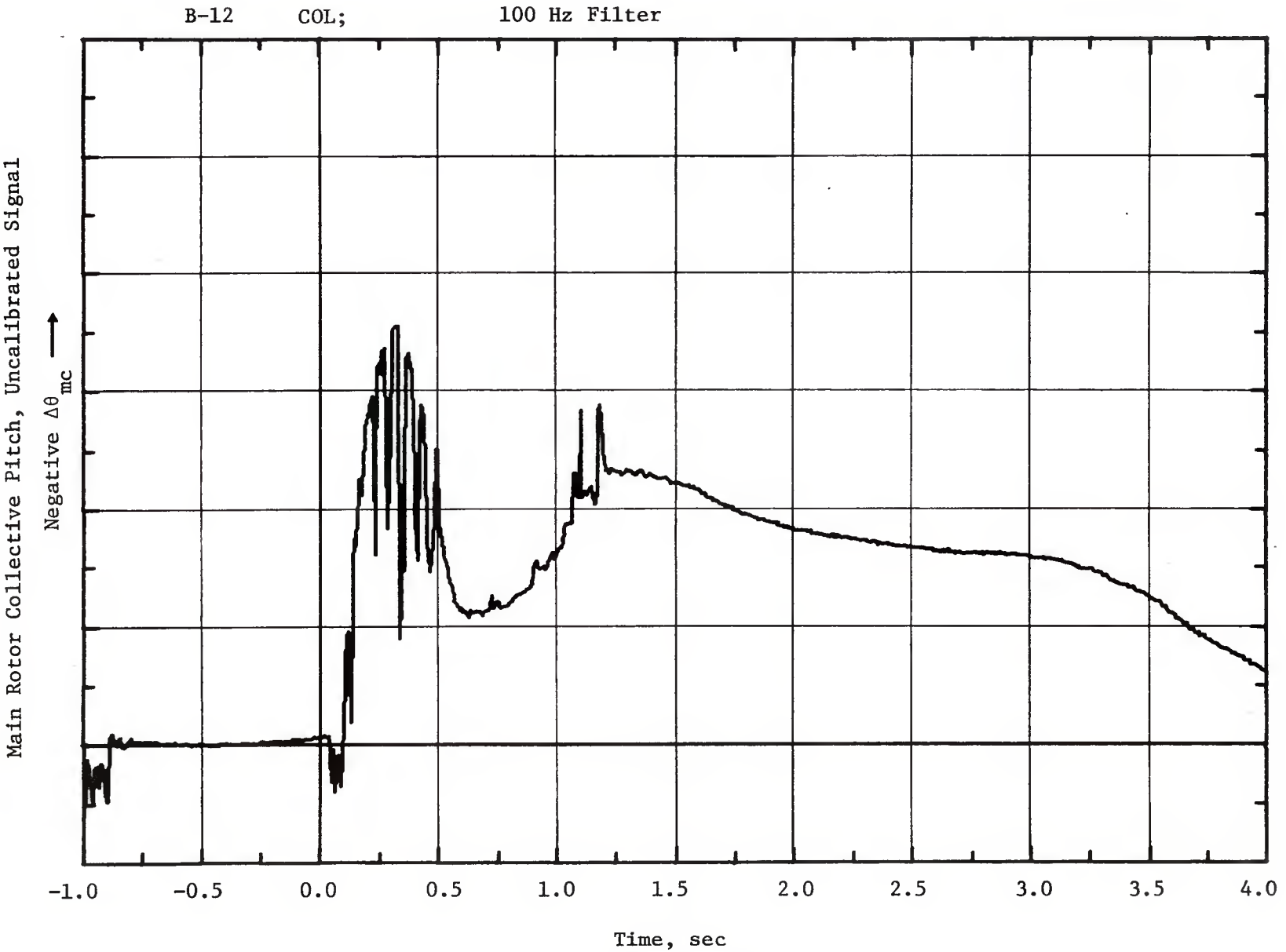

Figure 5.3. Time-Variation of Aircraft Collective Stick Deflection Interpreted as Time-Variation of Main Rotor Collective Pitch Angle. Channel B-12. (Valid Calibration Data Not Available.)

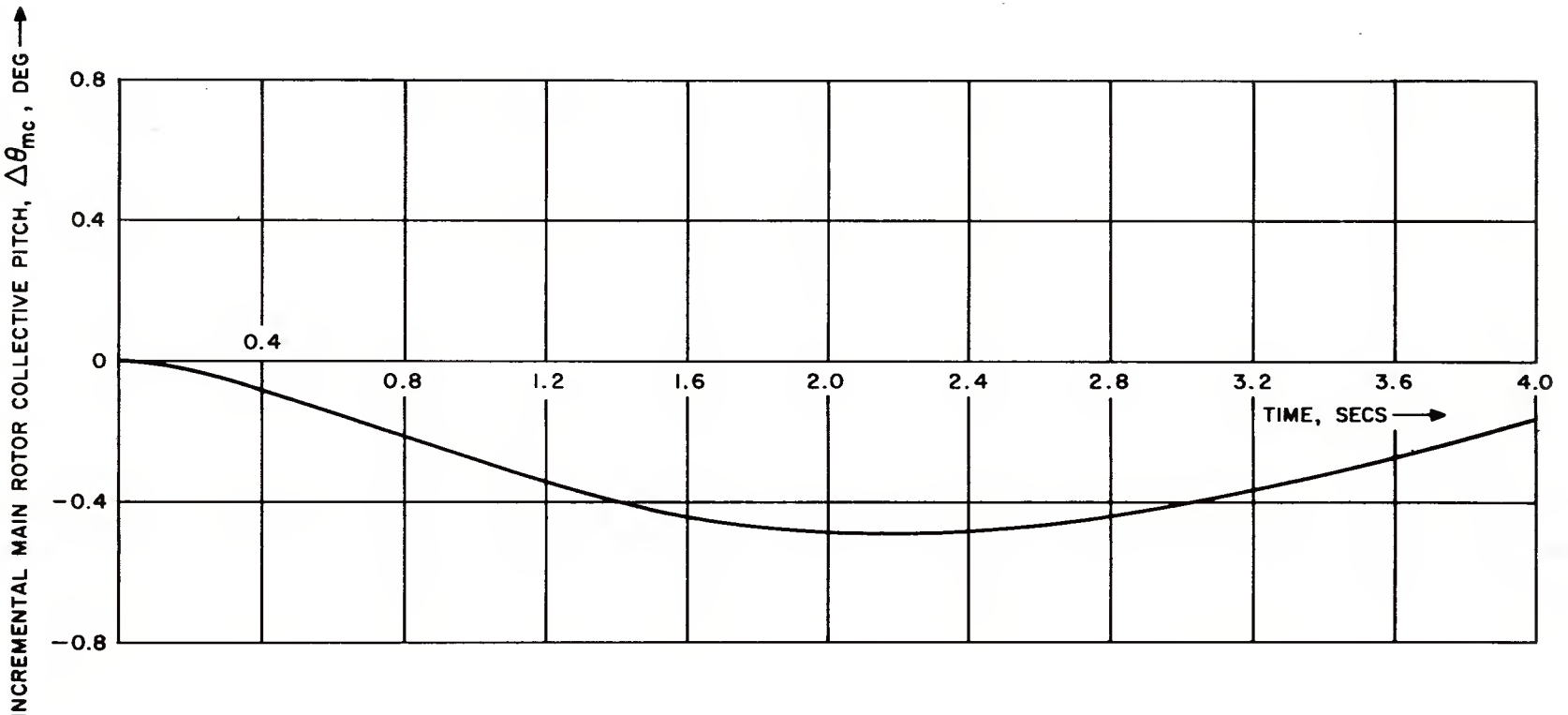

Figure 5.4. Time-Variation of Incremental Main Rotor Collective Pitch Due to Autopilot in Response to Blast. Analytical

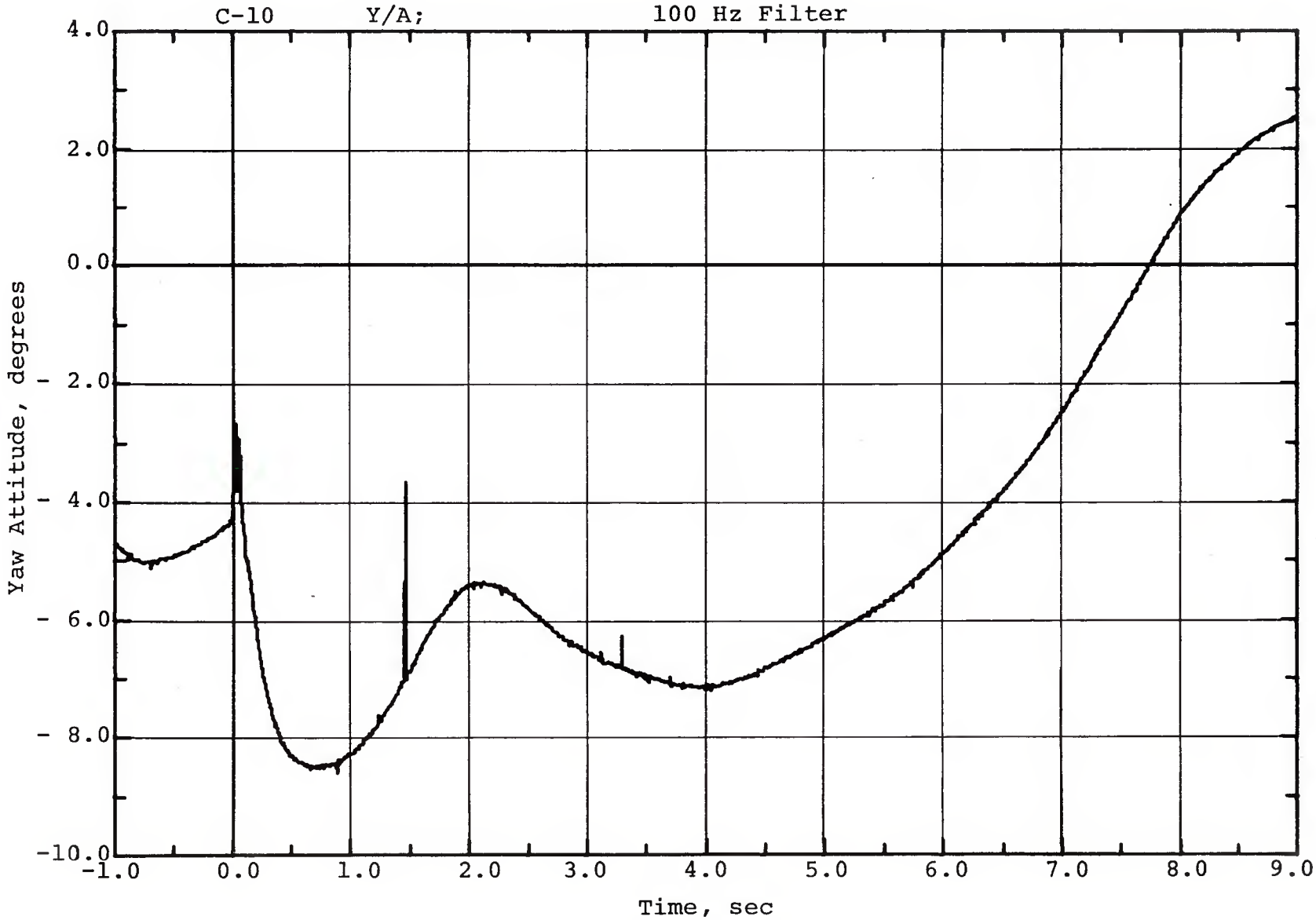

Figure 5.5a. Time-Variation of Yaw Attitude. Channel C-10

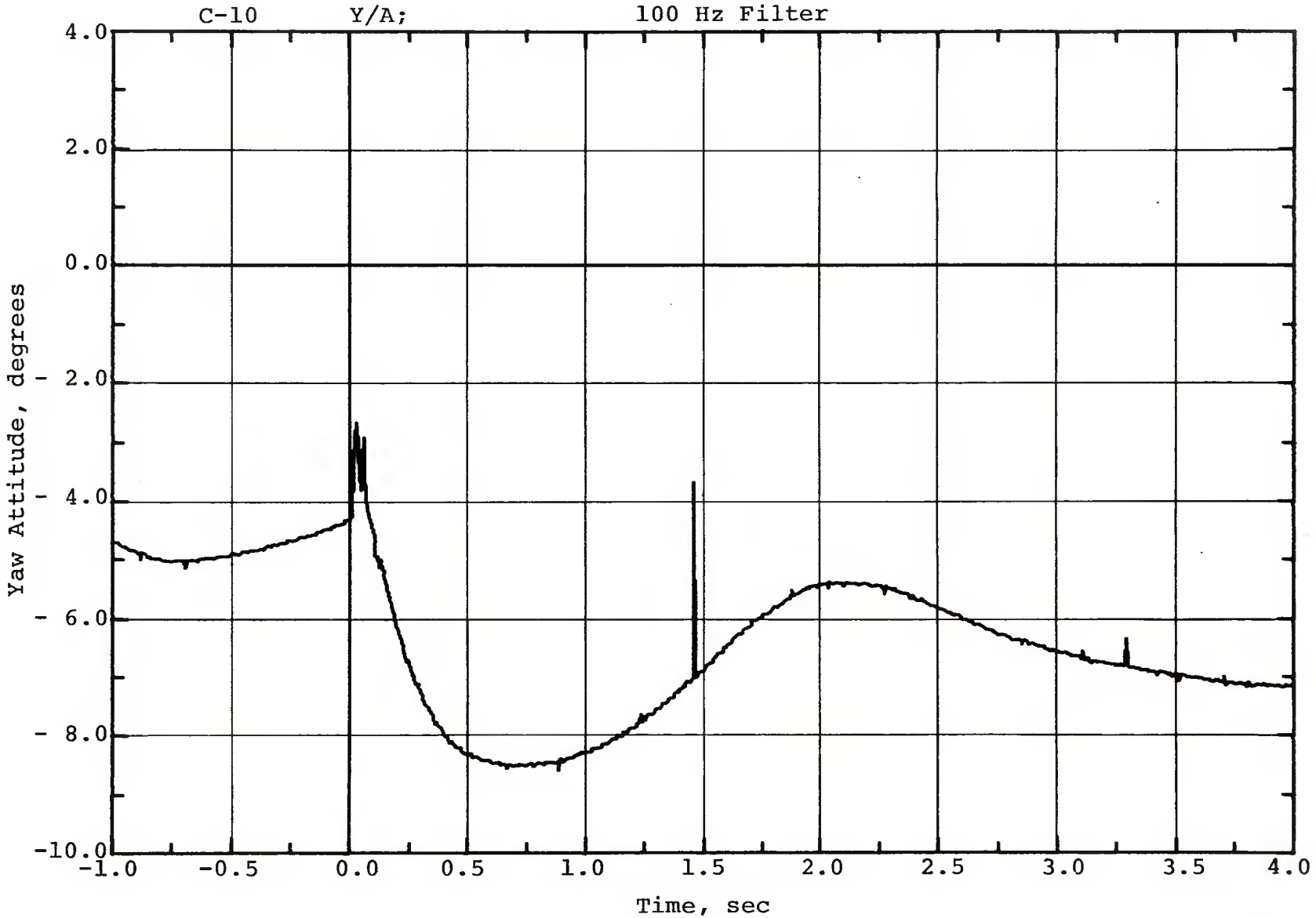

Figure 5.5b. Time-Variation of Yaw Attitude. Channel C-10

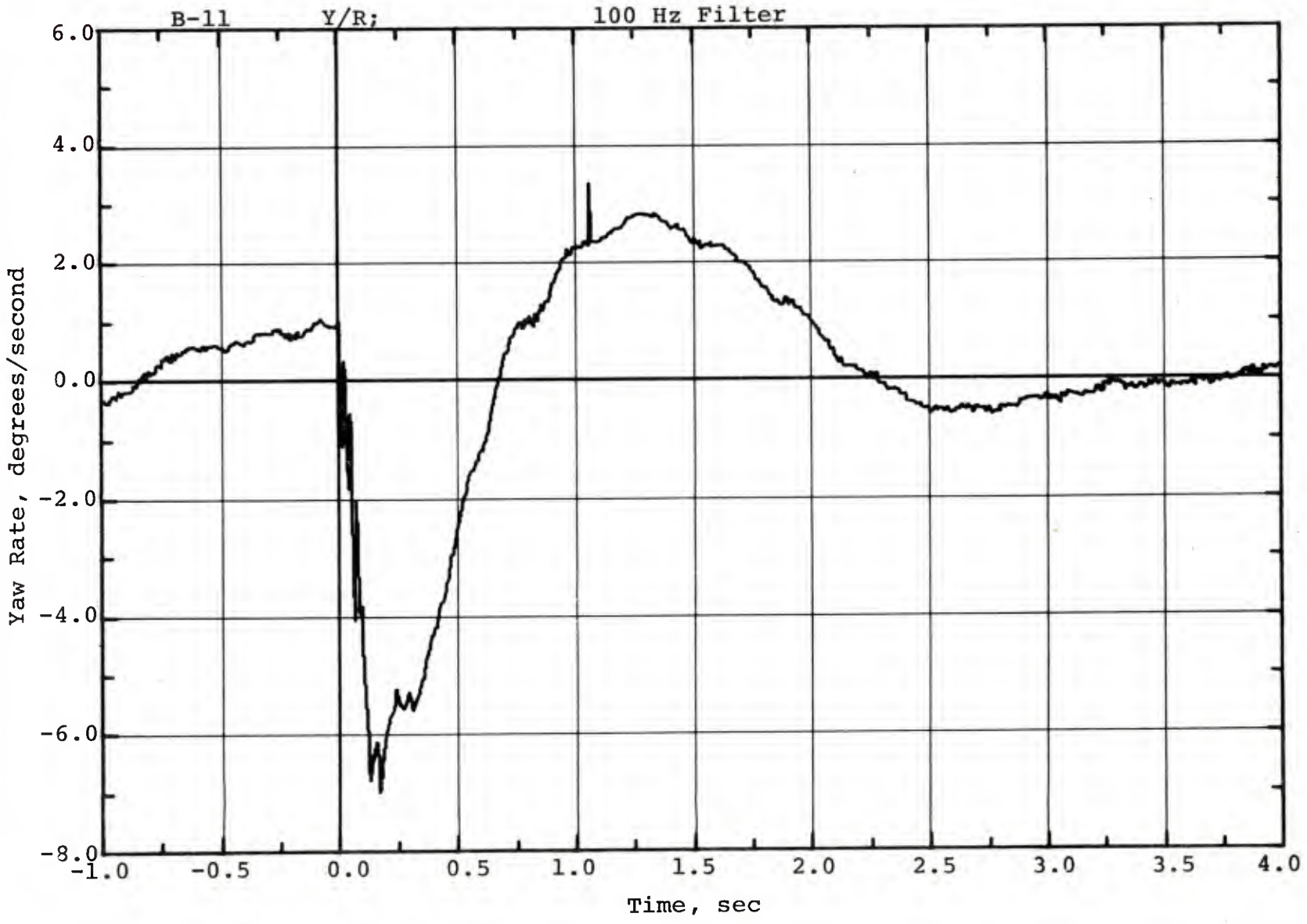

Figure 5.6. Time-Variation of Yaw Rate. Channel B-11

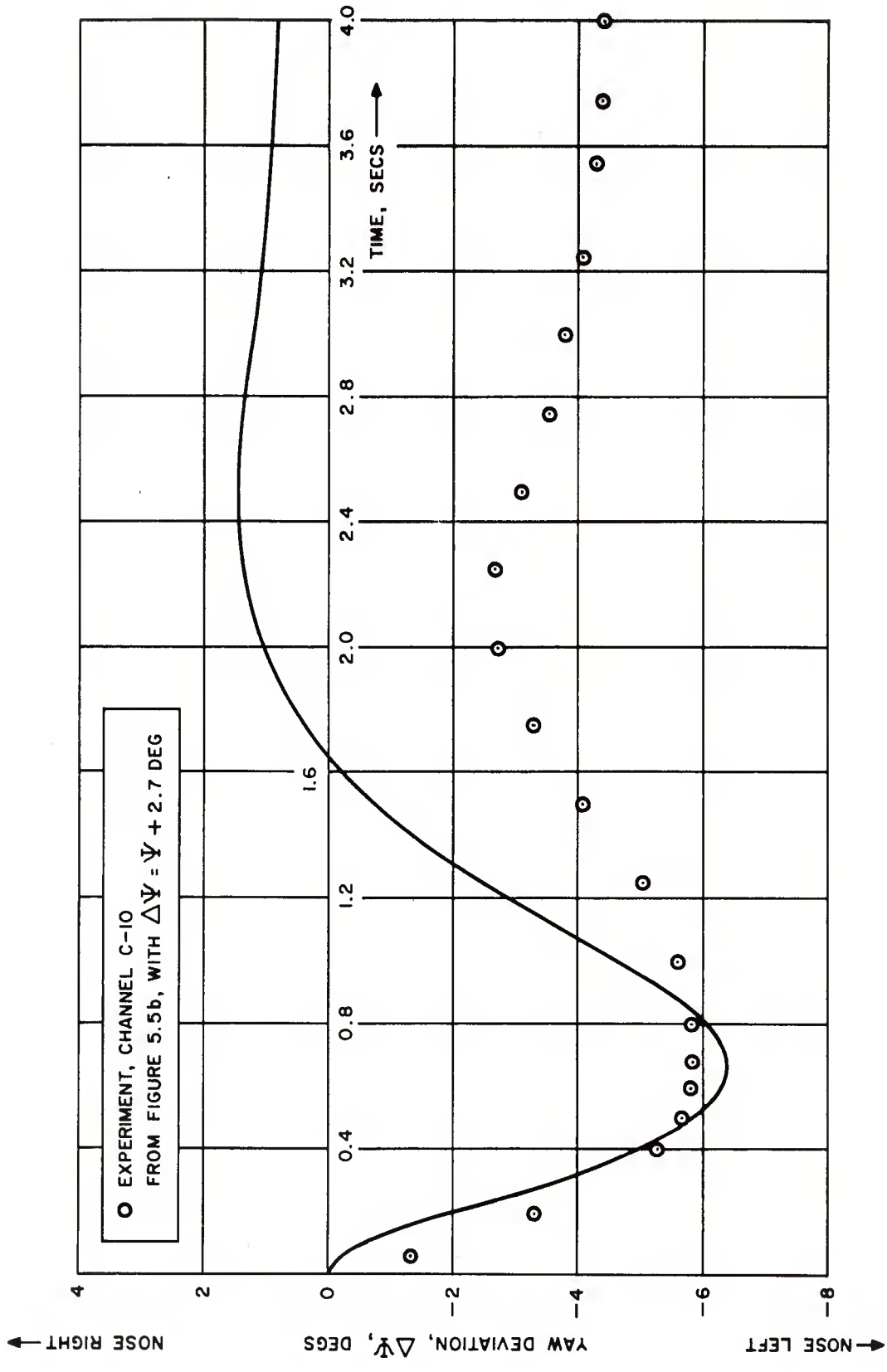

Figure 5.7. Time-Variation of Yaw Deviation (Azimuth). Analytical and Experimental

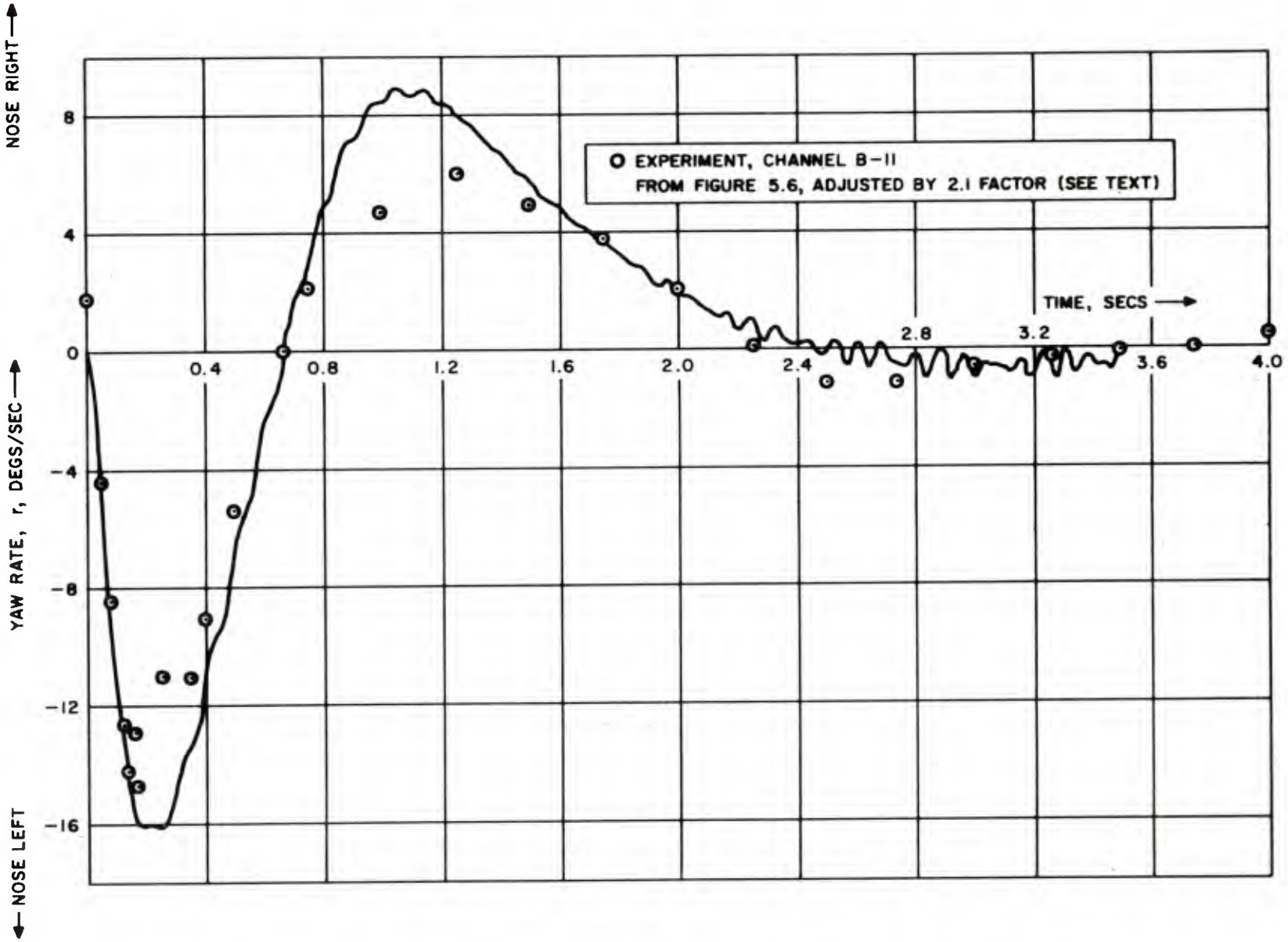

Figure 5.8. Time-Variation of Yaw Rate. Analytical and Experimental

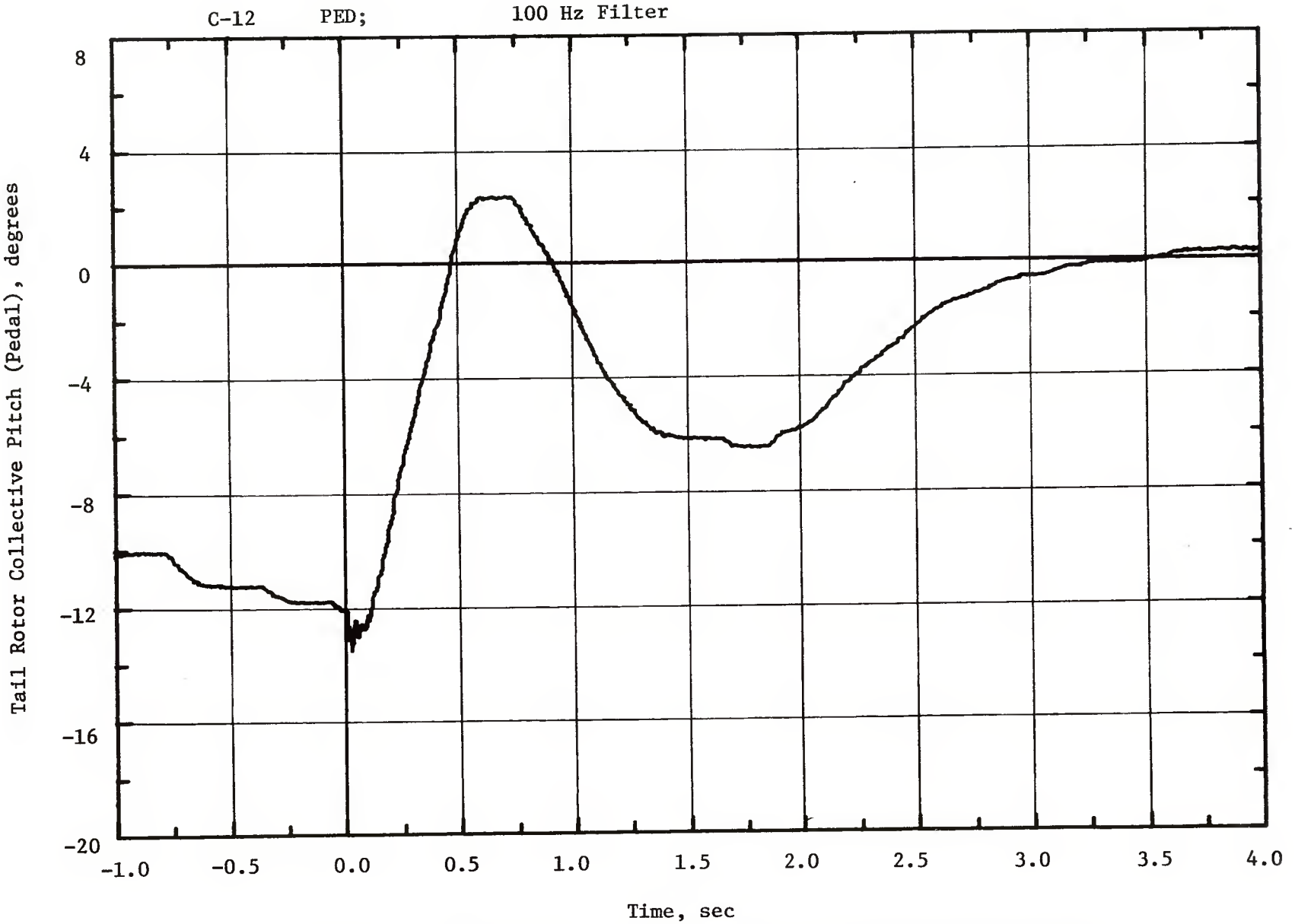

Figure 5.9. Time-Variation of Aircraft Pedal Deflection Interpreted As Time-Variation of Tail Rotor Collective Pitch Angle. Channel C-12

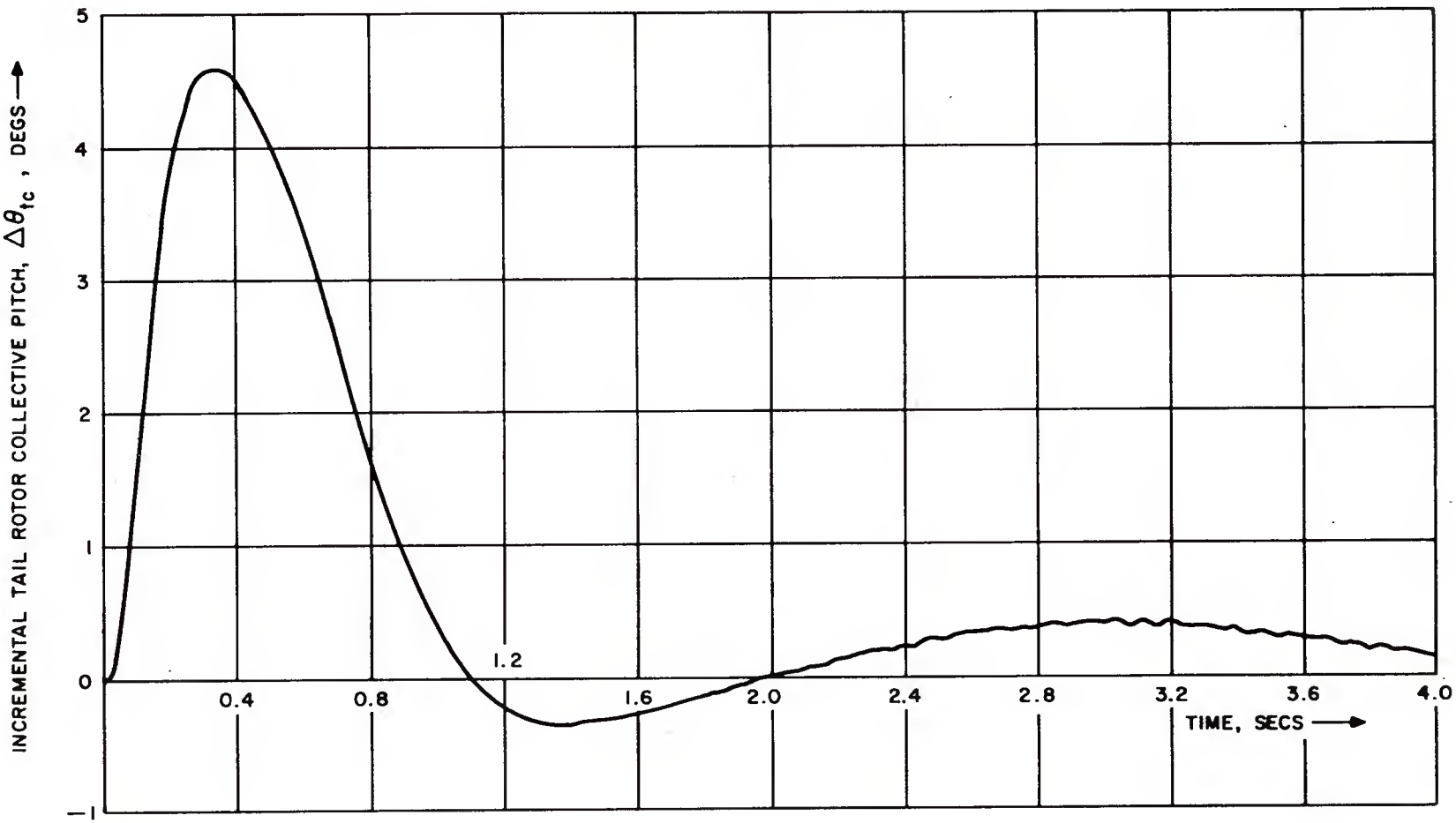

Figure 5.10. Time-Variation of Incremental Tail Rotor Collective Pitch Due to Autopilot in Response to Blast. Analytical

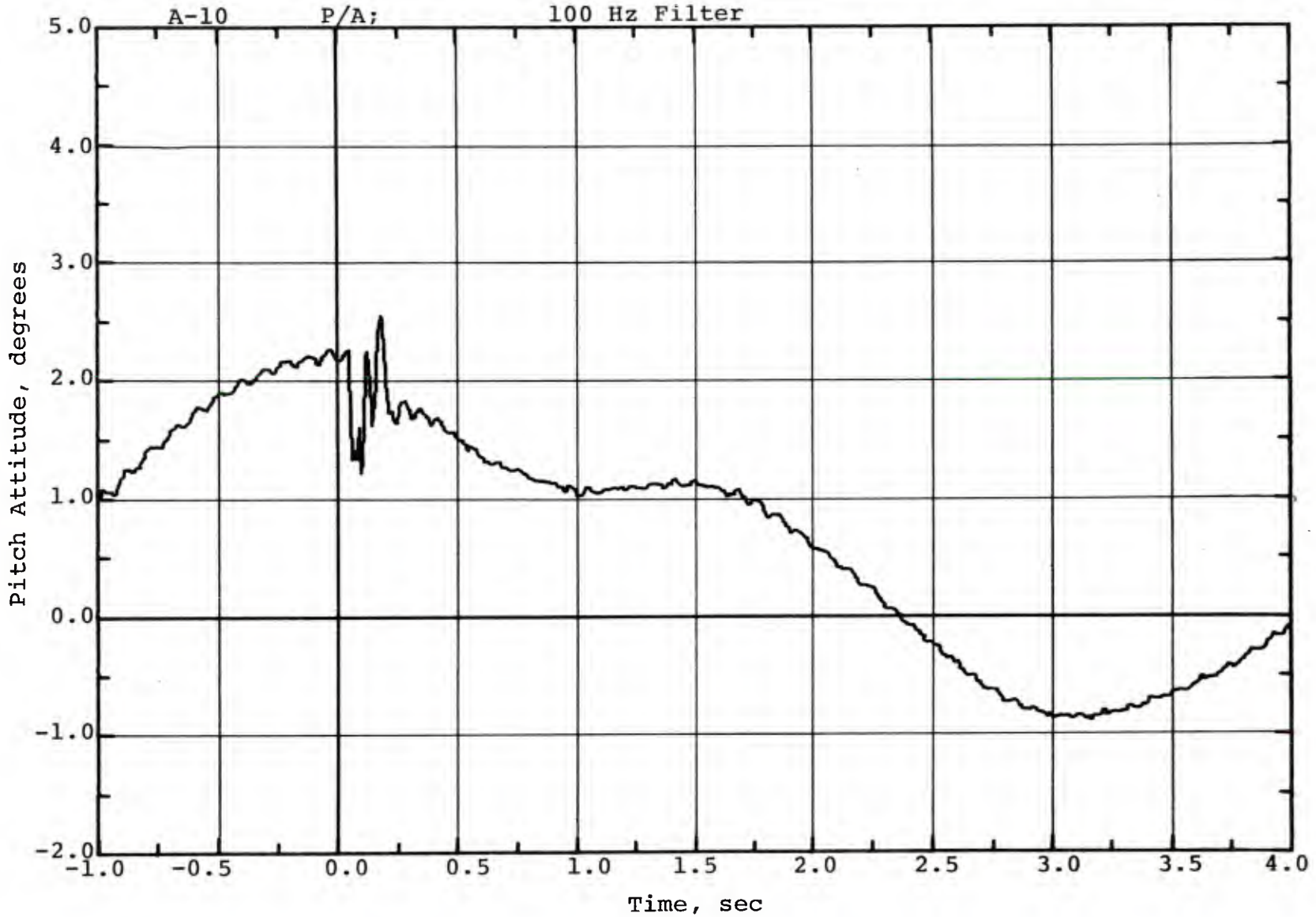

Figure 5.11a. Time-Variation of Pitch Attitude.
Channel A-10

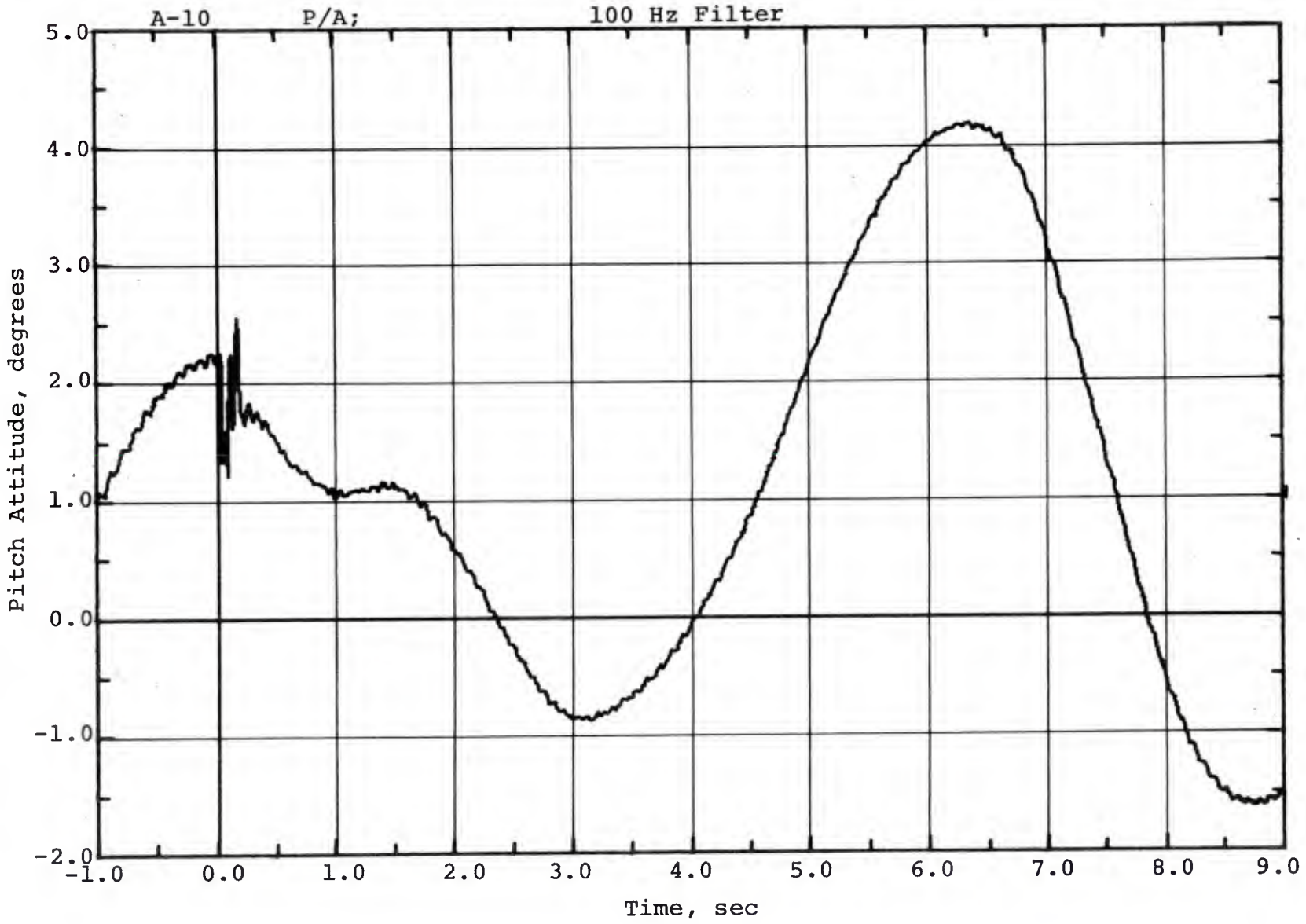

Figure 5.11b. Time-Variation of Pitch Attitude.
Channel A-10

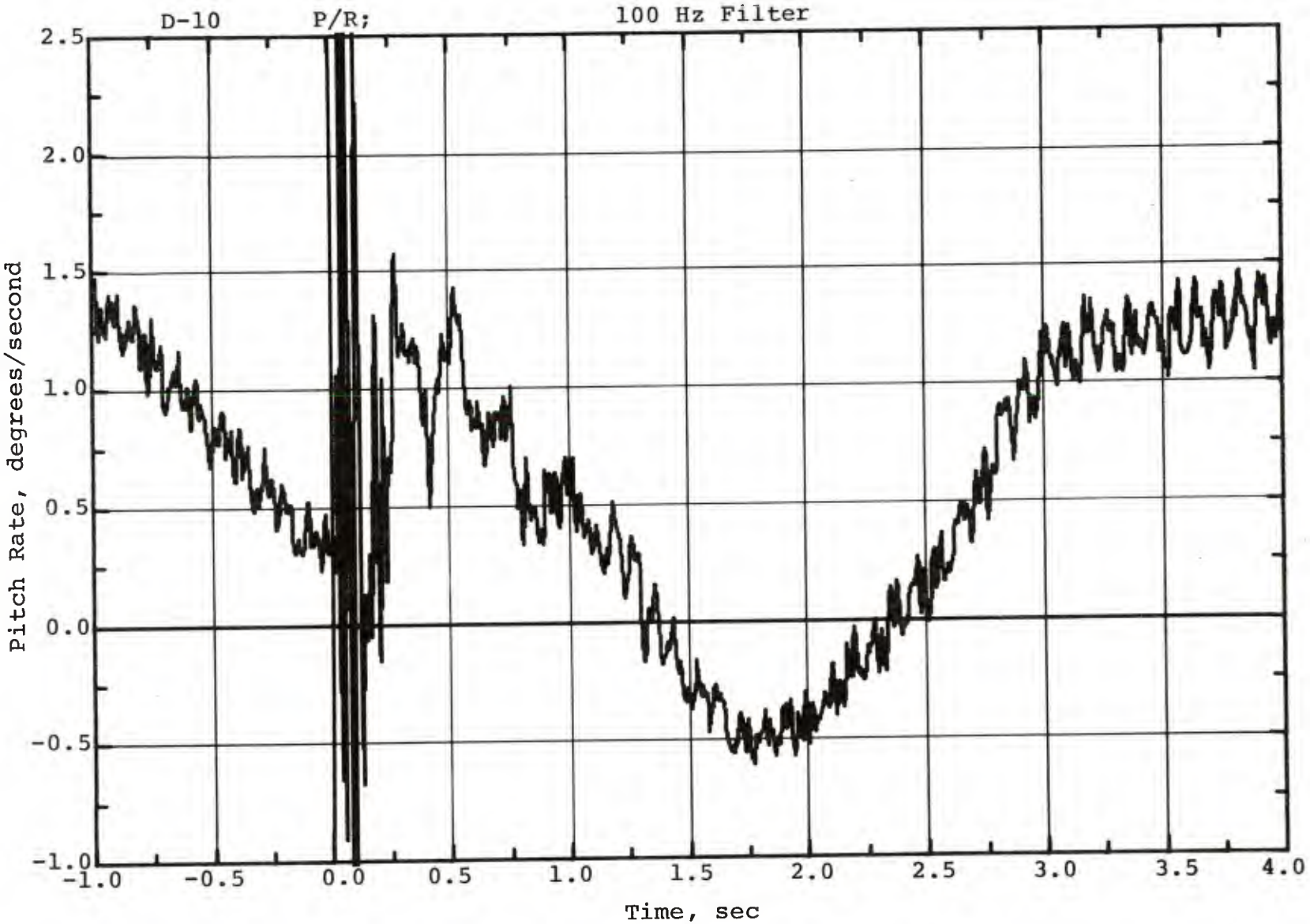

Figure 5.12. Time-Variation of Pitch Rate. Channel D-10

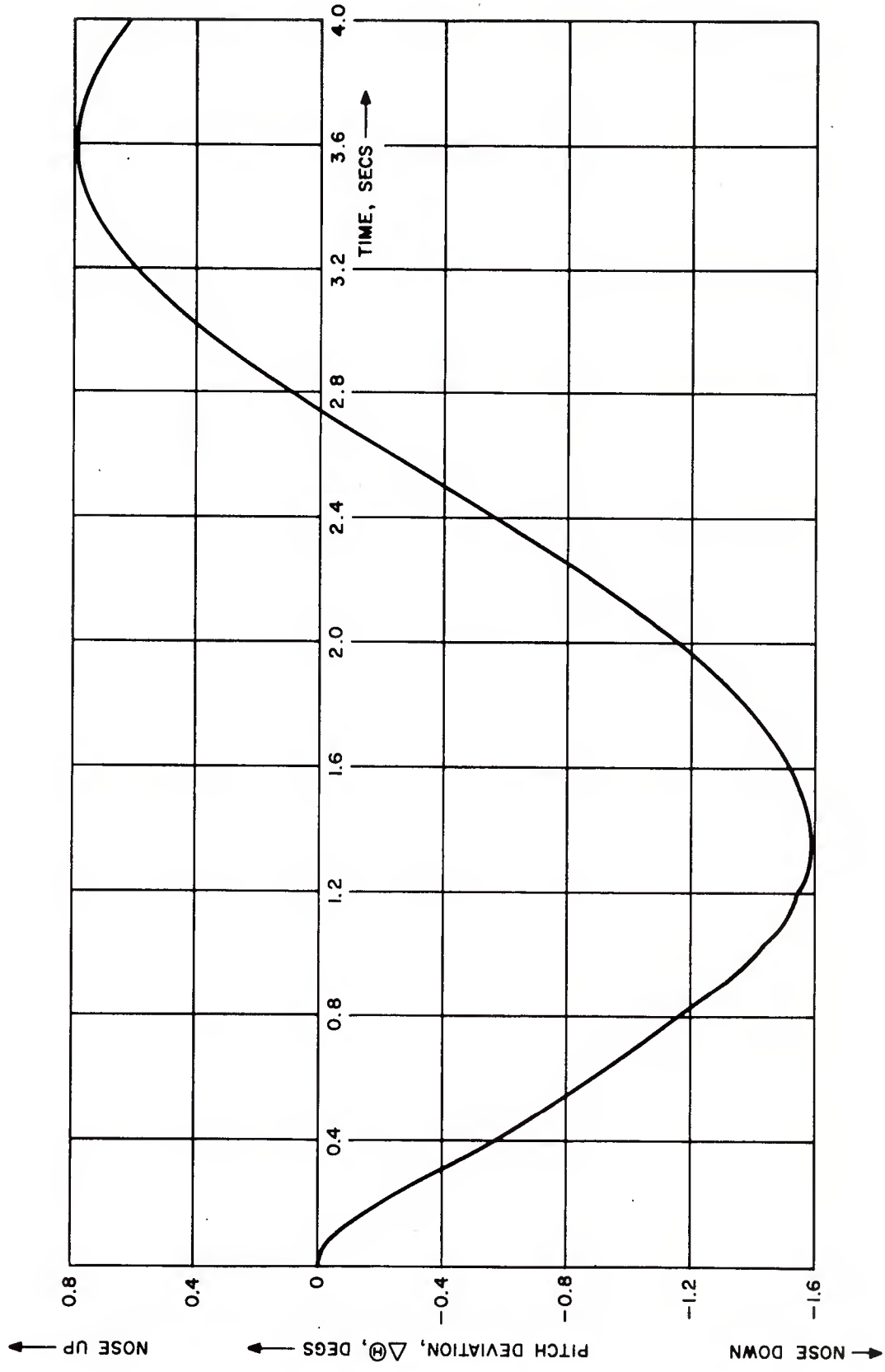

Figure 5.13. Time-Variation of Pitch Attitude Deviation. Analytical

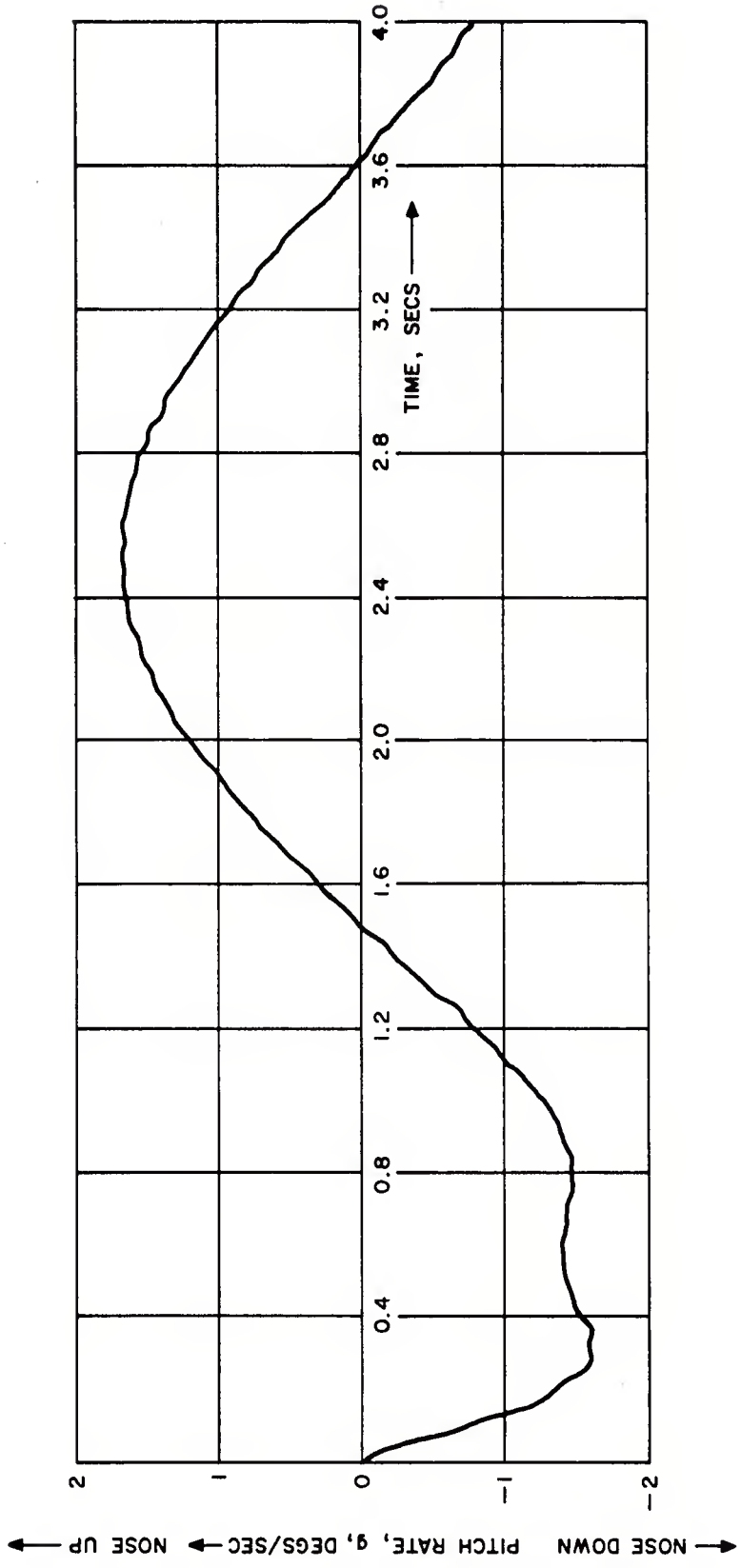

Figure 5.14. Time-Variation of Pitch Rate. Analytical

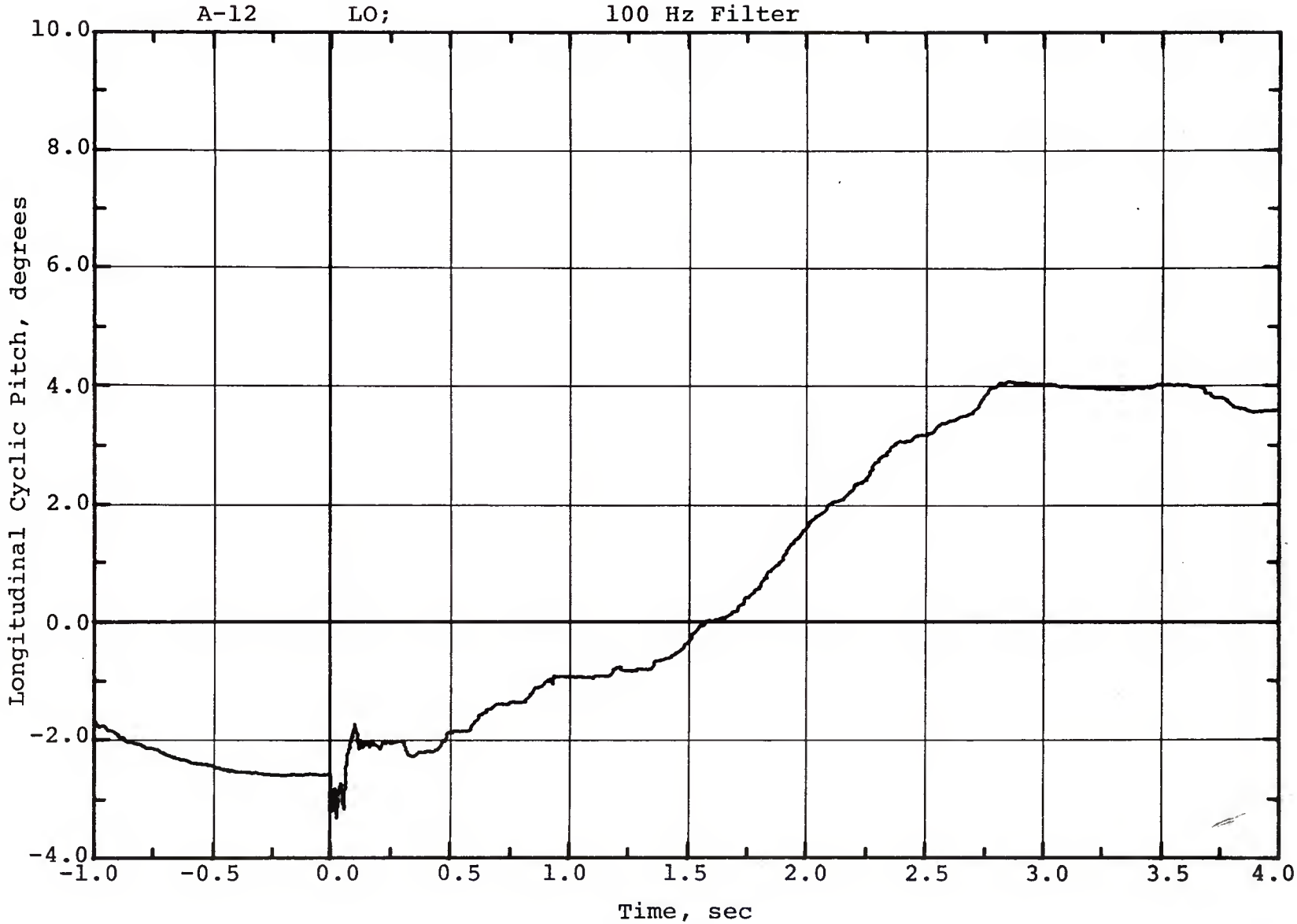

Figure 5.15. Time-Variation of Aircraft Fore-and-Aft Stick Deflection Interpreted as Time-Variation of Main Rotor Longitudinal Cyclic Pitch Angle. Channel A-12

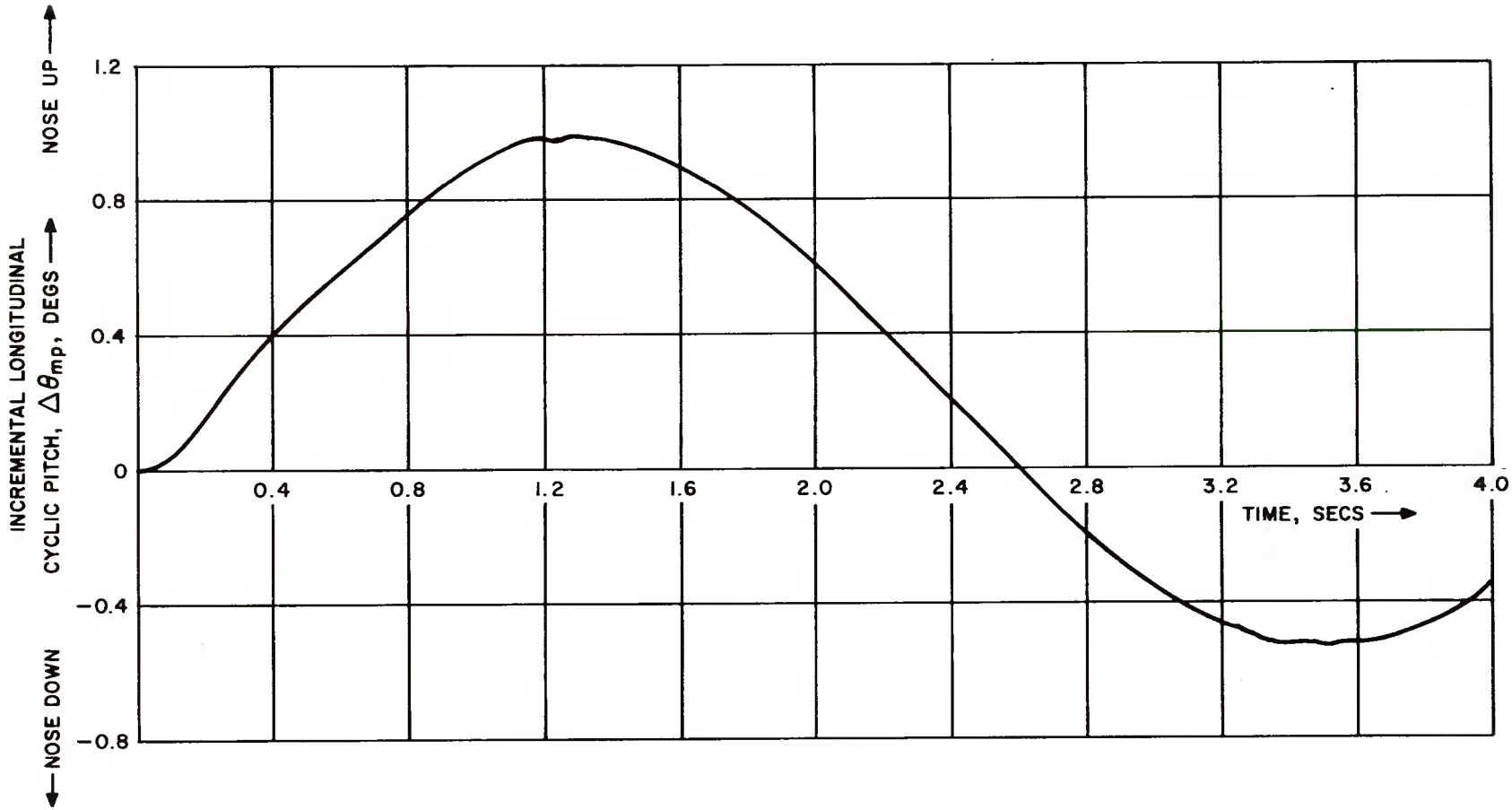

Figure 5.16. Time-Variation of Incremental Longitudinal Cyclic Pitch Due to Autopilot in Response to Blast. Analytical

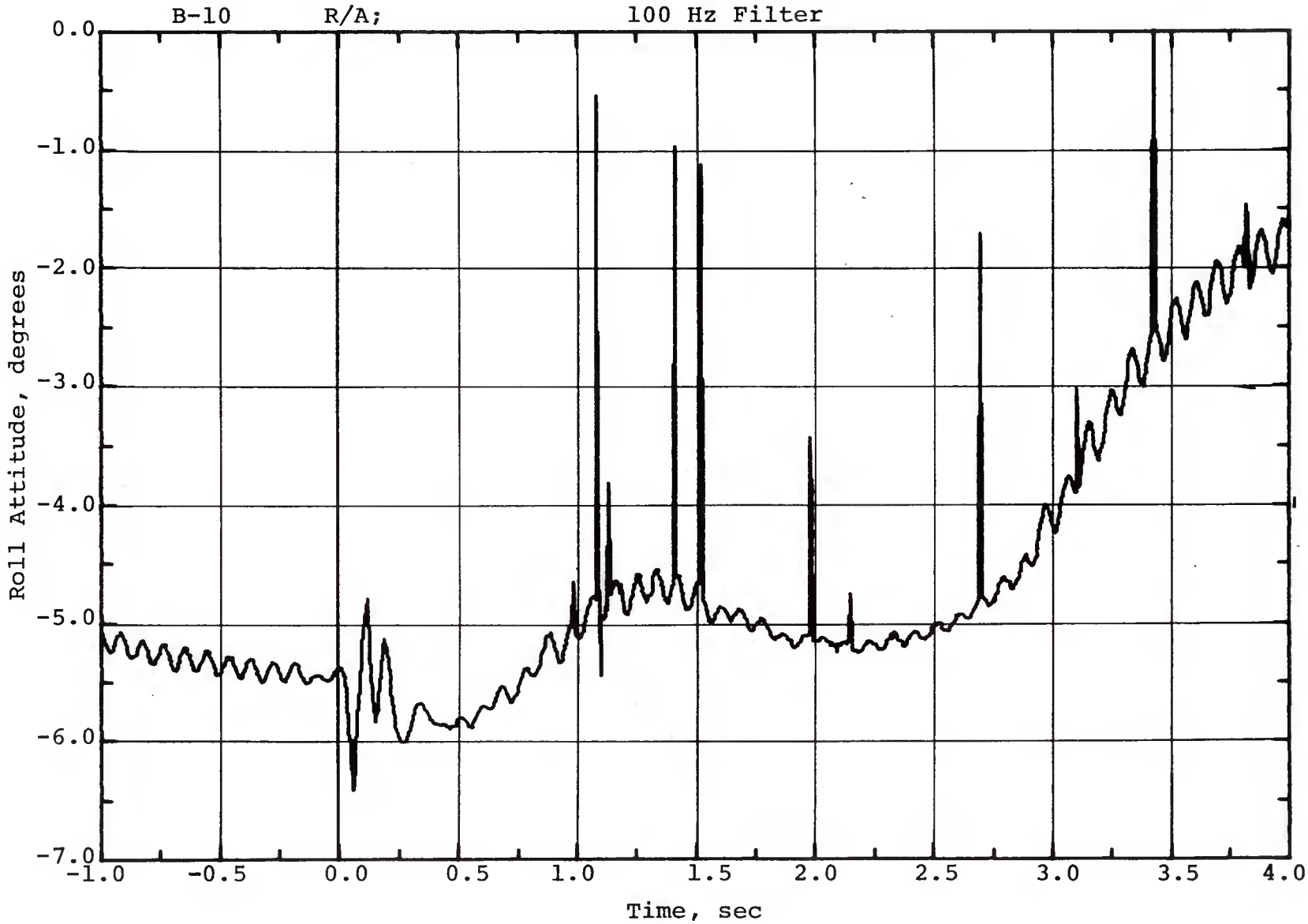

Figure 5.17a. Time-Variation of Roll Attitude.
Channel B-10

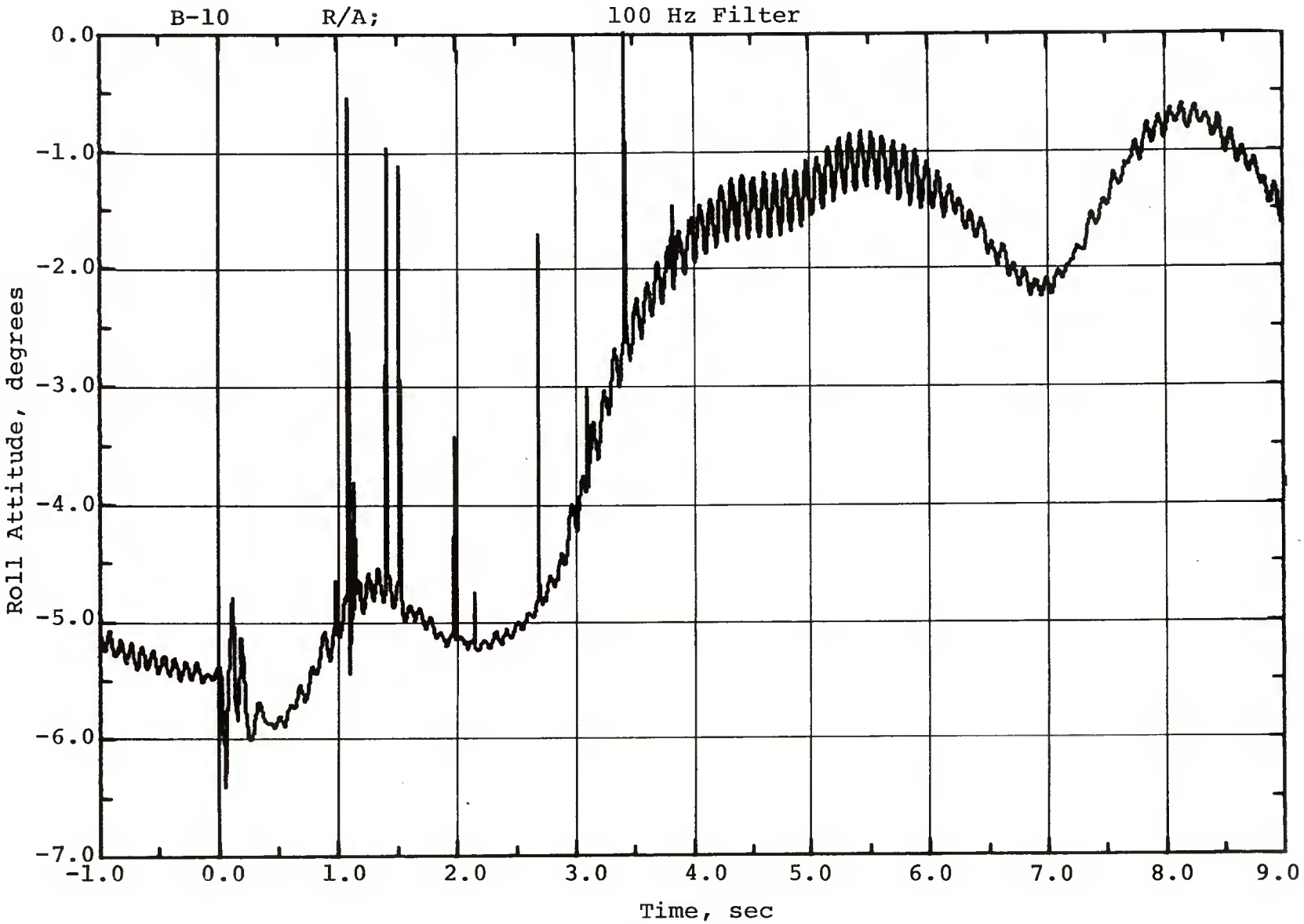

Figure 5.17b. Time-Variation of Roll Attitude. Channel B-10

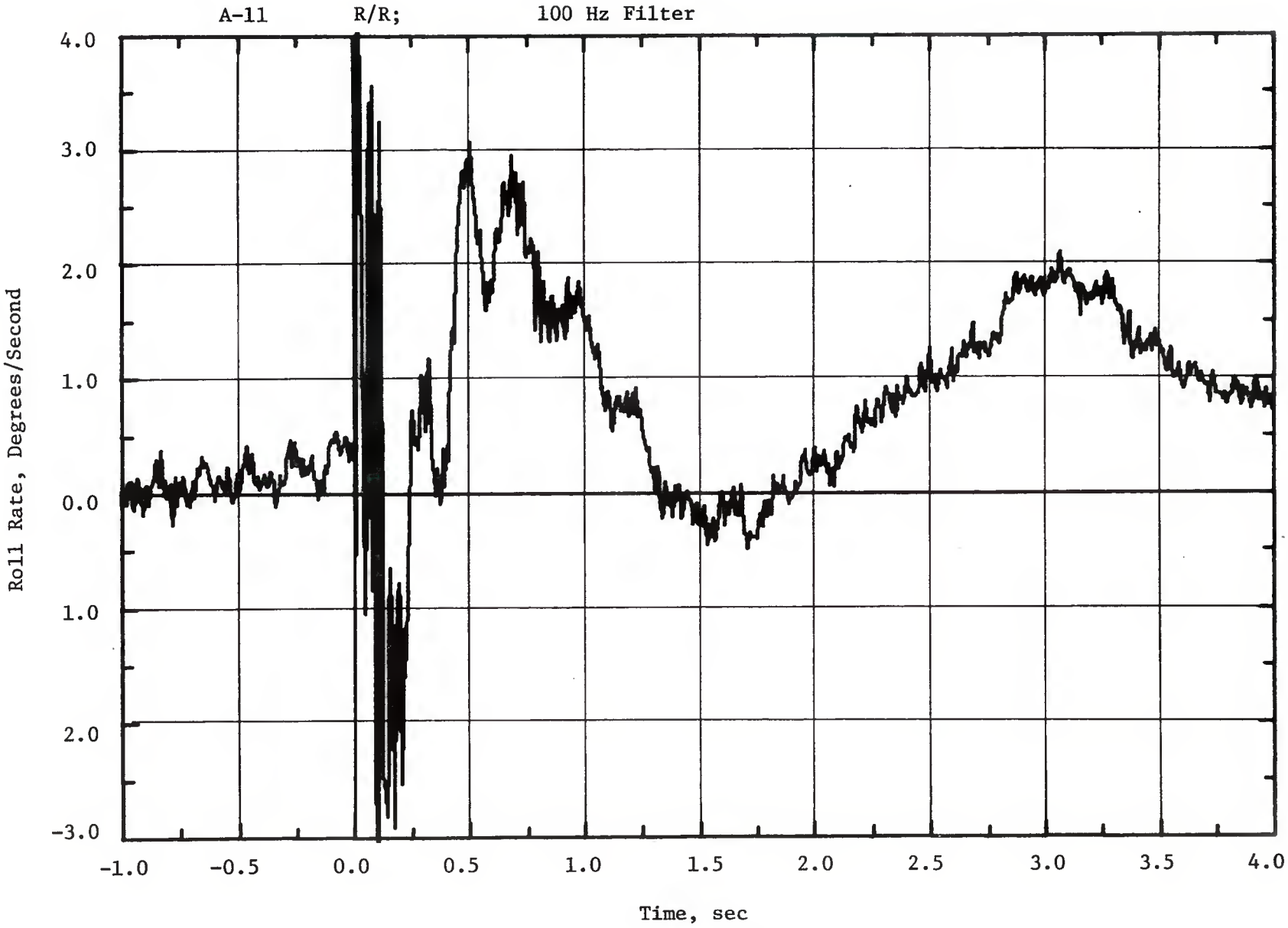

Figure 5.18. Time-Variation of Roll Rate.
Channel A-11

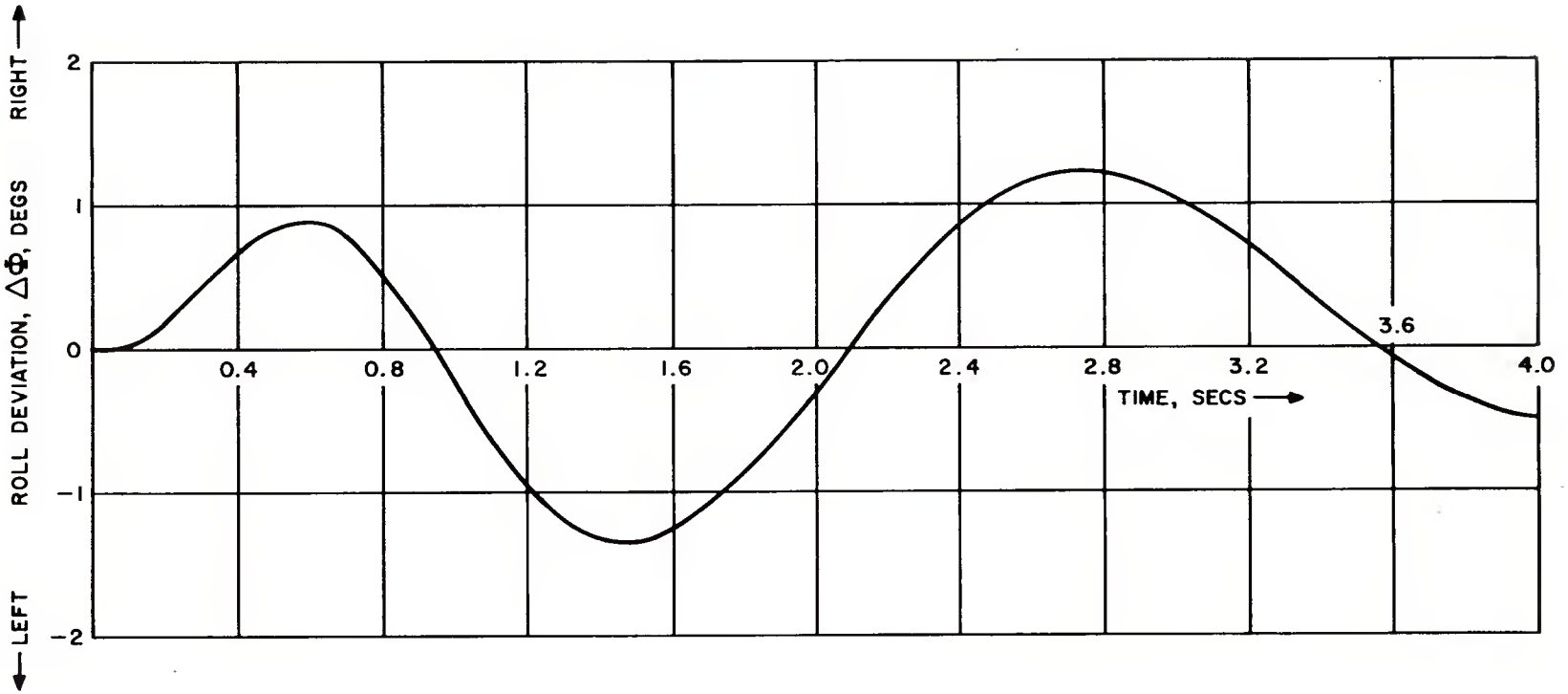

Figure 5.19. Time-Variation of Roll Attitude Deviation. Analytical

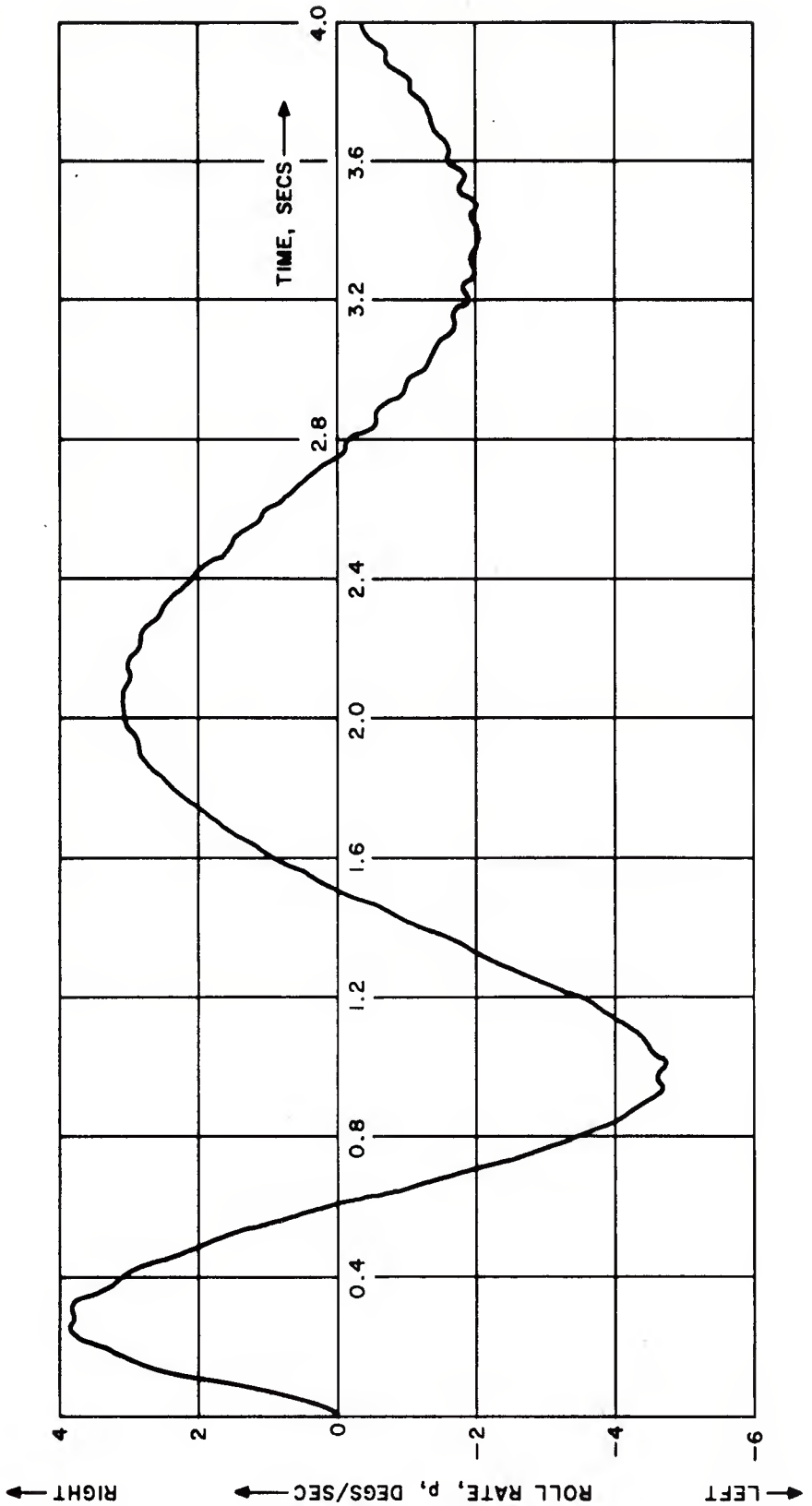

Figure 5.20. Time-Variation of Roll Rate. Analytical

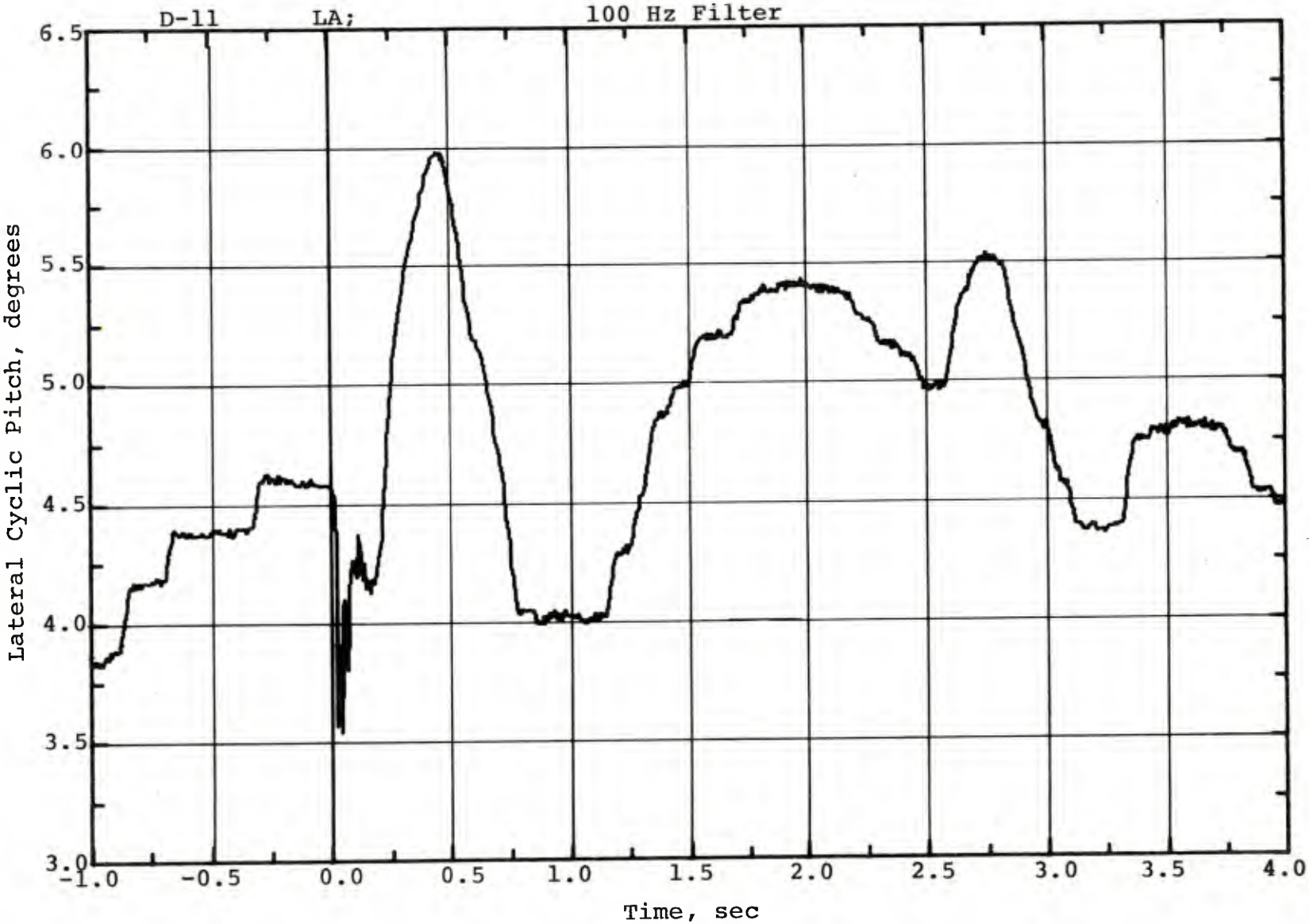

Figure 5.21. Time-Variation of Aircraft Lateral Stick Deflection Interpreted as Time-Variation of Main Rotor Lateral Cyclic Pitch Angle. Channel D-11

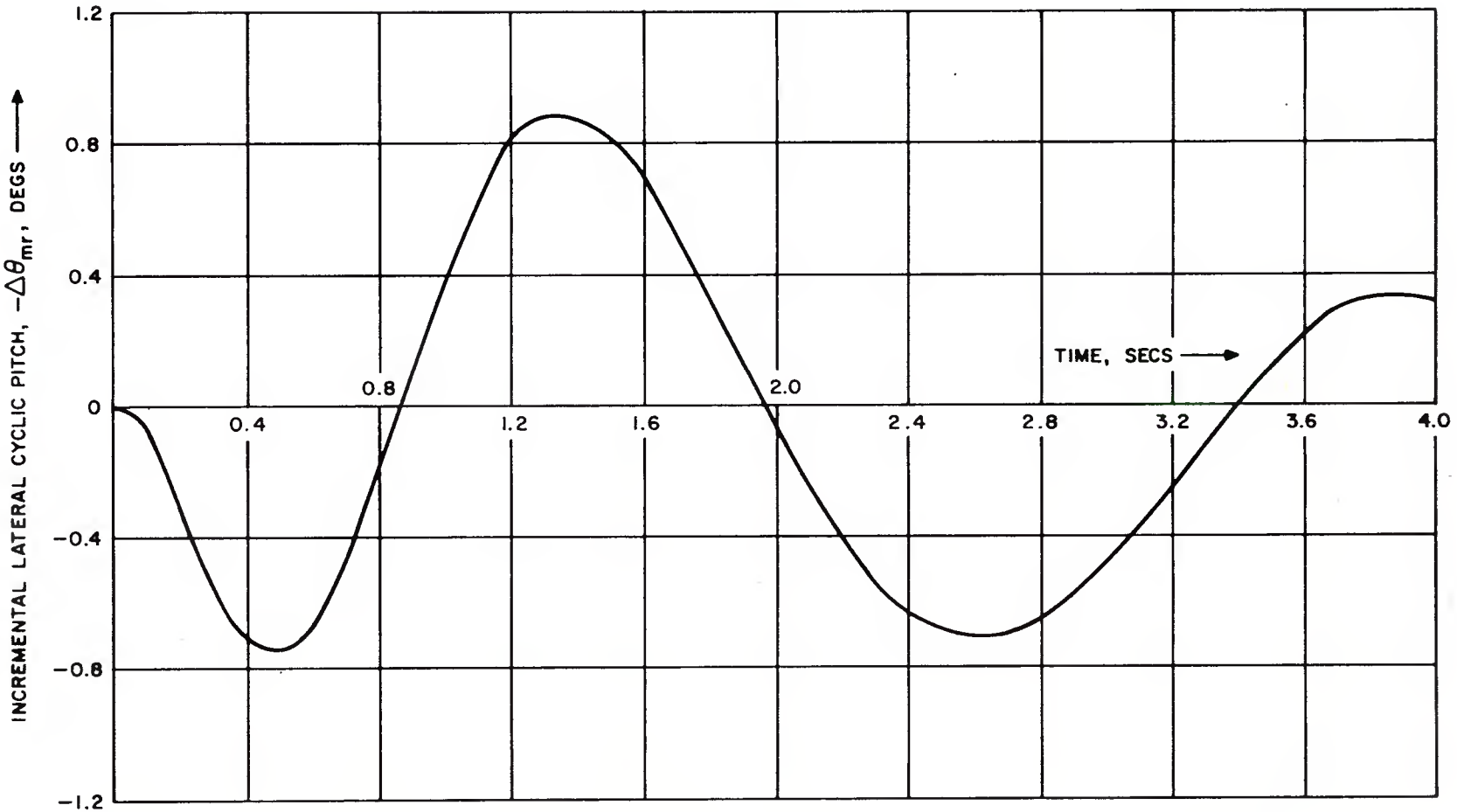

Figure 5.22. Time-Variation of Incremental Lateral Cyclic Pitch due to Autopilot in Response to Blast. Analytical

SECTION 6

FIN AND TAIL BOOM STRUCTURAL RESPONSES

This section presents the analytical procedures and the analytical-experimental correlations for the lateral bending moment responses of the fin-tail boom combination.

6.1 Some Remarks Pertaining to the Analysis

The fin and tail boom lateral bending moments were calculated in Reference 1 according to a simple single degree-of-freedom analysis. The assumptions of that approach are drastic and somewhat intuitive. The prediction for the peak lateral bending moment at fin station 46.5 correlated fairly well with experiment; but the other two peak lateral bending moments at tail boom stations 47 and 112 did not. With the availability of mass and structural data for the fin-tail boom combination, though scant, it was deemed worthwhile to develop and use a less restrictive and thus a more accurate procedure for the pre-test response predictions of Reference 2. The available mass and stiffness data are questionable. It is not known whether they include all the structural masses and whether they apply to the tested helicopter since a number of design changes and subsequent field modifications were made on some UH-1B's. The justifications for using the data are that they give roughly the correct fundamental side bending frequency and they are the only pertinent information available.

In Reference 2, three degrees-of-freedom were included and the calculations were carried out for the bending moments at several fin and tail boom stations to define the spanwise distributions of their peak values. In fact, the results indicated that these responses would exceed substantially the static yield allowables and thus would present a critical situation. In the analysis presented below, the following further improvements were made.

1. The lumped mass and stiffness modelings were revised slightly, except for the tail boom torsional stiffnesses. The latter were estimated separately from tail boom cross-sectional geometries at several stations. Their levels turned out to be half as much as those in Reference 2, primarily because it was found that the tail boom panels were made of magnesium rather than aluminum. Figure 6.1 may be compared with the corresponding Figure 2 of Reference 2 to identify these changes.

2. More accurate representations of the blast loading time-variations (i.e., the forcing functions) were effected.

3. Four elastic modes were included instead of three. And to accommodate the highest frequencies, a special integration routine was devised, precluding the necessity of very short time steps in the computations.

4. The tail boom torsional moments were also calculated. Although torsional moments were not measured, a knowledge as to their magnitudes is helpful in subsequent correlation discussions.

6.2 Details of the Analyses

As seen in Figure 6.1, the tail section is represented by seven lumped masses connected by beam elements, with each beam element having a constant EI (side-bending stiffness) and a constant GJ (torsional stiffness). (e_i and g_i represent EI and GJ divided by 10^8, respectively.) Masses m_5 and m_6 being off the tail boom axis induce torsional deflections of the boom, which in turn contribute to the lateral (side) deflections of mass points 5 and 6. The fin torsion is ignored by placing masses m_5 and m_6 on the fin elastic axis. The rotor attachment point is assumed to be at mass point 6, although in the actual craft it is slightly above and ahead of that point.

Based on this structural model, the influence coefficients (C_{ij}) were computed. Here, C_{ij} represents the lateral deflection at point i due to a unit force at point j. The frequencies and mode shapes may be obtained from the well-known matrix equation

$$[C]\ [\nwarrow M \nearrow]\ \{\phi\} = \frac{1}{\omega^2}\ \{\phi\}$$

where

[C] is the square symmetric influence coefficient matrix,

$[\nwarrow M \nearrow]$ is the square diagonal mass matrix,

ω is the circular frequency, i.e., in rad/sec., and

ϕ is the mode shape.

The solution to this equation is obtained by exercising the MSF subroutine (the mode shape and frequency subroutine), an in-house program based on Turner's matrix iteration procedure (e.g., see Reference 6). The results from the MSF calculations are shown in Table 6.1. If one assumes that the response is primarily from the first four modes, the lateral (side) deflection of any point i, w_i, is given approximately by

$$w_i(t) = \sum_{r=1}^{4} q_r(t)\phi_i^{(r)}$$

where for the r-th mode (r=1,...,4)

$q_r(t)$ is the generalized coordinate, and

$\phi_i^{(r)}$ is the modal deflection at point i.

The excitation forces at the mass points i, $F_i(t)$, have contributions from three sources:

$$F_i(t) = F_i^{(tr)}(t) + F_i^{(a)}(t) + F_i^{(d)}(t)$$

The components are:

(a) The blast-induced force from the tail rotor, $F_i^{(tr)}(t)$. This may be assumed to be concentrated at mass point 6, i.e.,

$F_i^{(tr)}(t)$ = Rotor force in the direction of deflection, y,

$= F_6^{(tr)}(t)$, for i = 6

$F_i^{(tr)}(t) = 0$, if $i \neq 6$

(b) The inertia forces on the masses, $F_i^{(a)}(t)$, due to their accelerations which arise from the rigid-body motions of the helicopter. (The inertia forces due to elastic mode accelerations are already included in the left-hand sides of the dynamical equations to be presented.) Thus,

$$F_i^{(a)}(t) = - a_{y,i}(t) m_i \qquad (i=1,\ldots 7)$$

where $a_{y,i}$ is the rigid-body acceleration in the lateral direction at point i. Since the roll and pitch angles are small, it can be shown from the helicopter rigid-body dynamics that

$$a_{y,i} = \dot{V}_t - \frac{1}{12} x_i \dot{r} + \frac{1}{12} \tilde{z}_i \dot{p}$$

where

the acceleration $a_{y,i}$ is in ft/sec^2,

$\dot{V}_y$ is the rate of change of the instantaneous y-component (V_y) of the vehicle c.g. velocity and is in ft/sec^2,

$\tilde{x}_i$, $\tilde{z}_i$ are the x- and z-coordinates from the vehicle c.g. to the mass point i, in inches, and

$\dot{r}$, $\dot{p}$ are the rates of change of the yaw and roll rates, respectively, in rad/sec^2.

(c) The distributed blast loads on the tail boom and the fin, which are replaced by equivalent concentrated loads $F_i^{(d)}(t)$ at mass points i.

The components $F_i^{(r)}(t)$, $F_i^{(a)}(t)$, and $F_i^{(d)}(t)$ are discussed in more detail later.

Since the four modes are orthogonal, i.e., they are inertially and elastically decoupled, the dynamical equations for the (assumed) cantilervered tail system may be written immediately: (See Reference 6)

$$\ddot{q}_r(t) + 2\zeta_r \omega_r \dot{q}_r(t) + \omega_r^2 q_r = \frac{1}{M_r} \sum_{i=1}^{7} F_i(t) \phi_i^{(r)} \equiv S_r(t)$$

where for each mode r (r=1,...4)

ζ_r is the damping ratio (assumed = 0.05 in the calculations), and

M_r is the generalized mass, $M_r = \sum_{i=1}^{7} m_i[\phi_i^{(r)}]^2$.

The above four independent equations, treated as single second-order linear differential equations, were integrated using a specially devised numerical procedure to yield the generalized coordinates, $q_r(t)$. The bending moment at any fin station (η) and the bending and torsional moments at any tail boom station (ξ) are calculated by the so-called "force summation" method after each time step of the numerical integration. Let ℓ_6 be the distance between points i=5 and i=6 which are on the fin. The η-coordinates of points 5 and 6 are then $\eta_5=\ell_6$ and $\eta_6=0$.

Define

$$\delta_{\eta i} = \eta - \eta_i \qquad \text{if } \eta > \eta_i$$

$$= 0 \qquad \text{if } \eta \leq \eta_i$$

and

$$\delta_{xi} = x_i - x \qquad \text{if } x_i > x$$

$$= 0 \qquad \text{if } x_i \leq x$$

Then the fin and tail boom lateral bending moments, FBM(η,t) and TBM (x,t), are given simply by:

$$\text{FBM}(\eta,t) = \delta_{\eta 6}\, T_{ss} + \sum_{i=5}^{6} \delta_{\eta i}\, V_i(t)$$

$$\text{TBM}(x,t) = \delta_{x6}\, T_{ss} + \sum_{i=1}^{7} \delta_{xi}\, V_i(t)$$

where T_{ss} is the constant pre-blast tail rotor force and

$$V_i(t) = F_i(t) - m_i \sum_{r=1}^{4} \phi_i^{(r)} \left\{ S_r(t) - \omega_r{}^2 q_r(t) \right\}$$

The terms with summations over i are the contributions from the blast, while $\delta_{\eta 6}\ T_{ss}$ and $\delta_{x6}\ T_{ss}$ represent the constant pre-blast bending moments. Similarly, for the tail boom torsional moment, TTM(x,t),

$$TTM(x,t) = z_6\ T_{ss} + \sum_{i=5}^{6} z_i\ V_i(t)$$

Returning to the components which make up the total excitation force system, consider first the major contribution $F_i^{(tr)}(t)=F_6^{(tr)}(t)$ for i=6 and $F_i^{(tr)}(t)=0$ for $i\neq 6$. This is the incremental force exerted by the tail rotor on the fin-tail boom combination. Its time-variation is available from the HELP code printouts. Two alternatives are available: use the result from the MODEOP=1 analysis or the result from the MODEOP=4 analysis. With MODEOP=1, the tail rotor blade elastic degrees of freedom are neglected, with the consequence that $F_6^{(tr)}(tr)$ is relatively "smooth". With MODEOP=4, in contrast, the vehicle rigid-body motion effects are neglected, but the $F_6^{(tr)}(t)$ results show oscillations reflecting the effects of the blade elastic deformations. The frequency contents of these oscillations are related to those in the tail rotor blade bending moments presented in Section 4. When filtered to remove its "high frequency" contents, the MODEOP=4 results for $F_6^{(tr)}(t)$ are reasonably close to those from MODEOP=1.

The MODEOP=1 result for $F_6^{(tr)}(t)$, shown in Figure 6.2, was used in the calculations for the correlation study, primarily because $F_6^{(tr)}(t)$ was available for a time period sufficiently long to cover three cycles of the predominant frequency of the fin-tail boom oscillations.

In contrast, MODEOP=4 was run for the period $0\leq t\leq$ 100 msecs, for reasons stated in Section 4. Thus with MODEOP=4 values for $F_6^{(tr)}(t)$, the analysis for the fin and tail boom responses would have been restricted to this shorter period which barely covers the first peak. Qualitatively, the latter analysis is expected to show larger excitations of the higher modes, due to the noted oscillations in $F_6^{(tr)}(t)$, and some differences in the local details of the predicted bending moment responses. Depending on the bending station, the amplitude and phasing of the response to these oscillations could be such that they could alter the predicted peak values <u>and</u> time of peak values as computed with the $F_6^{(tr)}(t)$ results from MODEOP=1.

Consider next the $F_i^{(a)}(t)$ component which was stated earlier to be

$$F_i^{(a)}(t) = -\ m_i \left\{ \dot{V}_y - \frac{1}{12}\ \tilde{x}\ \dot{r} + \frac{1}{12}\ \tilde{z}_i\ \dot{p} \right\}$$

The quantities $\dot{V}_y$, $\dot{r}$, and $\dot{p}$ are available from the MODEOP=1 printouts at 5 msec intervals. Being acceleration terms, they are largest for early times, i.e., during the first half of the overpressure positive phase duration. This component contributes significantly to the first peak values of the responses.

In the MODEOP=1 analysis, which gives the acceleration terms $\dot{V}_y$, $\dot{r}$, $\dot{p}$, the blast loads on the fuselage and the fin are computed on a quasi-steady basis neglecting the diffractive phase which is of very short duration, i.e., the blast aerodynamic forces are taken as "drag phase" forces. By drag phase forces it is implied that

$$F_i = S_i \, q(t) C_D$$

where S_i is the area of the i-th component normal to the shock velocity, C_D is a suitable steady-state drag coefficient, and $q(t)$ is the instantaneous dynamic pressure associated with the gust velocity (material velocity) at the surface. To be consistent, a similar approximate calculation is made for the third component of $F_i(t)$, which is $F_i^{(d)}(t)$. From the tail system geometry, the "side areas" of the boom and fin were split into seven areas; and the blast induced forces on the areas S_i were then assigned to the points i. C_D was taken equal to 0.35 for all areas, as in the HELP code, although a value as high as 0.85 may have been more appropriate for the fin segments. Thus, with $q_i(t)$ also available from the MODEOP=1 printouts, the components $F_i^{(d)}(t)$ were computed for the period of positive overpressure according to

$$F_i^{(d)}(t) = 0.35 \, S_i \, q(t)$$

For times beyond this period, $[F_i^{(d)}(t)]$'s are small and were set equal to zero.

6.3 Fin and Tail Boom Lateral Bending Moment Correlations

Figures 6.3-6.6 present the experimental time-variations of the lateral bending moments at fin station 32 (Channel D-07), fin station 52 (Channel A-09), tail boom station 47 (Channel B-07), and tail boom station 112 (Channel C-07).

The following behaviors may be noted in the figures:

(1) The average pre-blast levels are approximately:

9000 in-lbs for fin station 32,

11000 in-lbs for fin station 52,

55000 in-lbs for tail boom station 47, and

60000 in-lbs for tail boom station 112.

(2) In the D-07 and A-09 traces (fin stations), the responses show secondary oscillations near the major peaks which have periods of around 25-30 msecs and amplitudes of the order of 10% of the peak values. These oscillations, although lesser in magnitude, persist at later times. They are not present in a corresponding trace from PRE-MINE THROW IV for fin station 46.5. (See Figure 5.2 of Reference 1.) Also, the signal decays quite rapidly, indicating a high damping ratio. Compared with Figure 5.2 of Reference 1, the damping here appears much higher than for the helicopter used during PRE-MINE THROW IV. A further point worthy of note is that the fin bending responses (with the indicated secondary oscillations) peak at around t = 60 msecs.

(3) In contrast to the fin bending moment responses, the tail boom traces (B-07 and C-07) do not exhibit similar secondary oscillations with periods of around 25 msecs. Higher frequency components of lower amplitudes are present near the predominant peaks, amounting to a few percent of the total peak responses. When compared with the corresponding traces from the PRE-MINE THROW IV Test (Figures 5.3-5.4 of Reference 1), the shapes of the curves are somewhat different and the responses damp much faster. The minimum response (i.e., negative peaks) in B-07 and C-07 are not much below the pre-blast levels, whereas in Figures 5.3-5.4 of Reference 1, the blast-induced excursions in the negative direction are almost as large as those in the positive direction. No explanation can be offered for the differences in the responses from the DICE-THROW and PRE-MINE THROW IV tests. One may speculate the possibility that the structural properties (due to previous service) and perhaps even the mass properties of the fin-tail boom systems of the two helicopters were quite different.

(4) The calibration of the C-07 channel is suspect, because:
(i) The C-07 trace for tail boom station 112 gives higher pre-blast average value than the B-07 trace for station 47. See item (1) above. This should not be so. During pre-blast hover, the only force which imposes a bending moment on the tail boom is the essentially steady tail rotor thrust. The bending moment arm for station 112 is about 0.71 times the arm for station 47.

(ii) The first positive peak for station 112 exceeds the first positive peak for station 47. (Compare also Figures 5.3 and 5.4 from Reference 1.)

The calibration was checked to the extent possible at this time. No error was detected which could account for this inconsistency in the C-07 data.*

The time-variations of the predicted responses are shown in Figures 6.7-6.10. Also presented in Figure 6.11 is the corresponding variation in the total tail boom torsional moment. The latter applies to all tail boom station ahead of the fin-tail boom junction. Table 6.2 presents a summary of the comparisons between experimental and analytical results, including the pre-blast levels, the magniutude of the predominant peaks (i.e., the first positive peaks) and the times of occurrence of the same peaks. Finally, the spanwise distributions of the pre-blast and peak values are presented in Figures 6.12-6.13. Included in these plots are the experimental data from the four channels.

Figures 6.3-6.10 and Table 6.2 reveal the following:

(1) The ratio of the average pre-blast values from D-07 and A-09 is approximately 0.82. Since the only force (for $t<0$) which produces these bending moments is the tail rotor force located at fin station 0, the ratio should be $32/52 \cong 0.62$ The 0.82 ratio is close enough to its expected value of 0.62 considering (a) that it is difficult to read the average values from the traces due to the presence of some sizeable oscillations, and (b) possible slight drifts in one or both channels. The experimental values are somewhat lower than predicted, especially that from A-09.

(2) As stated earlier, there appear sizeable secondary oscillations with a period of about 25-30 msecs; and they are unaccounted for in the analysis inasmuch as the MODEOP=1 results for the $F_6^{(tr)}$ were used. If one filters these oscillations by "eyeballing" the peak values would be

*At this point, one could not check the possibility of having used the wrong calibration resistor during the field calibration sequences.

roughly 50,000 in-lbs (for D-07), 72,000 in-lbs (for A-09) and would occur at t = 65 msecs. The peak values would then be within 10% of the predictions; but the times to peak (65 msecs) would still be earlier than predicted (90 msecs). The experimental times for the first minima (182 msecs) are closer to the predicted times (193 msecs).

(3) The damping ratio used in the fin and tail boom analysis was 0.05 for all modes. It appears from all experimental results, and especially from the D-07 and A-09 traces, that the actual effective damping ratios must have been considerably higher than 0.05.

(4) By the same argument as in (1), the expected ratio of the average pre-blast value from C-07 to that from B-07 is around 0.71. But experiment shows this ratio to be almost 1.055. A difference of this magnitude cannot be attributed to reading errors or slight drifts in the channels. There are other reasons to believe that the C-07 calibration is in error.

(5) From the B-07 channel, the magnitude of the first positive peak (320,000 in-lbs) and its time of occurrence (95 msecs) agree reasonably well with the analytical values of 350,000 in-lbs. and t = 90 msecs. With ζ higher than 0.05, the predictions would have been even closer.

(6) As to the C-07 channel, the experimental peak value of 348,000 in-lbs is much higher than the predicted 242,500 in-lbs. (With the same channel in the PRE-MINE THROW IV, the analysis overestimated the response by a factor of over 2.) If one applies a factor of 0.71/1.055 (with the 0.71 and 1.055 values taken from item (4) above) to the experimental results of Figure 6.6, the resultant peak value would be around 234,000 in-lbs; and its predicted value of 242,500 in-lbs would be in much better agreement.

Before proceeding to the correlations of spanwise distributions of peak bending moments, a few words need be said about their allowables. Prior to the PRE-MINE THROW test, Bell Helicopter supplied a set of curves presenting the "allowable bending moments" versus tail boom and fin stations. These were taken to be as the anticipated failure loads, and they were used as such in Reference 2. (See pages 48-54 of Reference 2.) Conservatism in these allowable curves was suspected and pointed out in the cited reference. A recent communication with Bell Helicopter (22 Sept. 1976 and just before the DICE THROW test) confirmed this point. A new set of curves for the tail boom allowables was supplied.* The lateral bending moment allowable, M_z, was calculated assuming other parameters (M_x = torsional moment, M_y = vertical moment and the shears S_y, S_z) to be the same as in a yaw recovery with tail rotor

*No corresponding curves for the fin allowables are available.

thrust right. A reduction in one or more of these parameters would result in a higher lateral bending allowable. It was also indicated by Bell that the apparent mode of failure is crippling of the J-stringers due to combined loading (tension field analysis). The possible failure of the tail rotor drive shaft due to large tailboom deflections was not considered in this allowable. The new data reflects ultimate (anticipated failure) loads.

Briefly, the new allowables amount to the following:

(a) Allowable lateral bending: Linear variation between tail boom stations 40 and 200, with

$(BM)_{all}$ at sta 47 = 360,000 in-lbs

$(BM)_{all}$ at sta 112 = 244,000 in-lbs.

(b) Allowable torsional moment:

$(TM)_{all}$ at all tail boom stations = 73,000 in-lbs.

(c) Allowable shear in the lateral direction

$(S)_{all}$ = 1000 lbs to 1100 lbs between stations 47 and 112.

Although no full calculations were made for the shear S, a quick estimate indicates that the peak shear was around 1000 lbs. The peak torsion, as seen in Figure 6.11, is around 78,000 in-lbs, and thus close to the allowable 73,000 in-lbs. With the torsional moment and shear peaks being close to their allowables as defined above, the allowable lateral bending moment curve (also given above) is a reasonable "failure boundary". This boundary is shown in Figure 6.13.

The analytical boundary is just below the allowable boundary, indicating that the helicopter was "close" to failure. Movies, taken by the camera installed in the cabin and pointing aft, show the tail boom undergoing "large" torsional deflections. But the post-blast inspection of the vehicle revealed light tail boom damage consisting of: (a) Some opening (gap) at the tail boom - fuselage juncture on the blast side, (b) local damages in panels, and (c) slight wrinklings of frames.*

The experimental point for station 47 is about 10% below the boundary, while that for station 112 is above the boundary. This is another reason to suspect the data from the C-07 channel.

As to the spanwise distribution of the fin lateral bending moments, Figure 6.12, the analysis underestimates the measured levels by about 20% at station 32 and 8% at station 52. The major portions of the

*The vehicle sustained serious damage in other components: Cargo and side doors, engine cowling, overhead plexiglass window, etc...

differences are attributed to the neglect in the analysis of the high-frequency components of the tail rotor force resulting from the flexible motions of the rotor blades.

Discarding the suspected C-07 channel data, it is concluded from the above discussions that the fin and tail boom analysis gives reasonable estimates of the lateral bending moments. It is expected also that the predictions could be improved through the use of the MODEOP=4 outputs in lieu of the MODEOP=1 outputs for the time-variation of the tail rotor force.

TABLE 6.1

MODE SHAPES AND FREQUENCIES FOR THE FIN-TAIL BOOM COMBINATION

			Normalized Mode Shapes			
			First Mode	Second Mode	Third Mode	Fourth Mode
ω(rad/sec.) ω(Hz)			31.7 5.05	104.5 16.63	357.8 56.94	715.9 113.9
Mass Point i	x-Coord.*	z-Coord.*	$\phi_i^{(1)}$	$\phi_i^{(2)}$	$\phi_i^{(3)}$	$\phi_i^{(4)}$
i = 1	55.36	0.0	0.02579	0.08617	-0.29452	0.06817
i = 2	105.69	0.0	0.09414	0.28953	-0.71786	0.10051
i = 2	156.02	0.0	0.21124	0.57300	-0.70294	-0.04397
i = 4	205.8	0.0	0.38240	0.85021	0.19825	-0.29312
i = 5	226.19	17.41	0.53598	0.66541	0.53618	1.0
i = 6	266.97	52.24	1.0	-0.43452	-0.06769	-0.05199
i = 7	235.8	0.0	0.50094	1.0	1.0	-0.60455

*For x- and z- coordinates, see Figure 6.1
Tail structure assumed cantilevered at x=0.

TABLE 6.2 SUMMARY OF EXPERIMENTAL AND ANALYTICAL RESULTS

FOR THE FIN AND TAIL BOOM LATERAL BENDING MOMENTS

FIN	CHANNEL: D-07, STATION 32				CHANNEL: A-09, STATION 52			
	EXPERIMENT		ANALYSIS		EXPERIMENT		ANALYSIS	
	BM	t_p	BM	t_p	BM	t_p	BM	t_p
Average Pre-Blast	~9000	-	10250	-	~11000	-	16650	-
1st Pos. Peak (Largest)	58500	62	47000	90	83000	60	76200	90
1st Minimum	0	182	-7700	193	-2000	182	-13000	193
1st Pos. to 1st Minimum	-58500	-	-54700	-	-85000	-	-89200	-

TAIL BOOM	CHANNEL: B-07, STATION 47				CHANNEL: C-07, STATION 112			
	EXPERIMENT		ANALYSIS		EXPERIMENT		ANALYSIS	
	BM	t_p	BM	t_p	BM	t_p	BM	t_p
Average Pre-Blast	~55000	-	70200	-	~58000	-	49600	-
1st Pos. Peak (Largest)	320000	95	350000	90	348000	95	242500	90
1st Minimum	0	205	-105000	203	32000	200	-65000	203
1st Pos. to 1st Minimum	-320000	-	-455000	-	-316000	-	-307500	-

BM = Bending Moment, in-lbs

t_p = Time of Peak, msecs

~ Approximate Values, See Text

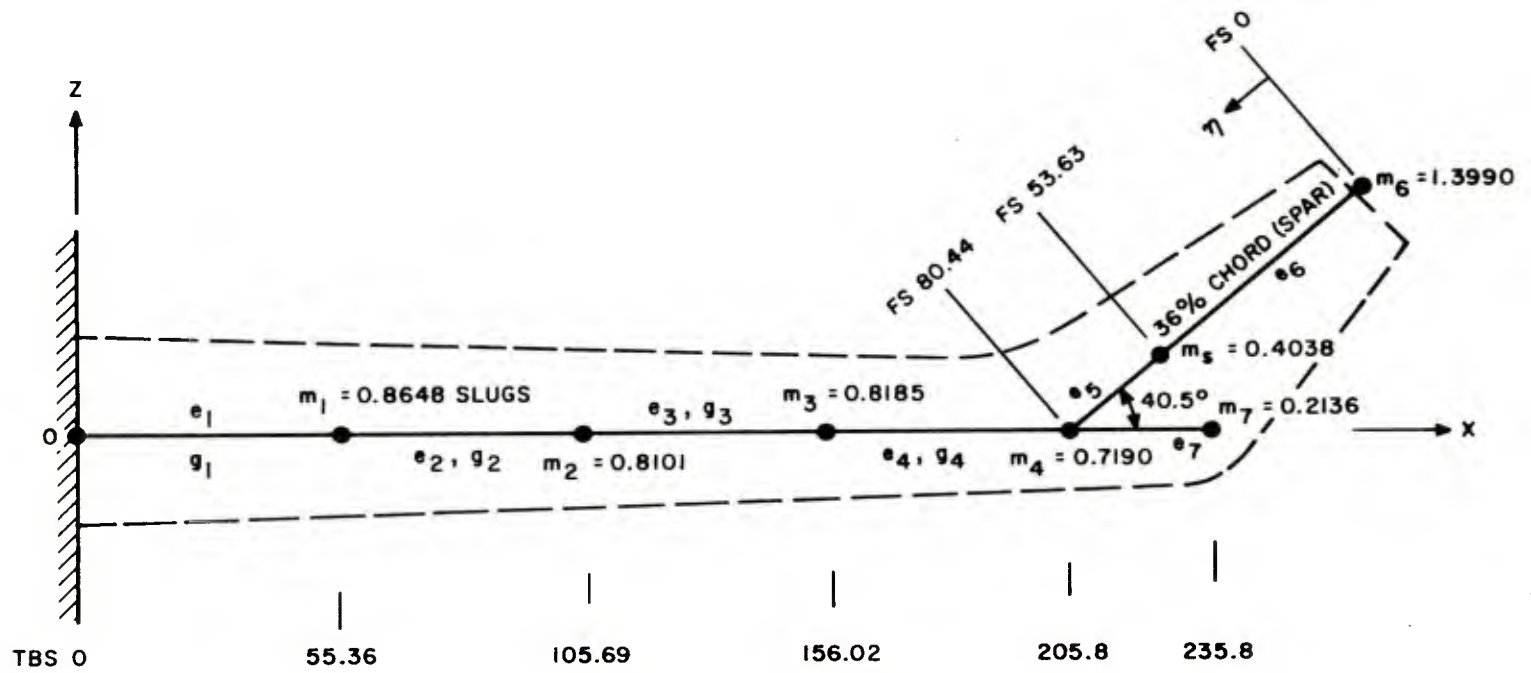

i →	1	2	3	4	5	6	7
$e_i = \frac{EI}{10^8}$, LB−IN^2, SIDE BENDING	24.81	17.08	10.18	5.21	2.19	0.455	3.38
$g_i = \frac{GJ}{10^8}$, LB−IN^2, TORSION	9.28	6.39	3.81	1.95	—	—	—

Figure 6.1. Mass and Structural Model for Fin-Tail Boom Combination

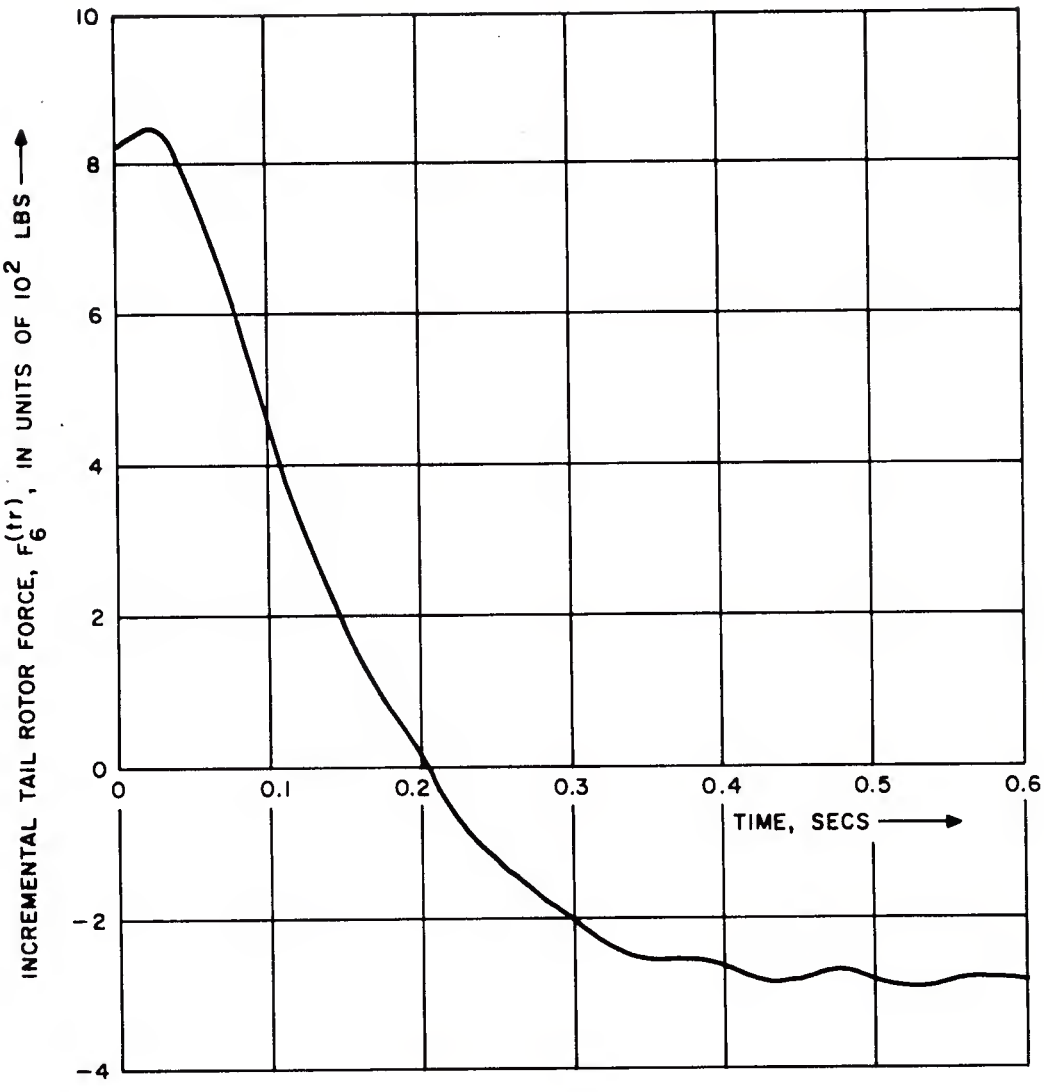

Figure 6.2. Time-Variation of Blast-Induced Tail Rotor Force. (From HELP Code, MODEOP=1.)

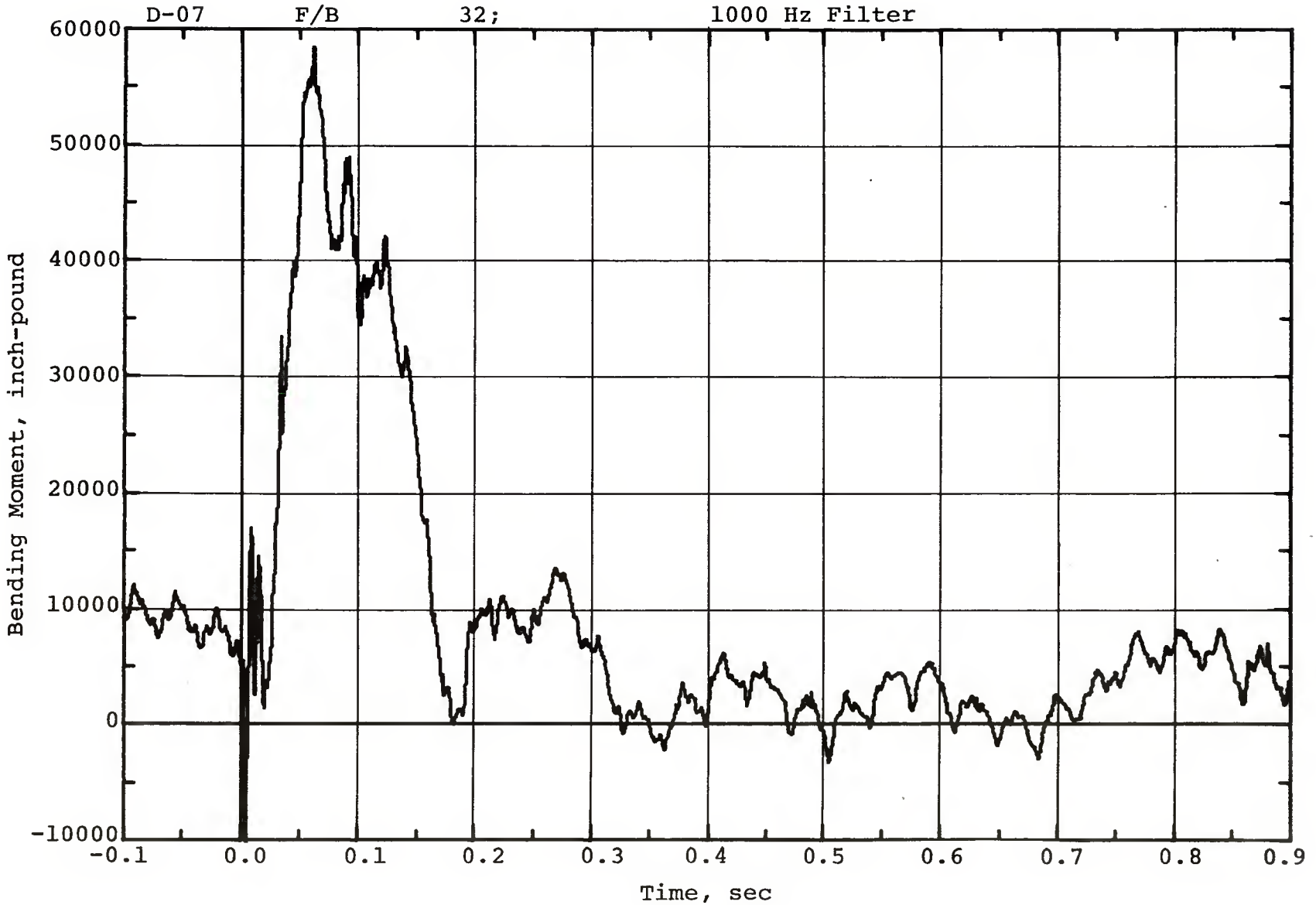

Figure 6.3. Time-Variation of Total Fin Lateral Bending Moment.
Fin Station 32. Channel D-07

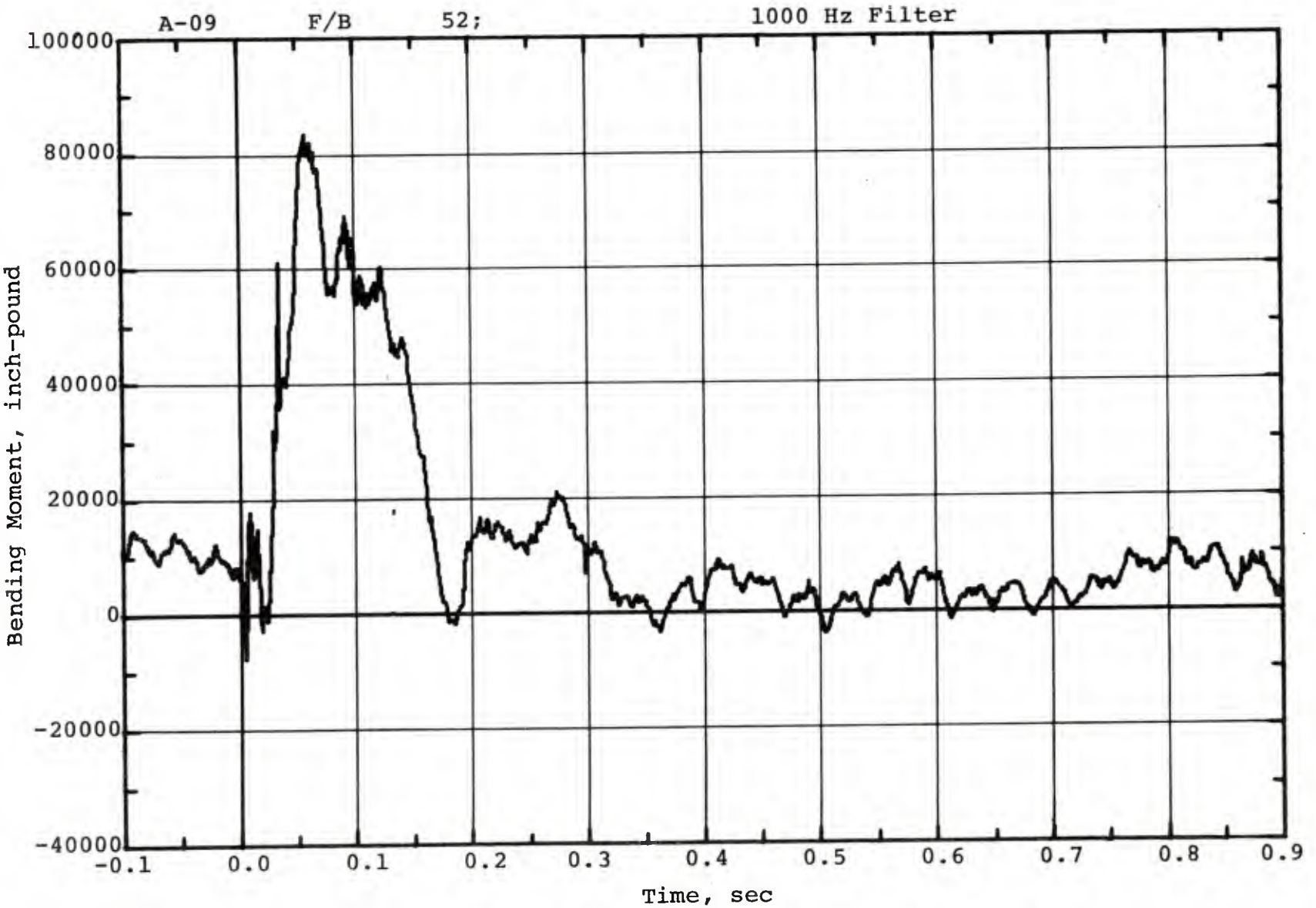

Figure 6.4. Time-Variation of Total Fin Lateral Bending Moment. Fin Station 52. Channel A-09

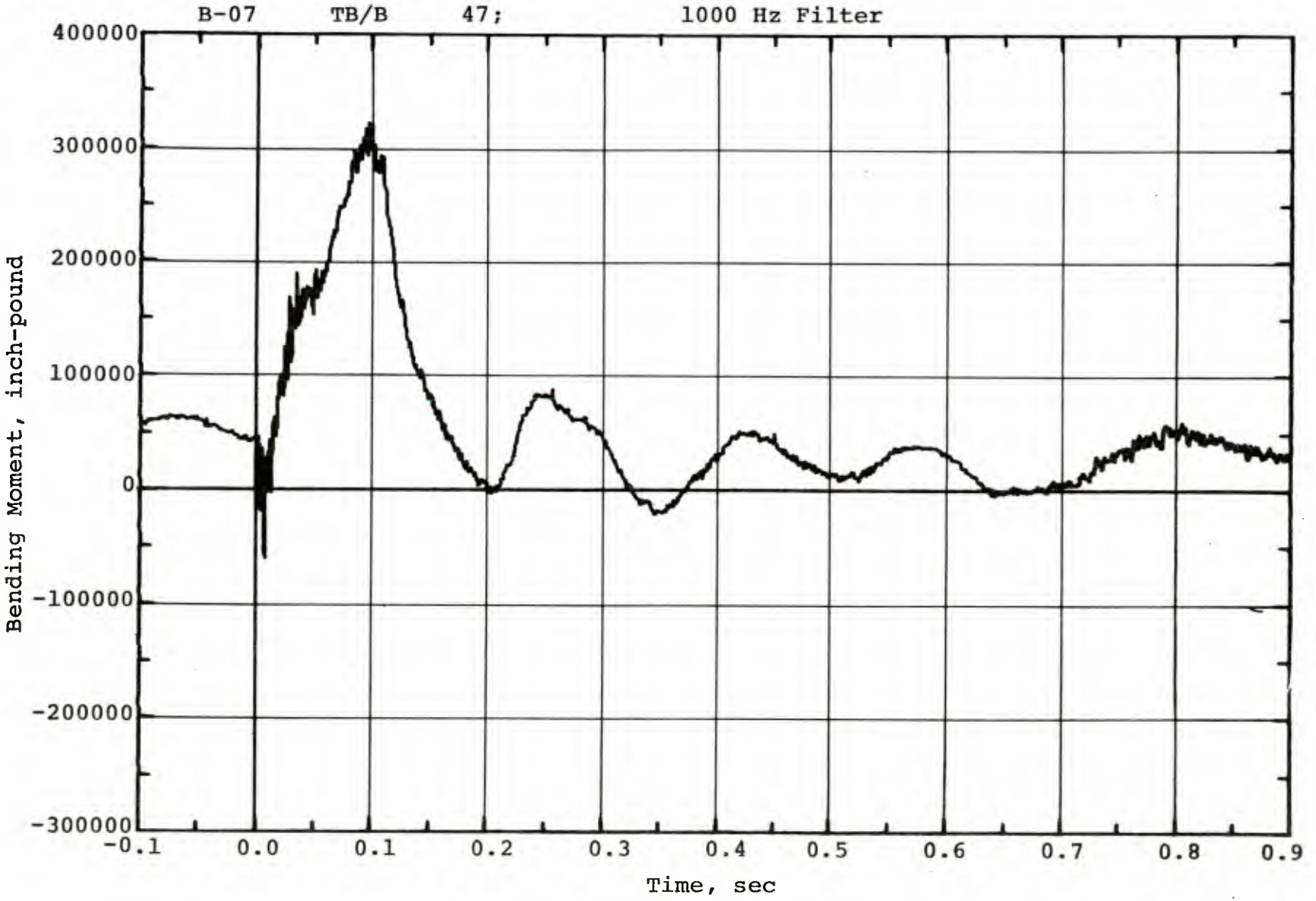

Figure 6.5. Time-Variation of Total Tail Boom Lateral Bending Moment. Tail Boom Station 47. Channel B-07

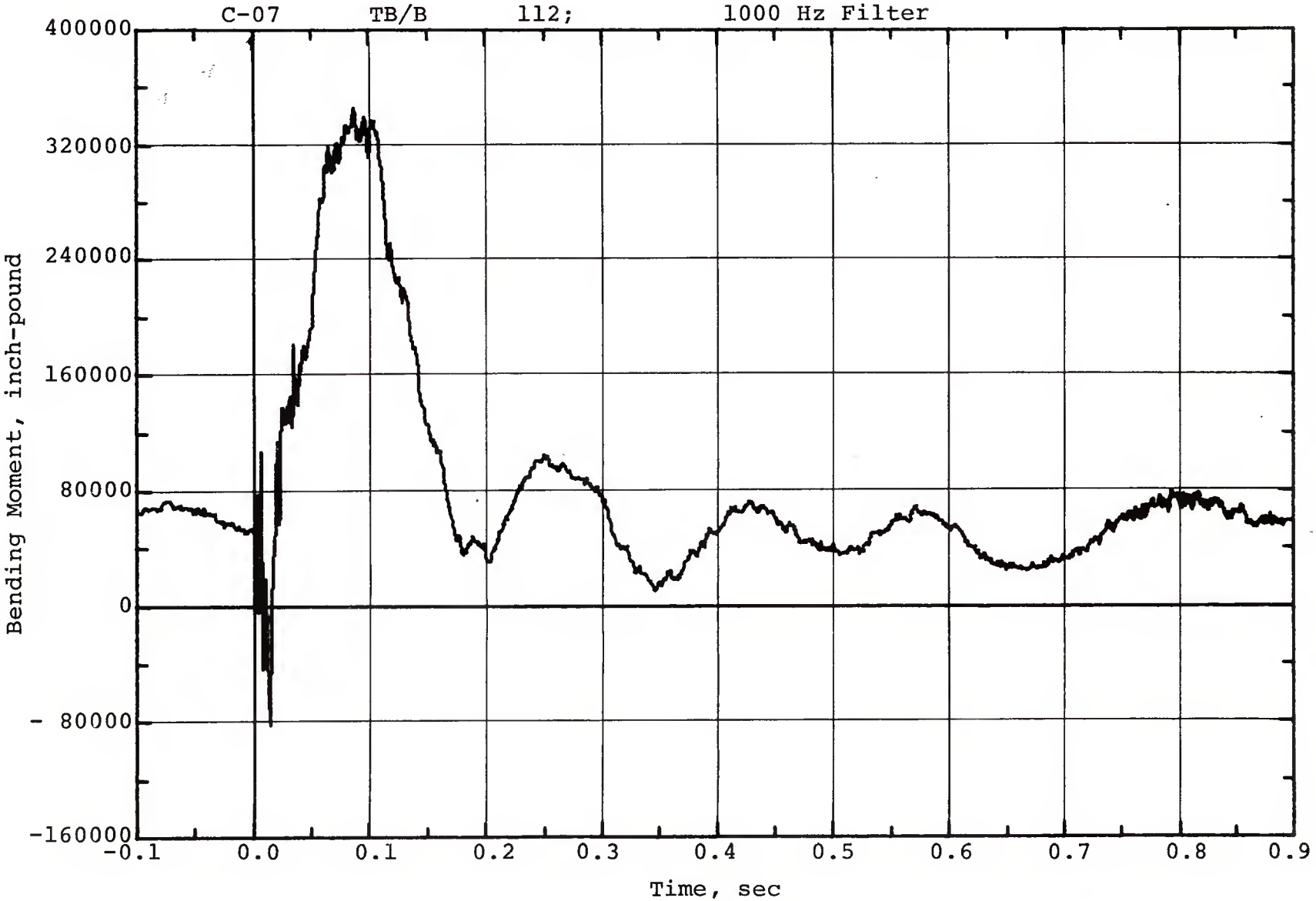

Figure 6.6. Time-Variation of Total Tail Boom Lateral Bending Moment. Tail Boom Station 112. Channel C-07

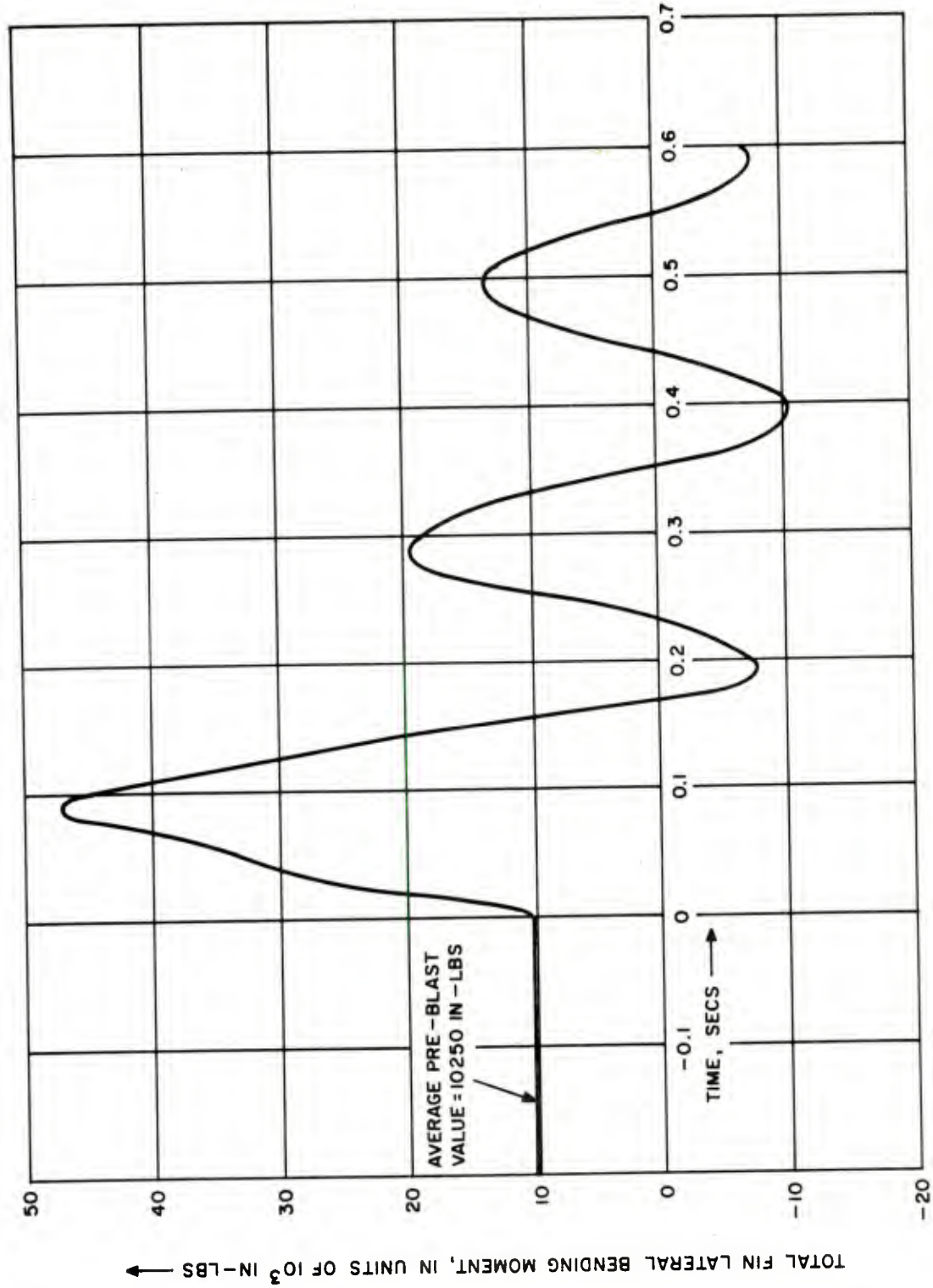

Figure 6.7. Time-Variation of Total Fin Lateral Bending Moment. Fin Station 32. Analytical

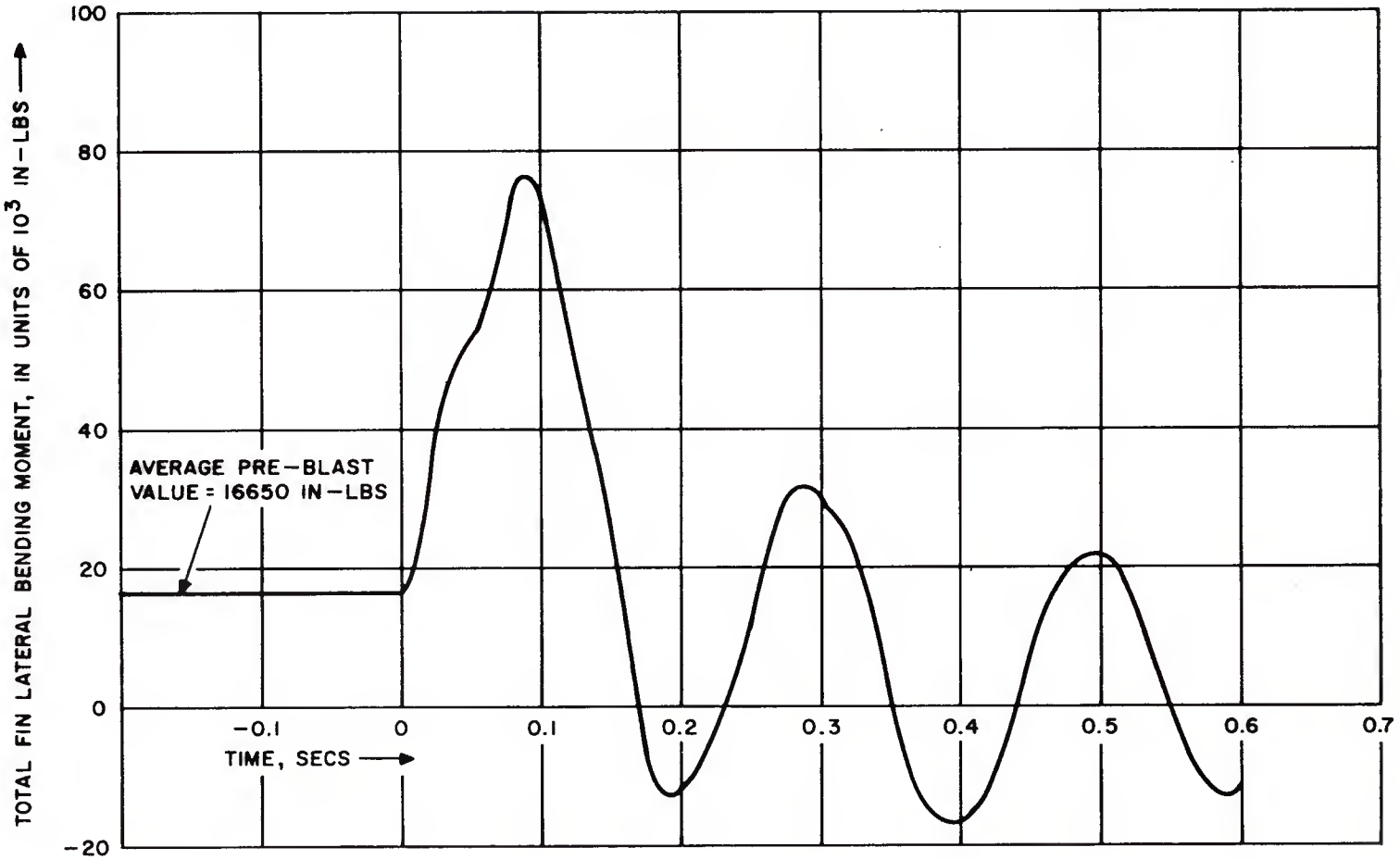

Figure 6.8. Time-Variation of Total Fin Lateral Bending Moment.
Fin Station 52. Analytical

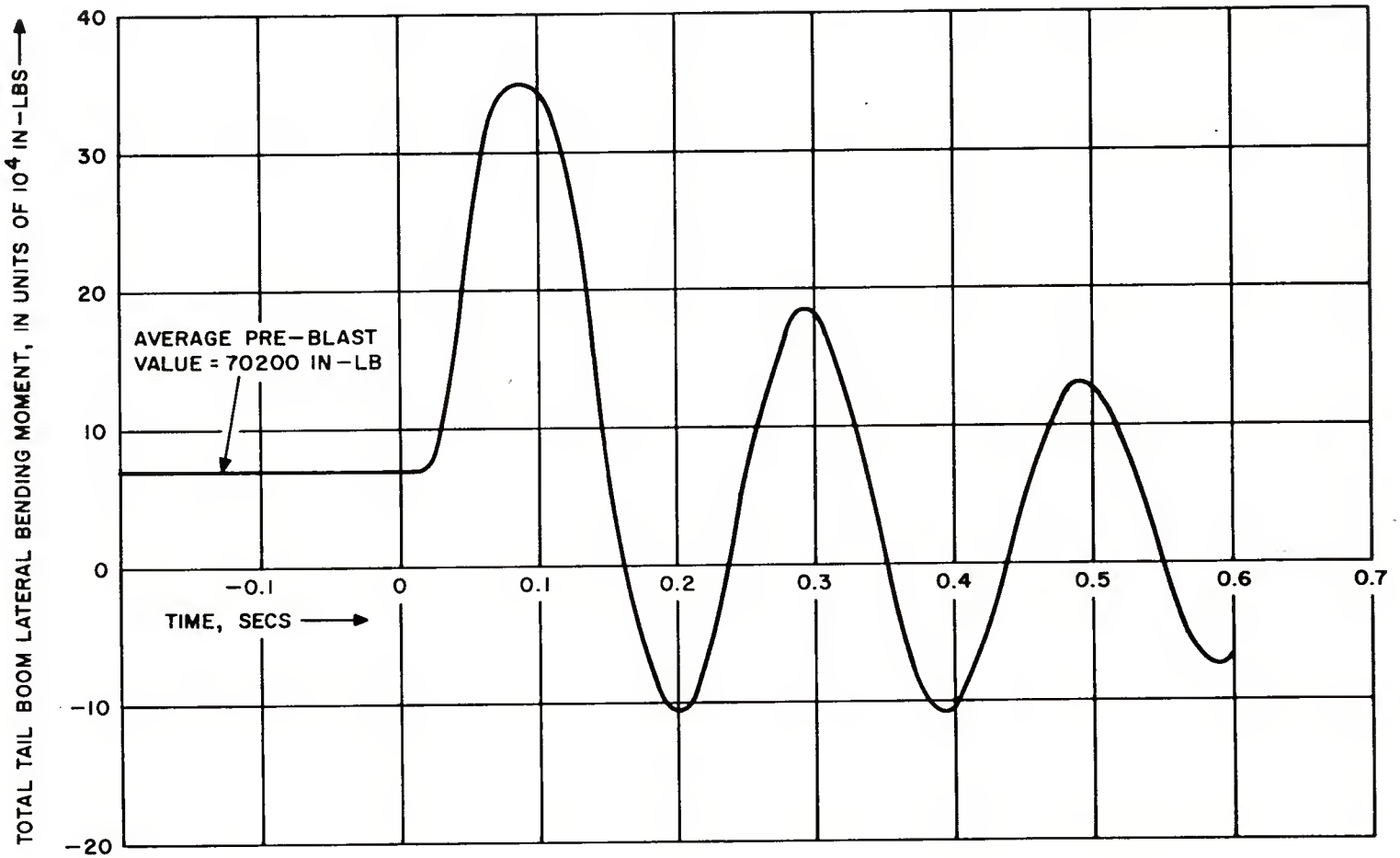

Figure 6.9. Time-Variation of Total Tail Boom Lateral Bending Moment, Tail Boom Station 47. Analytical

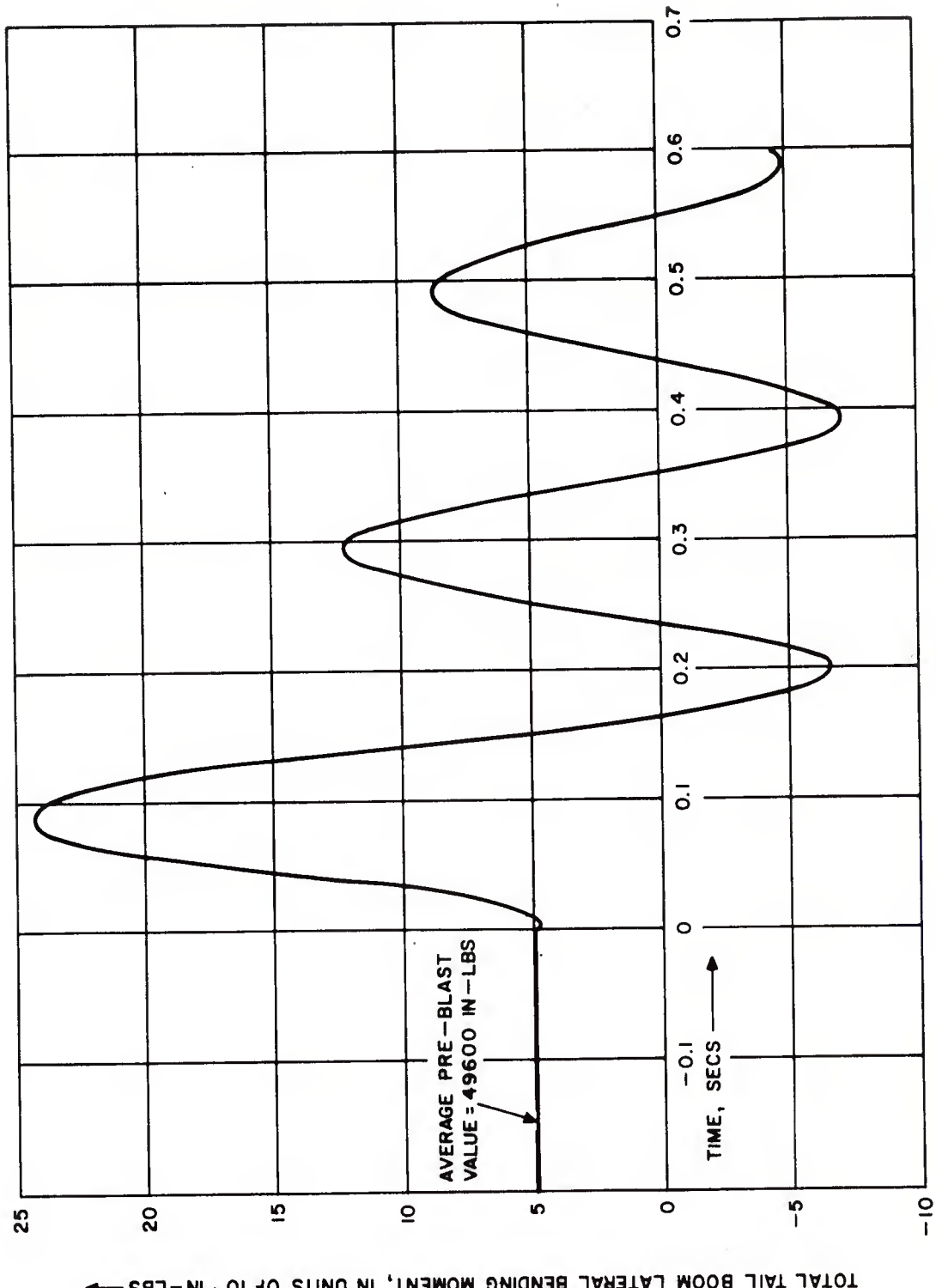

Figure 6.10. Time-Variation of Total Tail Boom Lateral Bending Moment. Tail Boom Station 112. Analytical

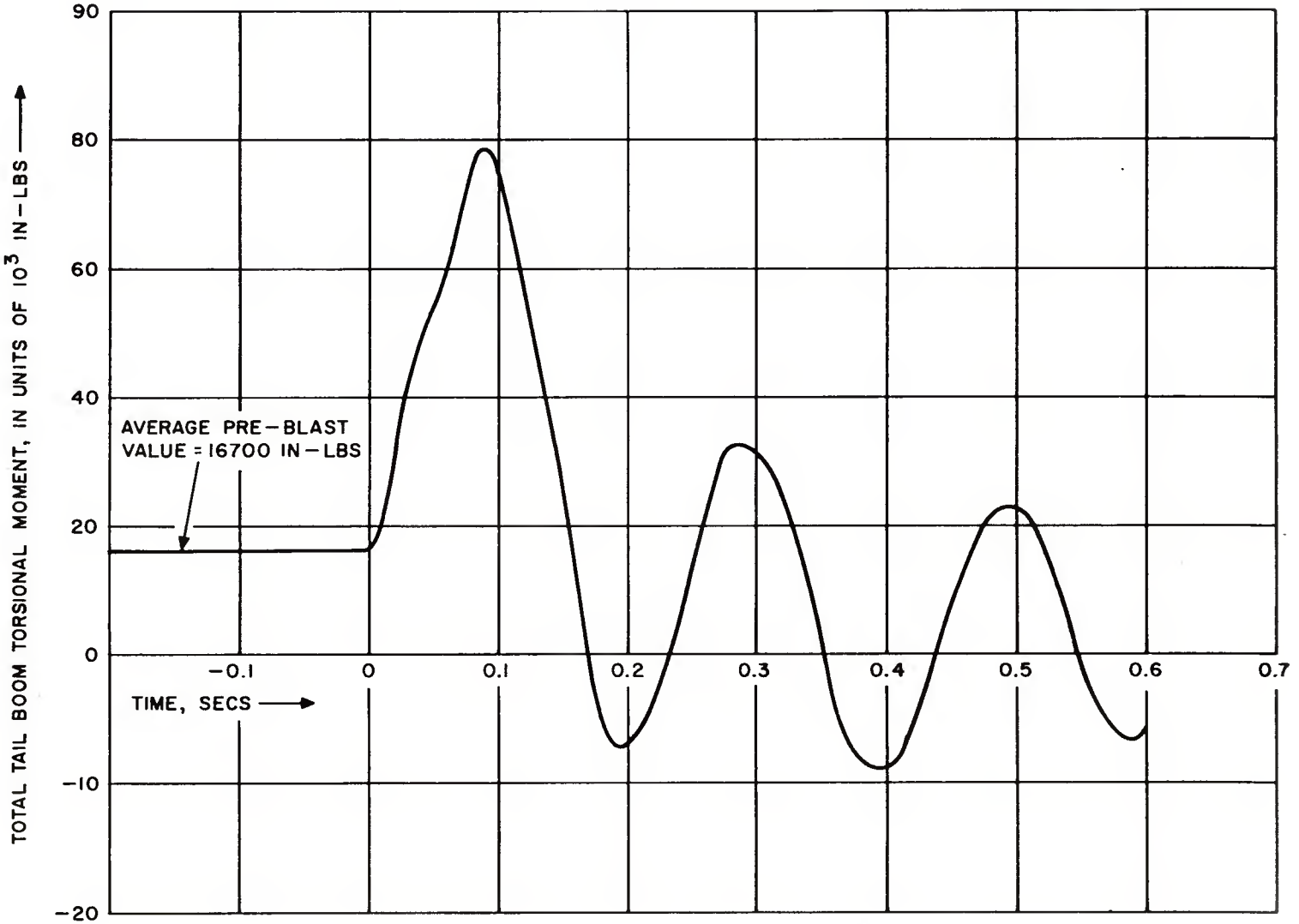

Figure 6.11. Time-Variation of Total Tail Boom Torsional Moment. Uniform All Along Tail Boom. Analytical

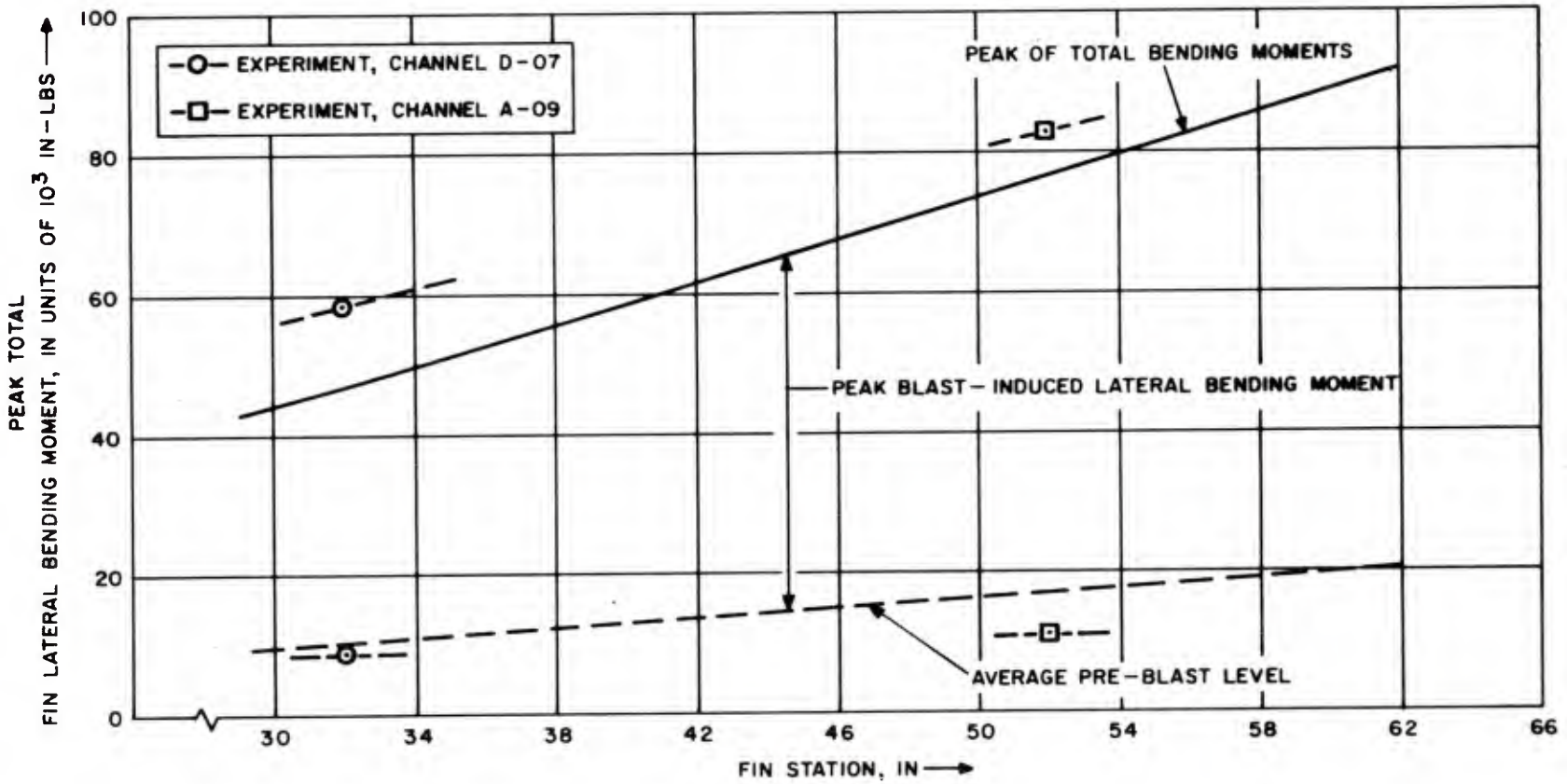

Figure 6.12. Spanwise Distribution of Peak Total Fin Lateral Bending. Analytical and Experimental

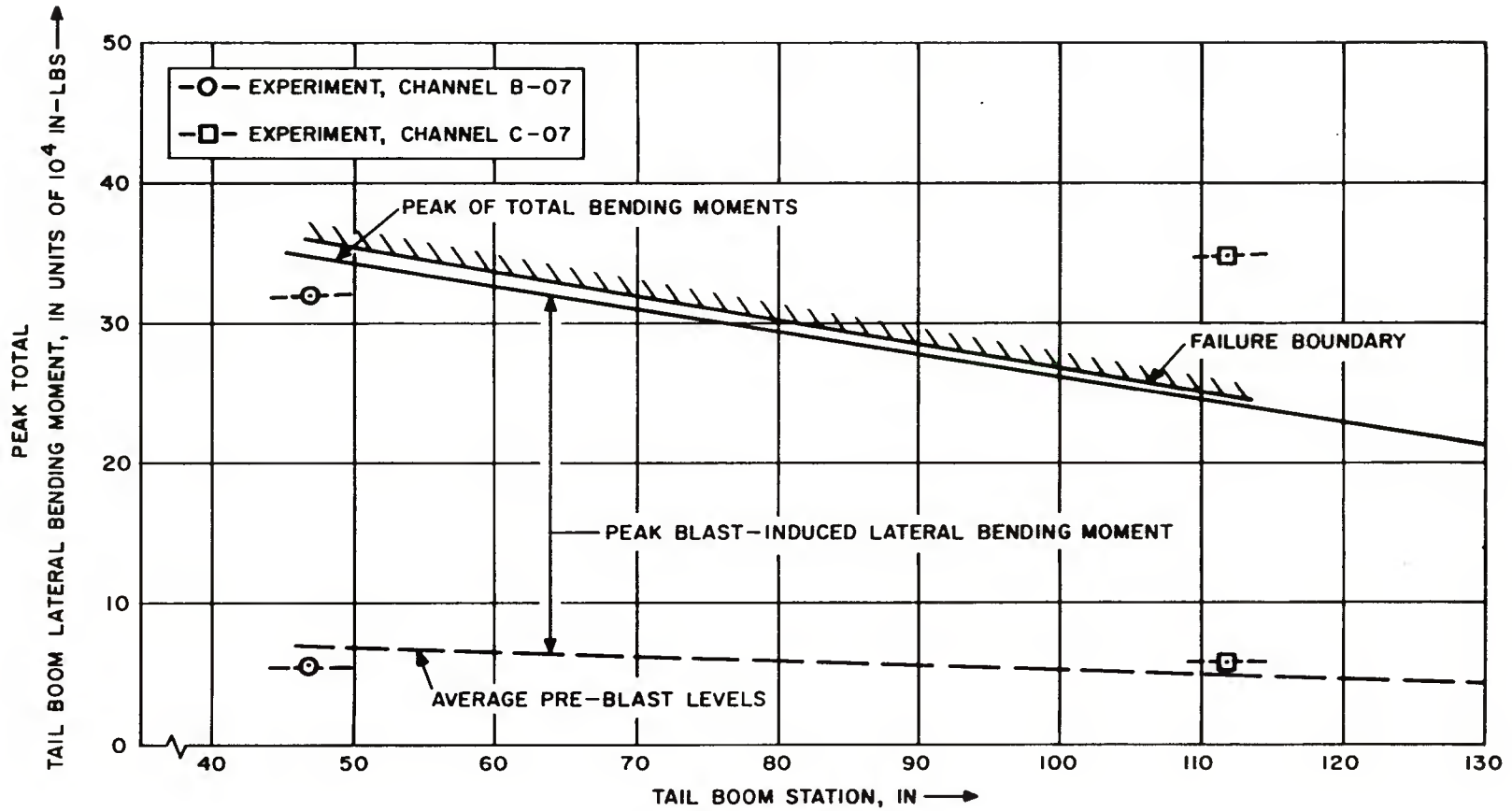

Figure 6.13. Spanwise Distribution of Peak Total Tail Boom Lateral Bending Moment. Analytical and Experimental

SECTION 7
PANEL, STRINGER, AND LONGERON STRAIN RESPONSES

Strain measurements were made on selected structural elements in the tail boom of the UH-1B helicopter for the purpose of assessing severity of response and of evaluating analytical techniques. These measurements consisted of seven skin panel strains and one strain each on the stringer and longeron supporting the panel. In this section the results of these measurements are discussed along with an attempt to correlate them with the NOVA-2 computer code predictions.

7.1 Description of the Test Section and of the Structural Model

The section of the UH-1B tail boom which was instrumentated for strain measurements in DICE THROW was the same as that considered in the PRE-MINE THROW IV experiment. This section is bounded vertically by the upper and lower longerons and longitudinally by bulkheads at body stations 38.6 and 59.4. Figure 7.1 depicts this section, which for simplicity is assumed to have parallel bulkheads, stringers, and longerons. Thus, the skin panels are assumed to be rectangular in shape, except for the slight curvature inherent in the design of the bulkheads. It is further assumed that this same curvature applies uniformly to the skin panel and that this curvature is of constant radius (a cylindrical section). Although a nominal radius of 60 inches was determined from a design drawing, much uncertainty exists as to the actual curvature and radial imperfections which probably exist. This uncertainty will be discussed further in conjunction with the correlation effort in Section 7.2.

As a further assumption, the three skin panels are taken to be identical since their dimensions differ by very little. This, then, means that the section is symmetrical in both directions, as indicated in Figure 7.1. Only a quarter of the center panel and half of the stringer need be analyzed. A clamped edge condition is assumed at the rivet lines of all members.

The material properties of the panel and stringers are summarized in Figure 7.2. The skin is 0.02 in magnesium alloy, while the stringers are made of 7075-0 aluminum.

Strain gage locations are delineated in Figure 7.3, where the flat, projected area of the structural section is shown for simplicity. It should be noted that the gages are fixed to either the inner or outer surface, except for the stringer, where the measurement was made 0.4375 inches from the outer skin surface. The small double-headed arrows in Figure 3 indicate the direction of the strain measurement, either longitudinally (horizontally) or circumferentially (vertically).

For the analytical predictions, the NOVA-2 code (Reference 4) was selected to provide panel and stringer response. (Longeron response will be discussed separately). NOVA-2 is an overpressure vulnerability code based on structural response of individual structural elements. The code was modified slightly to accept the measured pressure load at station 49 as a uniform load input. (See Section 3 for a complete description of the loading.)

An alternative computer code for this analysis is NASTRAN, which showed favorable results in the PRE-MINE THROW IV correlation of bulkheads strain. It was rejected here for the panel comparisons for basically the same reasons as in Reference 1, namely the lack of either membrane strain or inelastic effects in the NASTRAN code. Table 7.1 summarizes the important similarities and differences in the two computer codes.

For panel response, the membrane forces are particularly important due to the thinness of the skin. By contrast, the bulkheads respond mostly in bending, so that the NASTRAN approximation is much more appropriate. As for elastic-plastic response, NOVA-2 predicts minor edge yielding in the panel response, and photographs of the DICE-THROW experiment clearly indicate skin wrinkling. Thus, there is a strong evidence of inelastic panel response.

While NASTRAN lacks the non-linear capabilities, NOVA-2 lacks the ability to analyze a coupled system, where the load paths and dynamic response of the structural elements are dependent on overall skin-stringer-longeron-bulkhead structure. The importance of this is difficult to evaluate, but perhaps its best measure is in the correlation with the experimental results. Consequently, this will be discussed in conjunction with the results in Section 7.2.

The NOVA-2 code consists of two structural response options, DEPROP for panel response, and DEPROB for beam elements. The DEPROP model of the skin panel for DICE THROW was comprised of 25 modal combinations with the seventh symmetrical mode being the largest used in any combination. All edges were assumed perfectly clamped, and the solution was allowed to go inelastic. No radial imperfections were used. A time increment of 1.5 microseconds was used.

The DEPROB model of the "J" section stringer was similarly assumed clamped at the bulkheads. Ten mass points were used to define half the length of the stringer. Five layers were required to model the cross section, including an effective skin-width of 0.42 inches. Due to the attached skin, one half of the area from adjacent panels was assumed to provide pressure loading. A time interval of approximately 4.4 microseconds was used by the program.

Because of the relative speed of DEPROB, the stringer response was carried out further in time than the panel response. Without damping in either response, the results become less and less meaningful at later times anyway.

7.2 Comparison of Experimental and Theoretical Results

The experimental strains as measured in DICE THROW are presented in Figures 7.4 - 7.12. Figures 7.13 - 7.21 show the NOVA-2 comparisons, except for the longeron measurement. In general, the comparisons are not good, and it is felt the same two problems which plagued the PRE-MINE IV correlations hampered this effort as well, these being 1) uncertainty in the degree of curvature in the structure, and 2) coupling between individual components.

Consider first the panel response. Knowledge of the exact curvature and any imperfections is extremely important due to the "snap-through" type of response which occurs. Using mostly elastic runs and results from PRE-MINE THROW IV (Reference 1), the sensitivity to curvature was determined from NOVA-2. Although the nominal curvature corresponds to a radius of curvature of 60 inches, the correlation computer runs were made with a 180 inch radius (the analysis in Reference 1 went as high as 300 inches). Not only is the radius of curvature uncertain, but in actuality it is not even constant. Further, any pre-test stress could easily introduce additional imperfections. Even if careful measurements were taken prior to testing, these last-minute imperfections could still be very significant.

A better DEPROP model utilizing more modes in the solution was used in the present calculations as compared to those for the PRE-MINE THROW IV. Adding still more modes did not seem to significantly change the results.

Although the strain measurements did not indicate any yielding, the DEPROP solution does indicate yielding along the stringer boundary (the measurements were approximately 1 inch from the boundary).

The stringer strain measurement was made very near the middle of the cross-section and consequently recorded relatively low levels of strain. The comparison (Figure 7.20) indicates good frequency comparison, but far too large predicted amplitudes. This could easily be explained if the strain gage was actually closer to the vertical axis than was indicated. Substantial yielding is indicated by DEPROB both near the edge and at the center of the stringer.

The longeron trace (Figure 7.11) shows extraneous spikes for times t=25 to 50 msecs. Discarding these spikes, it is clear that the largest strain was around 500 micro in/in and occurred at the same time as the peak tail boom bending moment at station 47. From the tail boom data

presented in Section 6, the peak bending moment must have been around 320,000 in-lbs at t=95 msecs. At the longeron station, the tail boom cross-sectional area (lateral) moment of inertia is estimated to be 210 in^4. Since the strain gage is about 11 in from the neutral axis, the longitudinal stress must have been

$$\sigma = \frac{320{,}000 \times 11}{210} = 16{,}760 \text{ lb/in}^2$$

With the Young's modulus for aluminum = 10.5×10^6 lb/in^2, this stress corresponds to a strain of about 1600 micro in/in, which is about three times the maximum strain noted in Figure 7.11 at t = 95 msecs. No explanation can be offered for this disagreement between experiment and the simple estimate for the maximum longeron strain.

Referring to the panel strain results again, several differences are apparent. First, the NOVA-2 predictions generally indicate higher frequency characteristics. Secondly, at later times (like after 2.5 milliseconds by which time the load has decayed to less than half its peak value) the experimental traces tend to "drift" towards a significant level of strain, instead of returning to a more neutral value.

The explanation, it would appear, is due in part to the fact that the skin-stiffener structure is responding as a strongly coupled system. Figure 7.21 indicates the center deflection response predicted by NOVA-2 (no deflection measurements were made). Here the stringer is exibiting deflections on the same order as the small panel between stringers. If the entire section between longerons was considered, it would certainly exhibit lower frequency characteristics. Whether or not the response at later times could be explained is uncertain. The fact that dynamic coupling is important here is not unexpected, to be sure, but the capability to accurately include it in the analysis had to be compromised in the selection of the computer code.

7.3 Concluding Remarks

Comparisons of experimental and theoretical strains on the panel and stringer were generally inconclusive due to several restricting factors, most of which were also important in the PRE-MINE THROW IV experiment. First, the lack of precise information as to the degree of curvature represents probably the most severe limitation. Secondly, the NOVA-2 code, which can accurately represent the non-linearities of a membrane panel response, is unable to combine panel-stiffener-bulkhead response, and coupling appears to be important.

Relatively little panel damage is predicted by NOVA-2 (along the stringer boundary), although considerable wrinkling was observed. NOVA-2 predicts somewhat more permanent damage to the stringer, particularly near the bulkhead and also to a lesser degree at the center.

TABLE 7.1

COMPARISON OF NOVA-2 AND NASTRAN COMPUTER CODES

FEATURES	NOVA-2	NASTRAN
Analysis Method	Finite-difference	Finite-element
Type of Model	Single Element	Multiple Elements
Nonlinearities	Membrane and Bending Forces	Bending Forces Only
Inelastic Region of Response	Elastic-Plastic	Elastic Only
Relative Complexity of Operating Code	Moderate	High
Best Suited for Analysis	Panel	Bulkhead
Can Accommodate Curvature	Yes	Yes

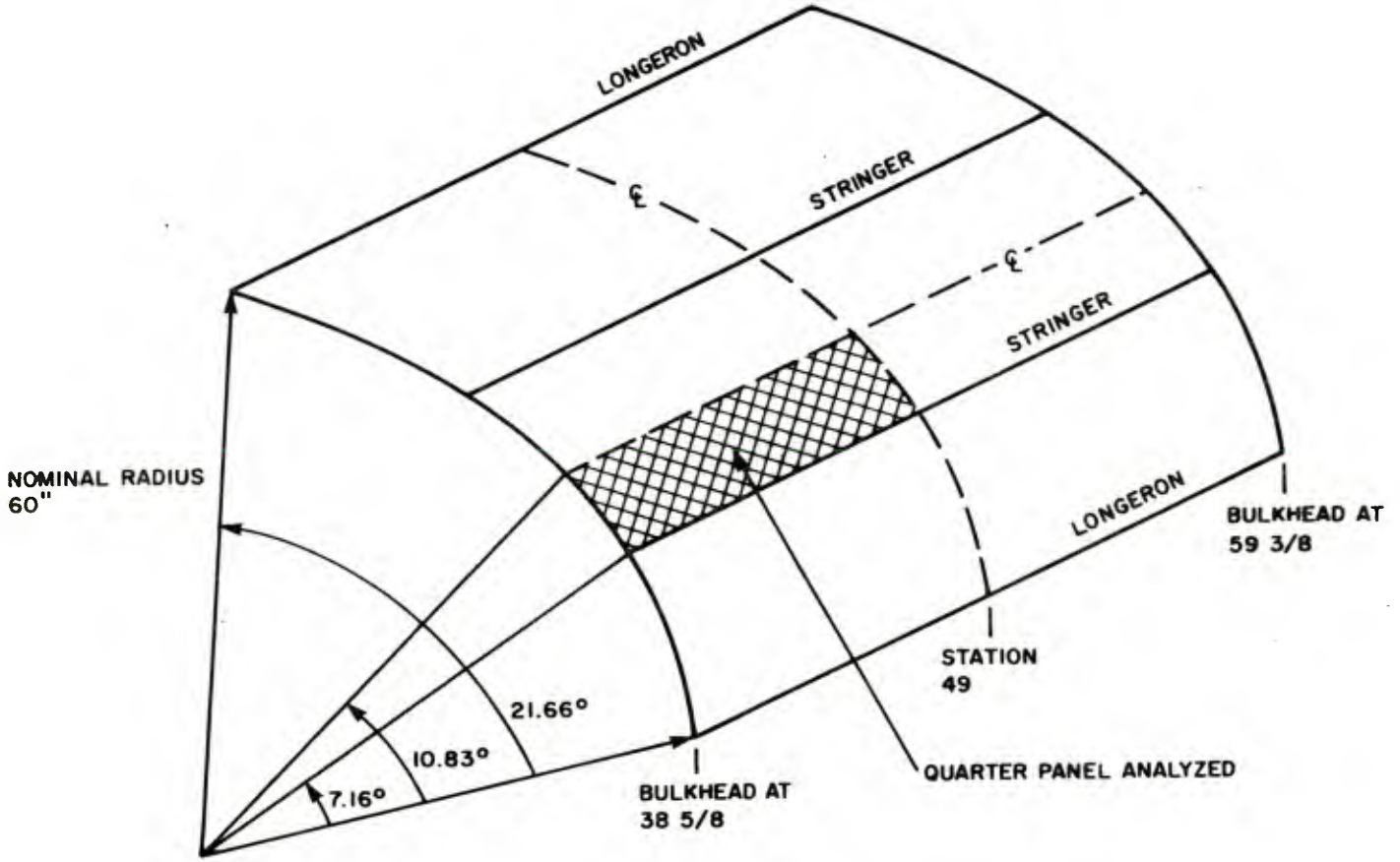

Figure 7.1. Structural Model of UH-1B Tail Boom Section Instrumented For DICE THROW Test

PROPERTIES	PANEL	STRINGER
Material	Magnesium	7075-0 Aluminum
Elastic Modulus, psi	6.5×10^6	10.5×10^6
Yield Stress, psi	30,000	67,000
Strain Hardening Slope, psi	1.67×10^5	1.22×10^5
Density, lb/in^3	0.064	0.1
Poisson's Ratio	0.33	--
Effective Skin width, in	--	0.42
Thickness, in	0.02	0.032
Dimensions, in		
a	--	0.20
b	--	0.75
c	--	0.175
d	--	0.815

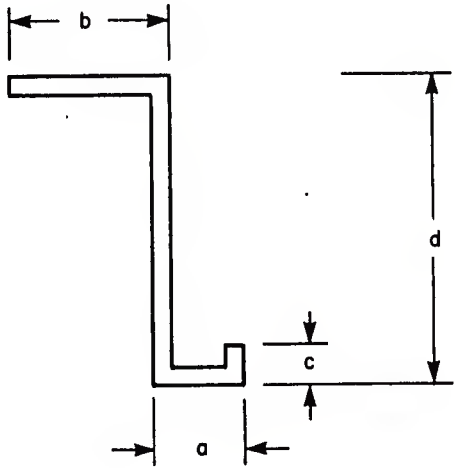

STRINGER
MODEL

Figure 7.2. Material Properties and Cross-Sectional Model for Panel and Stringer Structural Members

GAGE	SURFACE	CODE
1	Inner	A-05
2	Outer	B-05
3	Inner	C-05
4	Outer	D-05
5	Inner	C-06
6	Inner	A-06
7	Outer	B-06
8	Inner	D-06
9	0.4375 in. from outer surface	A-07

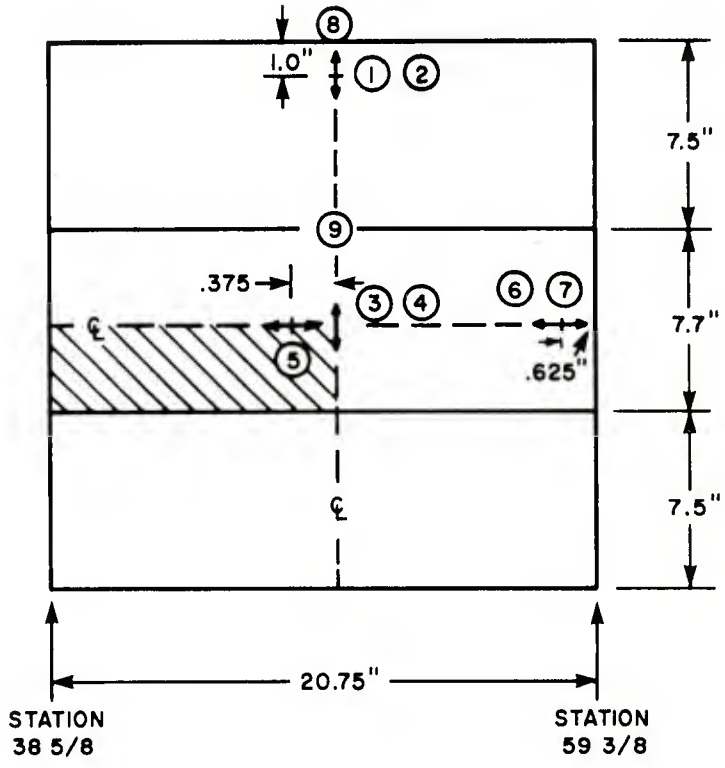

Figure 7.3. Strain Measurement Locations

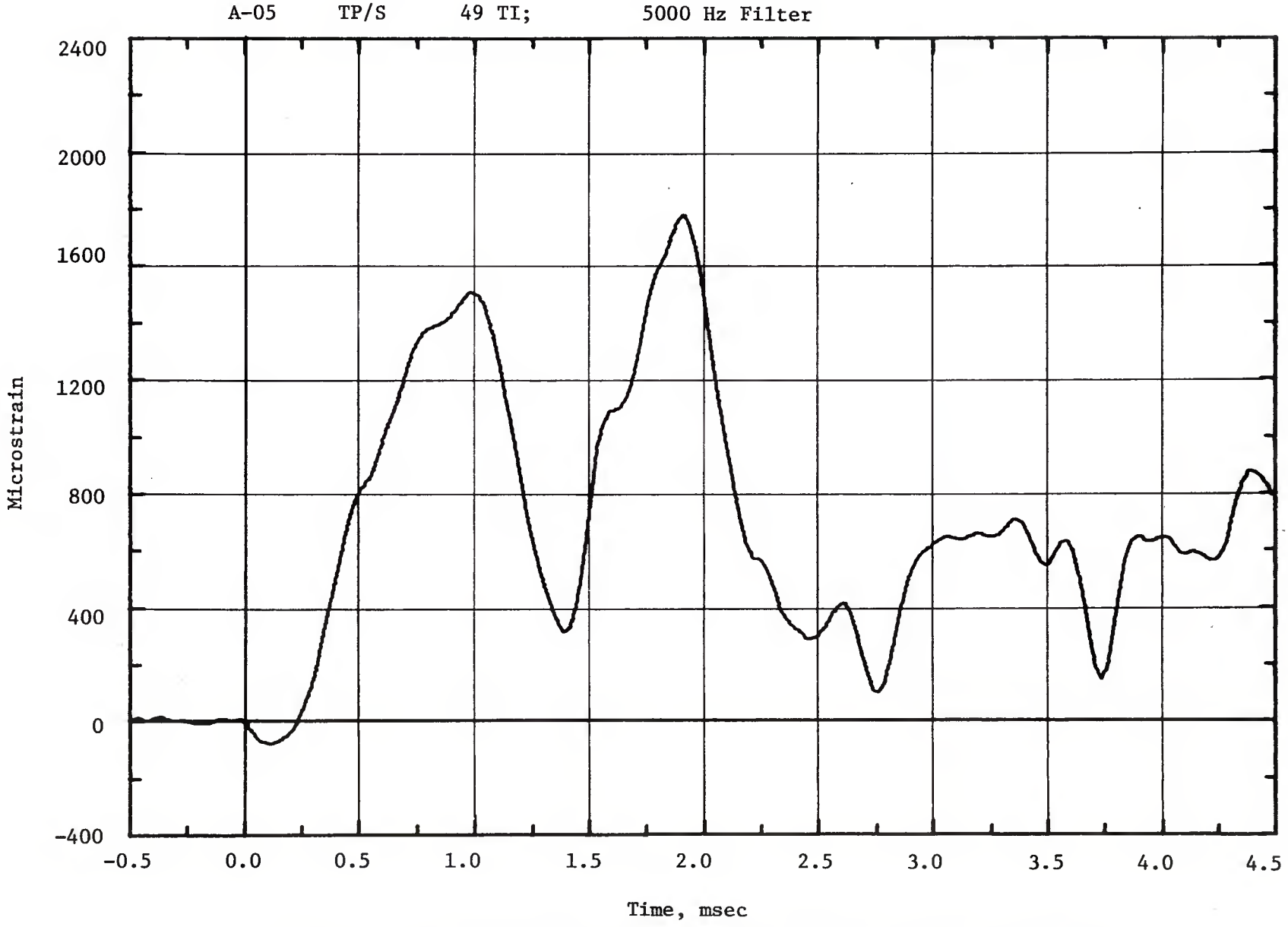

Figure 7.4. Time-Variation of Panel Circumferential Strain at Inner Surface Point Near Longeron and on Centerline. Channel A-05

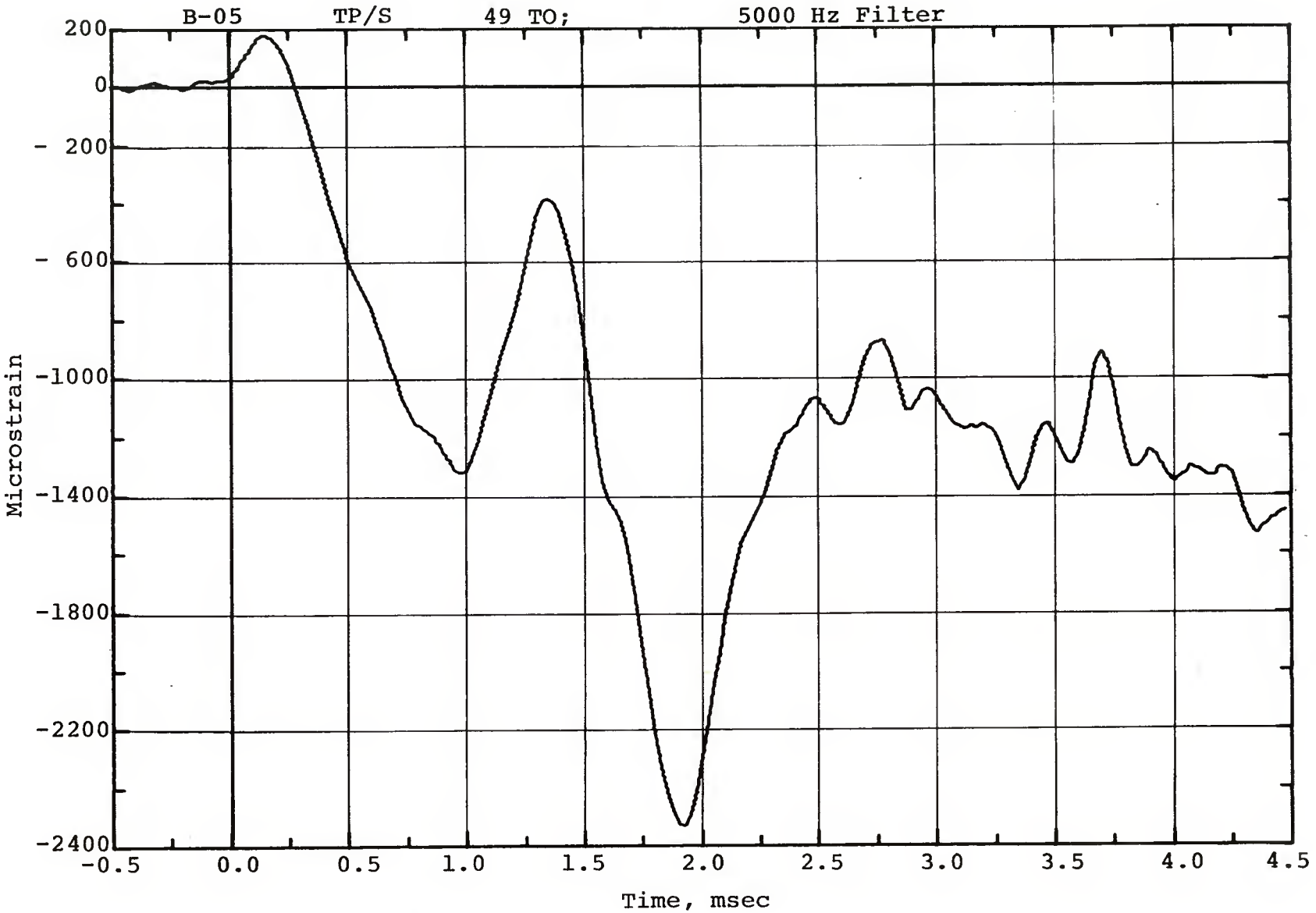

Figure 7.5. Time-Variation of Panel Circumferential Strain at Outer Surface Point Near Longeron and on Centerline. Channel B-05

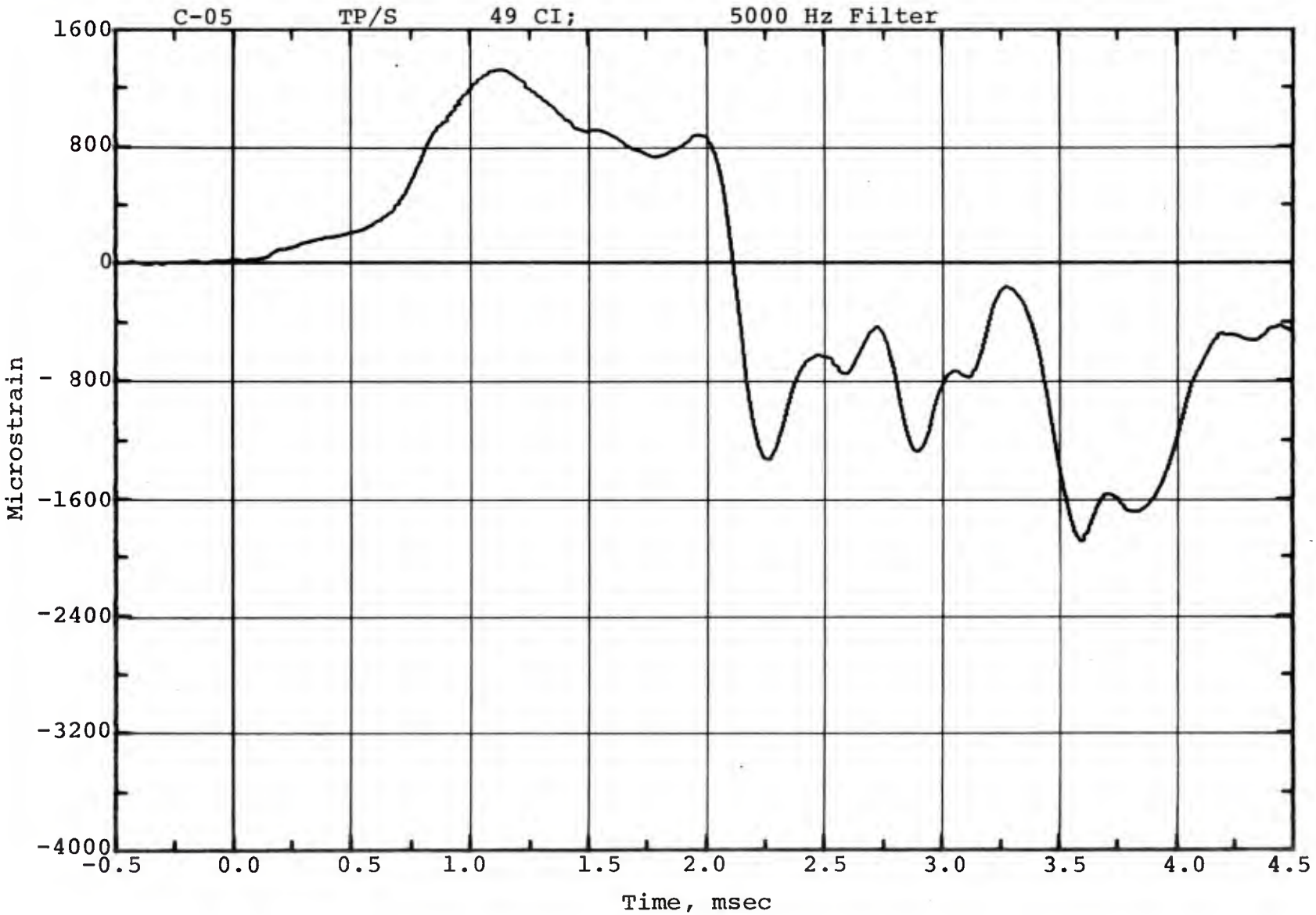

Figure 7.6. Time-Variation of Panel Circumferential Strain at Inner Surface Center Point. Channel C-05

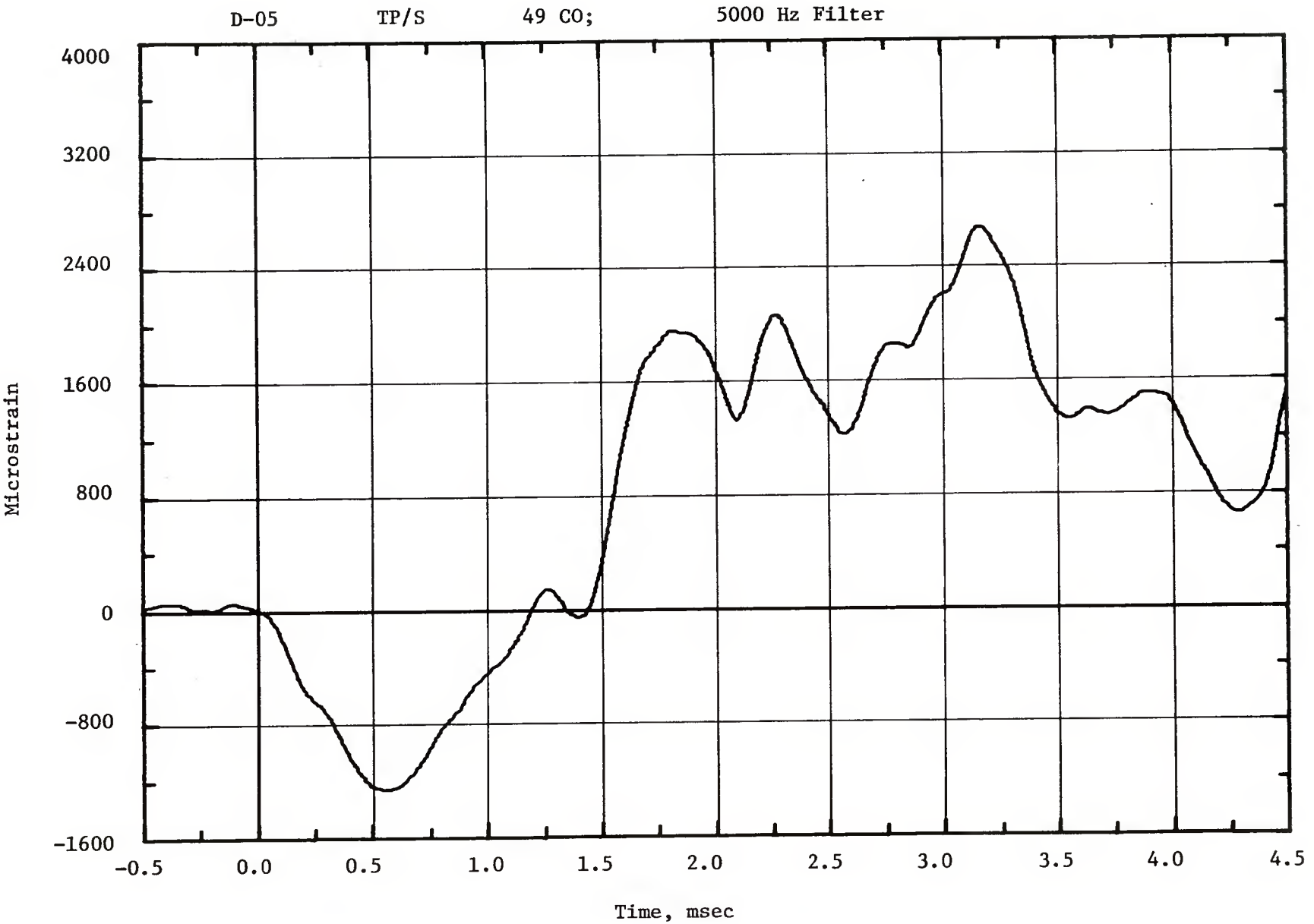

Figure 7.7. Time-Variation of Panel Circumferential Strain at Outer Surface Center Point. Channel D-05

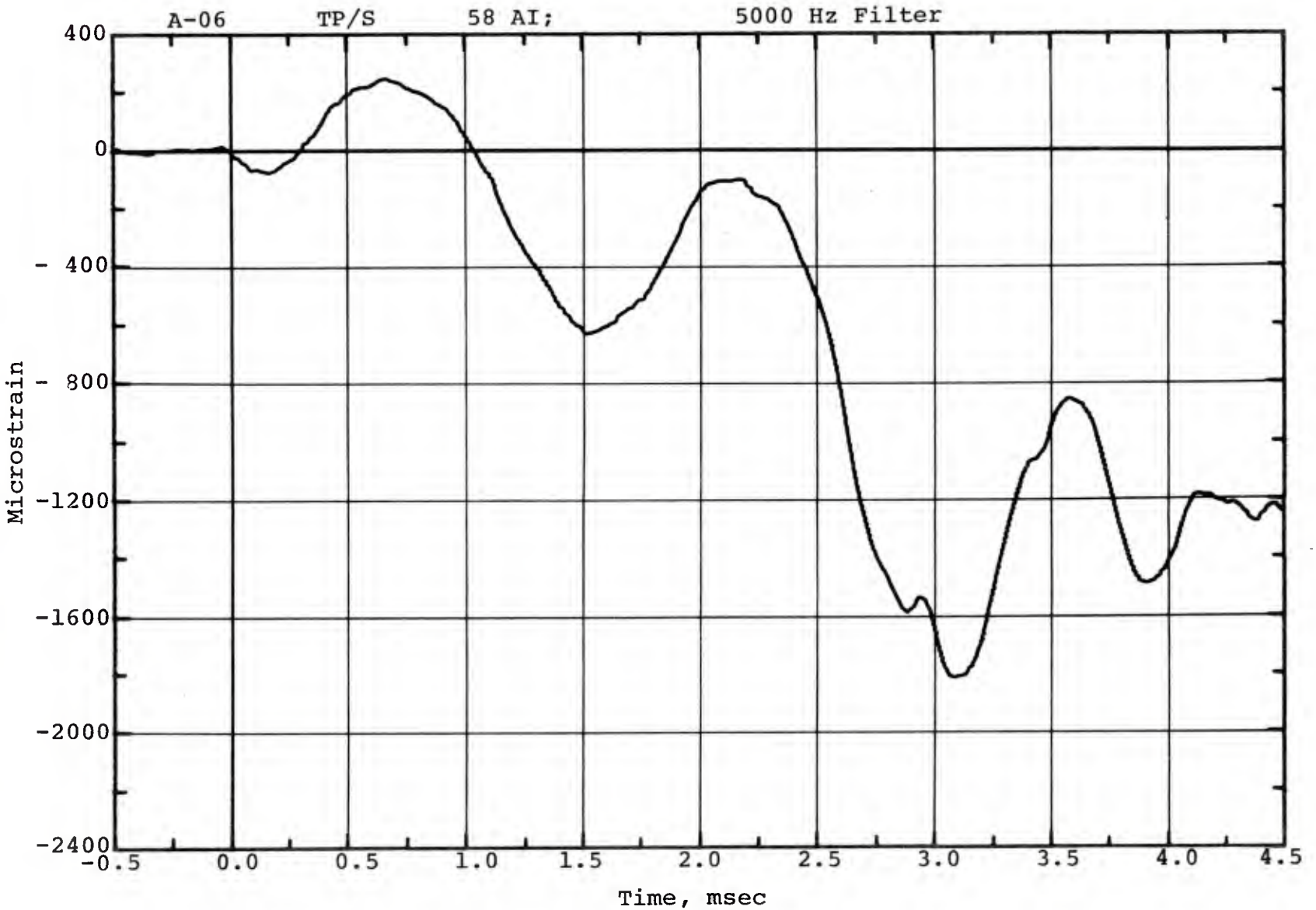

Figure 7.8. Time-Variation of Panel Longitudinal Strain at Inner Surface Point Near Bulkhead and on Centerline. Channel A-06

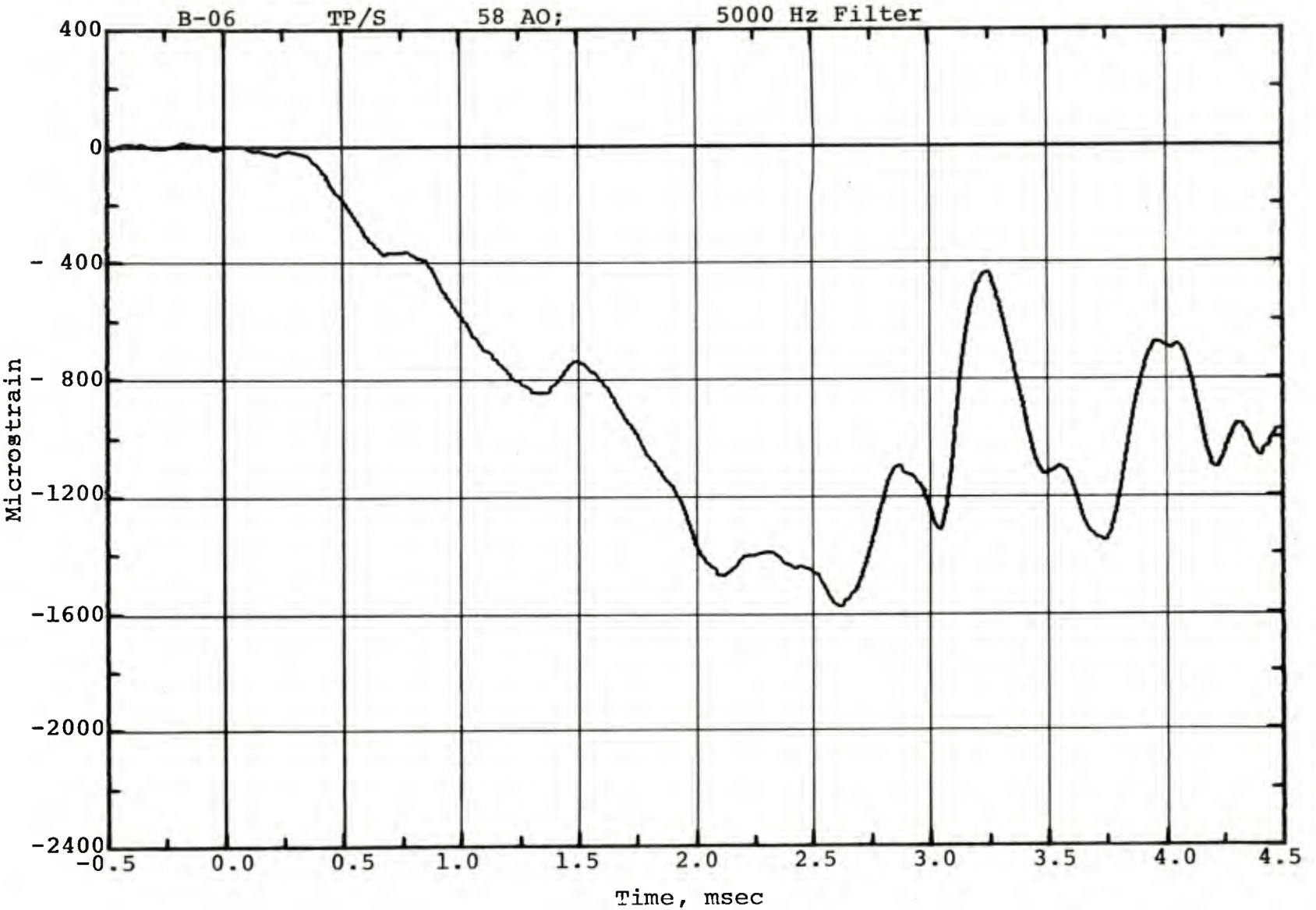

Figure 7.9. Time-Variation of Panel Longitudinal Strain at Outer Surface Point Near Bulkhead and on Centerline. Channel B-06

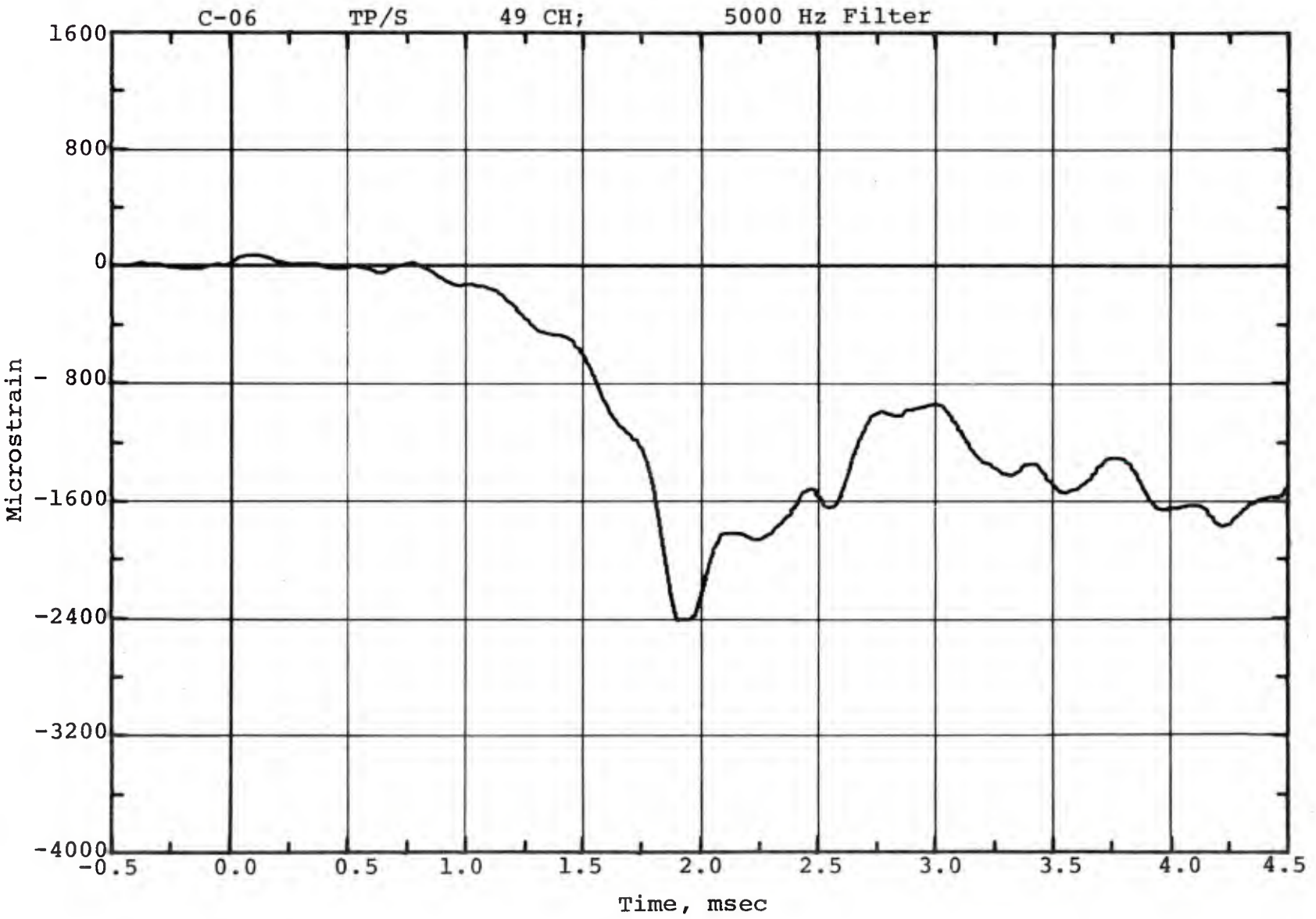

Figure 7.10. Time-Variation of Panel Longitudinal Strain at Inner Surface Near Center Point. Channel C-06

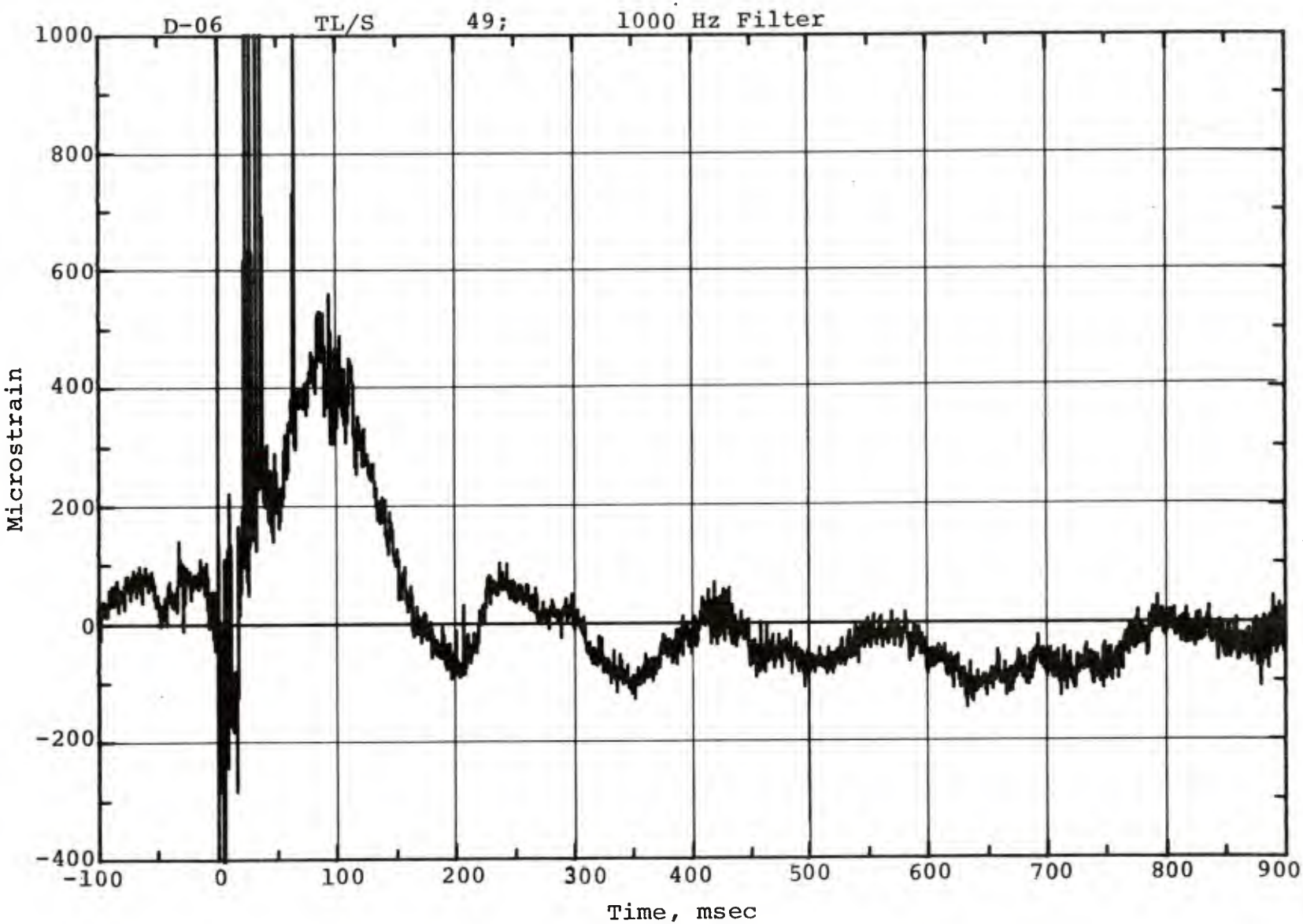

Figure 7.11. Time-Variation of Longeron Extensional Strain at Its Mid-Span Station. Channel D-06

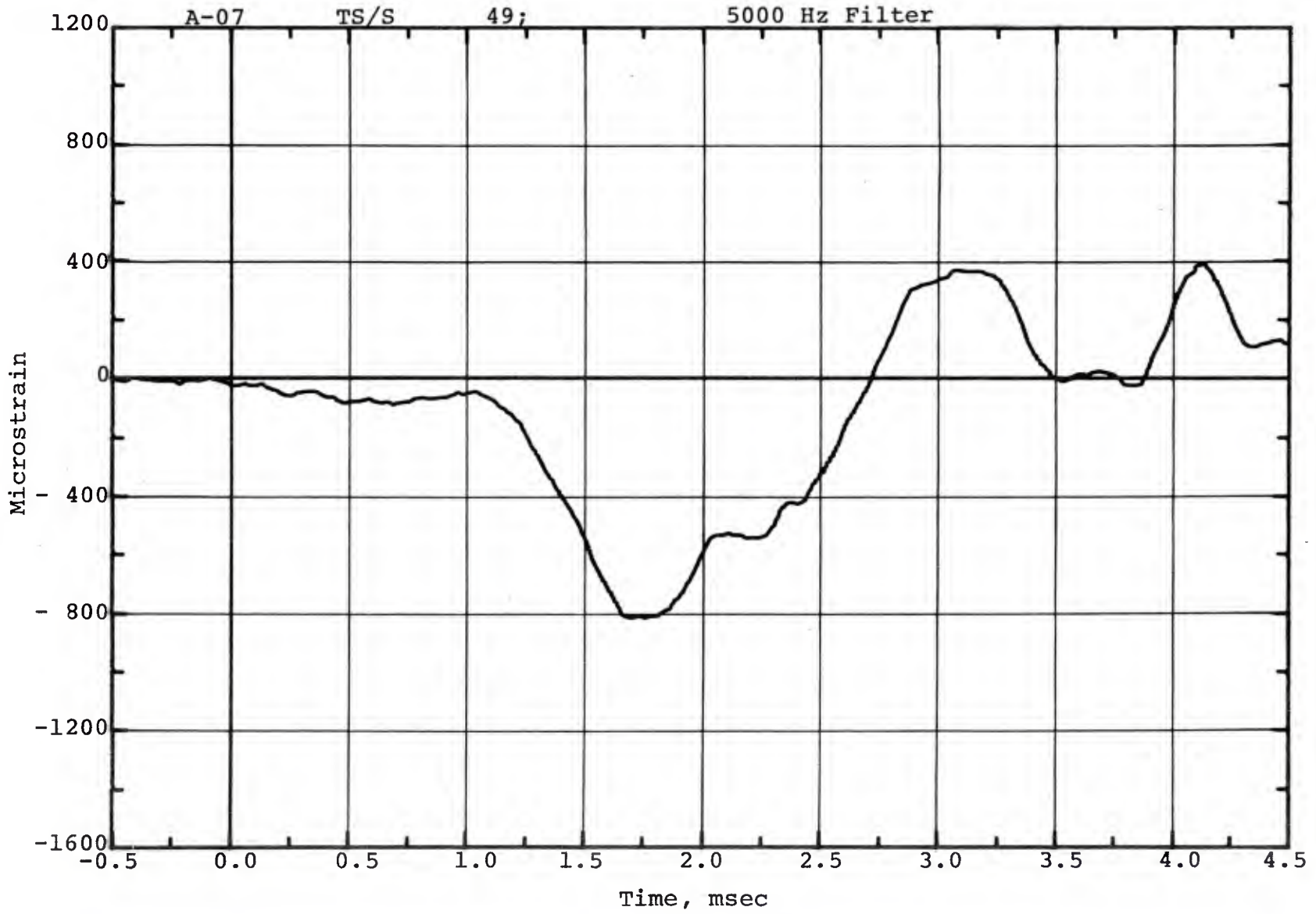

Figure 7.12. Time-Variation of Stringer Extensional Strain at Its Mid-Span Station. Channel A-07

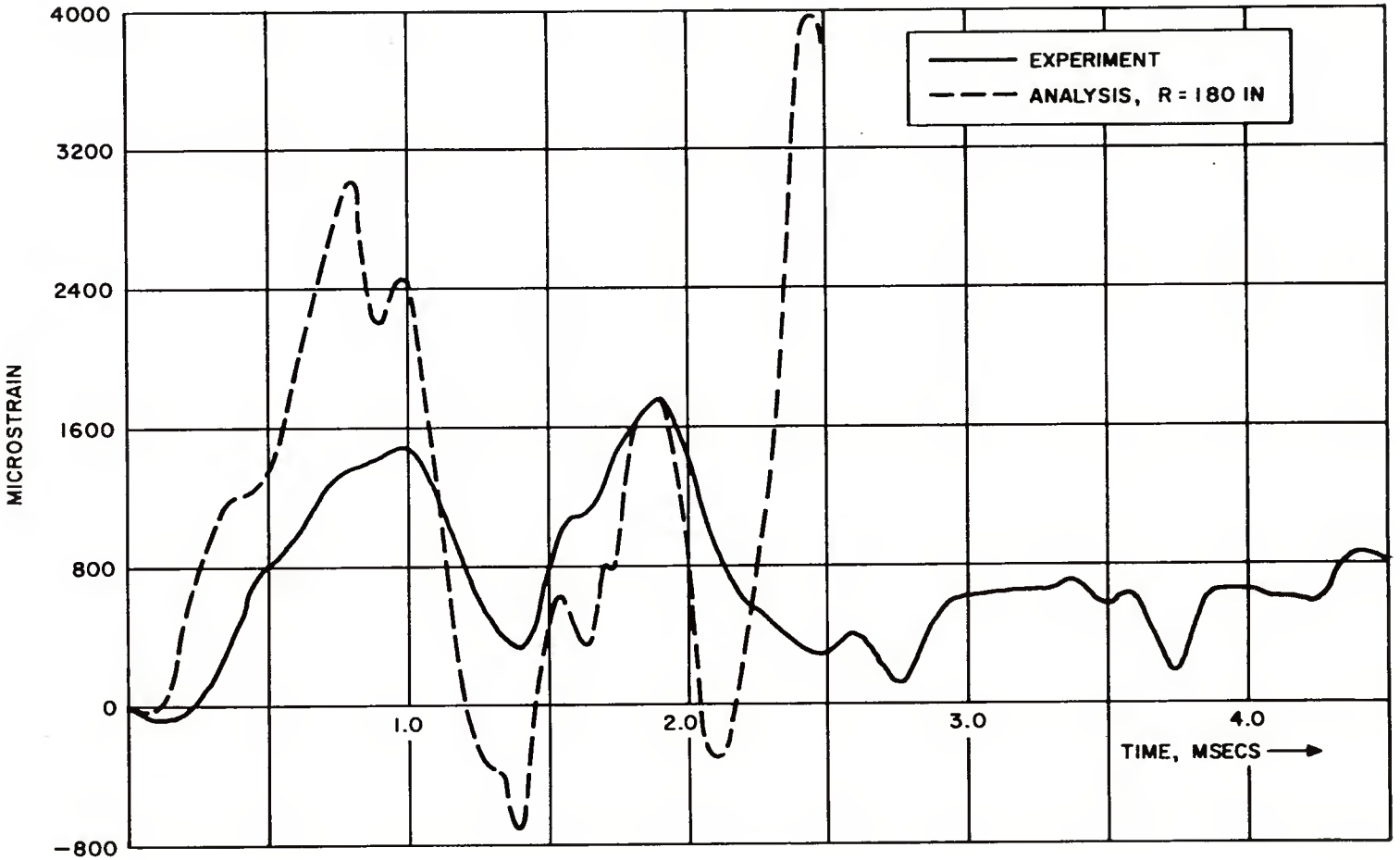

Figure 7.13. Comparison Between Experimental and Analytical Time-Variations of Panel Circumferentail Strain at Inner Surface Point Near Longeron and on Centerline. Channel A-05

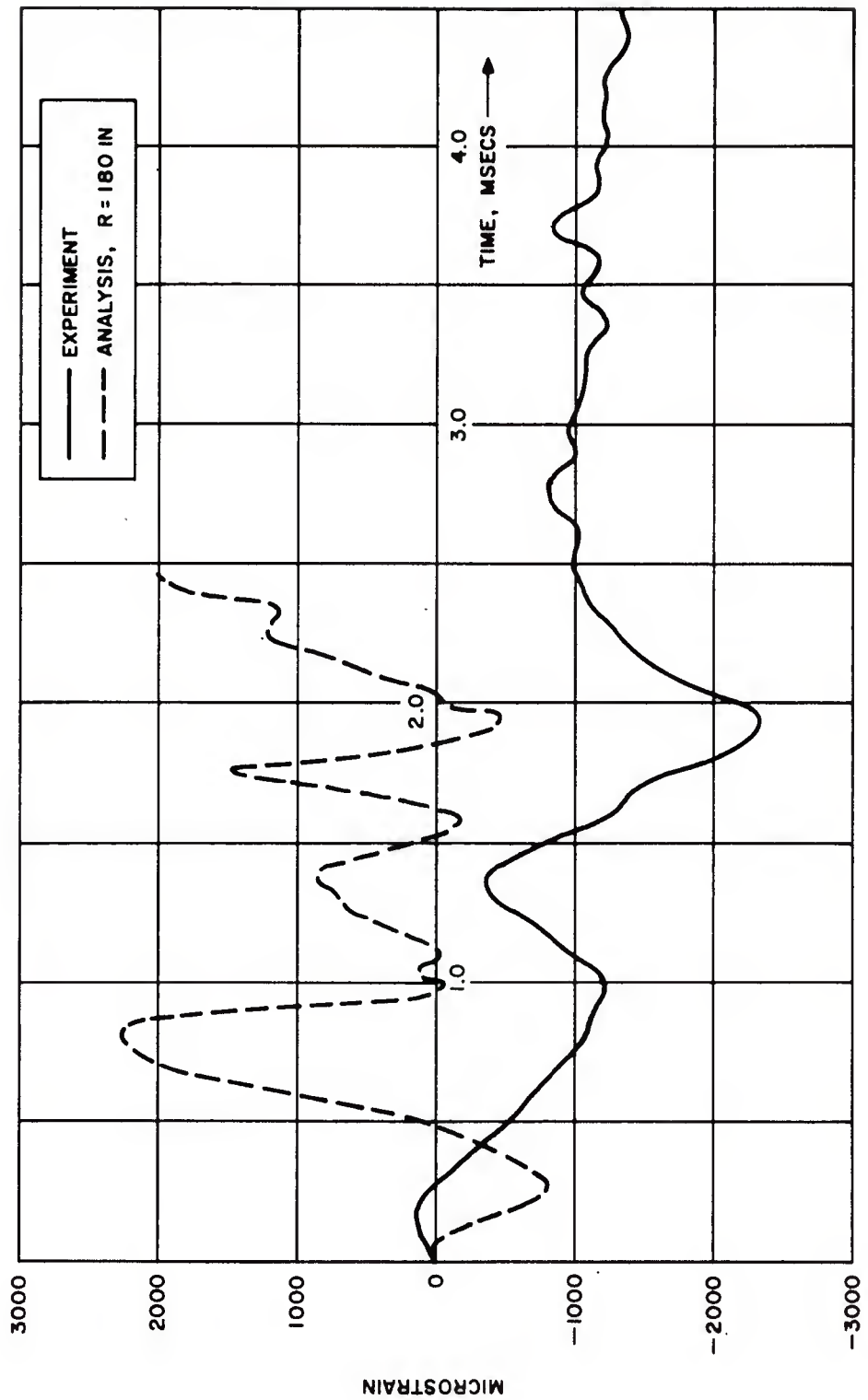

Figure 7.14. Comparison Between Experimental and Analytical Time-Variations of Panel Circumferential Strain at Outer Surface Point Near Longeron and on Centerline. Channel B-05

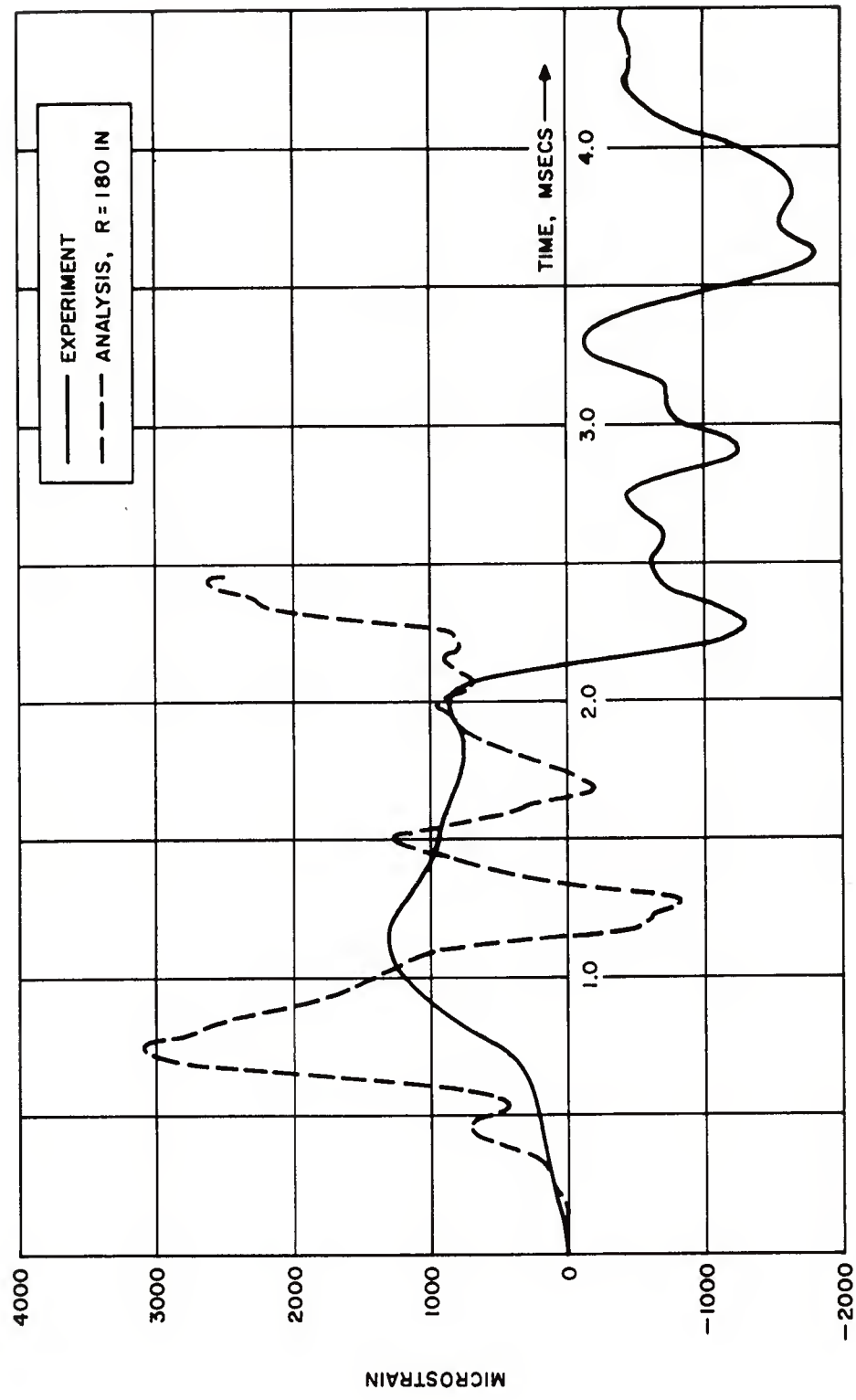

Figure 7.15. Comparison Between Experimental and Analytical Time-Variations of Panel Circumferential Strain at Inner Surface Center Point. Channel C-05

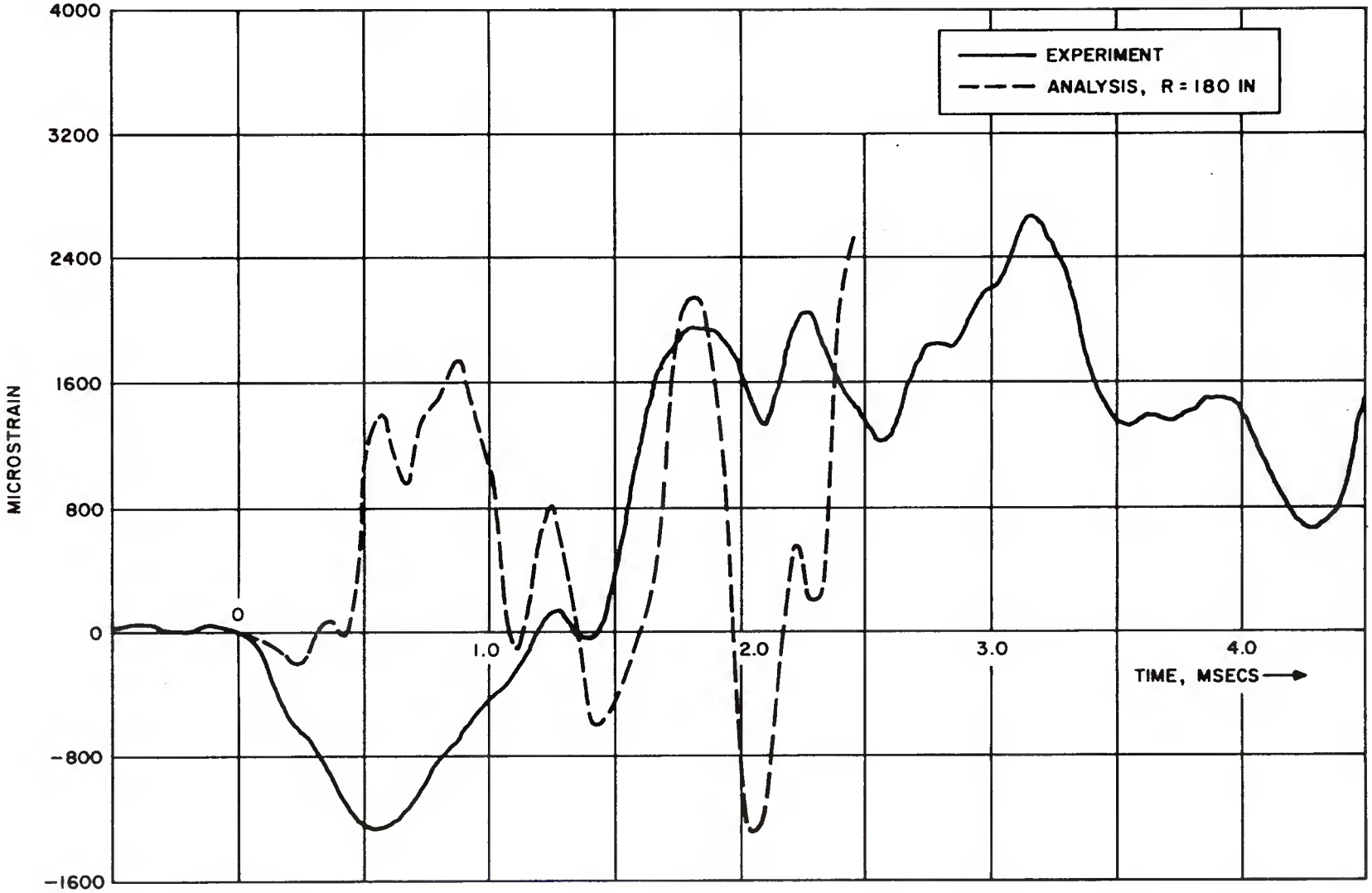

Figure 7.16. Comparison Between Experimental and Analytical Time-Variations of Panel Circumferential Strain at Outer Surface Center Poitn. Channel D-05

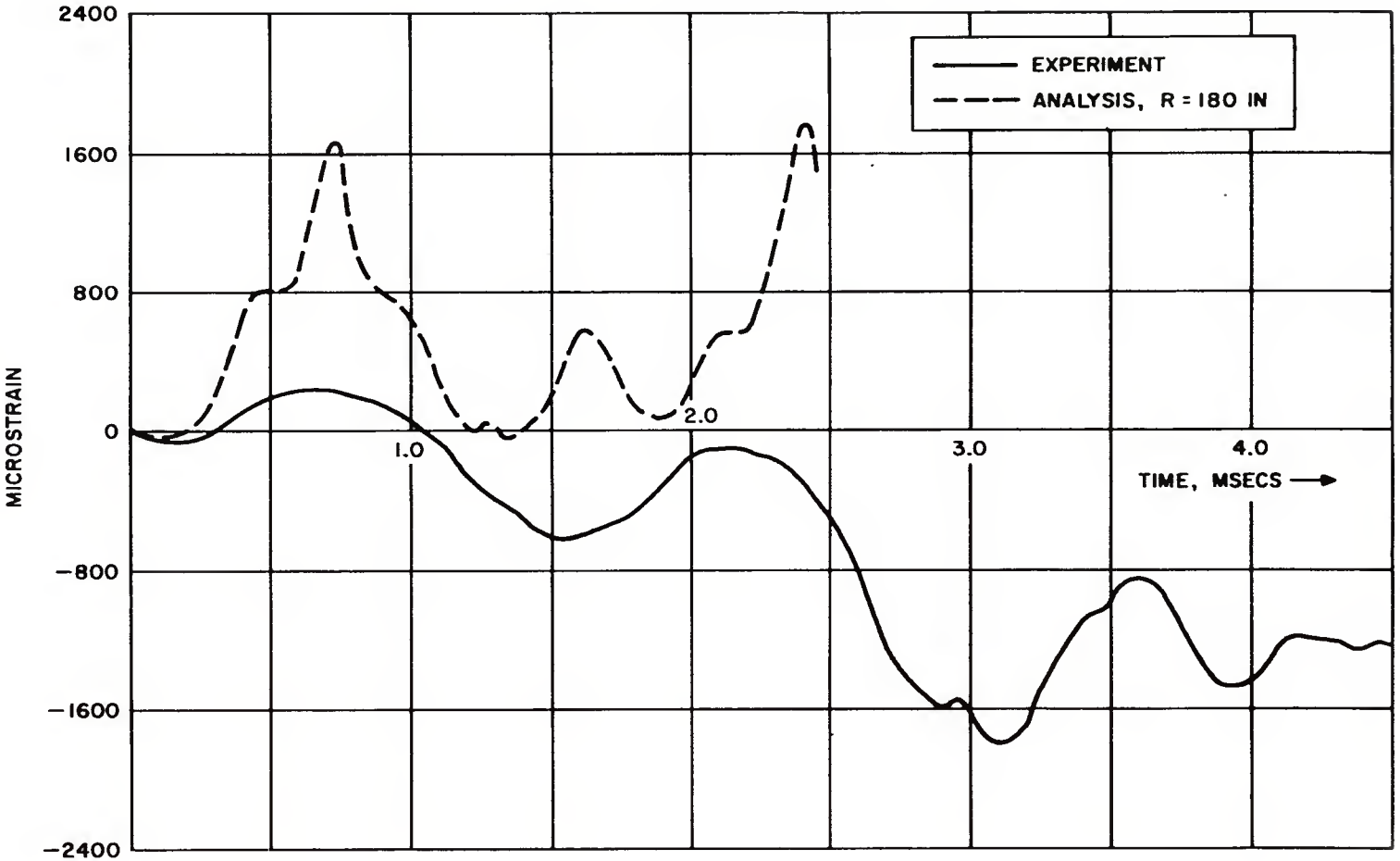

Figure 7.17. Comparison Between Experimental and Analytical Time-Variations of Panel Longitudinal Strain at Inner Surface Point Near Bulkhead and on Centerline. Channel A-06

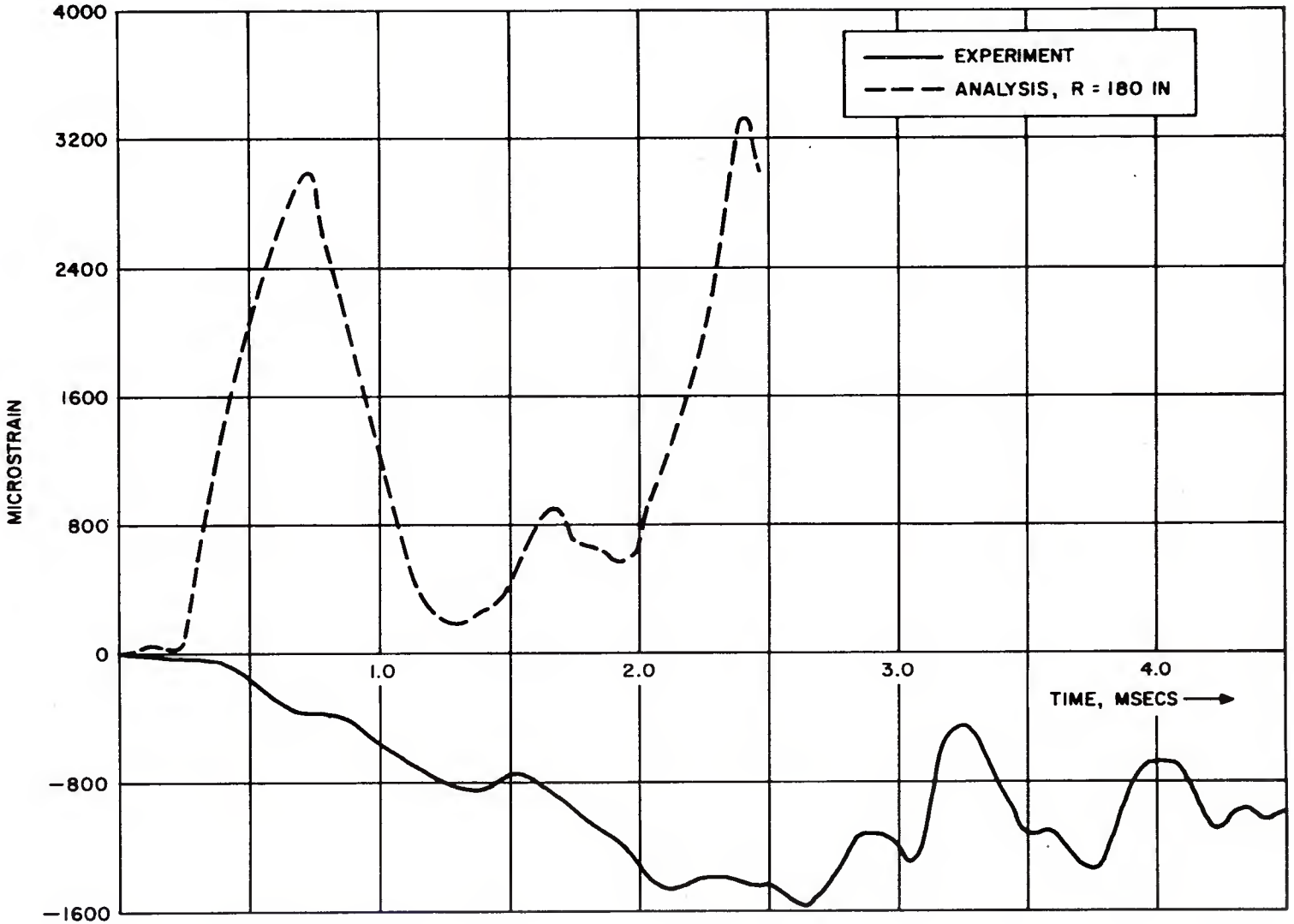

Figure 7.18. Comparison Between Experimental and Analytical Time-Variations of Panel Longitudinal Strain at Outer Surface Point Near Bulkhead and on Centerline. Channel B-06

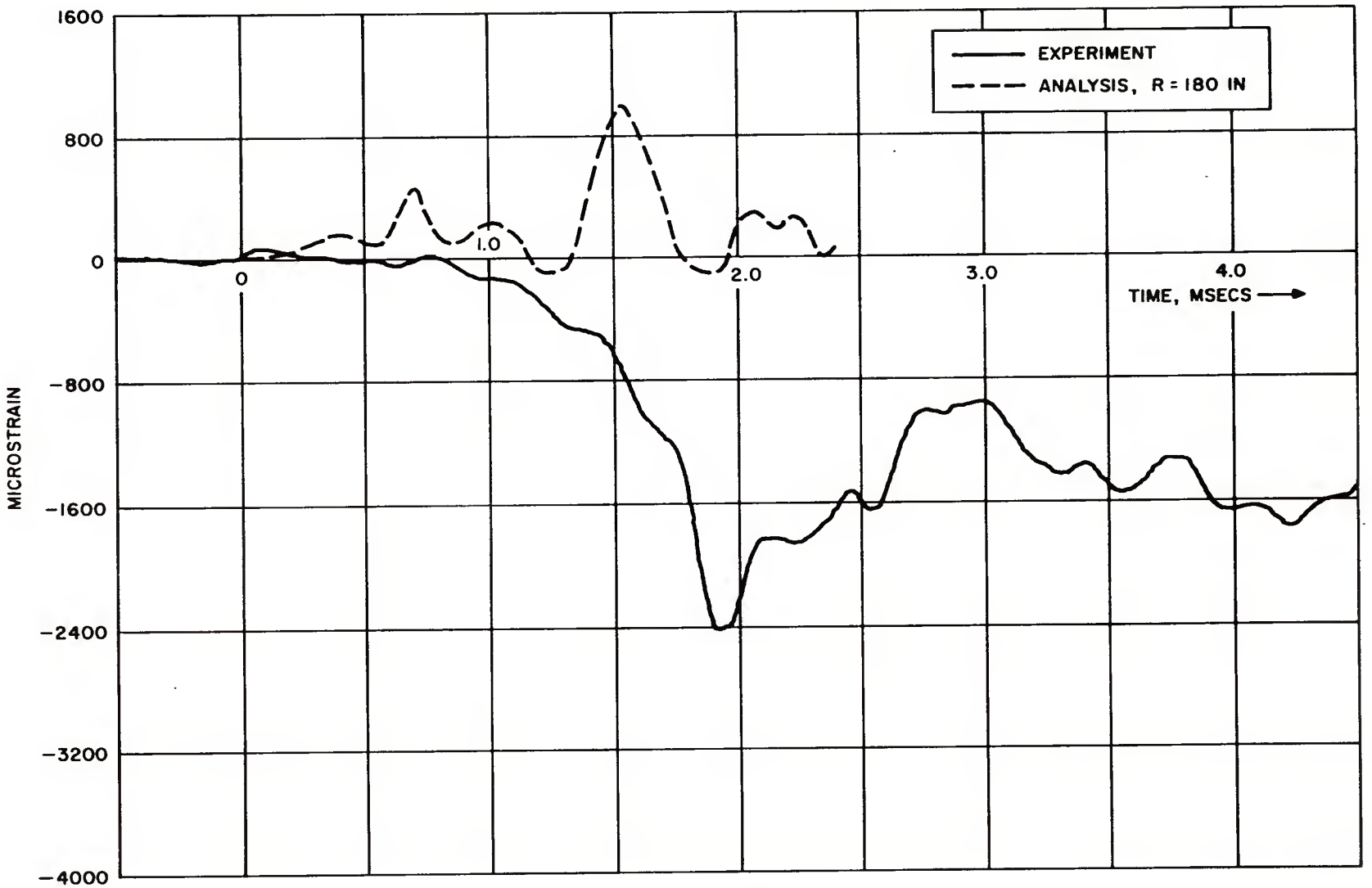

Figure 7.19. Comparison Between Experimental and Analytical Time-Variations of Panel Longitudinal Strain at Inner Surface Near Center Point. Channel C-06

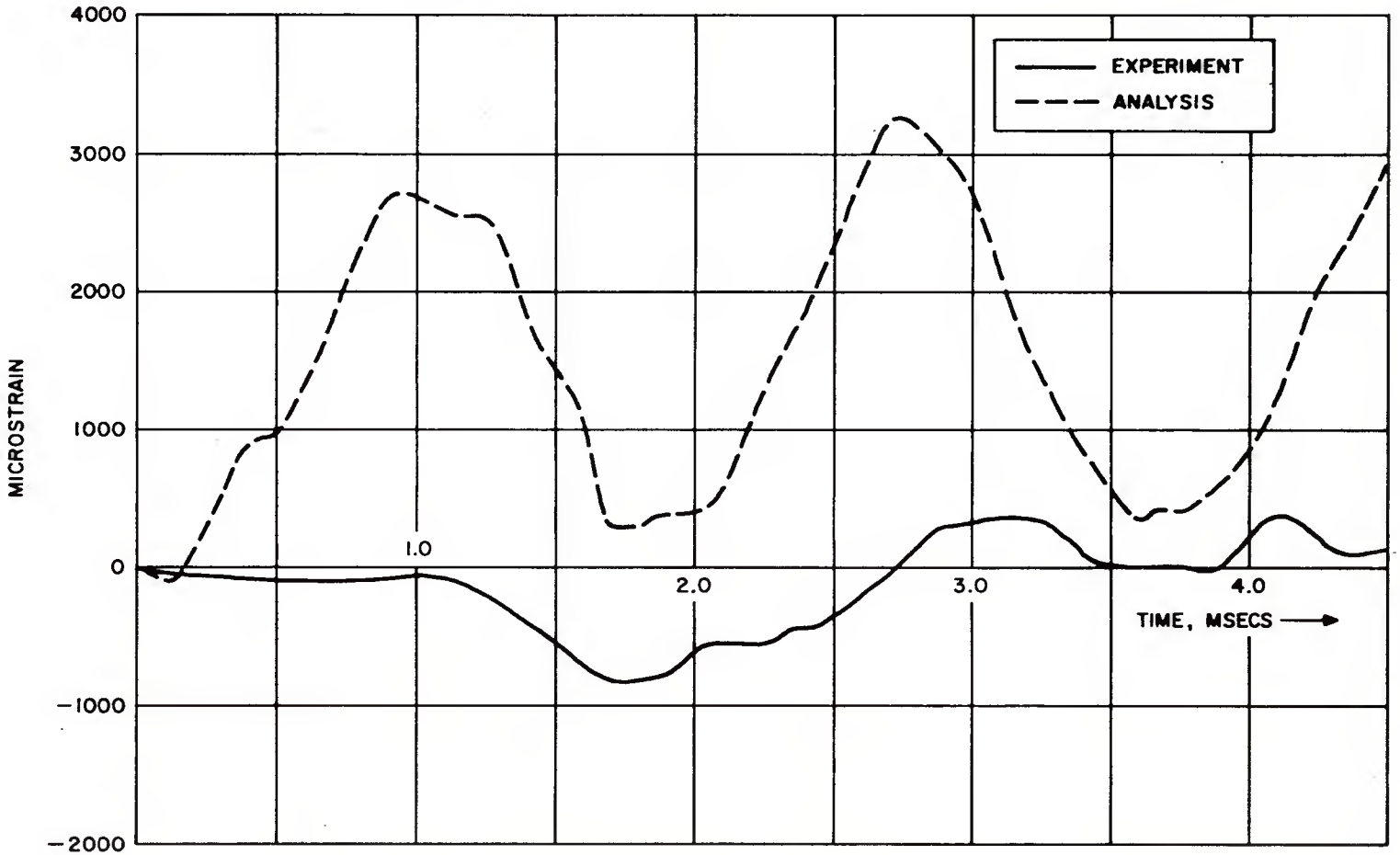

Figure 7.20. Comparison Between Experimental and Analytical Time-Variations of Stringer Strain at Center Mid-Depth Point. Channel A-07

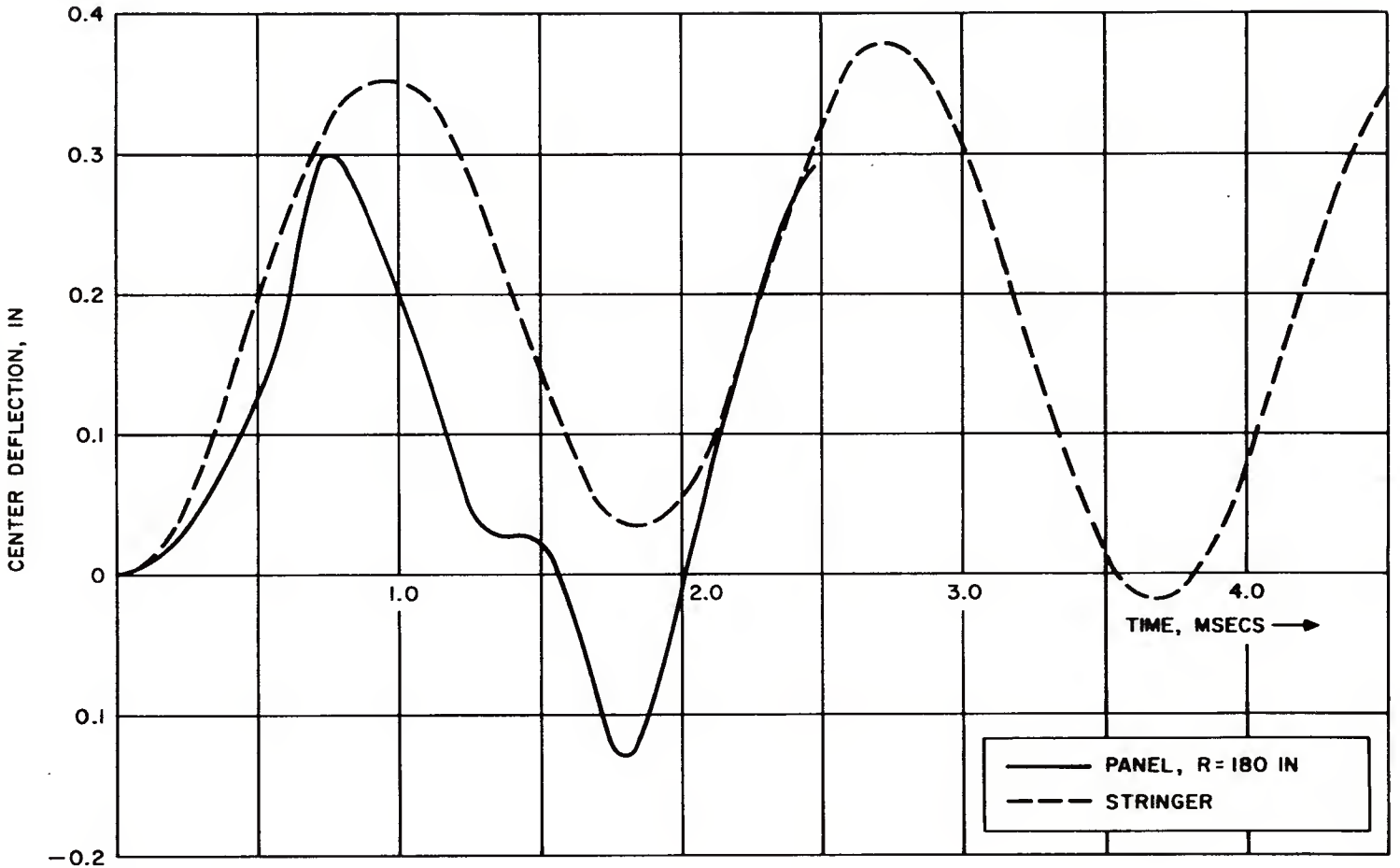

Figure 7.21. Time-Variations of Center Deflections for Panel and Stringer Elements. Analytical Results According to NOVA-2

SECTION 8
SUMMARY AND CONCLUSIONS

8.1 Summary

This report documents the motion and structural responses measured on a hovering and droned UH-1B helicopter subjected to a side-on blast during the DICE THROW event. The measurements are compared with corresponding analytical predictions based primarily on the helicopter code HELP and the aircraft structural code NOVA-2. The study is reported in six sections, the contents of which are summarized as follows:

Section 2 - The types of measurements and the data reduction procedures are outlined. The measurements and the experimental procedures are very similar to those for the PRE-MINE THROW IV test which are covered in Reference 1. Therefore, the detailed discussions have been confined to (a) the few changes from the previous test, and (b) the special problems faced in connection with the acquisition and processing of the new data. Summary tables of the experimental results are presented for each of the four recorders used, giving channel assignments, types and locations of sensors, and calibration data. The section includes oscillograph traces from the various channels, grouped to show similar or related types of data together. Each of these traces is of longer duration than its corresponding digitized curve (presented in a later section) which usually details the period of most significant blast-induced response. These "quick-look" traces also provide the reader with indications as to the pre-blast states which are needed in subsequent discussion. This section is concluded with a presentation of a sequence of consecutive frames from the real time oscillograph traces that were recorded during the test. They include traces for autopilot and remote control inputs as well as for altitude.

Section 3 - Following a presentation of two pressure measurements, one on the fin and one on a tail boom panel, a free blast field model is postulated. Utilizing (a) the pressure measurements to establish the actual peak free-field overpressure and pressure positive phase duration and (b) the ambient (pre-blast) conditions, an equivalent free-air (i.e., no ground reflection) nuclear blast model is established as required by the HELP code. The time-variation of the blast-induced loading on the panel as obtained from the tail boom pressure sensor, is curve-fitted for use in the NOVA-2 strain analysis presented in Section 7.

Section 4 - The analytical procedures in the HELP code for predicting the flapwise bending moments and flapping angles of the rotor blades are briefly discussed, following a presentation of relevant rotor and blade data. The experimental results for the flapwise bending moments at six blade stations are presented and compared with the corresponding predictions according to certain options

in the HELP code. The comparisons are (a) on the time variations of the bending moments at four fixed stations on the "red" blade and at two stations on the other blade, and (b) on the spanwise distributions of the extreme bending moment values. Finally, the experimental and analytical results for the blade flapping angles of both rotors are presented and discussed.

Section 5 - Following a presentation of the required vehicle and autopilot data, the analytical techniques are discussed with an emphasis on their assumptions and known limitations. The experimental results are then examined, pointing out some detected inconsistencies between related channels. These are then compared with their analytical predictions based on the MODEOP=1 option of the HELP code. Included in these comparisons are the following responses: (a) the vehicle altitude deviation, (b) the yaw, pitch, and roll attitudes and rates, and (c) the controls commanded by the autopilot in response to the blast encounter.

Section 6 - The experimental and analytical lateral bending moment responses at two fin and two tail boom stations are correlated in this section. The HELP code considers the vehicle to be rigid and therefore does not predict these responses. However, it does furnish the needed information for calculating externally the loads on the tail section. A four degree-of-freedom dynamic analysis, formulated especially for this application, utilizes the loads calculations to arrive at the predictions used in the correlations. In this analysis, the fin and the tail boom are represented by two non-uniform, weightless beams supporting seven lumped masses.

Section 7 - This section describes the attempts to correlate the experimental data with predictions based on the NOVA-2 code for the following responses:
(a) inner and outer surface strains, in the horizontal and vertical directions, at the center and near edges of a tail boom panel,
(b) extensional strains, at one point each on an upper longeron and a stiffener in the immediate vicinity of the panel. Panel curvature effects are examined analytically in an effort to explain the large noted differences between experiment and analysis.

8.2 Conclusions

During the correlation, a number of questions were raised concerning the calibration procedures and the validity of some of the provided calibration constants. The questions arose in connection with channels which (a) indicated physically unrealistic results, (b) displayed results inconsistent with results from related channels, and (c) gave unexpected poor correlations with predictions. The recorded data were checked. In some cases, errors were found and corrected. In others, it was clear that the constants furnished initially were incorrect, and there was no other choice but to resort to data from earlier calibration sequences or even from earlier tests. It turned out also that the test engineer

had placed too much reliance on earlier test calibration data and had not recalibrated the rate gyros for the DICE THROW IV.

With due considerations as to the uncertainties in some of the measurements and in the quality of the input data for the analyses, the following general conclusions are drawn:

1. The HELP code predictions correlate reasonably well with the measurements for those responses which are deemed most important for a blast encounter directly from the side. Included in these are the tail rotor blade flapwise bending moments, the yaw attitude deviation, and the yaw rate.

2. The NOVA-2 predictions for the strain responses of panels, stiffeners, and longerons fare poorly when compared with experiment.

3. The four degree-of-freedom dynamic analysis, which utilizes tail loadings based on the HELP calculations, provides a reliable means for estimating the most critical responses for the side-on encounter, namely the blast-induced lateral bending moments on the fin and the tail boom.

The detailed conclusions may be summarized as follows:

4. It has been possible to approximate the actual HE blast field by an equivalent free-air nuclear blast model. By taking the actual (measured) ambient conditions, a yield of 1.236KT, and a slant range of 2562 ft, the BLAST routine in HELP duplicates the peak free-field overpressure (p_{so} = 1.8 psi) and the pressure positive phase duration (t_p^+ = 343 msecs) which were measured during the test.

5. The measured early-phase, short-duration diffractive loading, obtained from the differential pressure gage on a tail boom panel, was fitted analytically with straight line segments. This approximate representation is sufficiently accurate and is used in the NOVA-2 structural response calculations.

6. The MODEOP=4 option in HELP treats each rotor independently and isolated from the vehicle and its controls. Its use is justified in calculating the flapwise bending moments of the tail rotor blades, because the maxima of these responses occur during the first 40 msecs or so, i.e., before vehicle motion and control effects become significant. On the other hand, the maxima of the corresponding main rotor blade responses occur at much later times; and one has less justification to use the MODEOP=4 option for the latter responses. Nevertheless, for reasons discussed in the text, this option has also been used for the main rotor blade calculations.

7. The experimental-analytical correlations of the tail rotor blade bending moments are deemed rather good, not only in terms of their time variations but also on the basis of the spanwise distributions of their peak values. These calculations use the first of two alternatives for computing the inflow velocity, namely the option NUOPT=1 wherein the induced flow is assumed to vary in a quasi-steady fashion based on the instantaneous flow conditions.

8. The tail rotor blade responses reach levels close to their yield allowables. In contrast, the corresponding main rotor blade bending moments attain peaks which are far below their yield allowables. The experimental-analytical correlations for the latter responses fare less favorably, especially in terms of their time variations. The poorer correlations are attributed to the inaccuracies in estimating the inflow velocities for a hovering rotor receiving the shock from a direction nearly parallel to its disk. For the main rotor blade calculations, both options for estimating the induced velocity (i.e., NUOPT=1 and 2) were considered.

9. For both rotors, the pre-blast blade bending moment variations as well as the pre-blast and post-blast flapping angles are much higher than predicted. Tail boom and fin interference effects are believed to be the primary cause for this lack of correlation.

10. The monitored rigid-body motion responses are affected to various degrees by large observed pre-blast motions and sizeable remote inputs. No attempt is made to include these factors in the analysis as they would involve extensive code modifications; and if effected, these modifications would be useful only for this single application. Furthermore, no appropriate data are available to relate <u>quantitatively</u> the measured remote control deflections to rotor blade angle variations as required by the analytical formulation.

11. The loss of altitude observed experimentally, amounting to about 12 ft, is attributed mainly to the inadvertent remote collective input. The analysis, which does not include the effects of remote inputs, predicts a 4 ft rise followed by a descent of about 7 ft with eventual stabilization about the pre-blast altitude.

12. Certain inconsistencies have been uncovered in the experimental results between the related yaw attitude and yaw rate channels. The calibration of the yaw rate channel is suspect. The indications are that the results of the yaw channel must be multiplied by 2.1 to reconcile them with the results of the azimuth (yaw) trace.

13. With the experimental results for the yaw rate adjusted by the 2.1 factor, the experimental-analytical comparisons are quite good for the first 0.7 seconds but start deteriorating thereafter due to remote pedal input which is unaccounted for in the analysis. However, the analysis duplicates fairly well the first and major negative peaks of the yaw attitude deviation and yaw rate which occur before t=0.7 secs.

14. Inconsistencies have also been detected in and between the pitch and roll channels. Attempts to locate the sources of the inconsistencies failed. The only conclusions that can be drawn from the efforts are: (a) one (or more) of the pitch and roll channels has calibration errors, and (b) there was a definite shift in the pitch rate trace zero level shortly after shock arrival.

15. The analytical result for the pitch attitude deviation shows a drop of 1.5 deg during the first 1.2 sec, and experimentally the drop amounts to 1.2 deg during the same period. For $t \geq 1.2$ secs, the agreement between experiment and analysis deteriorates; and again, the cause appears to be the observed significant F/A remote input which is unaccounted for in the analysis.

16. Although the pitch attitude correlation appears reasonable for the first second or so, the same cannot be said about the pitch rate correlation. This lack of correlation, especially during the early times when the largest yaw rates occur, is attributed to the difference between the experimental and analytical roll attitudes (not attitude deviations). The difference in levels between the predicted and measured pre-blast roll attitudes should be noted.

17. The experimental-analytical correlations for the roll attitude deviation and roll rate are also poor. The short-duration but large overpressure phase loading, which is neglected in the analysis, accounts in part for the differences between the analytical and experiment roll responses.

18. The peak fin lateral bending moments are underestimated by analysis, by about 20% at station 32 and 8% at station 52. The blast-induced tail boom force, which provides by far the largest loading component, is estimated from the MODEOP=1 calculations of the HELP code. A closer correlation would have been realized if the MODEOP=4 option of HELP had been exercised to include the high-frequency components of the tail rotor force resulting from the flexible motions of the rotor blades.

19. Except for the C-07 channel, the calibration data of which is suspect, the tail boom lateral bending moment correlation is also good. (The experimental peak value from the C-07 channel is way above the failure boundary; and yet the tail boom didn't break.) Analysis overpredicts slightly the peak response at tail boom station 47. The analytical and experimental indications are that the tail boom peak lateral bending moments reached levels just below the failure boundary. (Based on the pre-test calculations, the vehicle was positioned so that hopefully it would sustain a more severe damage than it did with a 1.8 psi shock encounter.)

20. The panel, stringer, and longeron strain correlations are poor. The panel responses are sensitive to skin curvature, edge conditions, and sensor locations especially when near edges. The panel curvature must be known accurately at blast intercept time in order to analytically predict the snap-through responses. Too many uncertainties are present in a field test such as DICE THROW; and only well-controlled measurements (e.g., laboratory tests) can provide the data to make fair evaluations of the NOVA-2 prediction capabilities.

21. Another factor which degrades the correlation of strains is the omission in the NOVA-2 analysis of the coupling between structural members. Due to other uncertainties, it is difficult to quantify the importance of coupling effects in the correlation.

REFERENCES

1. Zartarian, G., Cole, E.L., and Ayvazian, M., Correlation Study of the UH-1B Helicopter Blast Test Results From the Pre-Mine THROW IV Event. Defense Nuclear Agency Report DNA 3704F, 28 March 1975. Final Report, Contract No. DNA 001-73-C-0047, Prepared by Kaman AviDyne, A Division of Kaman Sciences Corporation.

2. Zartarian, G., Pre-Test Analysis for the Blast Response of the UH-1B Helicopter. DICE THROW Project No. 107. Report Submitted by Robert D. Mayerhofer, Project Engineer, Informal U.S. Army Ballistic Research Laboratory Report, Aberdeen Proving Ground, Maryland, August 1976. Contract No. DAAD05-76-C-0772.

3. Zartarian, G., Thompson, J.H., and Hobbs, N.P., Analysis of Helicopter Response to Nuclear Blast (U), in three volumes, Defense Nuclear Agency Reports DNA 2910F-1, DNA 2910F-2, and DNA 2910F-3, under Contract No. DASA01-70-C-0092. (Kaman AviDyne Reports KA TR-72(R), Vols. I, II, III.), November 1972.

   Volume I. Analytical Formulations
   Volume II. Computer Program Description
   Volume III. Example Application (CONFIDENTIAL)

4. NOVA-2 - A Digital Computer Program for Analyzing Nuclear Overpressure Effects on Aircraft. Volumes I and II, Technical Report No. AFWL TR-75-262, August, 1976. Report Prepared by Kaman AviDyne, a Division of Kaman Sciences Corporation, for the Air Force Weapons Laboratory, Air Force Systems Command, Kirtland Air Force Base, New Mexico.

5. Schramm, M., Real-Time Simulation of a Helicopter Rotor on an Analog Computer. Simulation, 1970, pp. 231-237. (A Publication of Simulation Councils, Inc.)

6. Bisplinghoff, R.L., Ashley, H., and Halfman, R.L., "Aeroelasticity", Second Printing, 1957, Addison-Wesley Publishing Company, Inc., Reading, Massachusetts.

DISTRIBUTION LIST

No. of Copies	Organization
12	Commander Defense Documentation Center Attn: DDC-TCA Cameron Station Alexandria, VA 22314
3	Director Defense Advanced Research Project Agency Attn: Tech Lib NMRO PMO 1400 Wilson Boulevard Arlington, VA 22209
4	Director of Defense Research and Engineering Attn: DD/TWP DD/S&SS DD/T&SS AD/SW Washington, DC 20301
2	Director Weapons Systems Evaluation Gp Attn: CPT Donald E. McCoy, USN Document Control Washington, DC 20305
1	Director Institute for Defense Analyses Attn: IDA Librarian, Ruth S. Smith 400 Army-Navy Drive Arlington, VA 22202
2	Asst to the Secretary of Defense (Atomic Energy) Attn: Document Control Donald R. Cotter Washington, DC 20301
1	Office Secretary of Defense Office DDR&E Attn: Mr. J. Persh, Staff Specialist Materials and Structures Washington, DC 20301
1	Director Defense Intelligence Agency Attn: DT-1C/Dr. J. Vorona DT-7D/E. O. Farrell DT-2/Wpns & Sys Div Technical Library Washington, DC 20301
6	Director Defense Nuclear Agency Attn: SPSS/Dr. E. Sevin SPAS/Mr. J. Moulton STSP STVL/Dr. La Vier RATN/Cdr Alderson Washington, DC 20305
6	Director Defense Nuclear Agency Attn: DDST/Mr. P. Haas DDST/Mr. M. Atkins STTL/Tech Lib (2 cy) STSI/Archives Washington, DC 20305
1	Director Defense Communications Agency Attn: NMCSSC (Code 510) Washington, DC 20305
1	Director Joint Strategic Target Planning Staff JCS Attn: Sci and Tech Info Lib Offutt AFB Omaha, NB 68113

DISTRIBUTION LIST

No. of Copies	Organization
2	Director National Security Agency ATTN: E. F. Butala, R154 P. E. Deboy, NSA 5232 Ft. George G. Meade, MD 20755
1	Commander US Army Materiel Development and Readiness Command ATTN: DRCDMA-ST 5001 Eisenhower Avenue Alexandria, VA 22333
1	Commander US Army Aviation Research and Development Command ATTN: DRSAV-E 12th and Spruce Streets St. Louis, MO 63166
1	Director US Army Air Mobility Research and Development Laboratory Ames Research Center Moffett Field, CA 94035
1	Commander US Army Electronics Command ATTN: DRSEL-RD Fort Monmouth, NJ 07703
1	Commander US Army Missile Research and Development Command ATTN: DRDMI-R Redstone Arsenal, AL 35809
1	Commander US Army Tank Automotive Development Command ATTN: DRDTA-RWL Warren, MI 48090
2	Commander US Army Mobility Equipment Research & Development Command ATTN: Tech Docu Cen, Bldg. 315 DRSME-RZT Fort Belvoir, VA 22060
1	Commander US Army Armament Materiel Readiness Command ATTN: DRSAR-LEP-L (Tech Lib) Rock Island, IL 61201
5	Commander US Army Harry Diamond Labs ATTN: DRXDO-TI DRXDO-TI/012 Mr. F. N. Wimenitz Mr. Jim Gaul DRXDO-NP Mr. J. Gwaltney DRXDO-RBH Mr. P. A. Caldwell 2800 Powder Mill Road Adelphi, MD 20783
1	Commander US Army Natick Research and Development Command ATTN: DRXRE, Dr. D. Sieling Natick, MA 01762
1	Commander US Army Foreign Science and Technology Center ATTN: Rsch & Data Branch Federal Office Building 220 7th Street, NE Charlottesville, VA 22901

DISTRIBUTION LIST

No. of Copies	Organization
1	Director US Army TRADOC Systems Analysis Activity ATTN: ATAA-SL (Tech Lib) White Sands Missile Range NM 88002
3	Commander US Army Nuclear Agency ATTN: ATCN-W/CPT Ader CDINS-E Technical Library 7500 Backlick Road Springfield, VA 22150
1	Commander US Army Communications Command Attn: Technical Library Kirtland AFB, NM 87115
3	Director US Army Advanced BMD Technology Center Attn: CRDABH-X/J. Davidson CRDABH-S/Mr. M. Capps N. J. Hurst Huntsville, AL 35807
1	Commander US Army Research Office P.O. Box 12211 Research Triangle Park NC 27709
2	Director Defense Civil Preparedness Agency Attn: Mr. George Sisson RF-SR Technical Library Washington, DC 20301
1	Superintendent US Naval Postgraduate School Attn: Code 2124/Tech Rpts Lib Monterey, CA 93940
5	Chief of Naval Research Attn: Code 464/Jacob L. Warner Code 464/Thomas P. Quinn N. Perrone (2 cy) Department of the Navy Washington, DC 20360
2	Chief of Naval Operations Attn: OP-03EG OP-985F Department of the Navy Washington, DC 20350
1	Director Strategic Systems Projects Ofc Attn: NSP-43, Tech Lib Department of the Navy Washington, DC 20360
3	Commander US Naval Surface Weapons Center Attn: Code 1224/Navy Nuclear Programs Office Code 730/Tech Lib Francis B. Porzel Silver Spring, MD 2091)
1	Commander US Naval Surface Weapons Center Attn: Technical Library Dahlgren, VA 22448
1	Commander US Naval Weapons Evaluation Facility Attn: Document Control Kirtland AFB Albuquerque, NM 87117
2	Director US Naval Research Laboratory Attn: Code 2027/Tech Lib Code 8440/F. Rosenthal Washington, DC 20390

DISTRIBUTION LIST

No. of Copies	Organization
1	HQ USAF (SAFRD) Washington, DC 20330
1	HQ USAF (INATA) Washington, DC 20330
1	HQ USAF (PRF) Washington, DC 20330
2	AFSC (DLCAW Tech Lib) Andrews AFB Washington, DC 20331
2	AFATL (ATRD R. Brandt) Eglin AFB, FL 32542
1	RADC (FMTLD Docu Lib) Griffiss AFB, NY 13340
1	AFSWC (SWTSX) Kirtland AFB, NM 87117
1	AFWL (SUL) Kirtland AFB, NM 87117
3	AFWL (Robert Port; DEV Jimmie L. Bratton; DEV M. A. Plamondon) Kirtland AFB, NM 87117
1	Commander-in-Chief Strategic Air Command Attn: NRI-STINFO Lib Offut AFB, NB 68113
1	AFML (MAMD/Dr. T. Nicholas) Wright-Patterson AFB OH 45433
1	FTD (TDPTN) Wright-Patterson AFB OH 45433
1	AFIT (Lib Bldg. 640, Area B) Wright-Patterson AFB OH 45433
1	US Energy Research and Development Administration Division of Headquarters Svcs Attn: Doc Control for Classified Tech Lib Library Branch G-043 Washington, DC 20545
1	Director NASA Scientific and Technical Information Facility Attn: SAK/DL P.O. Box 8757 Baltimore/Washington International Airport, MD 21240
1	The Boeing Company Attn: Aerospace Library P.O. Box 3707 Seattle, WA 98124
1	Calspan Corporation Attn: Technical Library P.O. Box 235 Buffalo, NY 14221
1	Civil/Nuclear Systems Corporation Attn: Robert Crawford 1200 University N.E. Albuquerque, NM 87102
1	J. G. Engineering Research Associates 3831 Menlo Drive Baltimore, MD 21215